Thèse présentée pour obtenir le grade de

DOCTEUR DE L'ECOLE POLYTECHNIQUE

Spécialité : **Physique - Sciences des Matériaux**

par

Fabien BRUNEVAL

**Exchange and Correlation
in the Electronic Structure of Solids,
from Silicon to Cuprous Oxide:
GW Approximation and beyond**

Soutenue le 7 octobre 2005 devant le jury composé de

Pr. Antoine Georges	Président
Pr. Giovanni Onida	Rapporteur
Dr. Christophe Delerue	Rapporteur
Dr. Martine Gautier-Soyer	Examinatrice
Dr. Lucia Reining	Directrice
Dr. Nathalie Vast	Directrice

Remerciements

Bien que ne faisant apparaître qu'un seul nom en première page, un travail de thèse n'est pas un effort individuel. Je tiens à exprimer ma gratitude à une multitude de personnes qui m'ont accueilli, encouragé, conseillé, aidé, envoyé en conférence, et tout simplement, fait confiance.

Ces trois années passées au Laboratoire des Solides Irradiés de l'Ecole Polytechnique se sont déroulées dans une excellente ambiance, en particulier, grâce à son directeur Guillaume Petite et à son équipe administrative et technique Catherine Julien, Marie-Madeleine Lemartinel, Christine Houy, Bernard Allali et Bernard Jouéo.

Dans l'ordre chronologique, je remercie tout d'abord les deux personnes qui m'ont donné envie de me plonger dans la physique numérique et m'ont accueilli au LSI pour mon stage de DEA et de fin d'études : Nathalie Vast et Silvana Botti.

Je remercie mes deux directrices de thèse, Nathalie Vast et Lucia Reining, pour leur encadrement, mais aussi pour la liberté dont j'ai joui quant aux orientations scientifiques de mes travaux. Grâce à elles, j'ai profité d'excellentes conditions de travail et j'ai été encouragé à présenter mon activité à des conférences variées. Ces quelques mots sont bien faibles pour exprimer toute ma reconnaissance.

Je remercie l'ensemble de l'équipe théorie du LSI, ceux qui restent, ceux qui sont arrivés et ceux qui sont partis, pour leur aide scientifique, leur compagnie, leur amitié : (par ordre approximatif d'apparition) Silvana Botti, Valerio Olevano, Francesco Sottile, Marc Hayoun, Olivier Hardouin-Duparc, Andrea Cucca, Hansi Weissker, Philippe Baranek, Virginie Trinité, Wojtek Welnic, Jorge Serrano, Louise Dash, Christine Georgetti, Valérie Veiniard, Jelena Sjakste, et Xavier Andrade-Valencia. J'aurais aimé dire quelques mots dédiés à chacun, mais pour cela, il aurait fallu rajouter un chapitre complet à ce manuscript. Je tiens notamment à louer la patience des différents occupants de la pièce 05 10 29 : Tolis Marinopoulos, Madeleine Meyer, Matteo Gatti et Françoise Maury-Levesque, qui ont supporté ma symphonie quotidienne en clavier mineur.

Mes collègues expérimentateurs m'ont permis d'élargir mon horizon. Je remercie particulièrement Manuel Izquierdo, Nick Barrett et Fausto Sirotti. Les réseaux européens NANOPHASE et NANOQUANTA sont à l'origine de rencontres et de collaborations fructueuses avec d'autres chercheurs eu-

ropéens, en particulier : Rodolfo Del Sole, Patrick Rinke, Gian-Marco Rignanese et Xavier Gonze. Merci également à Brice Arnaud pour ses calculs sur Cu_2O, mais aussi pour sa sympathie.

Je tiens à exprimer ma reconnaissance au jury de cette thèse : les rapporteurs, Christophe Delerue et Giovanni Onida, qui ont accepté de lire ce manuscript en plein cœur de l'été ; Martine Gautier-Soyer qui a permis de teinter ce jury d'une touche expérimentale ; Antoine Georges, enfin, qui m'a fait l'honneur de présider ce jury.

La lisibilité et la correction de ce manuscript ont été grandement améliorées par les lectures et relectures de Miguel Marques, Silvana Botti, Lucia Reining et Nathalie Vast. La rigueur et la pertinence de leurs remarques m'ont beaucoup aidé, aussi bien en ce qui concerne la grammaire anglaise que l'énergie d'ionisation des systèmes finis.

Ces remerciements seraient incomplets, si je ne soulignais le rôle de ma famille, mes parents et mes soeurs. Pour finir, mes pensées vont à Agnès qui m'a soutenu durant toute ma thèse, qui a fait l'effort d'apprendre ce qu'étaient un photon et un electron.

Contents

Notations

Here are some notations useful for the understanding of the manuscript.

$\mathbf{r}$	space index
t	time index
σ	spin index
1	index standing for position, time and spin $(\mathbf{r}_1, t_1, \sigma_1)$
$\mathbf{k}$	Brillouin zone point
$\mathbf{G}$	reciprocal lattice vector
$\mathbf{q}$	momentum transfer (i.e. difference between two $\mathbf{k}$-points)
$T[...]$	Wick's time-ordering operator
$\hat{S}$	time evolution operator
$\psi(\mathbf{r})$	annihilation field operator in Schrödinger picture
$\psi^\dagger(\mathbf{r})$	creation field operator in Schrödinger picture
$\hat{\psi}(1)$	annihilation field operator in Heisenberg picture
$\hat{\psi}^\dagger(1)$	creation field operator in Heisenberg picture
$\Psi(\mathbf{r}_1, \ldots, \mathbf{r}_N)$,	
$|N\rangle$,	
or $|N, 0\rangle$	ground-state wavefunction of the N particle system
$|N, i\rangle$	wavefunctions labeled i of the N particle system
$E_{N,i}$	energy corresponding to wavefunction $|N, i\rangle$
ϵ_i	ionization or affinity energy (difference of total energies)
$\phi_i(\mathbf{r})$	one-particle wavefunction corresponding to state i
ϵ_i	energy of state i corresponding to wavefunction $\phi_i(\mathbf{r})$

$U(1)$ or $v_{ext}(\mathbf{r}, t)$	external potential
$V(1) = U(1) + v_h(1)$	total classical potential
$G(1, 2)$	one-particle Green's function
$A(1, 2)$	spectral function of the one-particle Green's function
$G_0(1, 2)$	non-interacting one-particle Green's function
G_{KS}	Kohn-Sham one-particle Green's function
$G_2(1, 2; 1', 2')$	two-particle Green's function
$L(1, 2; , 1', 2')$	four point polarizability
$v(1, 2) = \frac{1}{\|\mathbf{r}_1 - \mathbf{r}_2\|}\delta(t_1 - t_2)$	Coulomb interaction
$W(1, 2)$	screened Coulomb interaction $W = v + v\chi v$
$\Sigma(1, 2)$	self-energy
Σ_x	Fock operator or bare exchange self-energy
$\Sigma_c = \Sigma - \Sigma_x$	correlation part of the self-energy
$\tilde{\Gamma}(1, 2; 3)$	irreducible vertex function
$\chi(1, 2) = \delta\rho(1)/\delta U(2)$	reducible polarizability
$\tilde{\chi}(1, 2) = \delta\rho(1)/\delta V(2)$	irreducible polarizability
$\chi_0(1, 2) = -iG(1, 2)G(2, 1)$	RPA irreducible polarizability
$\varepsilon^{-1}(1, 2) = \delta V(1)/\delta U(2)$	inverse testcharge-testcharge dielectric function
$\Xi(1, 2; 3, 4)$	kernel of the Bethe-Salpeter equation
$\rho(\mathbf{r})$	ground-state electronic density
$v_h(\mathbf{r}) = \int d\mathbf{r}' v(\mathbf{r} - \mathbf{r}')\rho(\mathbf{r}')$	Hartree potential
$v_{xc}(\mathbf{r}) = \delta E_{xc}/\delta\rho(\mathbf{r})$	exchange-correlation potential
$f_{xc}(\mathbf{r}, \mathbf{r}', t - t')$	exchange-correlation kernel
$\chi_{\mathrm{KS}}(1, 2)$ $= -iG_{\mathrm{KS}}(1, 2)G_{\mathrm{KS}}(2, 1)$	non-interacting response function of the Kohn-Sham system

Feynman diagrams

Here are some Feynman diagrams useful for the understanding of the manuscript.

Feynman diagram	Symbol	Meaning
	G_0 or G_{KS}	non interacting fermion
	G	interacting fermion
	v	Coulomb interaction
	W	screened Coulomb interaction
	Σ	self-energy
	$G_2(1, 2; 3, 4)$	two-particle Green's function
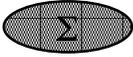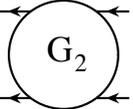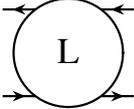
Feynman diagram	Symbol	Meaning
L	$L(1,2;3,4)$	4-point polarizability
L	$L(1,2;1,2)$ or χ	2-point polarizability
(zigzag line)	χ_0^{-1}	inverse independent particle polarizability
(coil line)	f_{xc}	TDDFT kernel
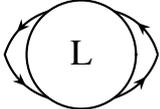
Introduction

Electronic structure of crystals is a polymorphic name that covers a wide range of properties of electrons in periodic solids. For instance, it can refer to the probability to find an electron at space point $\mathbf{r}$, in other words, to the electronic density. It can refer to the energy needed to extract an electron of the material, the ionization energy, or alternatively, the energetic gain when an electron is added to the system, the electron affinity. It can also stand for the response of the electrons of the solid to an external perturbation (a photon or a fast electron). All these properties characterize the electronic structure of the solid. They describe indeed different aspects. Some of them are ground-state properties, others correspond to excited states. Some of them conserve the number of particles, others do not.

As a consequence, the properties that are generically called "electronic structure" are measured with distinct experimental setups, e.g. direct and inverse photoemission, optical absorption, electron energy-loss... And analogously, the theoretical description and prediction of these properties require distinct frameworks. This thesis work will handle the issue of the electronic structure of the cuprous oxide, Cu_2O. Therefore, different theoretical methods will be used and results will be compared to a wide range of experimental techniques.

The present manuscript contains different parts, which may seem at first sight independent. It is therefore instructive to draw here quickly, what has been the historical development of this work, from the original project to the final achievements.

Three years ago, I started this thesis work with the purpose to describe theoretically the electronic structure of copper oxides, begining with the simplest one Cu_2O, going to the antiferromagnetic CuO, and possibly to the CuO_2 planes of high T_c superconducting cuprates. The cuprous oxide, Cu_2O, with its closed electronic d shell was thought as a starting point to initiate the study of the Cu–O bonding in the different oxides. Cu_2O is also interesting because spectacular excitonic series have been measured in its optical absorption or reflectivity spectra during the sixties [1–3].

However, it has been quickly clear that the usual electronic structure methods, as density-functional theory (DFT) or even the state-of-the-art GW approximation of the many-body perturbation theory (MBPT), were unable to give a proper description of Cu_2O. Comparison with existing pho-

toemission or optical measurements were surprisingly bad. This unexpected failure changed the aims of my thesis, which turned into the analysis and the cure of the shortcomings of the theoretical methods applied to Cu_2O. I have been motivated to develop a number of theoretical and technical tools that, as I hope, will also be useful in future studies of other materials.

The failure of the state-of-the-art GW approximation could come from two distinct reasons: either the current implementation of the method that worked well with simpler materials uses further assumptions, that are not anymore valid with the complex oxide Cu_2O; or the GW approximation itself is not enough to account for the electronic structure of Cu_2O.

In order to check which hypothesis was the right one, I had first to identify, analyse and avoid all further approximations used in a standard GW, as it has most often been performed for 20 years. This part required some code and method development in order to remove the technical approximations that were used to make calculations easier, in our code or in most existing codes. This is what part II of this manuscript is concerned with. Of course, the implementation of new pieces of code had to be checked on simple textbook examples, before being applied to copper oxide. That is why part II provides many results on bulk silicon and solid argon. This methodological part aims at removing the single plasmon-pole approximation that models the dynamical behavior of the screened Coulomb interaction W in GW. It has also the purpose of going beyond the usual perturbative evaluation of GW and to perform real self-consistent calculations within GW or within simpler approximations. The application of these developments to cuprous oxide are postponed to part IV, where all results concerning Cu_2O are gathered.

Alternatively, if the failure of the GW approximation were really a breakdown of the first-order perturbation theory in W (the coupling constant of the perturbation procedure), one would have to include further correcting terms to improve the results: these terms are commonly called "vertex corrections". Due to their complexity, there is no unique method in literature to approximate them. Having in mind the purpose of applying vertex corrections to cuprous oxide, I had, first of all, the general task to define a proper scheme to do that, and to provide meaningful approximations to it. The basic idea was to start from the earlier developments made in our group concerning the comparison between time-dependent DFT (TDDFT) and MBPT [4–6] in order to simplify the otherwise untractable task of calculating vertex corrections. Deep insight in the respective role of the two theories was required and the study finally ended with theoretical achievements that went farther than the initial project. Part III exposes first the advances made in the understanding of the link between TDDFT and MBPT with a new simple equation that derives the crucial, but unfortunately unknown, kernel of TDDFT from the central quantity of MBPT, the self-energy. Second, part III shows how the same kind of

ideas can be used in the other direction (namely, use TDDFT in order to progress within MBPT), to make the calculation of vertex corrections easier. These developments were applied in practice to simple materials: once again bulk silicon and solid argon. In fact, even though the derived vertex correction are "simpler", the calculations remain orders of magnitude more complicated than the usual GW ones. It is still out of reach to apply these developments to cuprous oxide at present. Nevertheless, this derivation and study of vertex corrections allowed me to draw the general conclusion that strong cancellations between vertex corrections occur.

The last part of the present work (part IV) presents all my results concerning Cu_2O, from ground-state DFT studies to new self-consistent GW results, and also from theoretical data to experimental measurements. This part starts with a standard electronic structure study, first DFT geometrical structure, Kohn-Sham band structure and characterization of the orbitals, then standard perturbative GW evaluation of the quasiparticle band structure. As said earlier, this study unexpectedly fails, in particular, for the band gap and the optical threshold. That is why the methods developped in the previous parts are indeed needed in the study of Cu_2O. Moreover, existing valence band photoemission experiments did not allow one to detect some of the states found in our and previous bandstructure calculations. However, the experiments were performed on polycrystalline samples and therefore yielded spectra resulting from an integration over the whole Brillouin zone. This was the motivation to apply for beamtime at the synchrotron Elettra in Trieste, Italy together with my collaborators (theoreticians and experimentalists). The purpose was to obtain precise angle-resolved photoemission spectra of the valence states of Cu_2O. This means $\mathbf{k}$-point resolved information. After a one-week experimental shift at Elettra, an important part of the present work was to compare our state-of-the-art measurements to the theoretical data, taking into account the experimental aspects, as photoemission cross-sections, evaluation of the causes of experimental uncertainties... Indeed, it turned out that a careful comparison of state-of-the-art experimental and theoretical approaches could remove all existing or seeming contradictions, within the remaining uncertainty of the respective approaches. This is a significant part of the present study of the electronic structure of Cu_2O. This part ends with the calculation of energy-loss and optical absorption spectra of cuprous oxide, the latter being now also in good agreement with experiment.

The theories and methods used throughout this text are extensively described in the first part of the manuscript. It seemed important to me to provide an accurate account for the theoretical background, because most of the present work deals with improvements of existing methods, or going beyond some piece of the theory. In order to explain the achievements, one first needs to have clearly in mind the existing grounds. Let me then open this text with the part concerning the theoretical background my work is

based on.

Part I

Theoretical background

Chapter 1

Presentation of the tremendous problem of electrons in solids

The description of interacting electrons in solids is a formidable task. The problem is not to find the equation of motion of the electrons: it has been known for decades. It is the famous non-relativistic Schrödinger equation for the electrons of mass m_e and the nuclei of mass M_I:

$$\mathcal{H} = \sum_i -\frac{\hbar^2 \nabla_i^2}{2m_e} + \sum_I -\frac{\hbar^2 \nabla_I^2}{2M_I} + \frac{1}{2} \sum_{i \neq j} \frac{e^2}{|\mathbf{r}_i - \mathbf{r}_j|}$$
$$- \sum_{iI} \frac{Z_I e^2}{|\mathbf{r}_i - \mathbf{R}_I|} + \frac{1}{2} \sum_{I \neq J} \frac{Z_I Z_J e^2}{|\mathbf{R}_I - \mathbf{R}_j|}, \quad (1.1)$$

where the index i runs over electrons and I runs over nuclei. These are just the kinetic terms of nuclei and electrons, plus the instantaneous Coulomb interaction between all pairs of bodies. The problem is "simply" to solve the previous equation. The solution would require in principle to diagonalize this equation in order to obtain the energies and the wavefunctions Ψ. However, the wavefunctions are functions of all electronic variables and all nuclear variables $\Psi(\mathbf{r}_1, \ldots, \mathbf{r}_N, \mathbf{R}_1, \ldots, \mathbf{R}_M)$. It is known that the problem of two interacting particles in an arbitrary external potential can not be solved analytically in quantum mechanics, what about the problem of $N + M$ interacting bodies, with N and M of the order of the Avogadro number $\sim 10^{23}$ for a macroscopic solid?

The only hope to evaluate the solutions of the Schrödinger equation (1.1) is first to simplify the tremendous Schrödinger equation, and then to approach the problem with a different philosophy. This will be briefly outlined in the following.

Atomic units ($\hbar = e^2 = m_e = 1$) will be used from now on, and troughout the whole manuscript. Therefore, energies are evaluated in Hartree,

lengths in Bohr radius, masses in electron mass etc.

1.1 Electronic Hamiltonian in solids within Born-Oppenheimer approximation

A first harmless approximation is made in almost all studies of the static properties of solids. The so-called Born-Oppenheimer approximation (or adiabatic approximation) is based on the observation that the masses of nuclei and electrons are orders of magnitude different ($M_I \gg 1$). It is therefore sensible to decouple the fast dynamics of the electronic systems and the slow motion of the nuclei (due to their large mass). The nuclei can hence be thought as fixed during the motion of the electronic degrees of freedom. The nuclear variables are thus considered as parameters of the electronic equation,

$$\mathscr{H}_{\mathrm{BO}} = \sum_i -\frac{\nabla_i^2}{2} + \frac{1}{2}\sum_{i\neq j}\frac{1}{|\mathbf{r}_i - \mathbf{r}_j|} - \sum_{iI}\frac{Z_I}{|\mathbf{r}_i - \mathbf{R}_I|}. \qquad (1.2)$$

This Hamiltonian can be written using the second quantization framework (see, e.g., chapters 2 and 3 of reference [7]):

$$\mathscr{H}_{\mathrm{BO}} = \int d\mathbf{r}\psi^\dagger(\mathbf{r})h(\mathbf{r})\psi(\mathbf{r}) + \frac{1}{2}\int d\mathbf{r}d\mathbf{r}'\psi^\dagger(\mathbf{r})\psi^\dagger(\mathbf{r}')\frac{1}{|\mathbf{r}-\mathbf{r}'|}\psi(\mathbf{r}')\psi(\mathbf{r}), \ (1.3)$$

where the one-body Hamiltonian $h(\mathbf{r})$ contains the kinetic energy, plus the nuclear potential acting on the electrons and where $\psi^\dagger$ and ψ are the so-called creation and annihilation field operators of the second quantization in Schrödinger picture. The equation is now an equation of the electronic degrees of freedom only. One can further notice that the knowledge of the full $\Psi(\mathbf{r}_1,\ldots,\mathbf{r}_N)$ is actually not needed to determine the total energy of the electronic system. Instead, the knowledge of the two-particle density matrix

$$\begin{aligned}\rho_2(\mathbf{r}_1,\mathbf{r}_2,\mathbf{r}_1',\mathbf{r}_2') &= \langle N|\psi^\dagger(\mathbf{r}_1)\psi^\dagger(\mathbf{r}_2)\psi(\mathbf{r}_1')\psi(\mathbf{r}_2')|N\rangle && (1.4) \\ &= \frac{N(N-1)}{2}\int d\mathbf{r}_3\ldots d\mathbf{r}_N d\mathbf{r}_3'\ldots d\mathbf{r}_N'\Psi^*(\mathbf{r}_1,\mathbf{r}_2,\mathbf{r}_3,\ldots,\mathbf{r}_N) \\ &\quad \times\Psi(\mathbf{r}_1',\mathbf{r}_2',\mathbf{r}_3',\ldots,\mathbf{r}_N'), && (1.5)\end{aligned}$$

with $|N\rangle$ standing for the N electron ground-state wavefunction, is clearly sufficient to evaluate $\langle N|\mathscr{H}_{\mathrm{BO}}|N\rangle$. This can be understood by the fact that the Coulomb interaction involves bodies only two by two and h involves the electrons one by one. One can think of giving up with the calculation of the full wavefunction and prefering to deal with the "integrated" variable ρ_2, which only depends on 4 space variables. *Integrated* variable means that

the operator has been obtained from the full N variable wavefunction by integrating all space variable, but a few. Here for the two-particle density matrix all but two have been integrated.

1.2   Wavefunction methods or "integrated" variable methods

The purpose of quantum mechanical calculations is to predict the expectation values of observables. In other words, they primarily aim at calculating and interpreting what experiments can measure. Of course, the knowledge of wavefunctions permits one to answer all questions probed by any experiment.

The quantum chemistry methods generally deal directly with the wavefunctions. For instance, the Hartree-Fock approximation gives the variationally best wavefunction, which can be written as a single Slater determinant. Furthermore, as the Slater determinants form a basis on the Hilbert space of the wavefunctions, it is reasonable to look for the true wavefunctions as a linear combinations of Slater determinants (maybe millions of them): this is the configuration interaction method. Also the variational Monte-Carlo method is based on the optimization of the wavefuntions [8]. Unfortunately, all these methods, though systematic, suffer from an exploding computational time with the number of electrons treated (generally $\sim N^{4-6}$). Fortunately, the number of electrons is low in quantum chemistry applications.

On the contrary, the application of the Schrödinger equation (1.2) to solids quickly meets the problem of the large number of electrons and the wavefunction methods can only be implemented for restricted basis sets (gaussians...) for practical reasons. Fortunately, as said earlier, the knowledge of the whole wavefunction is not necessary, as one is interested in certain observables. For instance, one wants to evaluate the equilibrium lattice parameter of a crystal, the ionization energy, the electron affinity of a solid, or the dielectric properties... One can therefore abandon the idea of describing precisely all the electrons of the system, and just concentrate on the way to calculate the observable without having to follow all single electrons. The previous paragraph showed that the ground-state energy (and therefore the lattice parameter) can be obtained via the "integrated variable", the two-particle density matrix. We will see in the following chapters that this information can be also obtained in principle thanks to the ground-state electronic density $\rho(\mathbf{r})$, or to the one-particle Green's function $G(\mathbf{r}t, \mathbf{r}'t')$, which is a kind of dynamical density matrix. These quantities are even more "integrated", since they depend on only one or two space-time variables. For instance, if one wanted to evaluate the ionization energy
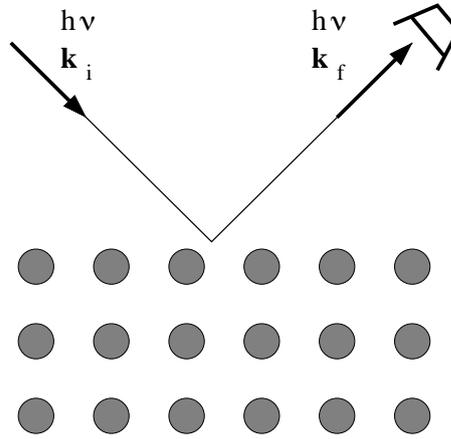
Figure 1.1: Schematic geometry of an X-ray diffraction experiment. $\mathbf{k}_i$ and $\mathbf{k}_f$ are the momentum of the incoming and scattered photon. The energy $h\nu$ of the photon is conserved.

of a solid, one would need the Green's function; the ground-state electronic density would not be sufficient here.

It is therefore crucial to know which experiment one has to describe in order to use the *minimum* consistent theory (i.e. to use the cheapest basic variable). The following sections depict the types of experiments this thesis is dealing with, and sketch their link to the variable, theory has to build on in each case.

1.3   Structural experiments

X-ray diffraction has been for almost a century the tool of choice to determine the structure of periodic systems. In this elastic process (i.e. with no energy loss), X-ray photons are scattered by the electrons of the crystal under study, as depicted on figure 1.1. If the wavelength of the impinging beam is of the order of the lattice periodicity of the crystal, this allows a direct mapping of the reciprocal space of the solid.

The intensity of the scattered beam I_s is proportional to the square of the Fourier transform of the electronic density (see chapter 10 of reference [9])

$$I_s(\Delta \mathbf{k}) \propto \left| \int \rho(\mathbf{r}) e^{-i\Delta \mathbf{k}.\mathbf{r}} \right|^2, \qquad (1.6)$$

where $\Delta \mathbf{k} = \mathbf{k}_f - \mathbf{k}_i$ is the change of momentum of the photons, when diffracted by the sample. As the sample is periodic, this Fourier transform is non-vanishing only for $\Delta \mathbf{k}$ equal to reciprocal lattice vectors (see appendix A). This is the famous *Bragg law*. Of course, once the reciprocal
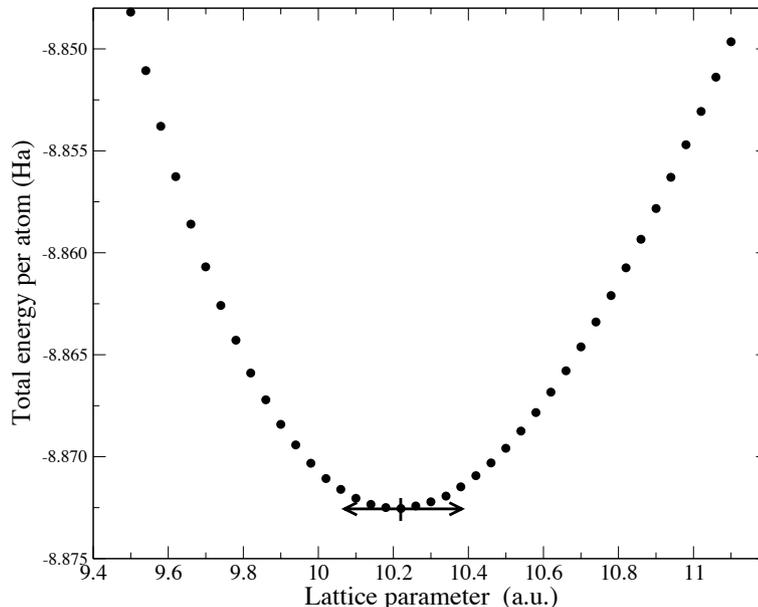
Figure 1.2: Theoretical total energy curve of a crystal as a function of the lattice parameter (here, silicon within local density approximation, see following).

lattice is known, so is the direct lattice. Extinctions of Bragg peaks give also access to the position of atoms inside the unit cell due to extinction rules (tabulated in crystallographic tables). In simple solids, all equilibrium lattice parameters and equilibrium atomic positions can be determined thanks to X-ray diffraction.

Equilibrium structural properties can be directly compared with theoretical predictions (disregarding the zero-point motion of the nuclei). The equilibrium parameters are those for which the total energy of the system is the lowest. For instance, figure 1.2 depicts the calculated change of energy of a crystal, when the lattice parameter is varied. The theoretical value of the lattice parameter corresponds to the minimum of the total energy curve.

If a stress is applied on the sample, experiments can furthermore measure the lattice parameter as a function of pressure. Therefore, it allows a direct determination of the elastic constants of the solid under study. For instance, the measured Young modulus B_0 can be compared with the one obtained by fitting an equation of state on a theoretical curve like the one of figure 1.2. The equation of state of Murnaghan [10]

$$E(V) = \frac{B_0 V}{B_0'(B_0' - 1)} \left[B_0' \left(1 - \frac{V_0}{V} \right) + \left(\frac{V_0}{V} \right)^{B_0'} - 1 \right] + E_0, \qquad (1.7)$$

which has 4 parameters (the energy and the volume at the minimun, E_0 and V_0, the Young modulus B_0, and its pressure derivative B_0') is widely used to extract the elastic constant and higher order derivatives from total energy curves.

An other type of diffraction, Low Energy Electron Diffraction (LEED), is widely used to determine the characteristics of a periodic surface. In fact, the impinging electrons are sensitive to the electrostatic forces arising from the electronic density and the nuclei of the sample. The mechanism of the experiment is similar to the X-ray diffraction, except that the slow electrons (10-1000 eV kinetic energy) have a short mean free path of a few Å inside the sample. This experiment is therefore sensitive only to the first layers of the material surface. LEED allows one essentially to measure the periodicity of a surface, whereas X-ray diffraction is rather sensitive to the periodicity of the bulk material.

The structural experiments are well described in terms of functional of the ground-state density or of the one-particle Green's function. These statements are not trivial at all and will be discussed in chapter 2 for the Green's function and in chapter 4 for the ground-state density.

1.4 Photoemission and inverse photoemission experiments

Direct and inverse photoemissions permit a direct measurement of the band structure. The photoelectric effect, first explained in 1905 by A. Einstein, is the process of extracting an electron by means of an impinging photon with an energy greater than the binding energy of the electron. It is indeed a mapping of the occupied states of a solid as a function of the binding energy. If the experiment is furthermore angle-resolved, it allows also one to discriminate between different **k**-points of the Brillouin zone of the solid.

Indeed, as depicted in figure 1.3, during a photoelectric process, a photon of a given energy ω impinges on the sample, extracts an electron, whose kinetic energy E_{kin} is measured. Once the electron is removed (it is sent above the vacuum level $E_{vac} = \mu + \phi$, where μ is the Fermi level and ϕ is the work function of the interface between the solid and vacuum), the solid remains in some excited state labeled i for a while, with a hole somewhere in the valence states. If the solid used to contain N electrons before the absorption of the photon, it only contains $N - 1$ of them at the end of the process. Let $E_{N-1,i}$ be the energy of the final state of the solid and $E_{N,0}$ the energy of the initial state. The conservation of the energy yields the following equation:

$$\omega + E_{N,0} = (E_{kin} + \phi) + E_{N-1,i}. \tag{1.8}$$
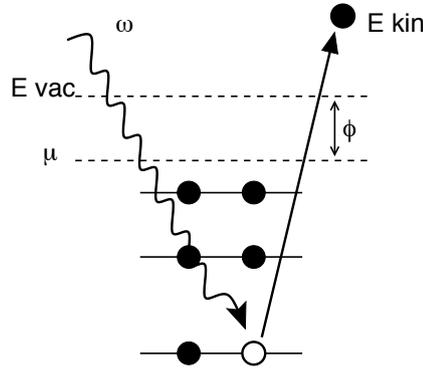
Figure 1.3: Schematic photoemission experiment. An impinging photon of energy ω extracts an electron of the solid. The photoelectron kinetic energy E_{kin} is then measured. The difference between the vacuum level E_{vac} and the Fermi level μ is the work function of the interface ϕ.

The definition of the energy of an occupied electronic state i is precisely the binding energy

$$\epsilon_i = E_{N,0} - E_{N-1,i}. \tag{1.9}$$

Therefore, with the measurement of ω and E_{kin}, photoemission can determine the occupied state energy up to the constant ϕ:

$$\epsilon_i = (E_{kin} + \phi) - \omega. \tag{1.10}$$

If the sample is a monocrystal and the electron detector has a finite acceptance angle, one can also use momentum conservation law. The **k** dependence of the states, i.e. the band structure, can hence be determined.

One should note that the final $N - 1$ electron excited state has a finite lifetime, because it has a hole in the occupied states. Indeed, the excitation remains coherent during some time, but after a while, electrons of higher energy tend to fall into the hole, because the situation is unstable. Intuitively, the deeper is the hole, the shorter the lifetime. The upper limit is reached by the edge of the top of the valence states, whose electronic lifetime is in principle infinite. But of course, there are many other causes for the damping of excitations: phonons, defects... The effect of the finiteness of the lifetime is to broaden the photoemission spectra due to the Heisenberg relation

$$\Delta\epsilon\Delta t \sim 1. \tag{1.11}$$

This shows that the smaller the lifetime, the larger the uncertainty on the initial state energy.

An inverse photoemission experiment is simply the opposite process. This allows a mapping of the empty states as a function of the energy

and of the **k**-point of the solid. Here an extra electron is injected with energy E_{kin} into the solid initially in the ground-state $|N, 0\rangle$, it goes down the surface potential barrier ϕ and arrives in some eigenstate of the solid, with emission of a photon of energy ω. The system of electrons ends in an $N + 1$ particle excited state labeled i. As in the direct case, the energy conservation law permits to evaluate the affinity energy of the empty states.

Finally, direct and inverse photoemission experiments are the most direct experimental way to measure the band structure of crystals. Theoretically, they require to be described with a framework that allows the number of electrons to vary. Therefore, the description in terms of the ground-state density is not possible here (in contrast with the case of structural properties). Instead, the one-particle Green's function is perfectly suited for that purpose (see chapter 2).

1.5 Optical measurements and energy-loss experiments

Optical absorption or reflectivity measurements are another type of spectroscopy that provides insight into the electronic structure of the solid under study. The impinging photon is a low-energy photon (a few eV, i.e. optical range or near ultra-violet). It is either absorbed, transmitted or reflected. In a one-particle picture, when it is absorbed, an electron from an occupied state gains the energy of the photon and is thus sent into the conduction bands. During this process, the excited electron keeps the same momentum (the transition is vertical), since the momentum carried by an optical photon is negligible. Beyond the independent-particle picture, this phenomenon is not so simple, since strong relaxations occur during the excitation of the electrons: (i) the excited electron interacts with its image (the hole it created, when leaving the occupied state); (ii) the other electrons react and give rise to screening.

The most remarkable feature in this type of spectroscopy is the creation of relatively localized electron-hole pairs, called excitons. If the interaction between the hole and the electron is strong enough in an absorption spectrum, bound excitons can be noticed inside the photoemission band gap. Due to the attractive nature of the Coulomb interaction between the electron and the hole, the absorption threshold is lowered below the band gap.

Optical experiments give access to the macroscopic optical constants that appear in the Maxwell equations in media [9], where a complex index $N = n + ik$ is introduced for the solution of the wave equation for the electric field:

$$E(z) = E_0 e^{i\omega/cNz}, \tag{1.12}$$

where z is the direction perpendicular to the surface of the sample. The intensity in the medium is then

$$I(z) = I_0 e^{-2\omega kz/c}. \tag{1.13}$$

The absorption coefficient α is therefore

$$\alpha(\omega) = \frac{2\omega k(\omega)}{c}. \tag{1.14}$$

One can make the link to the macroscopic dielectric function ε and polarizability χ

$$\varepsilon = N^2 \tag{1.15}$$
$$1/\varepsilon = 1 + v\chi, \tag{1.16}$$

where v is the Coulomb potential. We will see in the following chapters that the polarizability is indeed the response of the density to a variation of the external potential. The description of this will be in particular accessible to the integrated variables, the time-dependent electronic density and the two-particle Green's function (see chapters 3 and 4).

Another type of experiment will be considered in this thesis: the energy-loss experiments. In the case of a transmission experiment, a highly energetic particle ($\sim 10\,\mathrm{keV}$) is sent through a thin slab of the material . The particle undergoes an energy-loss by passing through the sample: this experiment is sensitive to inelastic diffusion of particles. Now, the momentum transfer is not necessarily zero, as the momentum carried by the impinging particle is not negligible anylonger. The position of the detector with respect to the source imposes a given momentum transfer $\mathbf{q}$. This experiment is called Electron Energy-Loss Spectroscopy (EELS) when the impinging particle is an electron, or Inelastic X-ray Scattering Spectroscopy (IXSS) when the impinging particle is an X-ray photon.

It is shown in chapter 7 of reference [9], that the energy-loss experiments measure the imaginary part of the inverse longitudinal dielectric function:

$$-\mathrm{Im}\,\varepsilon^{-1} = \frac{\mathrm{Im}\,\varepsilon}{|\varepsilon|^2}. \tag{1.17}$$

This means that the energy-loss spectra show large structures when the dielectric function is small. In particular, when $\mathrm{Re}\,\varepsilon = 0$, the system undergoes plasmon oscillations: a small external perturbation creates large charge oscillations in the sample. This type of spectroscopy is also theoretically accessible to the time-dependent density and to the two-particle Green's function, as it can be related to the density response function χ.

Chapter 2

Approach to the Many-Body Problem by means of Green's functions

2.1 Introduction of Green's functions

The purpose of many-body theory is of course not to find the full solution of the many-body Hamiltonian, i.e. to calculate all the N particle wavefunctions $\Psi(\mathbf{r}_1, \ldots, \mathbf{r}_N)$; but to provide reliable answers on the few quantities of interest for a human being. This is exactly the spirit of the Green's function theory. The one-particle Green's function can be viewed as a dynamical one-particle density matrix. The usual static density matrix is an object arising from integration of $N - 2$ space variables of the N particle wavefunction. The information contained in a Green's function are much less than the knowledge contained in the full wavefunction, but it still provides the very quantities one usually needs, let us say, the ones measured by experimentalists. As shown in Fetter and Walecka's book [11], the one-particle Green's function gives

- the expectation value of any single-particle operator in the ground-state of the system,

- the ground-state energy of the system,

- the single-particle excitation spectrum of the system.

Here follows the definition of the time-ordered one-particle equilibrium Green's function G. If $|N\rangle$ stands for the normalized wavefunction of the ground-state of the many-body Hamiltonian, it reads

$$iG(1,2) = \langle N|T\left[\hat{\psi}(1)\hat{\psi}^\dagger(2)\right]|N\rangle \qquad (2.1)$$

$$= \begin{cases} \langle N|\hat{\psi}(1)\hat{\psi}^\dagger(2)|N\rangle & \text{if} \quad t_1 > t_2 \\ -\langle N|\hat{\psi}^\dagger(2)\hat{\psi}(1)|N\rangle & \text{if} \quad t_1 < t_2 \end{cases}. \qquad (2.2)$$

The $\hat{\psi}$ and $\hat{\psi}^\dagger$ operators are annihilation and creation field operators within Heisenberg picture (they contain the whole time dependence). Index 1 is shorthand for position, time and spin variables $(\mathbf{r}_1, t_1, \sigma_1)$. T stands for the Wick time-ordering operator, which has the effect of ordering the operator with largest time on the left. This is a practical trick that allows one to use the Feynman diagram technique and moreover that permits to treat electrons and holes on the same footing.

By looking at definition (2.2), a physically intuitive interpretation of the time-ordered Green's function can be emphasized. When t_1 is larger than t_2, the Green's function describes the probability to find an electron in $\mathbf{r}_1$ with spin σ_1 at time t_1, when an electron was added in $\mathbf{r}_2$ with spin σ_2 at time t_2 to the system in its ground-state. Instead, when t_1 is smaller than t_2, the Green's function describes the probability to find a hole in $\mathbf{r}_2$ with spin σ_2 at time t_2, when an electron was previously removed in $\mathbf{r}_1$ with spin σ_1 at time t_1.

As claimed few lines before, the expectation value of a single-particle operator J can be easily evaluated provided the knowledge of the Green's function G. In the second-quantization framework, a single-particle operator J that depends on one time index is written $\mathscr{J}$ with

$$\mathscr{J} = \int d12\,\delta(t_2 - t_1)\hat{\psi}^\dagger(1)J(1,2)\hat{\psi}(2). \qquad (2.3)$$

The ground-state expectation value is then given by

$$
\begin{aligned}
\langle N|\mathscr{J}|N\rangle &= \int d12\,J(1,2)\delta(t_2 - t_1)\langle N|\hat{\psi}^\dagger(1)\hat{\psi}(2)|N\rangle \\
&= -\int d12\,\delta(t_2 - t_1^+)J(1,2)\langle N|T[\hat{\psi}(2)\hat{\psi}^\dagger(1)]|N\rangle, \quad (2.4)
\end{aligned}
$$

where t_1^+ stands for $t_1 + \delta$, with δ an infinitesimal positive real number. This has been chosen in order to introduce the time-ordering operator and to recognize the definition of the Green's function (2.2) in the previous line:

$$\langle N|\mathscr{J}|N\rangle = -i\int d12\,\delta(t_2 - t_1^+)J(1,2)G(2,1). \qquad (2.5)$$

The previous formula shows how the Green's function allows one to calculate the ground-state expectation value of any single-particle operator.

Moreover, the Galitskii-Migdal formula [12] gives the ground-state energy as a function of the one-particle Green's function only:

$$E = -\frac{i}{2}\sum_{\sigma_1\sigma_2}\delta_{\sigma_1\sigma_2}\int d\mathbf{r}_1 \lim_{\mathbf{r}_2\to\mathbf{r}_1}\lim_{t_2\to t_1^+}\left[i\frac{\partial}{\partial t_1} + h_0(\mathbf{r}_1)\right]G(1,2), \qquad (2.6)$$

where $h_0 = -\nabla^2/2 + v_{ext}$ is the one particle Hamiltonian. The one-particle excitation spectrum carried by the Green's function will be made obvious in the next section.

I would like to finally stress that the one-particle Green's function, however powerful, is not the answer to every question on the system. For instance, optical absorption can not be described in terms of the one-particle Green's function. Optical absorption is a low energy excitation of the system: the impinging photon excites an electron into a low-lying empty state (in a one-particle picture). Then, the motion of the excited electron can not be decoupled from the other ones, or in other words, from the hole created in the occupied states. This phenomenon requires one to describe fully the motion of the electron and the hole: it can not be described by the one-particle Green's function. Instead, the two-particle Green's function is needed, whose definition is

$$i^2 G_2(1,2;1',2') = \langle N|T\left[\hat{\psi}(1)\hat{\psi}(2)\hat{\psi}^\dagger(2')\hat{\psi}^\dagger(1')\right]|N\rangle. \qquad (2.7)$$

For completeness, one should notice that it is possible to define causal and advanced Green's functions, instead of the time-ordered one we are considering here. It is also possible to extend the definition of Green's function to the situation where the temperature is finite, or in presence of a time-dependent external potential [11]. We have so far implicitly considered the zero temperature equilibrium Green's functions.

From now on, the spin variables will be disregarded.

2.2 Lehmann representation and physical interpretation

The so-called Lehmann representation of the Green's function permits one to get insight into its physical meaning. It shows that the Green's function is closely related to the single-particle excitation energies of the system, by introducing excited states with $N-1$ or $N+1$ particles between the two creation-annihilation field operators of equation (2.2). As time is homogenous in absence of any time-dependent external potential, the Green's function depends only on the difference $\tau = t_1 - t_2$:

$$iG(\mathbf{r}_1, \mathbf{r}_2, \tau) = \theta(\tau) \sum_i \langle N|\hat{\psi}(1)|N+1, i\rangle\langle N+1, i|\hat{\psi}^\dagger(2)|N\rangle$$
$$- \theta(-\tau) \sum_i \langle N|\hat{\psi}^\dagger(2)|N-1, i\rangle\langle N-1, i|\hat{\psi}(1)|N\rangle, \quad (2.8)$$

where we have introduced the closure relation in the Fock space $\{|N, i\rangle\}$. Due to the creation or annihilation operators, only states with $N+1$ particles if $\tau > 0$ or with $N-1$ particles if $\tau < 0$ have survived. The index i runs over all states of a given particle number. The time dependence of the matrix elements can be put into evidence by introducing the Schrödinger

picture:

$$\hat{\psi}(1) = e^{i\mathscr{H}t_1}\psi(\mathbf{r}_1)e^{-i\mathscr{H}t_1}. \tag{2.9}$$

Hence, this gives

$$
\begin{aligned}
iG(\mathbf{r}_1, \mathbf{r}_2, \tau) = {}& \theta(\tau)\sum_i \langle N|\psi(\mathbf{r}_1)|N+1, i\rangle \\
& \times \langle N+1, i|\psi^\dagger(\mathbf{r}_2)|N\rangle e^{i(E_N - E_{N+1,i})\tau} \\
& - \theta(-\tau)\sum_i \langle N|\psi^\dagger(\mathbf{r}_2)|N-1, i\rangle \\
& \times \langle N-1, i|\psi(\mathbf{r}_1)|N\rangle e^{-i(E_N - E_{N-1,i})\tau}. \tag{2.10}
\end{aligned}
$$

The previous line contains total energy differences, that can be interpreted as excitation energies. Indeed, for positive times, $\epsilon_i = E_{N+1,i} - E_N$ represents the excitation energy of a system previously in its ground-state that, due to the addition of an electron, is now in the excited state i of $N+1$ particles. Alternatively, for negative times, $\epsilon_i = E_N - E_{N-1,i}$ represents a removal excitation energy, or a hole energy.

The minimum energy needed to add an electron $\epsilon_c = E_{N+1,0} - E_{N,0}$ is called the energy of the lowest conduction state, as all other possible $N+1$-particle states are energytically higher. Alternatively, the minimum energy required to remove an electron is $\epsilon_v = E_{N,0} - E_{N-1,0}$ is called the energy of the highest valence state. If the system under consideration is a metal, the energy $\epsilon_c = \epsilon_v$ is the chemical potential μ, or in other words, the energy cost of the addition $\epsilon_{\text{addition}}$ or removal $\epsilon_{\text{removal}}$ of a particle in the system. Instead, if the system is insulating, the band gap E_g is defined as the energy difference between conduction and valence states, i.e., $E_g = \epsilon_c - \epsilon_v$, and the chemical potential lies somewhere inside the gap. The definition of the band gap of insulators can also be recast in terms of total energies [13]:

$$E_g = E_{N+1,0} + E_{N-1,0} - 2E_{N,0}. \tag{2.11}$$

The inequality $\epsilon_{\text{removal}} \leq \mu \leq \epsilon_{\text{addition}}$ holds for all materials. Previous definitions may be summarized by

$$\text{if} \quad \epsilon_i > \mu, \quad \epsilon_i = E_{N+1,i} - E_N \tag{2.12a}$$

$$\text{if} \quad \epsilon_i < \mu, \quad \epsilon_i = E_N - E_{N-1,i}. \tag{2.12b}$$

Consequently, the so-called Lehmann amplitudes $f_i(\mathbf{r})$ can be defined:

$$f_i(\mathbf{r}) = \begin{cases} \langle N|\psi(\mathbf{r})|N+1, i\rangle & \text{if} \quad \epsilon_i > \mu \\ \langle N-1, i|\psi(\mathbf{r})|N\rangle & \text{if} \quad \epsilon_i < \mu \end{cases}. \tag{2.13}$$

The expression of the Green's function in real space, real time, is then recast as

$$iG(\mathbf{r}_1, \mathbf{r}_2, \tau) = \sum_i \left[\theta(\tau)\theta(\epsilon_i - \mu) - \theta(-\tau)\theta(\mu - \epsilon_i)\right]$$

$$\times f_i(\mathbf{r}_1)f_i^*(\mathbf{r}_2)e^{-i\epsilon_i \tau}. \tag{2.14}$$
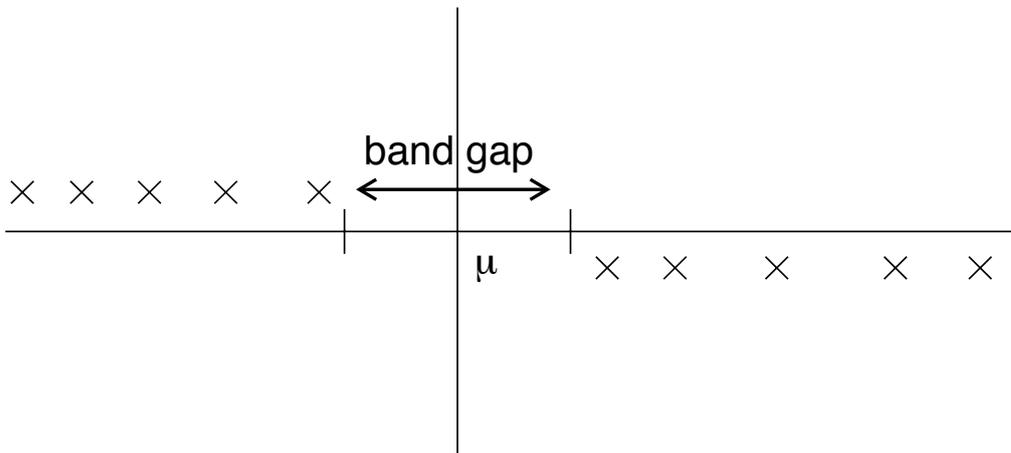
Figure 2.1: In the complex plane, the Green's function has poles (crosses) only along the real axis. As there is no allowed energy within the band gap, the Green's function has no pole there. The poles are located above the real axis for frequencies lower than the chemical potential μ, and below for frequencies greater than μ.

The Fourier transform (using the convention of equation (A.21a)) can be performed analytically if the definition of the time integral is enforced by adding or substracting a small imaginary part η in the argument of the exponentials. When τ is positive, i.e., for addition energies, we have to add a small η:

$$\lim_{\tau \to +\infty} e^{i(\omega - \epsilon + i\eta)\tau} = 0. \tag{2.15}$$

Reversely, a small η has to be subtracted for removal energies. Finally, the Lehmann representation of the Green's function in frequency space reads

$$G(\mathbf{r}_1, \mathbf{r}_2, \omega) = \sum_i \frac{f_i(\mathbf{r}_1) f_i^*(\mathbf{r}_2)}{\omega - \epsilon_i + i\eta \operatorname{sign}(\epsilon_i - \mu)}. \tag{2.16}$$

The polar structure of the frequency Green's function depicted on figure 2.1 is made obvious thanks to this representation. The poles lie along the real axis on excitation energies: infinitesimally below the axis for frequencies greater than μ, above for frequencies smaller than μ.

2.3 Definition of the spectral function

When looking at the Lehmann representation of G, it is tempting to apply the relation

$$\lim_{\eta \to 0^+} \frac{1}{x + i\eta} = \mathscr{P}\frac{1}{x} - i\pi\delta(x) \tag{2.17}$$

to equation (2.16) to extract e.g. the imaginary part of G:

$$\text{Im}\, G(\mathbf{r}_1, \mathbf{r}_2, \omega) = \pi \text{sign}(\mu - \epsilon_i) \sum_i f_i(\mathbf{r}_1) f_i^*(\mathbf{r}_2) \delta(\omega - \epsilon_i). \qquad (2.18)$$

The sign of $\text{Im}\, G$ is a general property of the Green's functions: it is positive for negative frequencies, and negative for positive frequencies.

Let us now define the so-called spectral function A:

$$A(\mathbf{r}_1, \mathbf{r}_2, \omega) = \frac{1}{\pi} \text{sign}(\mu - \omega) \text{Im}\, G(\mathbf{r}_1, \mathbf{r}_2, \omega) \qquad (2.19)$$

$$= \sum_i f_i(\mathbf{r}_1) f_i^*(\mathbf{r}_2) \delta(\omega - \epsilon_i). \qquad (2.20)$$

The spectral function A is a positive function of ω. Moreover, A is sufficient to give back the full G (real part and imaginary part) thanks to the relation

$$G(\mathbf{r}, \mathbf{r}', \omega) = \int_{-\infty}^{\mu} d\omega' \frac{A(\mathbf{r}, \mathbf{r}', \omega')}{\omega - \omega' - i\eta} + \int_{\mu}^{\infty} d\omega' \frac{A(\mathbf{r}, \mathbf{r}', \omega')}{\omega - \omega' + i\eta}. \qquad (2.21)$$

This is nothing else but a Cauchy relation in the domain of analyticity of G. This shows in particular that the spectral function carries the same quantity of information as the Green's function. It may be of numerical interest to deal with a real function of ω that is positive by definition, instead of the complex function G (see chapter 7).

Moreover, the spectral function can be of practical interest, as it yields the expectation values of some observables. First, there is a sum-rule on the spectral function:

$$\int_{-\infty}^{\infty} d\omega\, A(\mathbf{r}_1, \mathbf{r}_2, \omega) = \delta(\mathbf{r}_1 - \mathbf{r}_2), \qquad (2.22)$$

since

$$\sum_i f_i(\mathbf{r}_1) f_i^*(\mathbf{r}_2) = \sum_i \langle N|\psi^\dagger(\mathbf{r}_2)|N-1, i\rangle\langle N-1, i|\psi(\mathbf{r}_1)|N\rangle$$

$$+ \sum_i \langle N|\psi(\mathbf{r}_1)|N+1, i\rangle\langle N+1, i|\psi^\dagger(\mathbf{r}_2)|N\rangle$$

$$= \langle N| \left[\psi(\mathbf{r}_1), \psi^\dagger(\mathbf{r}_2)\right]_+ |N\rangle$$

$$= \delta(\mathbf{r}_1 - \mathbf{r}_2), \qquad (2.23)$$

where we used the definition of Lehmann amplitudes, the completeness of sets $\{|N-1, i\rangle\}$ and $\{|N+1, i\rangle\}$, and the anticommutation rule of field operators.

Second, the spectral function directly yields the ground-state density

$$\int_{-\infty}^{\mu} d\omega\, A(\mathbf{r}_1, \mathbf{r}_1, \omega) = \rho(\mathbf{r}_1), \qquad (2.24)$$

since, using the same steps as previously,

$$\int_{-\infty}^{\mu} d\omega A(\mathbf{r}_1, \mathbf{r}_1, \omega) = \langle N|\psi^\dagger(\mathbf{r}_1)\psi(\mathbf{r}_1)|N\rangle. \tag{2.25}$$

Third, the spectral function gives the total energy of the system if introduced in the Galitskii-Migdal formula (equation 2.6). And finally, the following section will show how it permits one to calculate the spectra of photoemission experiments.

2.4 Spectral function and photoemission

In order to appreciate the physics contained in the spectral function, it is interesting to demonstrate the link between the spectral function and the photoemission spectra. In a photoemission experiment, the detector measures electrons that are extracted from a solid due to an incident photon. The photocurrent is given by Fermi's golden rule:

$$\mathscr{J}_\mathbf{k}(\omega) = \sum_i |\langle N-1, i; \mathbf{k}|\Delta|N\rangle|^2 \delta(E_\mathbf{k} - \epsilon_i - \omega), \tag{2.26}$$

where Δ is the dipole transition operator in second quantization form, $|N - 1, i; \mathbf{k}\rangle$ is the excited state i of the solid with $N - 1$ electrons plus one photoelectron with momentum $\mathbf{k}$, and $E_\mathbf{k}$ is the energy of the photoelectron (kinetic energy plus vacuum level). The photocurrent is measured as a function of the incident energy ω and of the momentum $\mathbf{k}$ of the extracted electron (in an angle-resolved photoemission experiment).

This section shows how the photocurrent $\mathscr{J}_\mathbf{k}(\omega)$ can be evaluated via the spectral function A in the sudden approximation [14]. The sudden approximation precisely states that

$$|N - 1, i; \mathbf{k}\rangle = c_\mathbf{k}^\dagger|N - 1, i\rangle, \tag{2.27}$$

where $c_\mathbf{k}^\dagger$ is the creation operator of the state $\mathbf{k}$. This means that the photoelectron in the state $\mathbf{k}$ has no influence on the $N - 1$ particle state of the solid. It should be a good approximation if the state $\mathbf{k}$ is an almost free electron state.

Let us expand Δ operator in a complete set of single-particle wavefunctions ϕ_m:

$$\Delta = \sum_{lm} \Delta_{lm} c_l^\dagger c_m. \tag{2.28}$$

The preceding equation can be used to evaluate

$$\begin{aligned}
\langle N - 1, i| \sum_{lm} \Delta_{lm} c_\mathbf{k} c_l^\dagger c_m|N\rangle &= \sum_{lm} \Delta_{lm} \langle N - 1, i|c_\mathbf{k} c_l^\dagger c_m|N\rangle \\
&= \sum_m \Delta_{\mathbf{k}m} \langle N - 1, i|c_m|N\rangle. \tag{2.29}
\end{aligned}$$

To obtain the last line, one has moved $c_{\mathbf{k}}$ to the right using the commutation rules $c_{\mathbf{k}}c_l c_m^\dagger = \delta_{\mathbf{k}l}c_m + c_l^\dagger c_m c_{\mathbf{k}}$. One has also assumed that the ground-state has no component on the state $\mathbf{k}$ $c_{\mathbf{k}}|N\rangle \approx 0$, as the state $\mathbf{k}$ is a very high energy state.

Let us now introduce the matrix elements of the spectral function on the same set of one-particle states used previously and suppose furthermore that this particular set of ϕ_m makes A diagonal, $A_{mn} = \delta_{mn}\langle m|A|m\rangle$. One hence gets

$$
\begin{aligned}
\mathscr{J}_{\mathbf{k}}(\omega) &= \sum_{im} \Delta_{\mathbf{k}m}\langle N|c_m^\dagger|N-1,i\rangle\langle N-1,i|c_m|N\rangle\delta(E_{\mathbf{k}} - \epsilon_i - \omega) \\
&= \sum_m |\Delta_{\mathbf{k}m}|^2 A_{mm}(E_{\mathbf{k}} - \omega). \qquad (2.30)
\end{aligned}
$$

The photocurrent is therefore given by a sum of matrix elements of the spectral function. In order to directly calculate what is measured, one should also take into account dipole transition matrix elements $\Delta_{\mathbf{k}m}$, between occupied states m of the solid and high energy levels $\mathbf{k}$. In practical applications, the effect of the transition matrix elements is often disregarded.

2.5 Dyson equation and self-energy

Starting from the equation of motion for the Heisenberg creation and annihilation field operators $\hat{\psi}$ and $\hat{\psi}^\dagger$ (see references [15] or [7]), a hierarchy of equations of motion for the Green's function can be derived. The one-particle Green's function depends on the two-particle one:

$$
\left[i\frac{\partial}{\partial t_1} - h(\mathbf{r}_1)\right] G(1,2) + i \int d3\, v(1,3)G_2(1,3^+;2,3^{++}) = \delta(1,2), \quad (2.31)
$$

the two-particle one on the three-particle one, and so on... This system of equations is then as complex as the original problem of the 10^{23} electrons. We have not gained anything yet by reformulating the many-particle problem in terms of Green's function.

Here comes the fundamental idea of many-body perturbation theory: if one is interested in one-particle properties, one only needs to know the one-particle Green's function. As a consequence, let us try to find good approximations that allows one to express the two-particle Green's function in terms of one-particle ones. The same holds if one is interested in the two-particle Green's function (e.g. to calculate absorption spectra): one has to find approximations to get rid of the three-particle Green's function. Many-body perturbation theory provides a scheme to systematically find approximations for the higher-number of particle Green's functions in terms of the lower ones.

It is indeed possible (see next chapter) to reformulate the two-particle Green's function in terms of a formal operator Σ called self-energy that accounts for all two-particle effects:

$$\int d3\Sigma(1,3)G(3,2) = -i \int d3v(1,3)G_2(1,3^+;2,3^{++}). \qquad (2.32)$$

This definition can be introduced in equation (2.31) and yields the so-called Dyson equation:

$$\left[i\frac{\partial}{\partial t_1} - h(\mathbf{r}_1)\right] G(1,2) - \int d3\Sigma(1,3)G(3,2) = \delta(1,2). \qquad (2.33)$$

The purpose of many-body perturbation theory is then to find suitable approximations for the operator Σ as a function of the one-particle Green's function only.

In order to gain some insight on the role of the self-energy, let us show that it plays the role of a potential acting on the Lehmann amplitudes of the Green's function. If one introduces the Lehmann representation of the one-particle Green's function G in equation (2.33) after a Fourier transform into frequency space, one gets the following expression:

$$\int d\mathbf{r}_3 \left\{[\omega - h(\mathbf{r}_3)]\delta(\mathbf{r}_1 - \mathbf{r}_3) - \Sigma(\mathbf{r}_1,\mathbf{r}_3,\omega)\right\} \sum_i \frac{f_i(\mathbf{r}_3)f_i^*(\mathbf{r}_2)}{\omega - \epsilon_i \pm i\eta} = 0. \qquad (2.34)$$

If one supposes following reference [14] that state i is non-degenerate and that Σ has no pole in $\omega = \epsilon_i$, the limit $\omega \to \epsilon_i$ retains only state i in the sum over states:

$$\int d\mathbf{r}_3 \left\{[\epsilon_i - h(\mathbf{r}_1)]\delta(\mathbf{r}_1 - \mathbf{r}_3) - \Sigma(\mathbf{r}_1,\mathbf{r}_3,\epsilon_i)\right\} f_i(\mathbf{r}_3)f_i^*(\mathbf{r}_2) = 0. \qquad (2.35)$$

After dividing by $f_i^*(\mathbf{r}_2)$, this yields the equation

$$\int d\mathbf{r}_3 \left[h(\mathbf{r}_1)\delta(\mathbf{r}_1 - \mathbf{r}_3) + \Sigma(\mathbf{r}_1,\mathbf{r}_3,\epsilon_i)\right] f_i(\mathbf{r}_3) = \epsilon_i f_i(\mathbf{r}_1), \qquad (2.36)$$

which points out the meaning of the self-energy. The self-energy acts as a potential in the Schrödinger-like equation of motion of the Lehmann amplitudes and energies. Therefore, for an energy ϵ_i lower than the chemical potential, the self-energy has to describe the motion of the object $\langle N-1,i|\psi(\mathbf{r}_1)|N\rangle$, which is a removal amplitude. For ϵ_i higher than μ, it is same but for electron additions. This proves that the behavior of the "potential" Σ has to be different for full or empty states. In particular, the exact asymptotic behavior of Σ is different for holes and for electrons (see section 2.8).
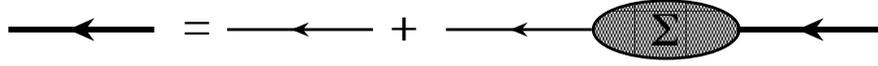
Figure 2.2: Feynman diagram representation of the Dyson equation.

2.6   Non-interacting and interacting Green's functions

All the previous developments apply also to non-interacting fermions, for which the formulas are much simpler. The equation of motion of the non-interacting Green's function G_0 is merely

$$\left[i\frac{\partial}{\partial t_1} - h(\mathbf{r}_1)\right] G_0(1,2) = \delta(1,2). \tag{2.37}$$

This proves that the non-interacting Green's function is formally the functional inverse of the operator $(\omega - h)$ in frequency space. This is the usual definition of a Green's function in other fields of physics. Such an interpretation of G_0^{-1} allows one to rewrite the Dyson equation (2.33) as

$$\left[G_0^{-1}(1,3) - \Sigma(1,3)\right] G(3,2) = \delta(1,2), \tag{2.38}$$

or, symbolically,

$$G = G_0 + G_0\Sigma G. \tag{2.39}$$

The self-energy can now be viewed as the connection between the non-interacting system, whose Green's function is G_0, and the interacting one with G. All the effects beyond non-interacting particles are included in Σ. The Dyson equation can be represented alternatively using Feynman diagrams (figure 2.2). The meaning of the different symbols is provided in page xi. The utility of the Feynman diagram technique will be made clear in section 2.8, when looking for approximations to the self-energy.

Concerning the spectral functions, the non-interacting system has a simple expression for A

$$A(\mathbf{r}, \mathbf{r}', \omega) = \sum_i \phi_i(\mathbf{r})\phi_i^*(\mathbf{r}')\delta(\omega - \epsilon_i), \tag{2.40}$$

where ϕ_i are the independent-particle wavefunctions and ϵ_i the corresponding energies. Therefore, the matrix element $A_{ii}(\omega) = \langle i|A(\omega)|i\rangle$ is a simple δ-peak located at ϵ_i, the non-interacting excitation energy (the solid line of figure 2.3).
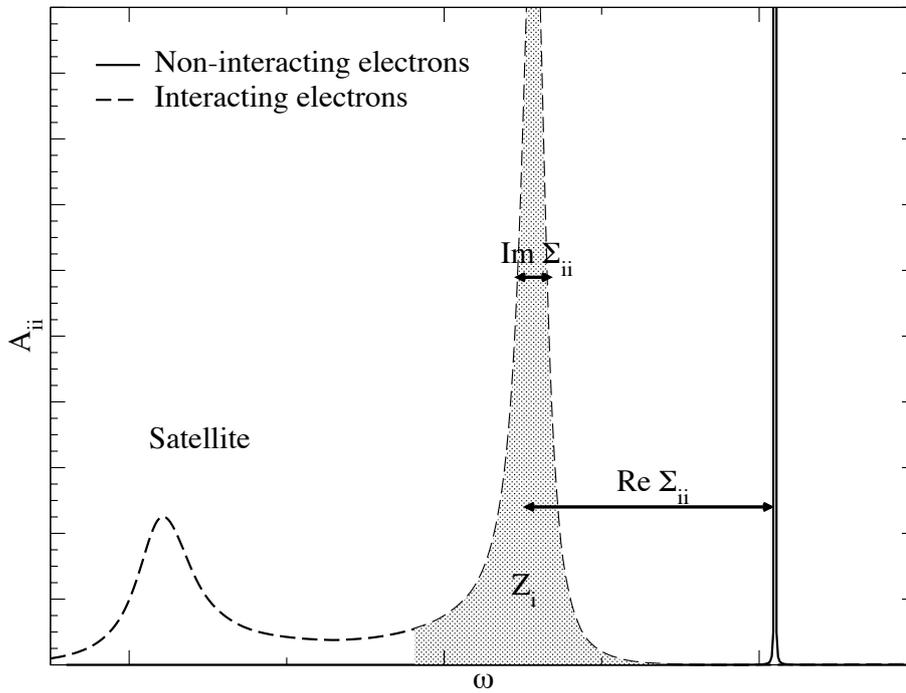
Figure 2.3: Matrix elements of the spectral functions of interacting (dashed line) and non-interacting (solid line) electron systems.

2.7   Quasiparticles and spectral functions

To interpret more easily the interacting spectral function, let us assume that both Σ and G are diagonal in the basis of one-particle wavefunctions (this assumption is in most cases harmless [14]). Then, from equation (2.38), one can write

$$\langle i|A(\omega)|i\rangle = \frac{1}{\pi}\text{Im}\left\{\frac{1}{(\omega - \epsilon_i) - \Sigma_{ii}(\omega)}\right\}. \tag{2.41}$$

The resulting spectral function is depicted in figure 2.3 with a dashed line. The main peak or *quasiparticle* peak has moved to E_i, which is called the quasiparticle energy,

$$E_i = \epsilon_i + \text{Re}\,\Sigma_{ii}(E_i). \tag{2.42}$$

The width of the quasiparticle peak is given by $\text{Im}\,\Sigma_{ii}(E_i)$ and can be interpreted as the inverse of the lifetime of the excitation i. When the energy of the excitation goes farther from Fermi level, the quasiparticle peak gets broader and the lifetime shorter. For instance, this means that an electron added in a high empty state will quickly fall into a lower energy state. This is easily interpreted: an electron excited in a high empty state will not stay there a long time, since it has many possibilities to decay into a lower empty

state. An electron added in the first empty state will have nowhere else to fly away and the corresponding excitation will have an infinite life time.

An interacting spectral function may have some extra peaks that cannot be interpreted as one-particle excitations (i.e. quasiparticles). The situation is then very far from the non-interacting particle case. These additional features in the spectral function are called *satellites*. If one Taylor expands $\Sigma_{ii}(\omega)$ around E_i, one can express the integral under the quasiparticle peak as

$$Z_i = \frac{1}{1 - \partial \Sigma_{ii}(\omega)/\partial \omega|_{\omega=E_i}}, \qquad (2.43)$$

called the renormalization factor. The Z_i factor is generally far from 1. The lower it is, the more correlated the system. If the spectral function had only one-peak, as in an independent particle approximation, the correlation would be low and Z_i would be equal to 1. The larger Z_i, the more important are the satellites with respect to the well-defined one-particle excitation (i.e. the quasiparticle peak).

It has been instructive to study in detail the different features of the spectral function to understand what is the influence of the many-body effects. In particular, one can note that, even when one is interested in one-particle properties (as e.g. in photoemission), the collective behavior of the fermion system may be important through quasiparticle energies, lifetime effects and satellites.

2.8   Hartree-Fock self-energy

Let us now approximate the self-energy using the Feynman diagram technique. We consider the equation of motion for the one-particle Green's function as a function of the two-particle Green's function (equation (2.31)). The left-hand side of figure 2.4 depicts the representation of the two-particle Green's function G_2 as the scattering of two particles. The simplest scattering process one can think about is the process involving two independent particles. Two particles enter the right-hand side of G_2, two particles go out the left-hand side of G_2. In between, one has two possibilities in the case of non-interacting particles: either the two particles have followed their way straightforwardly, or they have exchanged (as the particles are undistinguishable in quantum mechanics). The two possibilities are drawn on the right-hand side of figure 2.4. The plus and minus signs are due to Wick's theorem.

If one uses this expression of G_2 inside the integral $\int d3v(1,3)G_2(1,3;2,3)$ that appears in the equation of motion of G, one obtains the equality represented in figure 2.5. In this particular case, it is now obvious that an operator Σ can be found, such that the equation (2.32) is valid. The corre-
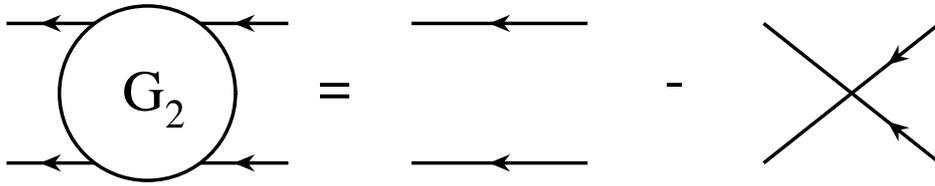
Figure 2.4: Feynman diagram representation of the approximation of the two particle Green's function that gives rise to the Hartree-Fock self-energy.
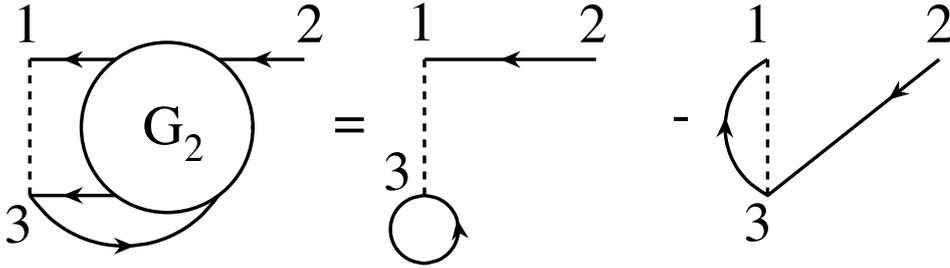
Figure 2.5: Feynman diagram representation of the integral $\int d3 v(1,3) G_2(1,3;2,3)$, where the labels 1,2,3 have been explicitly written.

sponding Σ would be

$$\Sigma(1,2) = -i\delta(1,2) \int d3 v(1,3) G(3,3^+) + iv(1,2) G(1,2^+), \qquad (2.44)$$

where the first term is the so-called *Hartree potential* v_h,

$$v_h(1,2) = \delta(1,2) \int d3 v(1,3) \rho(3), \qquad (2.45)$$

and the second term is the so-called *exchange operator* or Fock self-energy,

$$\Sigma_x(1,2) = iv(1^+,2) G(1,2), \qquad (2.46)$$

where the sign $+$ for times has been moved in a consistent way, since the Coulomb interaction v is instantaneous. The Fock self-energy is displayed in figure 2.6.

The famous Hartree-Fock (HF) approximation to the self-energy has come out in a natural way by using the simplest Feynman diagrams. As the Hartree term is local, it is usually put inside the one-particle Hamiltonian $h(1)$ and, as a consequence, the self-energy generally designates the remainder $\Sigma - v_h$. This convention will be used throughout this manuscript. According to this definition, the self-energy accounts exactly for what is called *exchange-correlation* or, in simple words, for all electron-electron interaction effects beyond Hartree.
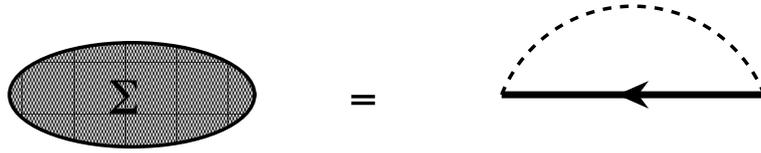
Figure 2.6: Feynman diagram representation of the Fock self-energy, which is the only other first-order contribution in term of bare Coulomb interaction, except the Hartree term.

In frequency space, the Fock self-energy becomes

$$\Sigma_x(\mathbf{r}_1, \mathbf{r}_2, \omega) = \frac{i}{2\pi} \int d\tau G(\mathbf{r}_1, \mathbf{r}_2, \tau) v(\mathbf{r}_1, \mathbf{r}_2) \delta(\tau + \eta) e^{i\omega\tau}, \qquad (2.47)$$

where η is a small positive quantity.

Using equation (2.14) to evaluate G that contains θ step functions, the Dirac function retains only contributions from negative times, i.e. from removal excitations. All the terms $e^{i(\epsilon_i - \omega)\eta}$ go to 1, when the parameter η is allowed to go to zero: there is no frequency dependence anymore. The Fock self-energy is static and therefore, there is no difference between Lehmann amplitudes and one-particle wavefunctions. All these simplifications yield the well-known expression for the Fock operator:

$$\Sigma_x(\mathbf{r}_1, \mathbf{r}_2) = -\sum_{i \, \mathrm{occ}} \phi_i(\mathbf{r}_1) \phi_i^*(\mathbf{r}_2) v(\mathbf{r}_1, \mathbf{r}_2). \qquad (2.48)$$

This non-local operator could have been obtained by minimizing the ground-state total energy in the space of single Slater determinant wavefunctions (see chapter 7 of reference [7]). The so-called Hartree-Fock approximation is therefore the variationally best single particle picture for the many-body wavefunction. In particular, the Fock term enforces the correct antisymmetric behavior of the fermionic wavefunction.

The study of solids will be the subject of choice of this thesis, in particular bulk silicon, solid argon, and cuprous oxide. These are three very different materials: silicon is highly polarizable, with delocalized valence electrons; argon is an molecular solid, with very weak interactions between atoms; and cuprous oxide is a complicated transition metal oxide, with localized d electrons, which are usually complicated for electronic structure calculations.

Table 2.1 shows how the Hartree-Fock approximation performs for these solids. The general trend is that the band gap (calculated as a difference of eigenvalues) is largely overestimated (from 125 % for slightly polarizable materials, as a rare-gaz solid, to 300 % for highly polarizable solids, as silicon). As a consequence, there is a great need to include other terms in the self-energy operator, to produce realistic results for the band gap.

Concerning the calculation of structural parameters, the HF approximation gives reliable results, not too far from experimental data. In general, HF has been shown to bind too weakly, i.e. the resulting lattice parameters are usually slightly too large. This statement is true for the solids under study. All terms beyond the HF approximation will account for the so-called *correlation*.

Moreover, the Hartree-Fock approximation yields a potential that has the correct leading term for the asymptotic behavior for finite systems. When one is far from the charge density, $|\mathbf{r} - \mathbf{r}'|$ can be approximated by a constant R on the range of variations of $\phi_i(\mathbf{r}')$. The Hartree potential applied to a state j gives

$$
\begin{aligned}
\langle \phi_j | V_{\mathrm{H}} | \phi_j \rangle &= \int d\mathbf{r} |\phi_j(\mathbf{r})|^2 \int d\mathbf{r}' \frac{\rho(\mathbf{r}')}{|\mathbf{r} - \mathbf{r}'|} \\
&\sim \frac{1}{R} \int d\mathbf{r} |\phi_j(\mathbf{r})|^2 \int d\mathbf{r}' \rho(\mathbf{r}') \\
&\sim \frac{N}{R},
\end{aligned}
\tag{2.49}
$$

Table 2.1: Theoretical and experimental lattice parameter, bulk modulus and direct gap of bulk silicon, solid argon, and cuprous oxide evaluated within Hartree-Fock approximation.

	Si		Ar		Cu$_2$O	
	HF	Expt.	HF	Expt.	HF	Expt.
lattice parameter (a.u.)	10.39[a]	10.263[b]	—	—	8.38[c]	8.068[b]
bulk modulus (GPa)	107[a]	99[b]	—	—	100[c]	112[d]
direct band gap (eV)	9.00[e]	3.40[f]	17.93[g]	14.20[h]	9.7,[c] 9.84[i]	2.17[j]

[a]Reference [16]
[b]Reference [17]
[c]Reference [18]
[d]Reference [19]
[e]Reference [20]
[f]Reference [21]
[g]Reference [22]
[h]Reference [23]
[i]Reference [24]
[j]Reference [1]

and the Fock term gives

$$
\begin{aligned}
\langle \phi_j | \Sigma_x | \phi_j \rangle & = -\sum_{iocc} \int d\mathbf{r} \int d\mathbf{r}' \phi_j^*(\mathbf{r}) \frac{\phi_i(\mathbf{r})\phi_i^*(\mathbf{r}')}{|\mathbf{r} - \mathbf{r}'|} \phi_j(\mathbf{r}') \\
& \sim -\frac{1}{R} \sum_{iocc} \int d\mathbf{r} \phi_j^*(\mathbf{r}) \phi_i(\mathbf{r}) \int d\mathbf{r}' \phi_i^*(\mathbf{r}') \phi_j(\mathbf{r}') \\
& \sim \begin{cases} -1/R & \text{if} \quad \epsilon_j < \mu \\ 0 & \text{if} \quad \epsilon_j > \mu \end{cases} .
\end{aligned} \tag{2.50}
$$

Therefore, for an occupied state j, the asymptotic behavior of the Hartree-Fock potential is $\sim \frac{N-1}{R}$. It describes the situation, when one has removed away an electron to an N electron system. As the removed electron is infinitely far from its origin, its interaction is purely classical: electrostatics theory states that the electron experiences the Coulomb potential created by the $N - 1$ remaining electrons (Gauss theorem).

On the contrary, for an empty state j, the asymptotic behavior of the Hartree-Fock potential is $\sim \frac{N}{R}$. It describes the situation, when one is adding an electron to an N electron system. This is consistent with the meaning we have given to the Lehmann amplitudes. When the extra electron is far away, it experiences just the classical Coulomb potential of the N electrons of the system.

The Hartree-Fock approximation gives therefore a reliable leading term for the asymptotic behavior of the potential to describe electron addition or removal processes.

Chapter 3

Hedin's equations, Bethe-Salpeter equation, and GW approximations

We have seen in the previous chapter, how useful the Green's function can be to evaluate the observables of an interacting system of fermions. Unfortunately, the equation of motion of the one-particle Green's function depends on the two-particle one. The two-particle one depends on the three-particle one, and so on... We assumed that the equations can be decoupled thanks to a self-energy operator. In this chapter, we show that this assumption is indeed justified and we provide a way to derive, in principle, the exact self-energy and some approximations to it.

3.1 Green's functions in presence of an external perturbation

In order to decouple the hierarchy of equations for the Green's functions, one can use the Schwinger derivative technique. To achieve that goal, one needs to introduce a small time-dependent external potential $U(\mathbf{r}_1, \mathbf{r}_2, t)$, that will be made vanish at the end of the derivation. This fictitious potential is introduced only to allow the evaluation of the derivative with respect to this potential.

In presence of the potential, the former definition (equation (2.1)) of the one-particle Green's function becomes

$$iG(1,2) = \frac{\langle N|T\left[\hat{S}\hat{\psi}(1)\hat{\psi}^\dagger(2)\right]|N\rangle}{\langle N|T[\hat{S}]|N\rangle},\tag{3.1}$$

where the creation field operator $\hat{\psi}^\dagger$ and annihilation field operator $\hat{\psi}$ are exactly the same as the ones in equation (2.1). However, as a time-dependent

external potential was added, $\hat{\psi}$ and $\hat{\psi}^\dagger$ are now in the so-called interaction picture: they still contain the time-dependence of the equilibrium Hamiltonian, while the time-dependence due to the additional potential is fully contained in the time evolution operator $\hat{S}$. The formal expression of $\hat{S}$ in the interaction picture is (see references [7, 15])

$$T[\hat{S}] = T\left[\exp\left(-i\int_{-\infty}^{+\infty} dt \int d\mathbf{r}_1 d\mathbf{r}_2 \hat{\psi}^\dagger(\mathbf{r}_1 t^+) U(\mathbf{r}_1, \mathbf{r}_2, t) \hat{\psi}(\mathbf{r}_2 t)\right)\right]. \quad (3.2)$$

Note that imposing $U = 0$ leads back to the definition of the usual equilibrium Green's function. The entire U dependence of this generalized Green's function lies in the time evolution operator $\hat{S}$. Therefore, the first-order variation of $\delta G(1, 2)$ with respect to $\delta U(\mathbf{r}_3, \mathbf{r}_4, t_3)$ (variation of a product) reads

$$i\delta G(1,2) = \frac{\langle N|T\left[\delta\hat{S}\hat{\psi}(1)\hat{\psi}^\dagger(2)\right]|N\rangle}{\langle N|T[\hat{S}]|N\rangle} - iG(1,2)\frac{\langle N|T[\delta\hat{S}]|N\rangle}{\langle N|T[\hat{S}]|N\rangle} \quad (3.3)$$

and the variation $\delta\hat{S}$ can be evaluated as

$$T[\delta\hat{S}] = -iT\left[\hat{S}\int_{-\infty}^{+\infty} dt \int d\mathbf{r}_3 d\mathbf{r}_4 \hat{\psi}^\dagger(\mathbf{r}_3 t^+) \delta U(\mathbf{r}_3, \mathbf{r}_4, t) \hat{\psi}(\mathbf{r}_4 t)\right]. \quad (3.4)$$

The previous line was obtained from the differentiation of the exponential of equation (3.2), by observing that the product of operators $\hat{\psi}^\dagger\hat{\psi}$ does commute with others two-field operator products inside a time-ordered product T.

When the equation (3.4) is inserted inside the expression 3.3, each $\delta\hat{S}$ adds two field operators. One can hence recognize a two-particle Green's function and a one-particle one:

$$\delta G(1,2) = -\int_{-\infty}^{+\infty} dt \int d\mathbf{r}_3 d\mathbf{r}_4 \delta U(\mathbf{r}_3, \mathbf{r}_4, t) \left[G_2(1, \mathbf{r}_4 t; 2, \mathbf{r}_3 t^+)\right.$$
$$\left. -G(1,2)G(\mathbf{r}_4 t, \mathbf{r}_3 t^+)\right]. \quad (3.5)$$

Finally, we obtain the final formula of the Schwinger derivative technique, which is also valid for $t_3 \neq t^+$:

$$\frac{\delta G(1,2)}{\delta U(3,4)} = -G_2(1,4;2,3) + G(1,2)G(4,3). \quad (3.6)$$

This equation is obviously of great practical interest: it allows one to get rid of the two-particle Green's function, while retaining only the terms dependent on one-particle Green's functions.

For instance, if one uses this equation with a local $U(3)\delta(3, 4)$, the equation of motion of the one-particle Green's function (2.31) immediately becomes

$$\left[i\frac{\partial}{\partial t_1} - h(\mathbf{r}_1)\right]G(1, 2) + i\int d3 v(1, 3)G(3, 3^+)G(1, 2)$$
$$- i\int d3 v(1^+, 3)\frac{\delta G(1, 2)}{\delta U(3)} = \delta(1, 2) \quad (3.7)$$

or, after introducing $\int d5 G^{-1}(4, 5)G(5, 2) = \delta(4, 2)$,

$$\left[i\frac{\partial}{\partial t_1} - h(\mathbf{r}_1) + i\int d3 v(1, 3)G(3, 3^+)\right]G(1, 2)$$
$$- i\left[\int d345 v(1^+, 3)\frac{\delta G(1, 4)}{\delta U(3)}G^{-1}(4, 5)\right]G(5, 2) = \delta(1, 2). \quad (3.8)$$

As $-iG(3, 3^+)$ is the electronic density, $-i\int d3 v(1, 3)G(3, 3^+)$ is nothing else but the Hartree potential. The last member of the previous equation provides the definition of the self-energy operator:

$$\Sigma(1, 2) = i\int d345 v(1^+, 3)\frac{\delta G(1, 4)}{\delta U(3)}G^{-1}(4, 2), \quad (3.9)$$

or, using the relation (B.3),

$$\Sigma(1, 2) = -i\int d345 v(1^+, 3)G(1, 4)\frac{\delta G^{-1}(4, 2)}{\delta U(3)}, \quad (3.10)$$

that accounts for all the many-body effects beyond the Hartree term. We know that the one-particle Green's function furthermore satisfies the Dyson equation (2.38) introduced in the previous chapter. The next step is to find a way to properly evaluate this definition of the self-energy and to design efficient approximations to it.

3.2   Hedin's equations

In 1965, L. Hedin proposed a set of coupled equations that yields the exact self-energy [25]. These equations are based on two fundamental quantities G, the exact Green's function and W, the dynamical screened Coulomb interaction. In contrast with the usual many-body perturbation theory developed during the 50's [11], where the basic quantities were the non-interacting Green's function G_0 and the bare Coulomb interaction v, Hedin's scheme provides directly a set of equations in terms of G and W. Developments in terms of v are known to fail: for instance, the second order term in v for the correlation energy of an homogenous electron gas is infinite

[7]. The idea of using an interaction, namely W, weaker than v as coupling constant of the perturbative expansion was already introduced by Hubbard [26]. The screened Coulomb interaction is intuitively smaller than the bare one, as the interaction between two electrons being part of a system is reduced by the dielectric constant of the medium or, in other words, by the screening due to all the other electrons of the system.

Of course, it is possible to establish the link between conventional perturbation theory and Hedin's. First, perform the summation on the class of the so-called ring diagrams or RPA diagrams. This will substitute everywhere in the equations v for W. Second, achieve the self-consistency in G. This will substitute everywhere in the equations G_0 for G. Hedin's equations have the advantage of directly providing expressions that use G and W.

Hedin's derivation starts by introducing the local classical potential V

$$V(1) = U(1) - i \int d2 v(1,2) G(2,2^+), \qquad (3.11)$$

which is the sum of the external perturbation U and the Hartree potential, in order to replace all references to U with expressions involving V.

Let us insert the chain rule (B.4) via V in the definition of the self-energy of equation (3.10):

$$\Sigma(1,2) = -i \int d345 \, v(1^+,3) \frac{\delta G^{-1}(1,4)}{\delta V(5)} \frac{\delta V(5)}{\delta U(3)} G(4,2), \qquad (3.12)$$

where the following definitions can be introduced:

$$\varepsilon^{-1}(1,2) = \frac{\delta V(1)}{\delta U(2)} \qquad (3.13)$$

is the time-ordered inverse dielectric function, and

$$\tilde{\Gamma}(1,2;3) = -\frac{\delta G^{-1}(1,2)}{\delta V(3)} \qquad (3.14)$$

is the irreducible vertex function. "Irreducible" refers to the fact that the differentiation is performed with respect to V and not to U.

At this point, one can introduce W, the dynamical screened Coulomb interaction, which plays the role of the coupling constant of the perturbative approach. W is defined by

$$W(1,2) = \int d3 v(1,3) \varepsilon^{-1}(3,2). \qquad (3.15)$$

According to the previous definitions, Σ finally reads

$$\Sigma(1,2) = i \int d34 \, G(1,4) W(3,1^+) \tilde{\Gamma}(4,2;3). \qquad (3.16)$$

It still remains to provide some tractable expressions for $\tilde{\Gamma}$ and ε^{-1}.

Using the Dyson equation $G^{-1} = G_0^{-1} - V - \Sigma$, equation (3.14) is worked out in the following way

$$\tilde{\Gamma}(1,2;3) = \delta(1,2)\delta(1,3) + \frac{\delta\Sigma(1,2)}{\delta V(3)} \qquad (3.17)$$

$$= \delta(1,2)\delta(1,3) + \int d45 \frac{\delta\Sigma(1,2)}{\delta G(4,5)} \frac{G(4,5)}{\delta V(3)}$$

$$= \delta(1,2)\delta(1,3) + \int d4567 \frac{\delta\Sigma(1,2)}{\delta G(4,5)}$$

$$\times G(4,6)G(7,5)\tilde{\Gamma}(6,7;3). \qquad (3.18)$$

First, the chain rule (B.4) via δG was used. Second, the derivative of the inverse (B.3) was introduced. Finally, one could recognize the expression of the irreducible vertex $-\delta G^{-1}/\delta V$ in the right-hand side of the equation. This is a closed integral equation for the 3-point vertex function, with a 4-point kernel $\delta\Sigma/\delta G$.

Concerning ε^{-1}, let us use the definition of V:

$$\varepsilon^{-1}(1,2) = \frac{\delta\left(U - i\int d3 v(1,3)G(3,3^+)\right)}{\delta U(2)}$$

$$= \delta(1,2) + \int d3 v(1,3)\chi(3,2), \qquad (3.19)$$

where

$$\chi(1,2) = -i\frac{\delta G(1,1^+)}{\delta U(2)} \qquad (3.20)$$

is the reducible polarizability of the system. "Reducible" means that the variations $G(1,1^+)$ are sensitive to the bare external potential U. One can alternatively define an irreducible polarizability

$$\tilde{\chi}(1,2) = -i\frac{\delta G(1,1^+)}{\delta V(2)}. \qquad (3.21)$$

The link between the two polarizabilities is made by using once more the chain rule and the relation (3.19):

$$\chi(1,2) = -i\int d3 \frac{G(1,1^+)}{V(3)} \frac{\delta V(3)}{\delta U(2)}$$

$$= \tilde{\chi}(1,2) + \int d34 \tilde{\chi}(1,3)v(3,4)\chi(4,2). \qquad (3.22)$$

The remaining quantity, that has still to be determined, is $\tilde{\chi}$. It can be obtained as a function of G and $\tilde{\Gamma}$ by using relation (B.3):

$$\tilde{\chi}(1,2) = i\int d34 G(1,3)\frac{\delta G^{-1}(3,4)}{\delta V(2)}G(4,1)$$

$$= -i\int d34 G(1,3)G(4,1)\tilde{\Gamma}(3,4;2). \qquad (3.23)$$
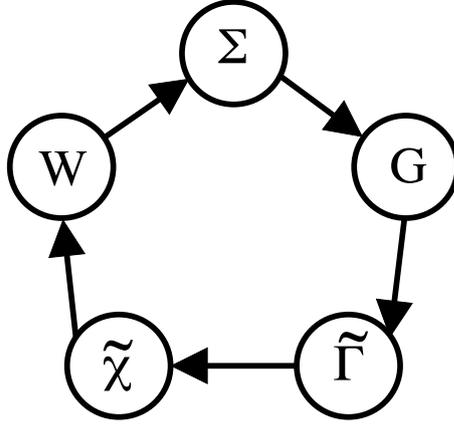
Figure 3.1: Symbolical representation of the practical solution of the Hedin's equation. This representation is probably due to V. Olevano [27].

At the present time, all introduced quantities are properly defined and the limit of vanishing external potential U can be safely performed. Let us gather Hedin's set of five equations of five variables:

$$G(1,2) = G_0(1,2) + \int d34 G_0(1,3)\Sigma(3,4)G(4,2) \qquad (3.24a)$$

$$\tilde{\Gamma}(1,2;3) = \delta(1,2)\delta(1,3) + \int d4567 \frac{\delta\Sigma(1,2)}{\delta G(4,5)}$$
$$\times G(4,6)G(7,5)\tilde{\Gamma}(6,7;3) \qquad (3.24b)$$

$$\tilde{\chi}(1,2) = -i \int d34 G(2,3)G(4,2)\tilde{\Gamma}(3,4;1) \qquad (3.24c)$$

$$W(1,2) = v(1,2) + \int d34 v(1,3)\tilde{\chi}(3,4)W(4,2) \qquad (3.24d)$$

$$\Sigma(1,2) = i \int d34 G(1,4)W(3,1^+)\tilde{\Gamma}(4,2;3) \qquad (3.24e)$$

Only the definition of W was worked out to avoid the introduction of the intermediate quantities ε^{-1} and χ.

In his original paper, Hedin mentioned that these equations can be viewed as an iterative solution of the many-body problem, but he stressed that they would be interesting if only very few iterations were actually needed. Initiate with some hypothesis on Σ and G, evaluate $\tilde{\Gamma}$, then $\tilde{\chi}$. Calculate W and then Σ. Now one knows an improved Green's function G and one can start again the same procedure, with the new Σ and G. This procedure can be represented by the pentagon in figure 3.1, where each summit symbolizes an unknown variable and each edge one of the five Hedin equations. The exact solution can be obtained in principle upon completion of numerous cycles of the pentagon.

Figure 3.2: Feynman diagram representation of the GW self-energy, which is the only first-order contribution in terms of screened Coulomb interaction.

Figure 3.3: Feynman diagram representation of the first-order irreducible polarizability.

3.3 GW approximation

Using W instead of v as basic interaction line is motivated by the hope that the perturbation theory will converge faster with respect to powers of W, than with respect to the powers of v. Having this hope in mind, Hedin proposed to retain only first-order contributions in W [25], or in other words, to perform one single cycle of the pentagon. This yields the so-called GW approximation that consists in initiating the iterative scheme with $\Sigma = 0$ in the vertex equation:

$$\tilde{\Gamma}(1, 2; 3) = \delta(1, 2)\delta(1, 3). \tag{3.25}$$

This provides indeed a first-order expansion in terms of W of the scheme, as depicted with the Feynman diagrams in figures 3.2 and 3.3. The symbols used in Feynman diagrams can be found on page xi.

On one hand, the resulting self-energy is just

$$\Sigma(1, 2) = iG(1, 2)W(2, 1^+). \tag{3.26a}$$

The form of equation (3.26a) gives the name to the approximation. On the other hand, the irreducible polarizability simply reads

$$\tilde{\chi}(1, 2) = -iG(1, 2)G(2, 1) = \chi_0(1, 2), \tag{3.26b}$$

which is the definition of the independent particle polarizability χ_0.

This approximation is justified only if one expects the sum of the higher-order terms in W to be small with respect to the first-order ones of equations (3.26a) and (3.26b). Symbolically, the second order term for the self-energy can be written as $GWGWG$. For instance, it is well known that the

effect of the higher-order terms in the polarizability is drastic on optical properties (as it will be discussed in the following).

In conclusion, there is no fundamental evidence that assesses the relevance of this approximation. However, many calculations using this approximation were performed successfully, and made this method the state-of-the-art for the evaluation of band structures [28, 29].

3.4 Static screened exchange and COHSEX approximation

In order to simplify, and to gain physical insight into the GW approximation, let us make some further approximations. We suppose that the screened Coulomb interaction is static

$$W(\mathbf{r}_1, \mathbf{r}_2, \tau) = \frac{1}{2\pi} W(\mathbf{r}_1, \mathbf{r}_2, \omega = 0)\delta(\tau). \tag{3.27}$$

Therefore, equation (3.26a) becomes

$$\Sigma(\mathbf{r}_1, \mathbf{r}_2, \omega) = \frac{i}{2\pi} \int d\tau G(\mathbf{r}_1, \mathbf{r}_2, \tau) W(\mathbf{r}_2, \mathbf{r}_1, \omega = 0)\delta(\tau + \eta)e^{i\omega\tau}. \tag{3.28}$$

Analogously to the Hartree-Fock derivation, this integral retains only contributions from occupied states. Finally, one obtains a *statically screened exchange approximation* for the self-energy:

$$\Sigma_{\text{SEX}}(\mathbf{r}_1, \mathbf{r}_2) = -\sum_i \theta(\mu - \epsilon_i) f_i(\mathbf{r}_1) f_i^*(\mathbf{r}_2) W(\mathbf{r}_2, \mathbf{r}_1, \omega = 0). \tag{3.29}$$

Equation (3.29) is identical to expression (2.48), except that the bare Coulomb interaction was replaced by the statically screened one. This static approximation for the self-energy should be an improvement with respect to the Hartree-Fock approach, as it includes the decrease of the exchange interaction due to the polarizability of the medium.

The assumption (3.27) on W is quite drastic. Let us make a slightly different approximation, proposed by L. Hedin [25] in 1965, that gives rise to additional static terms in the self-energy. Whereas the bare Coulomb part v of W is strictly speaking instantaneous, the polarizable part $W_p = W - v$ has a certain width in the time structure. This is implemented in equation (3.28) by removing the small η parameter in the polarizable part of W:

$$\Sigma(\mathbf{r}_1, \mathbf{r}_2, \omega) = \frac{i}{2\pi} \int d\tau G(\mathbf{r}_1, \mathbf{r}_2, \tau) \left[v(\mathbf{r}_2, \mathbf{r}_1)\delta(\tau + \eta) \right.$$
$$\left. + W_p(\mathbf{r}_2, \mathbf{r}_1, \omega = 0)\delta(\tau) \right] e^{i\omega\tau}. \tag{3.30}$$

This assumption still makes W_p a sharp peak, but now it is not able to retain only occupied states, as in the case of exchange (first term of equation (3.30)). Introducing the expression of the Green's function (equation (2.14)) and using the relation $\delta(\tau)\theta(\tau) = \delta(\tau)\theta(-\tau) = \frac{1}{2}\delta(\tau)$, one gets

$$
\begin{aligned}
\Sigma(\mathbf{r}_1, \mathbf{r}_2) &= -\sum_i \theta(\mu - \epsilon_i) f_i(\mathbf{r}_1) f_i^*(\mathbf{r}_2) v(\mathbf{r}_2, \mathbf{r}_1) \\
&\quad -\frac{1}{2}\sum_i \theta(\mu - \epsilon_i) f_i(\mathbf{r}_1) f_i^*(\mathbf{r}_2) W_p(\mathbf{r}_2, \mathbf{r}_1) \\
&\quad +\frac{1}{2}\sum_i \theta(\epsilon_i - \mu) f_i(\mathbf{r}_1) f_i^*(\mathbf{r}_2) W_p(\mathbf{r}_2, \mathbf{r}_1) \\
&= -\sum_i \theta(\mu - \epsilon_i) f_i(\mathbf{r}_1) f_i^*(\mathbf{r}_2) W(\mathbf{r}_2, \mathbf{r}_1) \\
&\quad +\frac{1}{2}\sum_i f_i(\mathbf{r}_1) f_i^*(\mathbf{r}_2) W_p(\mathbf{r}_2, \mathbf{r}_1). \qquad (3.31)
\end{aligned}
$$

To obtain the last line, we added and removed $\frac{1}{2}\sum_i \theta(\mu - \epsilon_i) f_i(\mathbf{r}_1) f_i^*(\mathbf{r}_2) W_p(\mathbf{r}_2, \mathbf{r}_1)$. The equation (3.31) now exhibits the same self-energy contribution Σ_{SEX} as previously. The remaining contribution Σ_{COH} is just a sum over all the states of Lehmann amplitudes, that reduces to a $\delta(\mathbf{r}_1, \mathbf{r}_2)$ function, due to the completeness of f_i's. The term

$$
\Sigma_{\text{COH}}(\mathbf{r}_1, \mathbf{r}_2) = \frac{1}{2}\delta(\mathbf{r}_1 - \mathbf{r}_2) W_p(\mathbf{r}_2, \mathbf{r}_1, \omega = 0) \qquad (3.32)
$$

is known as the *Coulomb hole contribution* to the self-energy. This term is static, and moreover local in space.

This static approximation to the full *GW* self-energy elucidates the meaning of the different contributions with more understandable pictures. One can think of the screened exchange operator as the usual Fock operator weakened by the presence of the other electrons, that screen the interaction. In a non-polarizable material, the screening would tend to 1 and the resulting screened exchange would just be the bare exchange.

The Coulomb hole term Σ_{COH} can be viewed in a totally classical picture [25], once one has assumed that the added or removed particle is just a point charge. Let us evaluate the classical potential felt by a point charge $\pm\delta(\mathbf{r} - \mathbf{r}_0)$ (that can represent a hole or an electron according to the sign), via the polarization of the medium surrounding it. The scheme of the interactions is given in figure 3.4

In any place of the material, this addition or removal of a charge leads to a variation of the Coulomb potential:

$$
\delta V_{\text{ext}}(\mathbf{r}') = \int d\mathbf{r}\, v(\mathbf{r}', \mathbf{r}) \left(\pm\delta(\mathbf{r} - \mathbf{r}_0)\right). \qquad (3.33a)
$$
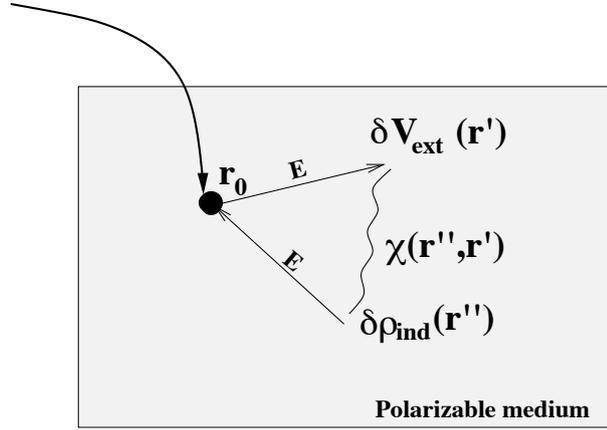
Figure 3.4: Evaluation of the potential felt by a point charge introduced at $\mathbf{r}_0$ in a polarizable medium, which induces a potential δV_{ext}, which, on its turn, creates induced charges $\delta \rho_{\text{ind}}$. The latter finally act on the introduced charge. The straight arrows labeled E represent the interaction due to the electric field. The wiggly line represents the polarizability.

As the material is polarizable, a change of the potential at any point $\mathbf{r}'$ gives rise to variation of charge in $\mathbf{r}''$:

$$\delta \rho_{\text{ind}}(\mathbf{r}'') = \int d\mathbf{r}' \chi(\mathbf{r}'', \mathbf{r}') \delta V_{\text{ext}}(\mathbf{r}'). \tag{3.33b}$$

On its turn turn, this change in the charge density in all possible $\mathbf{r}''$ creates an induced potential in $\mathbf{r}$, via

$$\delta V_{\text{ind}}(\mathbf{r}''') = \int d\mathbf{r}'' v(\mathbf{r}''', \mathbf{r}'') \delta \rho_{\text{ind}}(\mathbf{r}''). \tag{3.33c}$$

If the equations (3.33) are combined, one obtains the classical potential felt by an small variation of the density on itself, via the polarizability of the medium:

$$\delta V_{\text{ind}}(\mathbf{r}''') = \int d\mathbf{r} d\mathbf{r}' d\mathbf{r}'' v(\mathbf{r}''', \mathbf{r}'') \chi(\mathbf{r}'', \mathbf{r}') v(\mathbf{r}', \mathbf{r}) \left(\pm \delta(\mathbf{r} - \mathbf{r}_0) \right), \tag{3.34}$$

where $v \chi v$ is W_p. Finally, the energy consumed to adiabatically build the charge distribution $\pm \delta(\mathbf{r})$ in a polarizable medium is given by

$$E_{\text{ind}} = \int_0^1 \alpha d\alpha \int d\mathbf{r}''' \left(\pm \delta(\mathbf{r}''' - \mathbf{r}_0) \right) \delta V_{\text{ind}}(\mathbf{r}''') = \frac{1}{2} W_p(\mathbf{r}_0, \mathbf{r}_0). \tag{3.35}$$

The 1/2 factor accounts for the adiabatic building up of the charge density. Since there are two occurrences of $\pm$ in δV_{ind} and in E_{ind}, the sign of this energy is always positive, both for holes and for electrons. It is compliant

with the classical intuition, that the polarization tends to oppose to the causes that have created it. As the probability to find the electron or hole labelled i in $\mathbf{r}_0$ is $|\phi_i(\mathbf{r}_0)|^2$, the energy corresponding to this charge distribution is nothing else but

$$\frac{1}{2} \int d\mathbf{r}_0 W_p(\mathbf{r}_0, \mathbf{r}_0) |\phi_i(\mathbf{r}_0)|^2 = \langle i|\Sigma_{\text{COH}}|i\rangle. \tag{3.36}$$

This energy is exactly what we called the Coulomb hole self-energy.

The COHSEX approximation to the self-energy is of physical interest, but it is still approximative. For instance, we considered only an instantaneous polarization of the medium by the classical charge. In reality we do know that the polarizability χ is a frequency dependent function! We also considered the added hole or electron as a point charge $\pm\delta(\mathbf{r} - \mathbf{r}_0)$ with no spatial extension weighted by the probability to find the particle there. This is a crude approximation to the quantum mechanical formalism.

This physics of the response of the medium to the addition of an extra-particle is also contained in the GW approximation, with even less assumptions. But they are more difficult to analyze in the full GW expression.

3.5 Bethe-Salpeter equation for the polarizability

It is interesting to know also the two-particle Green's function G_2. For instance, in an absorption experiment, two particles are involved: an electron and a hole. It is obvious that describing the two particles in terms of two independent particles would neglect the mutual attraction of the hole and the electron. This approximation would disregard all the excitonic effects. Therefore, to draw a realistic description of optical absorption phenomena, the calculation of G_2 is really required (to be precise a contracted G_2 is needed).

Let us introduce the quantity L defined in terms of G_2:

$$iL(1, 2; 1', 2') = -G_2(1, 2; 1', 2') + G(1, 1')G(2, 2'). \tag{3.37}$$

L describes the coupled motion of an electron and a hole minus the motion of the two independent particles. L is called the 4-point polarizability, because, when it is contracted, it gives back the usual 2-point polarizability (this will be made clear in the following). According to equation (3.6), L can be written as the derivative of the one-particle Green's function $G(1, 1')$ with respect to a nonlocal external potential $U(2', 2)$:

$$L(1, 2; 1', 2') = -i\frac{\delta G(1, 1')}{\delta U(2', 2)}. \tag{3.38}$$
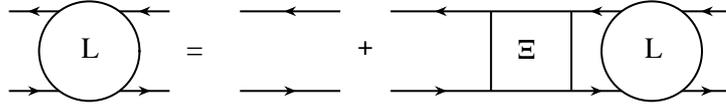
Figure 3.5: Feynman diagram representation of the 4-point Bethe-Salpeter equation. The 4-point polarizability is drawn as a circle and the 4-point Bethe-Salpeter kernel as a square.

Using the same functional tricks (chain rules, derivative of inverse...) as in the derivation of Hedin's equations, we can get a closed integral equation for L, namely the Bethe-Salpeter equation. First, we introduce the derivative of G^{-1}:

$$L(1,2;1',2') = i \int d34 G(1,3) G(4,1') \frac{\delta G^{-1}(3,4)}{\delta U(2',2)}. \tag{3.39}$$

Second, we use the Dyson equation (2.38) to get rid of G^{-1}:

$$L(1,2;1',2') = i \int d34 G(1,3) G(4,1')$$
$$\times \frac{\delta}{\delta U(2',2)} \left[G_0^{-1}(3,4) - U(3,4) - v_h(3)\delta(3,4) - \Sigma(3,4) \right]. \tag{3.40}$$

As G_0 does not depend on U, this gives

$$L(1,2;1',2') = L_0(1,2;1',2') + \int d3456 L_0(1,4;1',3)$$
$$\frac{\delta}{\delta G(5,6)} \left[v_h(3)\delta(3,4) + \Sigma(3,4) \right] \frac{\delta G(5,6)}{\delta U(2',2)}, \tag{3.41}$$

where $L_0(1,2;1',2') = -iG(1,2')G(2,1')$ is the noninteracting L, and the chain rule via $G(5,6)$ was used. Finally, if Ξ stands for the Bethe-Salpeter kernel,

$$\Xi(3,6;4,5) = i\frac{\delta \left[v_h(3)\delta(3,4) + \Sigma(3,4) \right]}{\delta G(5,6)}, \tag{3.42}$$

the final result is the Bethe-Salpeter equation

$$L(1,2;1',2') = L_0(1,2;1',2')$$
$$+ \int d3456 L_0(1,4;1',3) \Xi(3,6;4,5) L(5,2;6,2'). \tag{3.43}$$

This is a Dyson-like equation for the 4-point polarizability L. The kernel Ξ links the noninteracting L_0 to the true L. This is strictly analogous to the role of the self-energy Σ that links G_0 to G. The Bethe-Salpeter

equation can be drawn using the Feynman diagrams technique as depicted in figure 3.5.

The knowledge of the complete $L(1, 2; 1', 2')$ is actually not necessary to describe optical absorption experiments. In fact, they are sensitive to the reducible polarizability χ

$$\chi(1, 2) = -i\frac{\delta G(1, 1^+)}{\delta U(2, 2)} = L(1, 2; 1, 2). \qquad (3.44)$$

Only the two-point function $L(1, 2; 1, 2)$ is then required to account for absorption phenomena. Unfortunately, there is no closed equation within the Green's function framework for this two-point quantity. In practice, we need to solve the four-point Bethe-Salpeter equation and then to contract into the two-point polarizability. The solution of the Bethe-Salpeter equation gives much more information than needed for that purpose. One of the topics of the thesis is to circumvent this limitation (chapter 9)

3.6   Approximations to the kernel of the Bethe-Salpeter equation

In practical applications, the kernel of the Bethe-Salpeter equation has to be specified. As it depends on the self-energy Σ, one can immediately try to use the same approximation as the ones we used for Σ.

The complete neglect of Σ yields the so-called *time-dependent Hartree approximation* or, for historical reasons, the Random Phase Approximation (RPA). The self-energy Σ in Ξ now depends only on the electronic density (i.e. the diagonal of G), which adds a $\delta(5, 6)$ function in equation (3.43). In this particular case, due to the two δ functions, the Bethe-Salpeter equation reduces to a closed Dyson-like equation for χ:

$$\chi(1, 2) = \chi_0(1, 2) + \int d34 \chi_0(1, 3)v(3, 4)\chi(4, 2). \qquad (3.45)$$

The Coulomb interaction v comes out from the differentiation of the Hartree potential v_h with respect to ρ. This 2-point equation is depicted on figure 3.7, where the role of the δ functions can be graphically seen (note the contraction of the indexes of L).

Due to the interaction v, even when we are interested in the macroscopic dielectric constant $\varepsilon_M(\mathbf{q} \to 0)$ only, we need to consider χ_0 as a full matrix [31, 32]. In the plane-wave basis set, the macroscopic dielectric constant reads

$$\varepsilon_M(\mathbf{q} \to 0) = 1/(\delta_{\mathbf{G}=0\mathbf{G}'=0} + v_{\mathbf{G}=0}\chi_{\mathbf{G}=0\mathbf{G}'=0}). \qquad (3.46)$$

In order to calculate $\chi_{\mathbf{G}=0\mathbf{G}'=0}$, the calculation of the full matrix $\chi_{0\,\mathbf{G}\mathbf{G}'}$ is required according to equation (3.45). The term v in the time-dependent
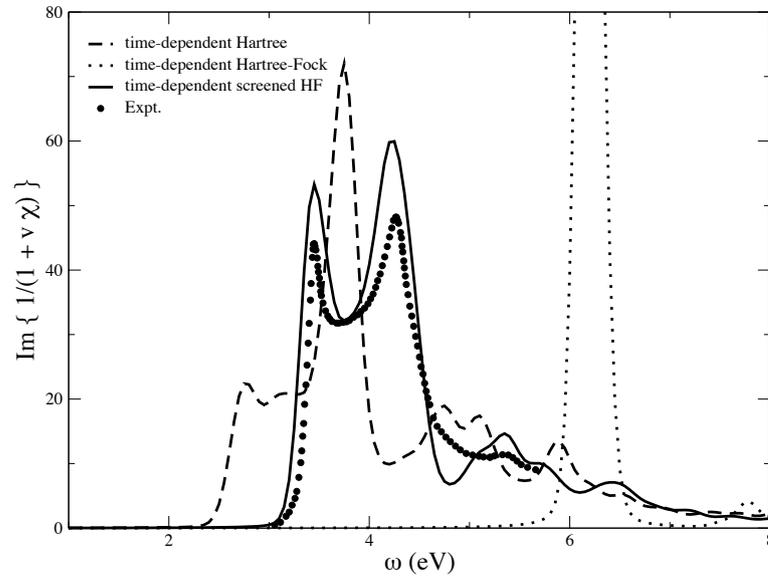
Figure 3.6: Optical absorption spectrum of bulk silicon calculated within time-dependent Hartree (constructed with an LDA χ_0, dashed line), time-dependent HF (dotted line), and time-dependent screened HF (full line) approximations of the Bethe-Salpeter kernel compared to the experimental curve (full circles) of reference [30]. A broadening of 0.1 eV has been used for all theoretical curves.

Figure 3.7: Feynman diagram representation of the Bethe-Salpeter equation within the time-dependent Hartree approximation (or RPA). It is now a 2-point equation, as the indexes can be contracted, such that one can get a closed equation for $L(1, 2; 1, 2) = \chi(1, 2)$.

Hartree approximation gives rise to the so-called *crystal local-field effects*. This effects account for the inhomogeneity in space of the material: in fact, in real space the response function does depend on $\mathbf{r}$ and $\mathbf{r}'$, and not simply on $\mathbf{r} - \mathbf{r}'$.

The performance of the time-dependent Hartree approximation for the calculation of optical absorption experiments is shown in figure 3.6. Note that the noninteracting polarizability χ_0 used to calculate the time-dependent Hartree spectrum of the figure is not the Hartree one, but the DFT-LDA one (see next chapters). Therefore, the curve depicted here is not, strictly speaking, the time-dependent Hartree one. Indeed, the true time-dependent

Hartree curve should be even in worse agreement with the experiment.

If the self-energy is now set equal to the exchange self-energy $\Sigma(1,2) = iG(1,2)v(1^+,2)$, the derivative with respect to G can be easily performed and yields two δ functions:

$$L(1,2;1',2') = L_0(1,2;1',2') + \int d3456 L_0(1,4;1',3)$$
$$\times \left[\delta(3,4)\delta(5,6)v(3,5) - \delta(3,5)\delta(4,6)v(3,4)\right]L(5,2;6,2'). \quad (3.47)$$

The indexes of the second v are in such an order hat it is impossible to write directly an equation for χ. This approximation is called *time-dependent Hartree-Fock*. It is not used in pratice for semiconductors, because the attraction between the hole and the electron carried by the second term of Ξ is too large. The solution of this equation would give bound excitons in all materials, as one can see in figure 3.6. For silicon, the calculated spectrum becomes one single sharp peak at too high energies (even if it is below the Hartree-Fock band gap). This is due to the fact that the Coulomb interaction between the hole and the electron should be screened by the other electrons of the system and that the Hartree-Fock approximation gives a very bad L_0 with a too large band gap (see table 2.1).

A simple manner to take into account the polarizability of the system is to choose the screened exchange approximation for the self-energy. The resulting Bethe-Salpeter equation is identical to equation (3.47), but with the statically screened Coulomb interaction $W(\omega = 0)$ instead of the second bare Coulomb interaction v, if one also neglects the derivative $\delta W/\delta G$ (which is believed to be second-order in W). The last approximation has for long been considered as a harmless approximation [33, 34]. The equation in the *time-dependent screened Hartree-Fock* approximation reads

$$L(1,2;1',2') = L_0(1,2;1',2') + \int d3456 L_0(1,4;1',3)\left[\delta(3,4)\delta(5,6)v(3,5)\right.$$
$$\left.-\delta(3,5)\delta(4,6)\frac{1}{2\pi}W(\mathbf{r}_3,\mathbf{r}_4,\omega=0)\delta(t_3-t_4)\right]L(5,2;6,2'), \quad (3.48)$$

which correspond of the Feynman diagram representation in figure 3.8. The Feynman diagrams make obvious that the wiggly line, that represents W, prevents from contracting the indexes of L to get a 2-point equation for χ (this limitation was already true within the time-dependent Hartree-Fock approximation).

The solution of the previous equation is the method of choice used in many practical *ab initio* applications [35]. It has been very successful for clusters [36], surfaces [37], and solids [38, 39]. In particular, for silicon, the almost perfect agreement between the time-dependent screened HF calculation and the experimental curve can be seen in figure 3.6. Note that the
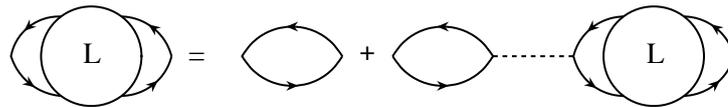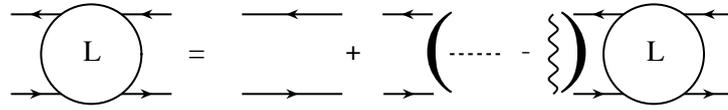
Figure 3.8: Feynman diagram representation of the Bethe-Salpeter equation within the time-dependent screened HF approximation. The Bethe-Salpeter kernel consists of two 2-point terms, but unfortunately, the contracted indexes are not the same for v (horizontal interaction) and for W (vertical interaction). The equation hence remains a 4-point one.

GW eigenvalues, which give a very good band gap, have been used to construct L_0 in equation (3.48). As a consequence, the calculation commonly made is not strictly speaking a time-dependent screened HF calculation, but, more precisely, a GW plus time-dependent screened HF calculation.

Note that, thanks to the $\delta(t_3 - t_4)$ function, the equation (3.48) depends on only one frequency. Some attempts were made to include further dynamical effects in W and in the Green's functions [40, 41]. The conclusions were that the dynamical effects essentially cancel out. As a consequence, the current recipe of using just a statically screened Hartree-Fock approximation for the kernel of the Bethe-Salpeter equation turns out to be justified. In particular, this method is successfully used for Cu_2O in chapter 16.

Chapter 4

Approach to the Many-Body Problem by means of the electronic density

4.1   Ground-state density as a basic variable

The idea of density-functional theory (DFT) is basically the same as in Green's functions approach: in order to avoid to use the full N-particle wavefunction, one considers instead an "integrated" variable. An integrated variable means that it is obtained from the original many-body wavefunction, but all variables except one, in the case of the density, are averaged out:

$$\rho(\mathbf{r}) = N \int d\mathbf{r}_2 \ldots d\mathbf{r}_N \left| \Psi_0(\mathbf{r}, \mathbf{r}_2, \ldots, \mathbf{r}_N) \right|^2, \tag{4.1}$$

where Ψ_0 is the ground-state wavefunction of the N-electron system. This is the simplest integrated quantity one can think of. Integrating on the only remaining variable yields N, the number of electrons.

The idea of using the ground-state density alone as a basic variable comes from the early works on quantum mechanics (L. H. Thomas [42] and E. Fermi [43]). The density can be intuitively felt as fundamental, since it yields directly the main contributions to the energy of a system. For example, the electrostatic part of the electron-electron interaction (the Hartree energy E_H) is readily obtained from the density,

$$E_H = \frac{1}{2} \int d\mathbf{r} d\mathbf{r}' \frac{\rho(\mathbf{r})\rho(\mathbf{r}')}{|\mathbf{r} - \mathbf{r}'|}, \tag{4.2}$$

as well as, the energy due to an external potential v_{ext},

$$E_{ext} = \int d\mathbf{r} \rho(\mathbf{r}) v_{ext}(\mathbf{r}), \tag{4.3}$$

and the kinetic energy of a noninteracting homogeneous electron gas by means of the Thomas-Fermi formula.

But at this point, there are some open issues: neither the kinetic energy can be written in terms of ρ in the general case , nor the electron-electron interaction beyond the electrostatic term. The original paper of Hohenberg and Kohn [44] in 1964 justified, on firm mathematical grounds, approaches using the density only.

4.1.1 Hohenberg-Kohn theorems

The Hohenberg-Kohn theorems are mathematical proofs for the following properties of a system of N-fermion interacting via a given potential v, subjected to a static external potential $v_{ext}(\mathbf{r})$:

- there is a one-to-one mapping up to a constant value between the space of external potentials and the space of the ground-state densities:

$$v_{ext} \Leftrightarrow \rho; \tag{4.4}$$

- the ground-state expectation value of any observable $\mathcal{O}$ is a functional of the ground-state density only:

$$\langle \Psi_0 | \mathcal{O} | \Psi_0 \rangle = O[\rho]; \tag{4.5}$$

- there is a variational principle on the density: the ground-state energy E_0 has its global minimum for the true ground-state density ρ

$$E_0[\rho] < E_0[\tilde{\rho}], \tag{4.6}$$

where $\tilde{\rho}$ is any trial ground-state density.

The proof of the previous statements can be found in the original Hohenberg-Kohn's paper [44] or in reviews about DFT (see e.g. reference [45]). The proof is made *ad absurdum*. This means that it does not give a practical expression for the one-to-one mapping between v_{ext} and ρ. It just states the existence of the one-to-one mapping: "it could not be else".

Looking at the many-body Hamiltonian of equation (1.2), it seems to be necessary, for instance, to know the one-particle *density matrix* in order to calculate the kinetic contribution to the energy. The power of DFT is that the simpler quantity ρ can *mathematically* give access to all ground-state properties of a system and in particular to the kinetic energy.

As the total energy is a functional of the density, it is possible extract some parts that are obviously density-functionals. The remainder will be still a density-functional:

$$\begin{aligned} E_0[\rho] &= \langle \Psi_0 | \mathcal{H} | \Psi_0 \rangle \\ &= \langle \Psi_0 | T + W | \Psi_0 \rangle + \int d\mathbf{r} v_{ext}(\mathbf{r}) \rho(\mathbf{r}), \end{aligned} \tag{4.7}$$

where T is the kinetic operator and W is the electron-electron interaction operator. One is allowed to go on and split the W term into two pieces: the Hartree part and a remainder E_{xc}:

$$E_0[\rho] = \langle \Psi_0 | T | \Psi_0 \rangle + \frac{1}{2} \int d\mathbf{r} d\mathbf{r}' \frac{\rho(\mathbf{r})\rho(\mathbf{r}')}{|\mathbf{r} - \mathbf{r}'|} + \int d\mathbf{r} v_{ext}(\mathbf{r})\rho(\mathbf{r}) + E_{xc}[\rho]. \quad (4.8)$$

The purpose is to make the remainder as small as possible. This unknown quantity E_{xc} is called the *exchange-correlation* energy. The kinetic energy is also a functional of the density, whose dependence with respect to the density is unknown.

4.1.2   Kohn-Sham approach to DFT

In 1965, W. Kohn and L. J. Sham [46] proposed a method to evaluate the main contribution to the kinetic energy. The aim is again to make the unknown part of $E_0[\rho]$ as small as possible. They proposed to split the kinetic contribution into to parts: the kinetic energy of a *fictitious system of noninteracting electrons* that would experience an external potential v_{KS}, such that it has the *same ground-state density* as the interacting system; and a remainder (the correlation part of the kinetic energy), which is recast inside the unknown quantity E_{xc}. In this approach, the ground-state energy reads

$$E_0[\rho] = -\sum_{i=1}^{N} \int d\mathbf{r} \phi_i^*(\mathbf{r}) \frac{\nabla_{\mathbf{r}}^2}{2} \phi_i(\mathbf{r})$$

$$+ \frac{1}{2} \int d\mathbf{r} d\mathbf{r}' \frac{\rho(\mathbf{r})\rho(\mathbf{r}')}{|\mathbf{r} - \mathbf{r}'|} + \int d\mathbf{r} v_{ext}(\mathbf{r})\rho(\mathbf{r}) + E_{xc}[\rho], \quad (4.9)$$

where E_{xc} differs from the definition(4.8) of the previous section, because it now contains the correlated part of the kinetic energy, and where $\phi_i(\mathbf{r})$ are the wavefunctions of the noninteracting system.

This procedure has, of course, a drawback: the wavefunction concept is re-introduced into the scheme. Fortunately, these wavefunctions $\phi_i(\mathbf{r})$ are noninteracting, i.e. one-particle ones. They can hence be calculated in practice. The wavefunctions ϕ_i are themselves density-functionals. Therefore, the Kohn-Sham technique remains within the DFT framework.

The Kohn-Sham potential v_{KS} is obtained by the fact that the energy is stationnary upon changes in the ground-state density of the true (or of the fictitious) system. It reads

$$v_{KS}(\mathbf{r}) = v_{ext}(\mathbf{r}) + \int d\mathbf{r}' \frac{\rho(\mathbf{r}')}{|\mathbf{r} - \mathbf{r}'|} + v_{xc}[\rho](\mathbf{r}), \quad (4.10)$$

where the second term is the usual Hartree potential and the last term is the exchange-correlation potential defined by

$$v_{xc}(\mathbf{r}) = \frac{\delta E_{xc}}{\delta \rho(\mathbf{r})}. \tag{4.11}$$

Gathering these considerations, the Kohn-Sham procedure reduces to solve an independent particle problem, with eigenfunctions ϕ_i and eigenvalues ϵ_i:

$$\left(-\frac{\nabla^2}{2} + v_{KS}(\mathbf{r})\right)\phi_i(\mathbf{r}) = \epsilon_i \phi_i(\mathbf{r}). \tag{4.12}$$

As the potential v_{KS} is given by equation (4.10), the eigenfunctions have the only required property: they yield the correct ground-state density

$$\rho(\mathbf{r}) = \sum_{i=1}^{N} |\phi_i(\mathbf{r})|^2. \tag{4.13}$$

Equations (4.10), (4.12), (4.13) form the set of closed equations of the Kohn-Sham scheme. It remains just to devise sensible approximations to v_{xc}.

4.1.3 Exchange-correlation potentials

The tiny part E_{xc} that still remains unknown has to be approximated in a convenient way. It has to be computationally cheap and give reliable results. The first approximation already devised in 1965 by Kohn and Sham [46], the Local Density Approximation (LDA), satisfies both requirements.

Local Density Approximation

One can write with no further assumption the exchange-correlation energy under the form

$$E_{xc} = \int d\mathbf{r}\rho(\mathbf{r})\epsilon_{xc}[\rho](\mathbf{r}), \tag{4.14}$$

with $\epsilon_{xc}[\rho](\mathbf{r})$ standing for the exchange-correlation energy density. This quantity is still a functional of the ground-state density.

The Local Density Approximation (LDA) proposes to assume that, at every point $\mathbf{r}$ of space, $\epsilon_{xc}[\rho](\mathbf{r})$ is just the exchange-correlation energy density of an homogeneous electron gas of the same density $\rho(\mathbf{r})$. Since Ceperley and Adler's [47] pioneering Quantum Monte Carlo calculations, exact data for ϵ_{xc} in an homogeneous electron gas are available. For practical purposes, Quantum Monte Carlo results were interpolated [48, 49] in order to have an analytic expression for ϵ_{xc} as a function of $\rho(\mathbf{r})$.

Note that, in this local approximation, ϵ_{xc} is not only a functional of the density ρ, it is, to be precise, a *simple function* of $\rho(\mathbf{r})$:

$$E_{xc} = \int d\mathbf{r}\rho(\mathbf{r})\epsilon_{xc}^{\mathrm{LDA}}(\rho(\mathbf{r})). \tag{4.15}$$

This approximation has been applied successfully for 20 years [50]. It has also been extended to the case of spin-polarized calculations (LSDA).

Gradient expansions beyond LDA

If the system under study were totally homogeneous, the LDA would be exact, by definition. A natural way to attempt improvements on LDA is to allow for a further dependence of ϵ_{xc} on the derivatives of the density, to account for the inhomogeneity of the density. This is a gradient expansion of the exchange-correlation energy with respect to the density.

In this kind of approximation, the dependence of ϵ_{xc} with respect to the density remains local: ϵ_{xc} is a function of $\rho(\mathbf{r})$, $\nabla\rho(\mathbf{r})$, ... The so-called Generalized Gradient Approximation (GGA) of reference [51] has become widely used, e.g. because it gives reliable results for molecules or for hydrogen bonds in water. Unfortunately, one cannot state that the GGA gives systematic improvements with respect to the LDA. That is why I have generally preferred the simpler LDA to the GGA in this thesis.

The Meta-GGA method [52] proposes to add a dependence on $\nabla^2\rho(\mathbf{r})$, and on $\tau(\mathbf{r}) = 1/2 \sum_i |\nabla\phi_i(\mathbf{r})|^2$. τ depends explicitly on the Kohn-Sham orbitals (which are themselves functionals of the density). The computational cost increases considerably as a consequence. This method is not currently wide spread in the DFT community.

Other approximations for the exchange-correlation

Improved exchange-correlation energies can also be obtained by indirect methods.

The adiabatic-connection fluctuation-dissipation theorem expresses the exchange-correlation energy as an integral over a coupling constant λ that scales the Coulomb interaction $\lambda/|\mathbf{r}-\mathbf{r}'|$. This method needs the calculation of response functions for many different values of λ. It is very involved and has been applied so far only to small systems [53].

Direct comparison with the Green's function approach (described in the previous chapters) can give access to expressions for the exchange-correlation potential, via the so-called Sham-Schlüter equation [13]. This procedure is described extensively in chapter 6.

4.2   Time-dependent density as the basic variable

We have so far studied only systems subjected to a static external potential. The ground-state density can then play the role of the basic variable, as its knowledge is sufficient to recover the external potential, and hence the

full Hamiltonian (provided that the two-body interaction is given). What happens when a time-dependent external potential is applied? This will for sure change the situation drastically, since there is no energy conservation, and the system leaves its ground-state.

A time-dependent external potential is very often met in experiments, for instance, in optical absorption. The theoretical description of optical absorption requires to know how the electronic density of the system responds to a change of the external potential $\delta U(\mathbf{r}'t')$. The observable of interest in linear response regime is the *causal response function* χ defined by

$$\delta\rho(\mathbf{r}t) = \int_{-\infty}^{t} dt' \int d\mathbf{r}'\chi(\mathbf{r},\mathbf{r}',t-t')\delta U(\mathbf{r}'t'). \tag{4.16}$$

Causal means that variations of $\rho(\mathbf{r}t)$ only depends on time t' smaller than t.

It seems natural to extend the static formalism of DFT to the dynamical case. This was the implicit point of view of Zangwill and Soven [54], who performed the first time-dependent density-functional calculation in 1980. But there were no mathematical grounds to justify the use of the time-dependent density-functional approach. The cornerstone was put by Runge and Gross in 1984 [55].

4.2.1   Runge-Gross theorem and time-dependent Kohn-Sham

Runge and Gross established in 1984 [55] (for a recent review, see reference [56]) a series of theorems, which are the dynamical equivalent of the static Hohenberg-Kohn and Kohn-Sham theorems. Under some mild assumptions, they proved that there is a one-to-one mapping between the time-dependent external potentials (up to a purely time-dependent constant) and the time-dependent densities.

The two requirements of this theorem are first a well-defined initial state $|\Psi(t_0)\rangle$ and second that the time-dependent external potential is Taylor-expandable at the initial time t_0. The first requirement is very important, as one can start at the initial time t_0 with an excited state, whose wavefunction is not, strictly speaking, a density-functional. The second one excludes all the adiabatic switching-on processes that are non-Taylor expandable.

Runge and Gross also showed the validity of the Kohn-Sham procedure for time-dependent systems. The Kohn-Sham orbitals are now time-dependent $\phi_i(\mathbf{r}t)$ and obey a one-particle time-dependent Schrödinger equation:

$$i\frac{\partial}{\partial t}\phi_i(\mathbf{r}t) = H_{KS}(\mathbf{r},t)\phi_i(\mathbf{r}t), \tag{4.17}$$

where the KS Hamiltonian is a direct extension of the static one

$$H_{KS}(\mathbf{r}t) = -\frac{\nabla^2}{2} + v_{KS}[n](\mathbf{r}t).$$ (4.18)

The wavefunctions $\phi_i(\mathbf{r}, t)$ have the only property to yield the correct time-dependent density

$$\rho(\mathbf{r}t) = \sum_i |\phi_i(\mathbf{r}t)|^2.$$ (4.19)

The time-dependent Kohn-Sham potential $v_{KS}[n](\mathbf{r}, t)$ is the straightforward extension to time-dependent systems of the usual static Kohn-Sham.

Finally, whereas there is no minimum principle for systems subjected to a time-dependent perturbation, there exists a quantum mechanical action A, whose extrema describe the time evolution of the system between the time t_1 and the time t_2:

$$A[\Psi] = \int_{t_1}^{t_2} dt \langle \Psi(t)| i\frac{\partial}{\partial t} - \mathcal{H}(t)|\Psi(t)\rangle.$$ (4.20)

This expression for the action A does not satisfy the causality requirement. Instead, A is symmetric with respect to the time arguments. This theoretical issue can be circumvented using the Keldysh contour technique [57, 58].

With this series of theorems, the use of only the time-dependent density is justified, and a practical Kohn-Sham procedure to evaluate the main contributions is established.

4.2.2   Linear-response regime

TDDFT is hence justified in particular for the linear-response regime [59], which is very useful to compare with experimental data. Our purpose is to calculate the causal response function χ, that links variations of the density $\delta\rho$ to variations of the external potential δU, as said earlier,

$$\delta\rho(\mathbf{r}t) = \int_{-\infty}^{t'} dt' \int d\mathbf{r}' \chi(\mathbf{r}, \mathbf{r}', t - t') \delta U(\mathbf{r}'t').$$ (4.21)

As time is homogeneous, the response function depends only on the difference between times. Moreover, causality has been explicitly enforced here thanks to the upper limit of the time integral. Note that this definition of χ is equivalent to the one met in the Hedin's equation of the previous chapter (equation (3.22)), except for the fact that the response is now causal instead of time-ordered.

The response function χ can alternatively be written as

$$\chi(\mathbf{r}, \mathbf{r}', t - t') = \left.\frac{\delta\rho(\mathbf{r}t)}{\delta U(\mathbf{r}'t')}\right|_{U=v_{ext}},$$ (4.22)

where the derivative is evaluated at a vanishing perturbing potential δU. Therefore, U reduces to the static external potential v_{ext}. This expression can be worked out in order to introduce the Kohn-Sham response function χ_{KS}, which is the response of the independent Kohn-Sham particles:

$$\chi_{KS}(\mathbf{r}, \mathbf{r}', t - t') = \left. \frac{\delta\rho(\mathbf{r}t)}{\delta v_{KS}(\mathbf{r}'t')} \right|_{v_{KS\mathrm{static}}}. \qquad (4.23)$$

The time-dependent Kohn-Sham potential v_{KS} has been introduced

$$v_{KS}(\mathbf{r}t) = U(\mathbf{r}t) + v_h(\mathbf{r}t) + v_{xc}(\mathbf{r}t), \qquad (4.24)$$

where all these potentials are functional of the time-dependent density.

The chain rule via v_{KS} can be used in equation (4.22)

$$
\begin{aligned}
\chi(\mathbf{r}, \mathbf{r}', t - t') &= \int_{-\infty}^{t} dt'' \int d\mathbf{r}'' \frac{\delta\rho(\mathbf{r}t)}{\delta v_{KS}(\mathbf{r}''t'')} \frac{\delta v_{KS}(\mathbf{r}''t'')}{\delta U(\mathbf{r}'t')} \\
&= \int_{-\infty}^{t} dt'' \int d\mathbf{r}'' \chi_{KS}(\mathbf{r}, \mathbf{r}'', t - t'') \\
&\quad \times \frac{\delta}{\delta U(\mathbf{r}'t')} \left[U(\mathbf{r}''t'') + v_h(\mathbf{r}''t'') + v_{xc}(\mathbf{r}''t'') \right] \\
&= \chi_{KS}(\mathbf{r}, \mathbf{r}', t - t') \\
&\quad + \int_{-\infty}^{t} dt'' \int_{-\infty}^{t''} dt''' \int d\mathbf{r}'' \int d\mathbf{r}''' \chi_{KS}(\mathbf{r}, \mathbf{r}'', t - t'') \\
&\quad \times \left[v(\mathbf{r}'', \mathbf{r}''', t'' - t''') + f_{xc}(\mathbf{r}'', \mathbf{r}''', t'' - t''') \right] \\
&\quad \times \chi(\mathbf{r}''', \mathbf{r}', t''' - t').
\end{aligned}
\qquad (4.25)
$$

The last step was reached by using the chain rule via $\rho(\mathbf{r}'''t''')$. Equation (4.25) is a Dyson-like equation for χ. The kernel of this integral equation is the quantity $(v + f_{xc})$, where v is the usual Coulomb potential and f_{xc} is the so-called *exchange-correlation kernel*:

$$f_{xc}(\mathbf{r}, \mathbf{r}', t - t') = \frac{\delta v_{xc}(\mathbf{r}t)}{\delta\rho(\mathbf{r}'t')}. \qquad (4.26)$$

This is the key quantity of linear response TDDFT.

The Kohn-Sham response function can be directly computed as a Fermi's golden rule (since the KS particles do not interact), or in a manner analogous to the time-ordered response function, which will be described in the next chapters. Therefore, once an approximation for f_{xc} is chosen, all the ingredients needed for χ are determined. Before moving to the topic of the approximations to the exchange-correlation kernel, it would be valuable to specify the equations of TDDFT for periodic solids, which are the subject of interest of the present work.

Using the definition of the Fourier transform of nonlocal but periodic quantities given in Appendix A, one can transform the real space and time equation (4.25) into an equation in reciprocal space and frequencies:

$$\chi_{\mathbf{GG'}}(\mathbf{q}, \omega) = \chi_{KS\mathbf{GG'}}(\mathbf{q}, \omega)$$
$$+ \sum_{\mathbf{G_1 G_2}} \chi_{KS\mathbf{GG_1}}(\mathbf{q}, \omega) \left[v_{\mathbf{G_1}}(\mathbf{q})\delta_{\mathbf{G_1 G_2}} + f_{xc\mathbf{G_1 G_2}}(\mathbf{q}, \omega) \right] \chi_{\mathbf{G_2 G'}}(\mathbf{q}, \omega), \quad (4.27)$$

where the vectors $\mathbf{G}$ are reciprocal lattice vectors and $\mathbf{q}$ belongs to the first Brillouin zone. Note that integrals in space become sums over $\mathbf{G}$ in the reciprocal space and convolutions of times become simple products in frequency space. The response function χ can be obtained by inverting equation (4.27):

$$\chi(\mathbf{q}, \omega) = \left[1 - v(\mathbf{q})\chi_{KS}(\mathbf{q}, \omega) - f_{xc}(\mathbf{q}, \omega)\chi_{KS}(\mathbf{q}, \omega) \right]^{-1} \chi_{KS}(\mathbf{q}, \omega). \quad (4.28)$$

As experiments usually measure macroscopic integrated quantities, they are sensitive to the *head* of the matrix $\chi_{\mathbf{GG'}}$ (i.e. just to the element χ_{00}). A straightforward approximation is to consider this matrices as diagonal, to get the more simple equation

$$\chi_{\mathbf{GG}}(\mathbf{q}, \omega) = \chi_{KS\mathbf{GG}}(\mathbf{q}, \omega) + \chi_{KS\mathbf{GG}}(\mathbf{q}, \omega) \left[v_{\mathbf{G}}(\mathbf{q}) + f_{xc\mathbf{GG}}(\mathbf{q}, \omega) \right] \chi_{\mathbf{GG}}(\mathbf{q}, \omega).$$
$$(4.29)$$

This approximation simplifies a lot the problem, as only few matrix elements are needed instead of the full matrix and the matrix inversion is thus avoided. This approximation is said to *neglect the crystal local-field effects* for the following reason: assuming that χ is diagonal gives, in direct space, the response function

$$\delta\rho(\mathbf{r}t) = \int_{-\infty}^{t'} dt' \int d\mathbf{r}' \chi(\mathbf{r} - \mathbf{r}', t - t')\delta U(\mathbf{r}'t'), \quad (4.30)$$

which depends only on differences of $\mathbf{r}$ and $\mathbf{r}'$. In other words, this means that the system is assumed to be homogeneous. It neglects the heterogeneities due to the local structure of the crystal. Therefore, this approximation performs better in systems where the electronic density is as homogeneous as possible and it fails completely in finite systems or in heterostructures [60, 61]. It also fails for localized states, as the semicore states of transition metals [62].

4.2.3 Exchange-correlation kernels

The quest for efficient and reliable approximations for the exchange-correlation kernel is 30 years younger than the one for the exchange-correlation potential. As a consequence, the variety of approximations is much smaller for the kernel. Furthermore, their agreement with experimental data is very different if they are compared to data for finite systems or for solids, or if they are compared to energy-loss experiments or to optical absorption ones.
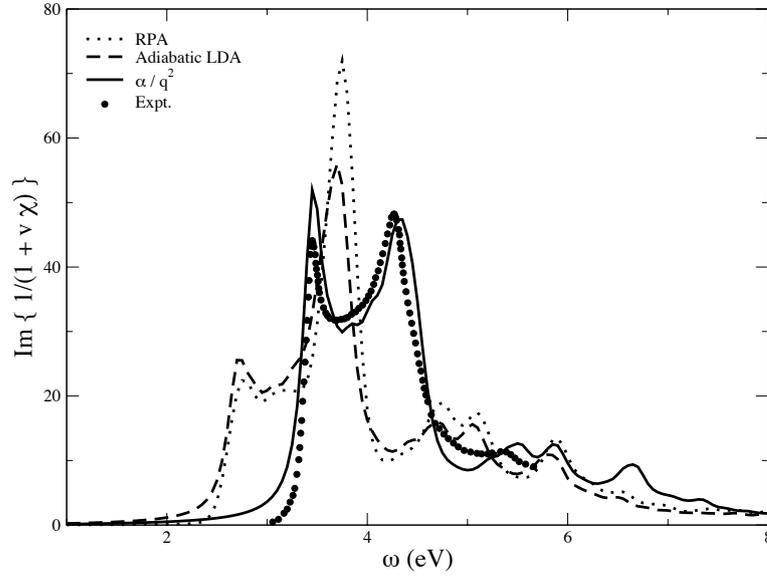
Figure 4.1: Optical absorption spectrum of bulk silicon calculated within RPA (dotted line), adiabatic LDA (dashed line), and using the α kernel of reference [4] (full line), compared to the experimental curve (full circles) of reference [30]. A broadening of $0.1\,\text{eV}$ was applied on all theoretical curves.

Random-Phase Approximation

The simplest approximation for f_{xc} is

$$f_{xc} = 0. \tag{4.31}$$

This is the Random-Phase Approximation (RPA) or time-dependent Hartree approximation. This approximation was already met in the framework of Green's function, when the exchange-correlation part of the Bethe-Salpeter kernel was fully neglected.

Figure 4.1 shows the comparison of the performance of the RPA with respect to an optical absorption experiment for the case of bulk silicon. As said earlier, the RPA gives a too small band gap and wrong oscillator strengths, since excitonic effects are not present at all. This calculation is equivalent to the time-dependent Hartree approximation of the previous chapter.

Adiabatic Local Density Approximation

Increasing the degree of sophistication of the kernel, the next step is to consider an LDA-like approximation. Within the local density approximation, the exchange-correlation potential at space point $\mathbf{r}$ depends only on

the density at the same point $\mathbf{r}$. Therefore, the kernel arising from the differentiation of this potential at $\mathbf{r}$ with respect to the density at point $\mathbf{r}'$ behaves like a function $\delta(\mathbf{r} - \mathbf{r}')$.

Concerning the time behavior of the kernel, the LDA kernel should, in principle, depend on all previous times before the time t, at which the potential is evaluated. There should be non trivial *memory* effects. As there is no clue of how to include these memory effects, one can add a further approximation: the *adiabatic* approximation assumes that the kernel depends only on the density at the present time. It has a $\delta(t - t')$ behavior and all memory effects are disregarded.

Finally, the expression of the adiabatic LDA (ALDA) kernel reads

$$f_{xc}^{\mathrm{ALDA}}(\mathbf{r}, \mathbf{r}', t - t') = \frac{dv_{xc}^{\mathrm{LDA}}(\mathbf{r}t)}{d\rho(\mathbf{r}t)}\delta(\mathbf{r} - \mathbf{r}')\delta(t - t'). \qquad (4.32)$$

This approximation proved to be quite successful for finite systems (see the review [35]). However in solid systems, the improvement of ALDA with respect to RPA is very small in the optical range. Figure 4.1 shows the tiny differences between RPA and ALDA calculations for bulk silicon. This has been interpreted by the lack of the proper $1/\mathbf{q}^2$ singularity in reciprocal space, that the exact kernel should have [63], and that neither RPA nor ALDA have.

Beyond ALDA

Going beyond LDA is even less straightforward than in the case of the exchange-correlation potential, since the differentiation of a GGA potential does not yield the correct asymptotic behavior neither. Thus, gradient expansions do not provide better results. As a consequence, the improvements over LDA came in particular from comparison with Green's function framework [4, 64, 65].

The $1/\mathbf{q}^2$ behavior in reciprocal space of the true kernel was for instance identified by L. Reining *et al.* [4] by comparing the Bethe-Salpeter equation and the TDDFT Dyson-like equation. An evidence of the importance of the $1/\mathbf{q}^2$ term in the kernel can be given by using a model kernel

$$f_{xc\mathbf{G}\mathbf{G}'}(\mathbf{q}, \omega) = -\delta_{\mathbf{G}0}\delta_{0\mathbf{G}'}\frac{\alpha}{\mathbf{q}^2}, \qquad (4.33)$$

where α is an empirical parameter related to the inverse of the dielectric constant. In order to reproduce the Bethe-Salpeter equation with this simple model kernel, one has to further apply some scissor operator in order to transform the LDA eigenvalues into the *GW* ones.

The agreement of the optical absorption spectra using this kernel with a proper value of α with experimental curves is assessed by figure 4.1, where $\alpha = 0.2$ has been used for silicon [66]. This way of connecting the Green's

function framework and TDDFT seems to be successful, either using direct comparison or using time-dependent optimized effective potential techniques. This is the topic of chapter (6).

Chapter 5

Practical implementation of standard GW

The GW self-energy, which is a simple product in time according to equation (3.26a), becomes a convolution in the frequency domain. The evaluation of

$$\Sigma(\mathbf{r}, \mathbf{r}', \omega) = \frac{i}{2\pi} \int d\omega' e^{i\omega'\eta} G(\mathbf{r}, \mathbf{r}', \omega + \omega') W(\mathbf{r}', \mathbf{r}, \omega') \qquad (5.1)$$

is a complicated task. The basic assumption is that the GW self-energy is not computed self-consistently, but using noninteracting inputs (usually Kohn-Sham wavefunctions and energies). This gives a simple expression for the Green's function. Then, one needs to calculate the screened Coulomb interaction W within RPA and the convolution of G and W to get the nonlocal energy-dependent self-energy.

The current chapter provides expressions and algorithms, as they are used in the codes used in the present thesis [67, 68]. They are dedicated to periodic systems, using the plane-wave basis set and pseudopotential. The first step is addressed in the first section. The second one needs further technical approximations to make it tractable in practice. This is described in the second section.

5.1 Evaluation of W

5.1.1 Representation of ε^{-1}

The evaluation of the screened Coulomb interaction $W(\mathbf{r}', \mathbf{r}, \omega)$ requires the evaluation of the inverse dielectric function $\varepsilon^{-1}(\mathbf{r}', \mathbf{r}, \omega)$. It is convenient to represent this quantity on the plane-wave basis set. One therefore needs to calculate the matrix

$$\varepsilon_{\mathbf{G}\mathbf{G}'}^{-1}(\mathbf{q}, \omega) = \delta_{\mathbf{G}\mathbf{G}'} + v(\mathbf{q} + \mathbf{G})\chi_{\mathbf{G}\mathbf{G}'}(\mathbf{q}, \omega). \qquad (5.2)$$

This equation is just equation (3.19) written on the plane-wave basis set. The reducible polarizability is given by

$$\chi_{\mathbf{G}\mathbf{G}'}(\mathbf{q},\omega) = \sum_{\mathbf{G}''} [\delta_{\mathbf{G}_1 \mathbf{G}_2} - \chi_{0\mathbf{G}_1\mathbf{G}_2}(\mathbf{q},\omega)v(\mathbf{q}+\mathbf{G}_1)]^{-1}_{\mathbf{G}\mathbf{G}''} \chi_{0\mathbf{G}''\mathbf{G}'}(\mathbf{q},\omega),$$

(5.3)

where the equation (3.22) for χ has been inverted, and the RPA was introduced $\tilde{\chi} = \chi_0$.

As a consequence, the only ingredient needed to achieve the calculation of W is the RPA polarizability χ_0.

5.1.2 RPA polarizability χ_0

The definition of the RPA polarizability is the simple product of two Green's functions in real space and time (equation (3.26b)):

$$\chi_0(1,2) = -iG(1,2)G(2,1).$$

(5.4)

According to that definition, the simple product in time becomes a convolution in frequency domain:

$$\chi_0(\mathbf{r}_1, \mathbf{r}_2, \omega) = -\frac{2i}{2\pi} \int d\omega' G(\mathbf{r}_1, \mathbf{r}_2, \omega + \omega')G(\mathbf{r}_2, \mathbf{r}_1, \omega'),$$

(5.5)

where the factor 2 accounts for spin degeneracy.

If one introduces the definition of the time-ordered Green's function of a non-interacting system (let us say the Kohn-Sham system), the Green's functions have single poles at each energy $\epsilon_{\mathbf{k}_i i}$:

$$\chi_0(\mathbf{r}_1, \mathbf{r}_2, \omega) = -\frac{2i}{2\pi} \sum_{\mathbf{k}_i i \mathbf{k}_j j} \int d\omega' \frac{\phi_{\mathbf{k}_i i}(\mathbf{r}_1)\phi^*_{\mathbf{k}_i i}(\mathbf{r}_2)}{\omega + \omega' - \epsilon_{\mathbf{k}_i i} + i\eta\,\mathrm{sign}(\epsilon_{\mathbf{k}_i i} - \mu)}$$
$$\times \frac{\phi_{\mathbf{k}_j j}(\mathbf{r}_2)\phi^*_{\mathbf{k}_j j}(\mathbf{r}_1)}{\omega' - \epsilon_{\mathbf{k}_j j} + i\eta\,\mathrm{sign}(\epsilon_{\mathbf{k}_j j} - \mu)}. \quad (5.6)$$

This frequency integral can be performed analytically thanks to the residue theorem, by closing the path of integration, either using an arc in the upper plan or in the lower plan. The poles are located at

$$\omega' = \begin{cases} \epsilon_{\mathbf{k}_i i} - \omega - i\eta\,\mathrm{sign}(\epsilon_{\mathbf{k}_i i} - \mu) \\ \epsilon_{\mathbf{k}_j j} - i\eta\,\mathrm{sign}(\epsilon_{\mathbf{k}_j j} - \mu). \end{cases}$$

(5.7)

Consequently, when the poles of the two Green's functions are located in the same half plane, the integral vanishes, since one can close the path in the opposite half plane, where there is no pole. Therefore, the only terms contributing are those for which one state is occupied and the other one is

empty. This condition describes transitions from full states to empty ones, and reversely:

$$\chi_0(\mathbf{r}_1, \mathbf{r}_2, \omega) = 2 \sum_{\mathbf{k}_i i \mathbf{k}_j j} \phi_{\mathbf{k}_i i}(\mathbf{r}_1) \phi^*_{\mathbf{k}_j j}(\mathbf{r}_1) \phi^*_{\mathbf{k}_i i}(\mathbf{r}_2) \phi_{\mathbf{k}_j j}(\mathbf{r}_2)$$

$$\times \left[\frac{\theta(\epsilon_{\mathbf{k}_i i} - \mu)\theta(\mu - \epsilon_{\mathbf{k}_j j})}{\omega - (\epsilon_{\mathbf{k}_i i} - \epsilon_{\mathbf{k}_j j}) + i\eta} - \frac{\theta(\mu - \epsilon_{\mathbf{k}_i i})\theta(\epsilon_{\mathbf{k}_j j} - \mu)}{\omega - (\epsilon_{\mathbf{k}_i i} - \epsilon_{\mathbf{k}_j j}) - i\eta} \right]. \quad (5.8)$$

We can remark that the location of the poles of the time-ordered χ_0: for positive transitions (when $\epsilon_i > \epsilon_j$), the poles are in the lower plane, for negative transitions (when $\epsilon_i < \epsilon_j$), the poles are in the upper plane. If the system under study has a band gap, χ_0 has no poles in the energy interval from minus the band gap to plus the band gap.

The remaining operation is the Fourier transform of the space variables according to the definitions of Appendix A. This leads to introduce the following matrix elements

$$\tilde{\rho}_{\mathbf{k}_i i j}(\mathbf{q} + \mathbf{G}) = \int d\mathbf{r} \phi^*_{\mathbf{k}_i i}(\mathbf{r}) e^{-i(\mathbf{q}+\mathbf{G}).\mathbf{r}} \phi_{\mathbf{k}_j j}(\mathbf{r}). \quad (5.9)$$

It is very useful to spend some time discussing these matrix elements, since they are recurrent in our derivations. The index $\mathbf{k}_j$ has not been written down explicitly, because it is imposed by the condition $\delta(\mathbf{q} + \mathbf{k}_i - \mathbf{k}_j - \mathbf{G}_0)$, with $\mathbf{G}_0$ a reciprocal lattice vector. The vector $\mathbf{q}$ is really the transfered momentum when a transition from $\mathbf{k}_i$ to $\mathbf{k}_j$ occurs and the δ function accounts for momentum conservation. The wavefunctions $\phi_{\mathbf{k}_i i}(\mathbf{r})$ are Bloch wavefunctions,

$$\phi_{\mathbf{k}_i i}(\mathbf{r}) = e^{i\mathbf{k}_i.\mathbf{r}} u_{\mathbf{k}_i i}(\mathbf{r}), \quad (5.10)$$

where $u_{\mathbf{k}_i i}(\mathbf{r})$ has the periodicity of the crystal. Introducing this definition in equation (5.9) gives

$$\tilde{\rho}_{\mathbf{k}_i i j}(\mathbf{q} + \mathbf{G}) = \int d\mathbf{r} u^*_{\mathbf{k}_i i}(\mathbf{r}) u_{\mathbf{k}_j j}(\mathbf{r}) e^{-i(\mathbf{q}+\mathbf{k}_i-\mathbf{k}_j).\mathbf{r}} e^{-i\mathbf{G}.\mathbf{r}}, \quad (5.11)$$

which is non-zero only if $\mathbf{q}+\mathbf{k}_i-\mathbf{k}_j$ is equal to a reciprocal lattice vector $\mathbf{G}_0$, since the functions u are periodic (see Appendix A). Finally, $\tilde{\rho}_{\mathbf{k}_i i j}(\mathbf{q} + \mathbf{G})$ is just a Fourier coefficient

$$\tilde{\rho}_{\mathbf{k}_i i j}(\mathbf{q} + \mathbf{G}) = \int d\mathbf{r} u^*_{\mathbf{k}_i i}(\mathbf{r}) u_{\mathbf{k}_j j}(\mathbf{r}) e^{-i(\mathbf{G}+\mathbf{G}_0).\mathbf{r}}, \quad (5.12)$$

and this is exactly the expression computed in the codes [67, 68].

The final expression, as it used in practice, reads

$$\chi_{0\mathbf{G}_1\mathbf{G}_2}(\mathbf{q}, \omega) = \frac{1}{V} \sum_{\mathbf{k}_i i j} (f_{\mathbf{k}_j j} - f_{\mathbf{k}_i i})$$

$$\times \frac{\tilde{\rho}_{\mathbf{k}_i i j}(\mathbf{q} + \mathbf{G}_1)\tilde{\rho}^*_{\mathbf{k}_i i j}(\mathbf{q} + \mathbf{G}_2)}{\omega - (\epsilon_{\mathbf{k}_i i} - \epsilon_{\mathbf{k}_j j}) + i\eta \, \text{sign}(\epsilon_{\mathbf{k}_i i} - \epsilon_{\mathbf{k}_j j})}, \quad (5.13)$$

where $f_{\mathbf{k}_i i}$ are the occupation numbers of state $\mathbf{k}_i i$ (value between 0 and 2). The value of ε^{-1} is hence obtained via matrix multiplications and inversions. Unfortunately, this calculation has to be done for each $\mathbf{q}$ vector and all frequencies ω. This is rather cumbersome, since many frequencies are needed: the function $\chi_0(\omega)$ is bad behaved, as all its poles lie close to the real axis.

5.1.3 Plasmon-pole model

It has been proposed since the 60's to model the dependence on ω of the matrix $\varepsilon_{\mathbf{GG'}}^{-1}(\mathbf{q}, \omega)$ by a single plasmon-pole model:

$$\varepsilon_{\mathbf{GG'}}^{-1}(\mathbf{q}, \omega) = \delta_{\mathbf{GG'}} + \frac{\Omega_{\mathbf{GG'}}^2(\mathbf{q})}{\omega^2 - (\tilde{\omega}_{\mathbf{GG'}}(\mathbf{q}) - i\eta)^2}, \qquad (5.14)$$

where $\Omega_{\mathbf{GG'}}^2(\mathbf{q})$ and $\tilde{\omega}_{\mathbf{GG'}}$ are the two parameters of the model. The small η is here just to ensure the right time-ordering. This model allows us to evaluate ε^{-1} everywhere in the complex plane, once the two parameters are fit.

There are various ways to fit these parameters. To this purpose, two constraints are needed. The ABINIT GW code [67, 69] chooses two frequencies where the RPA ε^{-1} is actually computed: $\omega = 0$ and $\omega \sim i\omega_p$ (ω_p is the classical plasmon frequency). These frequencies are convenient, because the fit is more stable on the imaginary axis, far from the poles of χ_0. Alternatively, Hybertsen and Louie [70] chose to calculate ε^{-1} at $\omega = 0$, and to enforce the f-sum rule.

The use of a plasmon-pole model not only reduces the calculation of $\varepsilon^{-1}(\omega)$ (as only two frequencies are required), but also permits an analytic calculation of the frequency integral in equation (5.1).

5.2 Evaluation of Σ

Once the screening is known, the self-energy can be evaluated. A direct calculation of $\Sigma(\mathbf{r}, \mathbf{r'}, \omega)$ is still nowadays out of reach. Fortunately, the purpose of a GW calculation is generally just to get a quasiparticle band structure, which does not require the knowledge of the full spatial and dynamical complexity of Σ.

5.2.1 First-order perturbation

If one remarks that the Kohn-Sham and the quasiparticle Hamiltonians are very similar, except for the replacement of exchange-correlation potential v_{xc} with the self-energy Σ, it is reasonable to consider $\Sigma - v_{xc}^{KS}$ as a first-order perturbation to the full Kohn-Sham Hamiltonian, which contains

large terms like the kinetic energy, the Hartree and the electron-ion terms. In a first-order perturbation scheme, the eigenvalues are simply obtained thanks to the evaluation of the diagonal matrix elements:

$$\epsilon_{\mathbf{k}_j j}^{GW} = \epsilon_{\mathbf{k}_j j}^{\text{KS}} + \langle \phi_{\mathbf{k}_j j} | \Sigma(\epsilon_{\mathbf{k}_j j}^{GW}) - v_{xc}^{KS} | \phi_{\mathbf{k}_j j} \rangle. \tag{5.15}$$

This equation shows clearly why the GW band structures are often referred to as the "GW corrections" over LDA, GGA, HF band structures.

The gain of computational time is drastic using this first-order perturbation approach. To get one GW correction, one needs only one matrix element, instead of calculating the N_r^2 terms of $\Sigma(\mathbf{r}, \mathbf{r}')$. This approximation is justified when the GW wavefunctions are very close to the Kohn-Sham wavefunctions. This is in practice well justified for simple materials, like bulk silicon (see chapter 8).

5.2.2   Linearization of the energy dependence

A second simplification concerns the evaluation of $\Sigma(\epsilon_{\mathbf{k}_j j}^{GW})$ in equation (5.15), which is in principle quite complicated, as Σ depends itself on the quasi-particle energy. A very efficient approximation is to linearize the dynamical behavior of Σ in the neighborhood of the Kohn-Sham eigenvalue:

$$\Sigma(\epsilon_{\mathbf{k}_j j}^{GW}) = \Sigma(\epsilon_{\mathbf{k}_j j}^{\text{KS}}) + \left(\epsilon_{\mathbf{k}_j j}^{GW} - \epsilon_{\mathbf{k}_j j}^{\text{KS}} \right) \left. \frac{\partial \Sigma}{\partial \epsilon} \right|_{\epsilon_{\mathbf{k}_j j}^{\text{KS}}}. \tag{5.16}$$

When this expansion is inserted in equation (5.15), we obtain

$$\epsilon_{\mathbf{k}_j j}^{GW} = \epsilon_{\mathbf{k}_j j}^{\text{KS}} + Z \langle \phi_{\mathbf{k}_j j} | \Sigma(\epsilon_{\mathbf{k}_j j}^{\text{KS}}) - v_{xc}^{KS} | \phi_{\mathbf{k}_j j} \rangle, \tag{5.17}$$

where

$$Z = \frac{1}{1 - \left. \frac{\partial \Sigma}{\partial \epsilon} \right|_{\epsilon_{\mathbf{k}_j j}^{\text{KS}}}}. \tag{5.18}$$

Equation (5.17) finally relies only on Kohn-Sham inputs, but the derivative of Σ is also needed.

The linearization of Σ works generally very well close to the band gap, as depicted in figure 5.1. Farther from the Fermi level, in the plasmon region (here $\omega_p \sim 16.7$ eV), the poles of Σ make it non-linear as seen in the figure. To get proper GW corrections for low- or high-energy bands it is necessary to go beyond this simple approximation.

Making use of all these technical approximations, one can provide the expression of Σ_x and Σ_c used in practice in the code.
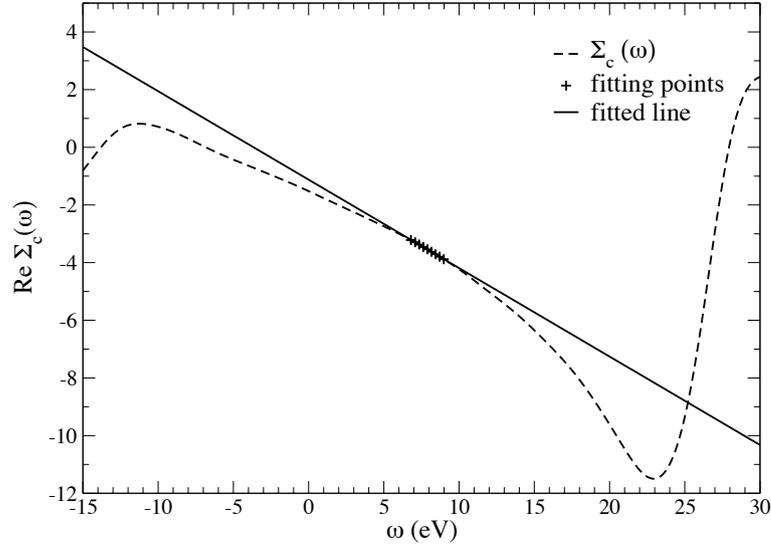
Figure 5.1: Performance of the linearization of $\Sigma(\omega)$ for the first conduction band of bulk silicon.

5.2.3   Bare exchange part Σ_x

According to the expression of the plasmon-pole model in equation (5.14), one can split ε^{-1} into two pieces: a δ function plus a non trivial part. The δ function gives rise to the bare exchange contribution Σ_x to the GW self-energy and, as a consequence, the remainder Σ_c accounts for the correlation.

Let us first deal with the bare exchange contribution of equation (5.1). The dynamical part is easily treated, as the only frequency dependence comes from the denominator of the Green's function:

$$\int d\omega' e^{i\omega'\eta} \frac{1}{\omega + \omega' - \epsilon_{\mathbf{k}_i i} + i\eta'\,\mathrm{sign}(\epsilon_{\mathbf{k}_i i} - \mu)} = 2\pi i \theta(\mu - \epsilon_{\mathbf{k}_i i}). \qquad (5.19)$$

The integration was performed via the residue theorem along a path enclosing the upper half plane, thus retaining only the poles corresponding to occupied states.

The matrix element of Σ_x hence reads

$$\langle \phi_{\mathbf{k}_j j} | \Sigma_x | \phi_{\mathbf{k}_j j} \rangle = -\sum_{\mathbf{k}_i i} \theta(\mu - \epsilon_{\mathbf{k}_i i}) \int d\mathbf{r} d\mathbf{r}' \phi^*_{\mathbf{k}_j j}(\mathbf{r}) \phi_{\mathbf{k}_i i}(\mathbf{r})$$

$$\times\, v(\mathbf{r} - \mathbf{r}') \phi^*_{\mathbf{k}_i i}(\mathbf{r}') \phi_{\mathbf{k}_j j}(\mathbf{r}'), \quad (5.20)$$

where the Fourier transform of $v(\mathbf{r} - \mathbf{r}')$ can be introduced

$$v(\mathbf{r} - \mathbf{r}') = \frac{1}{V} \sum_{\mathbf{q}, \mathbf{G}} e^{i(\mathbf{q}+\mathbf{G}).\mathbf{r}} \frac{4\pi}{|\mathbf{q} + \mathbf{G}|^2} e^{-i(\mathbf{q}+\mathbf{G}).\mathbf{r}'}. \qquad (5.21)$$

This operation makes once more appear the matrix elements $\tilde{\rho}_{\mathbf{k}_i ij}$.

The implemented expression of Σ_x is

$$\langle \phi_{\mathbf{k}_j j} | \Sigma_x | \phi_{\mathbf{k}_j j} \rangle = -\frac{4\pi}{V} \sum_{\mathbf{k}_i i} \theta(\mu - \epsilon_{\mathbf{k}_i i})$$

$$\times \sum_{\mathbf{G}} \tilde{\rho}^*_{\mathbf{k}_i ij}(\mathbf{q} + \mathbf{G}) \frac{1}{|\mathbf{q} + \mathbf{G}|^2} \tilde{\rho}_{\mathbf{k}_i ij}(\mathbf{q} + \mathbf{G}). \quad (5.22)$$

The sum over $\mathbf{q}$ has been removed thanks to the $\delta(\mathbf{q} + \mathbf{k}_i - \mathbf{k}_j - \mathbf{G}_0)$ coming from the $\tilde{\rho}_{\mathbf{k}_i ij}$, as discussed earlier in section 5.1.2. The scaling of the computational time of Σ_x is $N_v.N_{\mathbf{k}}.N_{\mathbf{G}}$, where N_v is the number of valence bands.

5.2.4 Correlation part Σ_c

The derivation of the correlation part Σ_c of the self-energy is analogous to the one for Σ_x, except for the fact that a special care has to be taken to evaluate the frequency integral. It reads

$$\langle \phi_{\mathbf{k}_j j} | \Sigma_c | \phi_{\mathbf{k}_j j} \rangle = \frac{i}{2\pi V} \sum_{\mathbf{k}_i i} \sum_{\mathbf{G}\mathbf{G}'} \tilde{\rho}^*_{\mathbf{k}_i ij}(\mathbf{q} + \mathbf{G}) \tilde{\rho}_{\mathbf{k}_i ij}(\mathbf{q} + \mathbf{G}') \frac{4\pi}{|\mathbf{q} + \mathbf{G}'|^2}$$

$$\int d\omega' \frac{1}{\omega + \omega' - \epsilon_{\mathbf{k}_i i} + i\eta \operatorname{sign}(\mu - \epsilon_{\mathbf{k}_i i})} \frac{\Omega^2_{\mathbf{G}\mathbf{G}'}(\mathbf{q})}{\omega'^2 - (\tilde{\omega}_{\mathbf{G}\mathbf{G}'}(\mathbf{q}) - i\eta)^2} e^{i\omega'\eta}, \quad (5.23)$$

where $\mathbf{q}$ is again constrained to be equal to the difference $\mathbf{k}_j - \mathbf{k}_i$, modulo a $\mathbf{G}_0$ vector.

By closing the integration path thanks to an arc in the upper half plane, one can apply the residue theorem, which yields for the integral over ω':

$$\int d\omega' \frac{1}{\omega + \omega' - \epsilon_{\mathbf{k}_i i} + i\eta \operatorname{sign}(\mu - \epsilon_{\mathbf{k}_i i})} \frac{1}{\omega'^2 - (\tilde{\omega}_{\mathbf{G}\mathbf{G}'}(\mathbf{q}) - i\eta)^2} =$$

$$= \frac{-2\pi i}{2\tilde{\omega}_{\mathbf{G}\mathbf{G}'}(\mathbf{q})} \left[\frac{\theta(\mu - \epsilon_{\mathbf{k}_i i})}{\omega + \tilde{\omega}_{\mathbf{G}\mathbf{G}'}(\mathbf{q}) - \epsilon_{\mathbf{k}_i i} - i\eta} + \frac{\theta(\epsilon_{\mathbf{k}_i i} - \mu)}{\omega - \tilde{\omega}_{\mathbf{G}\mathbf{G}'}(\mathbf{q}) - \epsilon_{\mathbf{k}_i i} + i\eta} \right].$$

$$(5.24)$$

The poles of Σ_c in this approximation are located, as imposed by the theory, above the real axis, for $\omega < \mu$, and below, for $\omega > \mu$. The poles arising from empty states are at $\tilde{\omega} + \epsilon_{\mathbf{k}_i i}$ and those coming from occupied states at $-\tilde{\omega} + \epsilon_{\mathbf{k}_i i}$. There are therefore no poles of Σ_c in an interval of width $2\tilde{\omega}$ around the Fermi level. The correlation part of the self-energy should be well behaved in this region, as it can be noticed from figure 5.1.

Gathering equations (5.23) and (5.24) yields the final expression for Σ_c. The evaluation of Σ_c scales as $N_b.N_{\mathbf{k}}.N^2_{\mathbf{G}}$, where N_b stands for the total number of bands used in G. This is therefore the most cumbersome part in the calculation of Σ.

Chapter 6

Connecting DFT and Green's function theory

The density-functional and the many-body perturbation approaches give both, in principle, exact answers to the many-body problem. They have both avantages and drawbacks.

On the one hand, MBPT provides systematic approximations for the self-energy, but quite often, there is no piece of evidence whether the perturbation series converges, i.e. the second-order term is not always smaller than the first-order one. Moreover, MBPT gives usually expressions that are computationally expensive.

On the other hand, DFT and TDDFT approaches are synthetic and elegant theories, that only need a "simple" exchange-correlation potential and kernel as functional of the density to account for all the quantum behavior of electrons. However, DFT and TDDFT provide, following a direct approach for closed systems, only certain informations on the N-electron system: the ground-state properties and the neutral excitations. For instance, ionization processes are not described in these frameworks. DFT (respectively TDDFT) is finally just a mathematical proof of the existence of a one-to-one mapping between ground-state properties (respectively neutral excitations) and the density (respectively the time-dependent density); there is *a priori* no clue how to find this mapping. Finally, there is no systematic recipe how produce exchange-correlation potentials or kernels.

Since the early days of DFT, the idea of connecting MBPT and DFT has been used [71]. The purpose has been to benefit both from the ability of MBPT to design sensible approximations and from the simplicity of DFT.

6.1 Exchange-correlation potentials derived from MBPT

6.1.1 Sham-Schlüter equation

The idea of Sham-Schlüter equation is to use the fact that DFT and MBPT give the same exact ground-state density, in order to find good approximations for the exchange-correlation potential from the suitable approximations for the self-energy [13, 72]. One should note that this operation is far from trivial, as the self-energy is a nonlocal and energy-dependent operator.

Let us introduce the Kohn-Sham Green's function G_{KS} constructed from Kohn-Sham wavefunctions and energies. The diagonal of G_{KS}, as well as the diagonal of the true Green's function G, provide the true ground-state density:

$$-iG(1, 1^+) = -iG_{\text{KS}}(1, 1^+). \tag{6.1}$$

This relation can be inserted into the Dyson equation that makes the link between the Kohn-Sham Green's function and the exact one

$$G(1, 2) = G_{\text{KS}}(1, 2) + \int d34 G_{\text{KS}}(1, 3) \left[\Sigma(3, 4) - v_{xc}(3)\delta(3, 4) \right] G(3, 2), \tag{6.2}$$

to yield an equation for the unknown exchange-correlation potential

$$\int d34 G_{\text{KS}}(1, 3) \left[\Sigma(3, 4) - v_{xc}(3)\delta(3, 4) \right] G(3, 1^+) = 0 \tag{6.3}$$

or, in frequency domain (we are here in the framework of a *static* external potential. Hence G and Σ depend only on time *differences* and v_{xc} is frequency independent),

$$\int d\mathbf{r}_3 d\mathbf{r}_4 d\omega e^{i\omega\delta} G_{\text{KS}}(\mathbf{r}_1, \mathbf{r}_3, \omega) \left[\Sigma(\mathbf{r}_3, \mathbf{r}_4, \omega) \right.$$
$$\left. - v_{xc}(\mathbf{r}_3)\delta(\mathbf{r}_3 - \mathbf{r}_4) \right] G(\mathbf{r}_3, \mathbf{r}_1, \omega) = 0. \tag{6.4}$$

This is the so-called Sham-Schlüter equation [13, 72]. This equation is not of great practical interest, as it requires, in principle, the knowledge of the exact Green's function to determine v_{xc}.

An approximated version of the Sham-Schlüter equation has been found successful in determining reliable exchange-correlation potentials. In the linearized version of equation (6.4), it is assumed that the difference between G and G_{KS} yields small effects. Hence, one simply replaces all occurrences of G in equation (6.4) by G_{KS}:

$$\int d\mathbf{r}_3 d\omega \chi_{\text{KS}}(\mathbf{r}_1, \mathbf{r}_3) v_{xc}(\mathbf{r}_3)$$
$$= -\frac{i}{2\pi} \int d\mathbf{r}_3 d\mathbf{r}_4 d\omega e^{i\omega\delta} G_{\text{KS}}(\mathbf{r}_1, \mathbf{r}_3, \omega) \Sigma[G_{\text{KS}}](\mathbf{r}_3, \mathbf{r}_4, \omega) G_{\text{KS}}(\mathbf{r}_3, \mathbf{r}_1, \omega) = 0.$$
$$\tag{6.5}$$

The functional dependence of Σ with respect to G_{KS} instead of G has been written explicitly and $\chi_{KS} = iG_{KS}G_{KS}$ has been introduced. This equation has been applied by Godby *et al.* [73] using the *GW* approximation of the self-energy, in order to study the Kohn-Sham potential and in particular the band gap, with respect to the LDA result. It has been moreover shown recently [74] that this linearized version of Sham-Schlüter provides potentials with the exact asymptotic behavior (up to the second term), when applied with the *GW* self-energy.

As a by-product, the linearized Sham-Schlüter equation conducts to the same potential as the one provided by Optimized effective potential (OEP) procedure.

6.1.2 Optimized effective potentials

The spirit of OEP is very close to the one of Sham-Schlüter equation: from a nonlocal operator, how to find a local one that reproduces best certain quantities calculated with the former? Indeed, both approaches yields the same answer. Let us show how linearized Sham-Schlüter equation leads to the most used OEP, namely exact-exchange [75]. The previous procedure is applied to the nonlocal (but static) Fock operator Σ_x (see section 2.8).

The equation (6.5) is recast into

$$\int d\mathbf{r}_3 d\omega \chi_{KS}(\mathbf{r}_1, \mathbf{r}_3) v_{xc}(\mathbf{r}_3) =$$
$$= -\frac{i}{2\pi} \sum_{i,j} \int d\mathbf{r}_3 d\mathbf{r}_4 \int d\omega e^{i\omega\delta} \frac{\phi_i(\mathbf{r}_1)\phi_i^*(\mathbf{r}_3)}{\omega - \epsilon_i + i\eta \operatorname{sign}(\epsilon_i - \mu)}$$
$$\times \Sigma_x(\mathbf{r}_3, \mathbf{r}_4) \frac{\phi_j(\mathbf{r}_4)\phi_j^*(\mathbf{r}_1)}{\omega - \epsilon_j + i\eta \operatorname{sign}(\epsilon_i - \mu)}. \quad (6.6)$$

The right hand side has the same polar structure as χ_0 and χ_{KS}, and then the ω integral is easily performed, and gives the final expression for v_{xc}:

$$v_{xc}(\mathbf{r}) = \int d\mathbf{r}_1 \sum_{i,j} (f_i - f_j) \frac{\phi_i(\mathbf{r}_1)\phi_j^*(\mathbf{r}_1)}{\epsilon_i - \epsilon_j} \langle \phi_i | \Sigma_x | \phi_j \rangle \chi_{KS}^{-1}(\mathbf{r}_1, \mathbf{r}). \quad (6.7)$$

This expression is precisely the result of Görling [75] and has been applied to a wide range of materials. Generally this potential gives band gaps that are closer to the experimental ones than the LDA results [76].

6.2 Exchange-correlation kernels derived from MBPT

The relative success of exchange-correlation potentials derived from MBPT can consequently give the idea to look for exchange-correlation kernels in a

similar manner. To my knowledge, at least three independent derivations used the comparison of MBPT and TDDFT to get an explicit expression of the time-dependent exchange-correlation kernel. These approaches are crucial, since the ALDA kernel yields very poor results for absorption spectra in solids, and no other effective kernel had led to significant improvements in this context.

6.2.1 Time-dependent optimized effective potentials

In reference [77], Kim and Görling differentiated the OEP potential v_{xc} of equation 6.7 with respect to the time-dependent density in order get an expression of the exchange-correlation kernel of TDDFT. The derivation and the obtained formula (a whole page) is rather lengthy, and will not be reproduced here. This paragraph just insists on the principle: a simple differentiation.

Kim and Görling [78] applied the time-dependent OEP scheme using the exchange self-energy: this is so-called the time-dependent exact-exchange approach. They provided calculations of the imaginary part of the dielectric function of silicon in pretty good agreement with absorption experiments. But this success was not reached in a straightforward way: Kim and Görling had to use a cut-off on the bare Coulomb interaction that arose from the differentiation of the bare exchange operator. In this way, they eliminated artificially some components of the Coulomb potential, else the spectra "collapse", as they say in reference [78]. In other words, they decreased somehow the Coulomb potential – this is a kind of screening! In conclusion, their result is a piece of evidence that the bare exchange is a too strong interaction, instead one should use a somehow screened Coulomb interaction.

6.2.2 Direct comparison between BSE and TDDFT

The idea of Reining *et al.* [4], formalized and implemented in references [5, 6] by Sottile *et al.*, is to directly map matrix elements of the Bethe-Salpeter equation onto matrix elements of the TDDFT linear-response equation. The problem is that Bethe-Salpeter equation is a four-point equation, and TDDFT Dyson equation is a two-point one.

To achieve the mapping, the first task is to write the equations in a similar manner: let us write the TDDFT Dyson equation (4.25) in a four-point way making use of Dirac δ functions:

$$ {}^4\chi = {}^4\chi_{\mathrm{KS}} + {}^4\chi_{\mathrm{KS}} \left({}^4v + {}^4f_{xc} \right) {}^4\chi, \qquad (6.8) $$

where one introduced a four-point Coulomb interaction and a four-point kernel

$$ {}^4v(1,2;3,4) + {}^4f_{xc}(1,2;3,4) = \delta(1,2)\delta(3,4)(v(1,3) + f_{xc}(1,3)). \qquad (6.9) $$

If the Kohn-Sham response function χ_{KS} are further replaced by χ_0 that use quasiparticle energies (and in principle quasiparticle wavefunctions), this allows one to avoid the difficulties concerning the quasiparticle shift, as it is already included at the χ_0 level. The remaining kernel f_{xc} just accounts for the electron-hole interaction (as the W term in Bethe-Salpeter equation).

The four-point Coulomb interaction arising from the TDDFT equation can now be directly identified with the equivalent contribution in the Bethe-Salpeter equation (3.43). On the other hand, the TDDFT kernel has to be identified with the screened Coulomb interaction of the Bethe-Salpeter equation:

$$\delta(1,2)\delta(3,4)f_{xc}(1,3) = -\delta(1,3)\delta(2,4)W(1,2). \qquad (6.10)$$

One can see immediately that the previous equation will be problematic because of the different δ functions: they do not contract the same indexes. Fortunately, the purpose is not to find a hypothetical (and in general not existing) TDDFT kernel that reproduces the Bethe-Salpeter results everywhere for the four-space indexes. No, the aim is practical: one wants a TDDFT kernel that reproduces the Bethe-Salpeter *spectra*, and this only in the energy region of interest. This is more easily expressed in the LDA transition space [35]. The TDDFT kernel becomes

$$\mathcal{F}^{(\mathbf{k}'v'c')}_{(\mathbf{k}vc)}(\mathbf{q},\omega) = \int d\mathbf{r}_1 d\mathbf{r}_3 \phi_{\mathbf{k}+\mathbf{q}c}(\mathbf{r}_1)\phi^*_{\mathbf{k}v}(\mathbf{r}_1)f_{xc}(\mathbf{r}_1,\mathbf{r}_3,\omega)\phi^*_{\mathbf{k}'+\mathbf{q}c'}(\mathbf{r}_3)\phi_{\mathbf{k}'v'}(\mathbf{r}_3)$$

$$(6.11)$$

and the Bethe-Salpeter kernel (just the problematic part W) reads

$$\mathcal{W}^{(\mathbf{k}'v'c')}_{(\mathbf{k}vc)}(\mathbf{q}) = \int d\mathbf{r}_1 d\mathbf{r}_2 \phi_{\mathbf{k}v'}(\mathbf{r}_1)\phi^*_{\mathbf{k}v}(\mathbf{r}_1)W(\mathbf{r}_1,\mathbf{r}_2,\omega=0)\phi^*_{\mathbf{k}'+\mathbf{q}c'}(\mathbf{r}_2)\phi_{\mathbf{k}+\mathbf{q}c}(\mathbf{r}_2).$$

$$(6.12)$$

The mapping of the two equations (TDDFT and Bethe-Salpeter) imposes the central equation of references [4–6]:

$$\mathcal{F}^{(\mathbf{k}'v'c')}_{(\mathbf{k}vc)}(\mathbf{q},\omega) = -\mathcal{W}^{(\mathbf{k}'v'c')}_{(\mathbf{k}vc)}(\mathbf{q}). \qquad (6.13)$$

Note that the mapping is not imposed for the four space indexes, but only *on the transitions of interest* for the type of spectroscopy one is calculating. This equation intends to yield meaningful results in the frequency region studied, but outside the result is uncontrolled. Note also that $\mathcal{F}$ is hence a static quantity. The equality is then introduced in a straightforward manner into a symmetrized version of the linear-response TDDFT:

$$\chi = \chi_0 \left(\chi_0 - \chi_0 v\chi_0 - \chi_0 f_{xc}\chi_0\right)^{-1}\chi_0, \qquad (6.14)$$

with

$$(\chi_0 f_{xc} \chi_0)(\mathbf{r}, \mathbf{r}', \omega) = \sum_{(\mathbf{k}vc)(\mathbf{k}'v'c')} (f_{\mathbf{k}+\mathbf{q}c} - f_{\mathbf{k}v}) \frac{\phi_{\mathbf{k}v}(\mathbf{r})\phi^*_{\mathbf{k}+\mathbf{q}c}(\mathbf{r})}{\omega - (\epsilon_{\mathbf{k}v} - \epsilon_{\mathbf{k}+\mathbf{q}c})}$$
$$\times \mathcal{F}^{(\mathbf{k}'v'c')}_{(\mathbf{k}vc)}(\mathbf{q})(f_{\mathbf{k}'+\mathbf{q}'c'} - f_{\mathbf{k}'v'}) \frac{\phi^*_{\mathbf{k}'v'}(\mathbf{r}')\phi_{\mathbf{k}'+\mathbf{q}c'}(\mathbf{r}')}{\omega - (\epsilon_{\mathbf{k}'v'} - \epsilon_{\mathbf{k}'+\mathbf{q}'c'})}. \quad (6.15)$$

Now $\mathcal{F}$ appears explicitly and equation (6.13) can be used. This gives the kernel used in practice by Sottile *et al.* [5, 6]. This procedure gave, for the resonant only part (just positive transitions) and at $q \to 0$, promising results of the same quality as Bethe-Salpeter equation. The only drawback was that the diagonal of $\mathcal{F}^{(\mathbf{k}vc)}_{(\mathbf{k}vc)}$, which has the effect of shifting the poles in all the χ_0's, has been found to make the scheme unstable. Fortunately, this diagonal part can be accounted for by directly shifting the pole in the χ_0 and setting this contribution to zero.

For the computational point of view, one still calculates the cumbersome creation of the matrix $\mathcal{W}$. But the next step of the usual solution of the Bethe-Salpeter equation solution, the diagonalization, is then avoided, instead one needs only matrix products.

6.2.3 Perturbative approach of the TDDFT/BSE comparison

Another approach of the TDDFT/BSE comparison was proposed by Adragna and co-workers [64], which surprisingly led to the same equations as the previous derivation. They imposed, as in the approach described above, the equality between the reducible polarizabilities (i.e. without the Coulomb contribution v) coming from the Bethe-Salpeter equation and from linear-response TDDFT. This equality was then truncated to the same level of approximation in both members, symbolically,

$$\tilde{\chi}^{\text{TDDFT}} = \chi_0 + \chi_0 f_{xc} \chi_0 + \chi_0 f_{xc} \chi_0 f_{xc} \chi_0 + \dots \quad (6.16a)$$
$$\tilde{\chi}^{\text{BSE}} = \chi_0 + GGWGG + GGWGGWGG + \dots, \quad (6.16b)$$

where again the quasiparticle shift had been already included in the χ_0's (instead of the χ_{KS}'s in the TDDFT equation).

Marini *et al.* [79], for instance, used the first-order formula, that retains only the first two terms of equations (6.16)

$$\chi_0 + \chi_0 f_{xc} \chi_0 = \chi_0 + GGWGG, \quad (6.17)$$

which yields the following expression for the TDDFT kernel

$$f_{xc} = \chi_0^{-1} GGWGG \chi_0^{-1}. \quad (6.18)$$

If further the expression of the Green's function is made explicit, one recovers *exactly* the final equation of the previous derivation of equation (6.15). Consequently, Marini *et al.* [79] had the same success in describing optical absorption. They applied their scheme moreover successfully to energy-loss spectroscopies with non-vanishing momentum transfer $\mathbf{q}$. Finally, they showed that inclusion of the second-order kernel does not produce important effects on the spectra.

The perturbative approach can be also understood in terms of Feynman diagrams as proposed by Stubner, Tokatly and Pankratov [65, 80]. Their derivation gives expressions for each order of the time-dependent exchange-correlation kernel, that are equivalent to the previous functional approach.

In the theoretical developments part, I will show that all these independent derivations are finally linked, thanks to a new general derivation.

Part II

Methodological developments

Chapter 7

GW with no plasmon-pole model

There are several different ways of calculating the GW frequency integral,

$$\Sigma(\omega) = \frac{i}{2\pi} \int d\omega' e^{i\omega'\delta} G(\omega + \omega') W(\omega').$$ (7.1)

The historical and most basic way of doing is to assume that the frequency dependence of W can be mimicked by a single plasmon-pole, as it was explained in chapter 5. This model was already used by L. Hedin in 1965 [25], or by Hybertsen and Louie in 1985 [81]. This approximation has been both efficient and successful for 40 years, as it allows one to perform the integral analytically and gives good results for the real part of the self-energy. This method is implemented in ABINIT package [67].

However, if one is interested in the satellites of the spectral function A or in quasiparticle lifetimes, the plasmon-pole model kills these many-body features. Or, if one doubts that a single pole can represent a realistic $\varepsilon^{-1}(\omega)$ for the material under study, one may need to get rid of the model and to calculate explicitly the integral of equation (7.1). There are several ways of doing so, but all have advantages and drawbacks, because $\Sigma(\omega)$ has to be evaluated in the vicinity to its poles. I investigated different methods: analytic continuation, use of spectral functions, or contour integral.

Analytic continuation will not be described much here (see reference [82]), because it is not realiable enough. This approach is tempting, as it only requires to calculate W and Σ on imaginary axis, where these functions have no poles. Then, $\Sigma(i\omega)$ is extrapolated from the imaginary axis to the real axis thanks to a model function, for instance a Padé approximant

$$P(z) = \frac{a_0 + a_1 z + \ldots + a_N z^N}{b_0 + b_1 z + \ldots + b_M z^M}.$$ (7.2)

Once the parameters a_i and b_j of the model function are fit on the calculated values of $\Sigma(i\omega)$, this gives $\Sigma(z)$ everywhere in the complex plane. I found

that this method is accurate in the vicinity of the band gap, but farther it is not true anymore. The Padé approximation can not account for Σ in the region where the self-energy has many poles, since the model has only M poles. Also, the imaginary part of Σ is highly sensitive to the fitting points, used to calculate the parameters.

I then turned to a spectral function method used by Aryasetwian [83] described in section 7.1. And finally the most precise, but also the most cumbersome, method investigated here is the contour integral of passing along the imaginary axis described in reference [82]. This is the topic of section 7.2.

7.1   Method using spectral functions

7.1.1   Formula for the imaginary part of the self-energy

Following Aryasetiawan and Gunnarson [28], spectral representations of G and W can advantageously be used to derive a simple formula for the imaginary part of the GW self-energy.

Let us first remind the properties of the spectral functions, that will be useful in the following. The spectral representation of $W_p = W - v$ is

$$W_p(\mathbf{r}, \mathbf{r}', \omega) = \int_{-\infty}^{0} d\omega' \frac{D(\mathbf{r}, \mathbf{r}', \omega')}{\omega - \omega' - i\eta} + \int_{0}^{\infty} d\omega' \frac{D(\mathbf{r}, \mathbf{r}', \omega')}{\omega - \omega' + i\eta}, \qquad (7.3)$$

where $D(\mathbf{r}, \mathbf{r}', \omega)$ is the spectral function of W_p. As W_p is an even function of ω, D has to change its sign at zero frequency:

$$D(\mathbf{r}, \mathbf{r}', \omega) = -\frac{1}{\pi} \text{Im} \, W_p(\mathbf{r}, \mathbf{r}', \omega) \text{sign}(\omega). \qquad (7.4)$$

According to this definition, D is positive for $\omega > 0$, and negative elsewhere.

The spectral representation of G is

$$G(\mathbf{r}, \mathbf{r}', \omega) = \int_{-\infty}^{\mu} d\omega' \frac{A(\mathbf{r}, \mathbf{r}', \omega')}{\omega - \omega' - i\eta} + \int_{\mu}^{\infty} d\omega' \frac{A(\mathbf{r}, \mathbf{r}', \omega')}{\omega - \omega' + i\eta}, \qquad (7.5)$$

where $A(\mathbf{r}, \mathbf{r}', \omega)$ is the spectral function of G. As $\text{Im} \, G(\omega)$ changes its sign at μ, the definition

$$A(\mathbf{r}, \mathbf{r}', \omega) = -\frac{1}{\pi} \text{Im} \, G(\mathbf{r}, \mathbf{r}', \omega) \text{sign}(\omega - \mu) \qquad (7.6)$$

makes $A(\omega)$ positive everywhere.

After having extracted a large static part of the self-energy in equation (7.1), the Fock contribution, that comes from a v contribution and

that accounts for bare exchange. The remainder that accounts for correlation will be just a function to W_p, instead of W. Remembering that integration paths can only be closed in the upper plane due to the $e^{i\omega'\eta}$ factor, we introduce the two spectral functions to obtain four contributions to Σ_c, the dynamical part of Σ. Two terms among the four ones vanish, when the $\int d\omega'$ integral is performed, as they contain poles in only one half plane (analogous to the derivation of χ_0, see chapter 5). The two remaining terms are called Σ_c^{p} and Σ_c^{h}, for reasons that will be made obvious in the following.

Let us evaluate the imaginary part of Σ_c^{h}.

$$\Sigma_c^{\mathrm{h}}(\mathbf{r}, \mathbf{r}', \omega) = \frac{i}{2\pi} \int d\omega' \int_{-\infty}^{\mu} d\omega_1 \frac{A(\mathbf{r}, \mathbf{r}', \omega_1)}{\omega + \omega' - \omega_1 - i\eta} \int_0^{\infty} d\omega_2 \frac{D(\mathbf{r}', \mathbf{r}, \omega_2)}{\omega' - \omega_2 + i\eta}$$
(7.7)

The integral on ω' is performed thanks to the residue theorem, using an anticlockwise contour, in the upper half plane. The poles enclosed in the path are $\omega' = \omega_1 - \omega + i\eta$. These give

$$\Sigma_c^{\mathrm{h}}(\mathbf{r}, \mathbf{r}', \omega) = -\int_{-\infty}^{\mu} d\omega_1 \int_0^{\infty} d\omega_2 \frac{A(\mathbf{r}, \mathbf{r}', \omega_1)D(\mathbf{r}', \mathbf{r}, \omega_2)}{\omega_1 - \omega - \omega_2 + 2i\eta}.$$
(7.8)

The imaginary part of Σ_c^{h} could be evaluated thanks to the relation (2.17):

$$\mathrm{Im}\,\Sigma_c^{\mathrm{h}}(\mathbf{r}, \mathbf{r}', \omega) = \pi \int_{-\infty}^{\mu} d\omega_1 \int_0^{\infty} d\omega_2 A(\mathbf{r}, \mathbf{r}', \omega_1)D(\mathbf{r}', \mathbf{r}, \omega_2)\delta(\omega_1 - \omega - \omega_2).$$
(7.9)

Furthermore, $A(\omega)$ is the spectral function of a non-interacting Green's function (in a non self-consistent *GW* approximation) and it can be written as a sum of δ-peaks according to equation (2.40):

$$\begin{aligned}
\mathrm{Im}\,\Sigma_c^{\mathrm{h}}(\mathbf{r}, \mathbf{r}', \omega) = &\ \pi \sum_i \int_{-\infty}^{\mu} d\omega_1 \int_0^{\infty} d\omega_2 \phi_i(\mathbf{r})\phi_i^*(\mathbf{r}')D(\mathbf{r}', \mathbf{r}, \omega_2) \\
&\ \times \delta(\omega_1 - \omega - \omega_2)\delta(\omega_1 - \epsilon_i) \qquad (7.10) \\
= &\ \pi \sum_i \int_0^{\infty} d\omega_2 \phi_i(\mathbf{r})\phi_i^*(\mathbf{r}')D(\mathbf{r}', \mathbf{r}, \omega_2) \\
&\ \times \delta(\epsilon_i - \omega - \omega_2)\theta(\mu - \epsilon_i) \qquad (7.11) \\
= &\ \pi \sum_i \phi_i(\mathbf{r})\phi_i^*(\mathbf{r}')D(\mathbf{r}', \mathbf{r}, \epsilon_i - \omega)\theta(\epsilon_i - \omega)\theta(\mu - \epsilon_i) \quad (7.12) \\
= &\ -\sum_i \phi_i(\mathbf{r})\phi_i^*(\mathbf{r}')\mathrm{Im}\,W_p(\mathbf{r}', \mathbf{r}, \epsilon_i - \omega)\theta(\mu - \epsilon_i)\theta(\epsilon_i - \omega). \ (7.13)
\end{aligned}$$

The last line used definition (7.4). This contribution to the self-energy is non-vanishing only for ω lower than μ. Therefore it accounts only for the hole part of Σ_c. Note that only hole states give rise to a contribution to this part of the self-energy, that has a positive sign.

In a similar manner, the particle part Σ_c^{p} of the imaginary part of the self-energy can be derived:

$$\mathrm{Im}\,\Sigma_c^{\mathrm{p}}(\mathbf{r},\mathbf{r}',\omega) = \sum_i \phi_i(\mathbf{r})\phi_i^*(\mathbf{r}')\mathrm{Im}\,W_p(\mathbf{r}',\mathbf{r},\omega-\epsilon_i)\theta(\omega-\epsilon_i)\theta(\epsilon_i-\mu), \quad (7.14)$$

that vanishes for frequencies lower than μ. When non-zero, $\mathrm{Im}\,\Sigma_c^{\mathrm{p}}$ is negative. Expressions of Σ_c^{p} and Σ_c^{h} are obviously coherent (same signs, same π factors) with the expression of Aryasetwian [83].

For band structure calculations, one needs of course also the real part of the self-energy. It can be recovered easily, using the definition of the spectral function of Σ_c:

$$\Sigma_c(\mathbf{r},\mathbf{r}',\omega) = \int_{-\infty}^{\mu} d\omega' \frac{\Gamma(\mathbf{r},\mathbf{r}',\omega')}{\omega-\omega'-i\eta} + \int_{\mu}^{\infty} d\omega' \frac{\Gamma(\mathbf{r},\mathbf{r}',\omega')}{\omega-\omega'+i\eta} \qquad (7.15)$$

where $\Gamma(\mathbf{r},\mathbf{r}',\omega)$, the spectral function of Σ_c, satisfies

$$\Gamma(\mathbf{r},\mathbf{r}',\omega) = -\frac{1}{\pi}\mathrm{Im}\,\Sigma_c(\mathbf{r},\mathbf{r}',\omega)\mathrm{sign}(\omega-\mu). \qquad (7.16)$$

7.1.2 Practical implementation

To carry out the calculation of $\langle\phi_{\mathbf{k}j}|\Sigma_c(\omega)|\phi_{\mathbf{k}j}\rangle$, one needs a pretty good evaluation of the dynamical behavior of the screened Coulomb interaction W for real-valued frequencies. W function shows broad structures on the real axis, such as plasmon peaks. Therefore, in the calculation, the time-ordered $\epsilon^{-1}(\omega)$ was evaluated between 0 and 80 eV (this is an even function), on a regular grid with a 1 eV spacing. These parameters are a bit overconverged with respect to reference [82].

Once the W function is known on a regular grid, we need an interpolation scheme to approximate the value of the function. Indeed, the interpolation was not applied on W, but rather on $\tilde{\rho}_{\mathbf{k}ij}^* W \tilde{\rho}_{\mathbf{k}ij}$ (the $\tilde{\rho}_{\mathbf{k}ij}$ were defined in equation (5.9)). This allows us to decouple the calculation in two steps.

- The first part to be computed is

$$C_{\mathbf{k}'ikj}(\omega') = \sum_{\mathbf{G}\mathbf{G}'} \tilde{\rho}_{\mathbf{k}ij}^*(\mathbf{q}+\mathbf{G})\mathrm{Im}\,W_{\mathbf{G}\mathbf{G}'}(\mathbf{q},\omega')\tilde{\rho}_{\mathbf{k}ij}(\mathbf{q}+\mathbf{G}'), \quad (7.17)$$

  where, as usual, $\mathbf{q}=\mathbf{k}-\mathbf{k}'$ modulo a $\mathbf{G}$ vector. It scales as $N_{\mathbf{k}}.N_b.N_{\mathbf{G}}^2.N_{\omega'}$, where N_b is the number of bands and $N_{\omega'}$ is the number of frequencies used to sample W. This is the costly part of the calculation.

- The second part to be computed is

$$\mathrm{Im}\,\Sigma_{\mathbf{k}jj}^{\mathrm{h\ or\ p}}(\omega) = \mp\frac{1}{V}\sum_{\mathbf{k}'i} C_{\mathbf{k}'ikj}(|\omega-\epsilon_{\mathbf{k}i}|) \qquad (7.18)$$
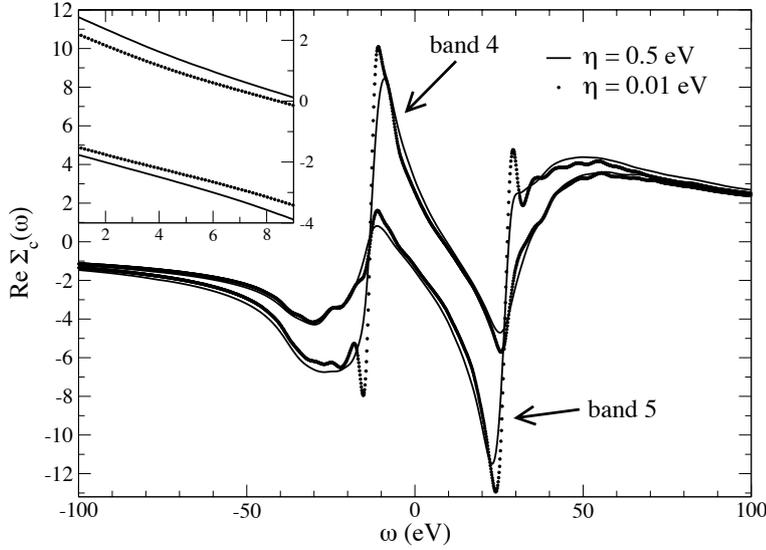
Figure 7.1: Real part of the correlation part of self-energy $\Sigma_c(\omega)$ for bulk silicon bands 4 and 5 at Γ point for two values of η. The line with small circles represent $\eta = 0.01\,\text{eV}$ and the full line is for $\eta = 0.50\,\text{eV}$. The inset provides a close-up of the band gap region ($\mu = 6.16\,\text{eV}$).

by means of a cubic spline interpolation in ω' of each $C_{\mathbf{k}'i\mathbf{k}j}(\omega')$ coefficient. This step scales as $N_b.N_{\mathbf{k}}.N_\omega$, where N_ω is the number of frequencies where the self-energy is evaluated. This part is very cheap and allows us to plot $\text{Im}\,\Sigma$ on a very dense grid, as required to perform the next integration.

The final result is recovered, as said before, by using a Kramers-Kronig-like transform. The numerical integration of $\text{Im}\,\Sigma$ yields the full Σ function.

7.1.3   Results for Silicon

Unfortunately, the imaginary part of Σ is very sensitive to the $i\eta$ parameter used in the calculation of W (described in chapter 5). And, as the real part of Σ_c is obtained from the imaginary part, the quasiparticle energies themselves are strongly dependent on η parameter.

This shortcoming is shown in figure 7.1. Only two values of η are displayed for clarity, but varying η makes the curve goes continuously from one to the other one. With a small η many more features can be seen in the real part of Σ_c. They are hidden by a too large η. But on the contrary, a too small η makes the band gap increase (region $\omega \sim 5 - 10\,\text{eV}$ of the figure). Table 7.1 provides quasiparticle energies around the band gap. It shows that the results strongly depend on η parameter. *The limit $\eta \to 0$ can not be taken*, since η parameter is needed in the calculation of χ_0 to

hide the fact that one has used a finite sum over **k**-points, instead of an integral. The last column of the table assesses this statement.

Quasiparticle band gap seem more reliable using a large value of η. But, the absolute values of the energies are always far from the values given by the plasmon-pole model. One can wonder whether this is due to a systematic shift between the plasmon-pole model energies and the true ones. The answer is no. The method employed in the next section will show that the plasmon-pole model and the true integration should compare pretty well in fact.

The instability of the present method is too large for practical applications. To make this method reliable enough, one should find a way to take properly the limit $\eta \to 0$, maybe using a tetrahedron integration in the calculation of χ_0 [83].

7.2   Method using contour integrals

7.2.1   Description of the method

The contour integral method [82] has been proposed to avoid as much as possible to deal with quantities close to the real axis, where the poles of G and W lie. The integral over real axis in equation (7.1) is transformed into an integral over the contour depicted in figure 7.2, plus contributions of the poles lying inside the contour:

$$\Sigma_c(\omega) = \frac{i}{2\pi} \left[2\pi i \sum_{z_p \in \text{ poles of } G \text{ or } W} \lim_{z \to z_p} G(z) W_p(z)(z - z_p) \right.$$
$$\left. - \int_{-\infty}^{+\infty} d(i\omega') G(\omega + i\omega') W_p(i\omega') \right] \quad (7.19)$$

as the integral along the arcs used to close the path of integration vanishes.

Let us deal with the sum over poles. According to figure 7.2, no poles of W_p are located inside the contour. On the contrary, some poles of G

Table 7.1: Silicon quasiparticle energies and band gap in eV at Γ point for top valence band (Γ'_{25v}) and first conduction band (Γ_{15c}), using the plasmon-pole model (PPM) or using different values of η in the spectral function method.

	PPM	$\eta = 0.50\,\text{eV}$	$\eta = 0.25\,\text{eV}$	$\eta = 0.01\,\text{eV}$
Γ'_{25v}	5.59	5.99	6.01	5.68
Γ_{15c}	8.74	9.04	9.00	9.39
Direct band gap	3.15	3.05	2.99	3.71
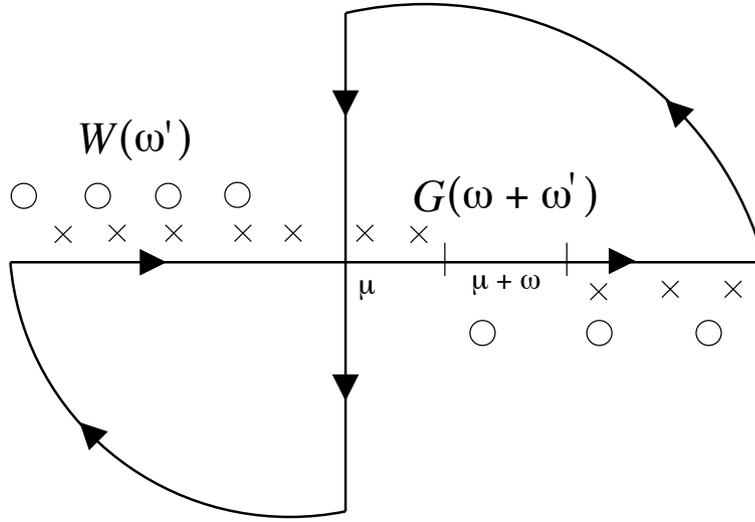
Figure 7.2: Location of the poles of the Green's function G (crosses) and of the screened Coulomb interaction W (open circles) and path of the contour integral (arrows) used in the method.

(located at energies $\omega' = \epsilon_i - \omega$) may enter the contour. For ω inside the band gap, there is obviously no pole inside the contour. For ω smaller than μ, the poles can enter in the upper-right quarter plane, only when $\epsilon_i - \omega > 0$. These are poles from the occupied states, therefore $\mu > \epsilon_i$. Finally the residues coming from poles in the upper-right quarter plane can be written

$$\sum_{\text{upper-right poles}} \ldots = \sum_i \theta(\mu - \epsilon_i)\theta(\epsilon_i - \omega)W_p(\epsilon_i - \omega + i\eta), \qquad (7.20)$$

where η is a vanishing positive real that reminds to take properly the limit. For ω larger than μ, an analogous derivation gives the final expression for the contribution from the lower-left quarter plane:

$$\sum_{\text{lower-left poles}} \ldots = \sum_i \theta(\omega - \epsilon_i)\theta(\epsilon_i - \mu)W_p(\epsilon_i - \omega - i\eta). \qquad (7.21)$$

Since the time-ordered W_p is an even function of ω and an odd function of the small $i\eta$ (see first section of this chapter), the total contribution from all poles is

$$\sum_{\text{all poles}} = \sum_i \left[-\theta(\mu - \epsilon_i)\theta(\epsilon_i - \omega) + \theta(\omega - \epsilon_i)\theta(\epsilon_i - \mu)\right] W_p(|\epsilon_i - \omega| - i\eta).$$
$$(7.22)$$

Concerning the remaining integral along imaginary axis, one can take advantage of the symmetry $W_p(-i\omega) = W_p^*(i\omega)$ to get

$$
\int d\omega' \ldots = i \int_{-\infty}^{+\infty} d\omega' \frac{\omega - \epsilon_i - i\omega'}{(\omega - \epsilon_i)^2 + \omega'^2} W_p(i\omega')
$$
$$
= 2i \int_0^{+\infty} d\omega' \frac{\omega - \epsilon_i}{(\omega - \epsilon_i)^2 + \omega'^2} \mathrm{Re}\, W_p(i\omega'), \qquad (7.23)
$$

since the integral from $-\infty$ to 0 yields the complex conjugate of the integral from 0 to $+\infty$.

The final result for $\Sigma(\omega)$ reads

$$
\Sigma(\mathbf{r}, \mathbf{r}', \omega) = \frac{1}{\pi} \sum_i \phi_i(\mathbf{r})\phi_i^*(\mathbf{r}') \int_0^{+\infty} d\omega' \frac{\omega - \epsilon_i}{(\omega - \epsilon_i)^2 + \omega'^2} \mathrm{Re}\, W_p(\mathbf{r}', \mathbf{r}, i\omega')
$$
$$
+ \sum_i \phi_i(\mathbf{r})\phi_i^*(\mathbf{r}') \left[\theta(\mu - \epsilon_i)\theta(\epsilon_i - \omega) \right.
$$
$$
\left. - \theta(\omega - \epsilon_i)\theta(\epsilon_i - \mu) \right] W_p(\mathbf{r}', \mathbf{r}, |\epsilon_i - \omega| - i\eta). \qquad (7.24)
$$

It is interesting to note that this expression is compliant with the one derived in the previous section. In fact, if one wants to retain only the imaginary part of Σ, one notes that the integral is real and thus, only poles give contribution to the imaginary part. The θ functions in the pole contribution are indeed the same as the ones in the spectral function technique. The derivation is therefore well established and now we have to check whether it performs better in pratice than the previous method.

7.2.2 Practical implementation

The two parts of Σ in equation (7.24), the integral along the imaginary axis and the sum over all poles, have to be evaluated.

First, concerning the integral, one has to find a reliable and efficient way to calculate it. Some authors [82] have chosen a fully numerical approach. Here, I preferred to take advantage on the possibility to perform some calculations analytically. Indeed, the ω' dependence of the integrand consists of two parts: the one from the Green's function, the one from the screened Coulomb interaction. As $\varepsilon^{-1}(i\omega')$ is numerically calculated in the step preceding the proper GW calculation, the dependence of W with respect to ω' is not known analytically, but one knows that along imaginary axis, W is a smooth function of $i\omega'$. On the contrary, the ω' dependence of G is explicitly known to be

$$
\frac{\omega - \epsilon_i}{(\omega - \epsilon_i)^2 + \omega'^2}. \qquad (7.25)
$$

Let us precise the notations: W is known at frequencies $i\omega_0 < i\omega_1 < \ldots < i\omega_n$ where $\omega_0 = 0$. Let $i\Omega_l$ be equal to $(i\omega_{l-1} + i\omega_l)/2$, with $\Omega_0 = 0$. It
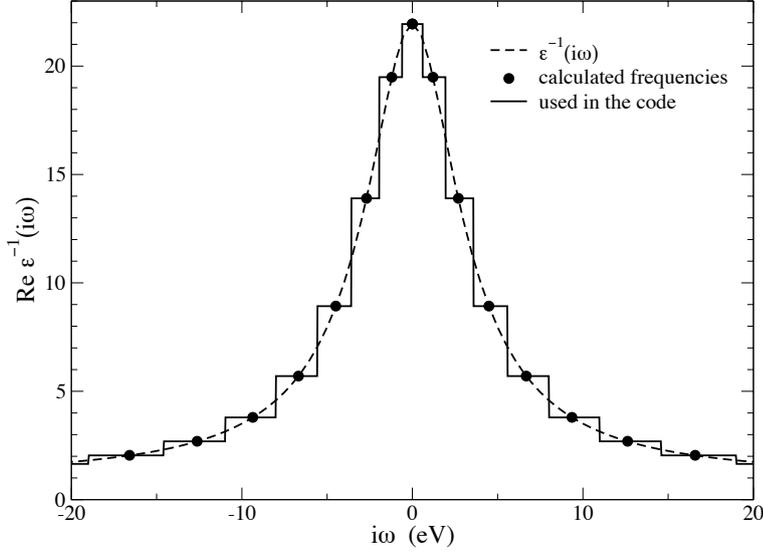
Figure 7.3: Reliability of the assumption on $\varepsilon^{-1}(i\omega)$ used in the algorithm. The dashed line is a full calculation of $\mathrm{Re}\,\varepsilon^{-1}$ as a function of $i\omega$, given as a reference. The full circles are the few frequencies calculated in practice for a *GW* run. The full line is the extrapolation of the few calculated frequencies used in the algorithm.

seems sensible to assume that it is constant around each $i\omega_l$ (to be precise, on the interval $[\Omega_l, \Omega_{l+1}]$), since it is a very smooth function of $i\omega'$:

$$\int_0^{+\infty} d\omega'\varepsilon^{-1}(i\omega')\frac{\omega - \epsilon_i}{(\omega - \epsilon_i)^2 + \omega'^2} = \sum_l \varepsilon^{-1}(i\omega_l) \int_{\Omega_l}^{\Omega_{l+1}} d\omega'\frac{\omega - \epsilon_i}{(\omega - \epsilon_i)^2 + \omega'^2}.$$
(7.26)

The performance of this model can be evaluated from figure 7.3, where the behavior of ε^{-1} as a function of $i\omega'$ seems smooth enough to guaranty the reliability of the approximation. This approximation sometimes overestimates ε^{-1}, sometimes underestimates it. As this scheme is used only inside an integral over $i\omega'$, the errors should compensate pretty well.

Consequently, the integral can be performed analytically on each small interval:

$$
\begin{aligned}
\int_0^{+\infty} d\omega'\varepsilon^{-1}(i\omega')\frac{\omega - \epsilon_i}{(\omega - \epsilon_i)^2 + \omega'^2} &= \sum_l \varepsilon^{-1}(i\omega_l) \int_{\Omega_l/(\omega-\epsilon_i)}^{\Omega_{l+1}/(\omega-\epsilon_i)} dx\frac{1}{1 + x^2} \\
&= \sum_l \varepsilon^{-1}(i\omega_l)\left[\mathrm{atan}\left(\frac{\Omega_{l+1}}{\omega - \epsilon_i}\right)\right. \\
&\qquad\qquad\left. -\mathrm{atan}\left(\frac{\Omega_l}{\omega - \epsilon_i}\right)\right] (7.27)
\end{aligned}
$$

Is this semi-analytical procedure efficient? I chose non-equidistant $i\omega_l$ with a finer sampling between 0 and i times the classical plasmon resonance and a coarser sampling beyond. Table 7.2 provides the value of Σ_c for silicon at the LDA fundamental gap (therefore there is no pole inside the contour), for different discretization of the imaginary axis. The convergence of the semi-analytical procedure is impressive: except the dummy values for 2 $i\omega_l$, the result is converged within few meV, already with only 4 $i\omega_l$. Note that with this procedure the plasmon-pole model code and the new one give absolute results in very good agreement, in contrast with the spectral function method.

Second, concerning the evaluation of the pole contribution, one has to evaluate $\varepsilon^{-1}(\omega)$ close to the real axis, where its poles lie. Here, it is convenient to choose equidistant frequencies and to interpolate somehow the calculated $\varepsilon^{-1}(\omega)$ in order to evaluate $\varepsilon^{-1}(\omega)$ where one needs it. In reality, it is computationally convenient to interpolate the quantity $\tilde{\rho}^*_{\mathbf{k}ij}\varepsilon^{-1}\tilde{\rho}_{\mathbf{k}ij}$ instead of ε^{-1}, as in the spectral function method. I first chose a linear interpolation and then turn to cubic spline interpolation. The difference between both interpolation modes in displayed on the left panel of figure 7.4. Although there are almost no differences between both schemes in the region of interest for the quasiparticle energy ($\epsilon_4 = 5.81$ eV), they are noticeable deviations where Σ is a fast varying function of ω. The linear interpolation seems to slightly minimize the fast variations of Σ.

Now, comparison to the previous spectral function method confirms the conclusions of the previous section. The spectral function method suffers from the drastic dependence on η parameter. Looking at the region important for the quasiparticle energy, i.e. around 5.81 eV, one remarks a very good agreement between the contour method and the spectral function method with a large η, however the curve for $\eta = 0.01$ eV is really different (the scale of the figure is large!). On the contrary, for the regions at ± 20 eV, the large η calculation underestimates much the variations of Σ, whereas the small η curve agrees more with the contour integration curve.

The overall scaling of the method is $N_{\mathbf{G}}^2.N_b.N_{\mathbf{k}}.N_{\omega_l}$. Note that the main

Table 7.2: Evaluation of Σ_c at LDA energy for top valence Γ'_{25v} (band 4 at Γ point) and bottom conduction X_{1c} (band 5 at X point) of bulk silicon with different discretization of the imaginary axis (ω_l). Plasmon-pole model (PPM) values are given as a comparison.

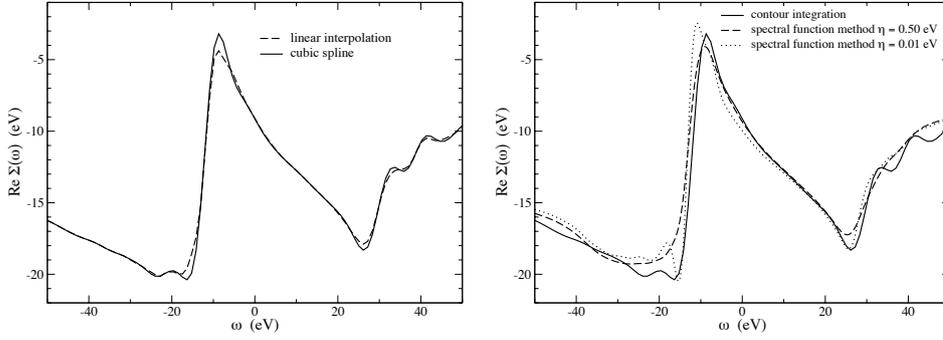|	PPM	2 $i\omega_l$	4 $i\omega_l$	8 $i\omega_l$	14 $i\omega_l$
Γ'_{25v}	0.977	-1.165	0.964	0.958	0.959
X_{1c}	-3.494	-1.025	-3.488	-3.484	-3.481

Figure 7.4: Left panel: Calculation of $\mathrm{Re}\,\Sigma(\omega)$ for top valence band of bulk silicon at Γ using two different interpolation schemes for the residues of poles in equation (7.24). Right panel: Comparison of the spectral function method for two values of η and the contour methods for the same state as the left panel.

calculation is the evaluation of the vector-matrix-vector products

$$\sum_{\mathbf{G}\mathbf{G}'} \tilde{\rho}^*_{\mathbf{k}ij}(\mathbf{q}+\mathbf{G})W_{\mathbf{G}\mathbf{G}'}(\mathbf{q},\omega_l)\tilde{\rho}_{\mathbf{k}ij}(\mathbf{q}+\mathbf{G}'), \qquad (7.28)$$

that is calculated thanks to optimized BLAS libraries.

7.2.3   Results for bulk Silicon

This section provides fully converged data for band structure of bulk silicon. ε^{-1} has been expanded in 113 plane-waves ($\sim 4\,\mathrm{Ha}$ cut-off) and 35 bands have been used. Wavefunctions and Σ_x have been expanded in 169 plane-waves ($\sim 5\,\mathrm{Ha}$ cut-off), the Green's function has been calculated with 100 bands.

Figure 7.5 gives data for the real and imaginary part of Σ, which are directly comparable to the results published in references [84] and [82]. Concerning the real part, the agreement is fairly good for all bands, except that the present data have more fluctuations in the 30 eV region. This may be due to the effect of the θ function in the sum over poles, that may induce discontinuity when a pole enters the contour. A solution could be to smoothen somehow the θ functions. The true solution would be to increase the number of $\mathbf{k}$-points, in order to go towards the situation where one has a branch cut on the real axis, instead of isolated poles. These oscillations are not observed in the two cited works, maybe because they use an analytic continuation to get these pictures. The analytic continuation forces $\Sigma(z)$ into having only a few poles (according to e.g. the Padé approximant of equation (7.2)) and thus could remove most of the oscillations due to poles close to the real axis.
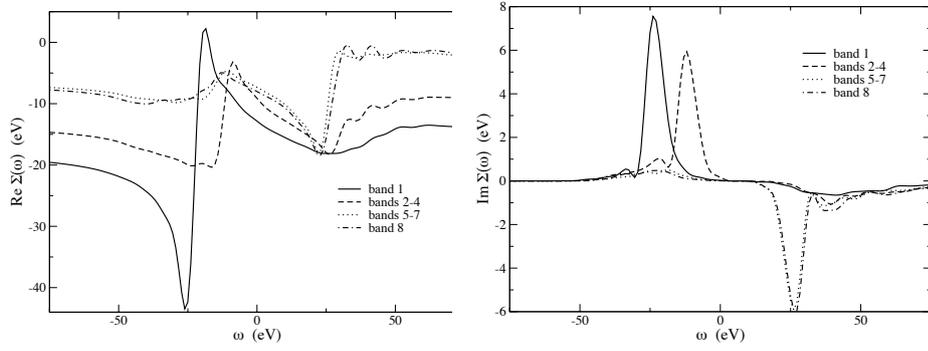
Figure 7.5: Calculation of $\text{Re}\,\Sigma(\omega)$ (left panel) and $\text{Im}\,\Sigma(\omega)$ (right panel) for the first eight bands of bulk silicon at Γ point.

The imaginary parts of Σ on the right panel of figure 7.5 are reasonable, but not in perfect agreement with other published works [82, 84]. I did not put much effort on that point, as I think it is related to the small η parameter issue. Since the integral over imaginary axis gives no contribution to $\text{Im}\,\Sigma$, the only contribution comes from the imaginary part of the residues, whose dependence with respect to η has been shown to be important. With the contour, the η factor influences only the imaginary part of the GW self-energy.

Finally, results for the band structure of bulk silicon are provided in table 7.3. The absolute values with and without plasmon-pole model agree very well. GW corrections give, as usual [82, 85], good quasiparticle energies compared to experimental data. The band gap is very close to the experimental value.

Table 7.3: Absolute band energies (energy reference is the LDA top valence band), band gaps and band width for bulk silicon in eV. Experimental data from references [21] and [86] are provided.

	LDA	GW approximation		Expt.
		with PPM	without PPM	
Γ_{1v}	-11.99	-11.67	-11.98	
Γ'_{25v}	0.00	-0.25	-0.26	
Γ_{15c}	2.53	2.94	2.93	
X_{1c}	0.62	1.02	1.03	
E_g	0.48	1.13	1.15	1.17
$\Gamma_{15c} - \Gamma'_{25v}$	2.53	3.19	3.19	3.05 - 3.40
Valence bandwidth	11.99	11.42	11.72	12.5 ± 0.6

Chapter 8

Self-consistent quasiparticle calculations

8.1 Looking for a better starting point for GW

The common paradigm to perform GW evaluation of the band structure is to use elements (energies and wavefunctions) from a self-consistent DFT calculations to construct G and W, and then calculate once $\Sigma = iGW$. This procedure is not assessed by theoretical derivations of the Many-Body Perturbation Theory, but grounded on practical experience accumulated on model systems [25, 87] or on realistic systems [73, 81].

One may doubt that DFT within the usual approximations yields reliable inputs for a GW calculation. In particular, the well-known underestimation of the band gap in DFT will generally provide a too large dielectric constant and, as a consequence, a too strongly screened Coulomb interaction W. This underestimation of the band gap may be fixed easily by performing a "poor man" self-consistent GW calculation: calculate the GW eigenvalues and use them for a next GW calculation until the input and output energies are equal.

On the contrary, if one has suspicion that the Kohn-Sham wavefunctions are not adequate, there is no straightforward way to get rid of this assumption. Even calculations, claimed as "self-consistent" as the work of W. Ku and A. G. Eguiluz [88, 89], do not relax the equality of GW and LDA wavefunctions. Indeed, the Green's functions are always assumed to be diagonal in the basis set of LDA wavefunctions in their work. That is why S. Faleev and coworkers [90] propose a smart way to handle modified self-energies in order to get proper wavefunctions. The problem is that the true self-energy is non-hermitian, hence the left and right eigenvectors differ, and dynamic, hence the eigenvectors are energy-dependent. The idea of reference [90] is to impose an hermitian and static self-energy by using

the modified self-energy $\tilde{\Sigma}$

$$\langle \mathbf{k}i|\tilde{\Sigma}|\mathbf{k}j\rangle = \frac{1}{4}\left(\langle \mathbf{k}i|\Sigma(\epsilon_{\mathbf{k}j})|\mathbf{k}j\rangle + \langle \mathbf{k}j|\Sigma(\epsilon_{\mathbf{k}j})|\mathbf{k}i\rangle^* \right.$$
$$\left. + \langle \mathbf{k}i|\Sigma(\epsilon_{\mathbf{k}i})|\mathbf{k}j\rangle + \langle \mathbf{k}j|\Sigma(\epsilon_{\mathbf{k}i})|\mathbf{k}i\rangle^*\right), \quad (8.1)$$

where ϵ_i and $|\mathbf{k}i\rangle$ are the self-consistent eigenvalues and eigenvectors of the procedure. Note that Σ operator has the symmetries of the solid and therefore, does not mix wavefunctions with different $\mathbf{k}$ indexes. This object is, from the mathematical point of view, much simpler than the true GW self-energy, but it still requires large calculations, since the full matrix $\langle \mathbf{k}i|\Sigma|\mathbf{k}j\rangle$ is needed. It still requires large sums over empty states. This is the reason why this study considers also the use of a simpler approximation for the self-energy, the COHSEX approximation, that is directly static and hermitian and thus, avoids the modeling step of equation (8.1).

The idea of the present work is to implement both a self-consistent COHSEX code and a self-consistent GW code, using the assumption of reference [90]. COHSEX will be used a starting point for a single subsequent GW iteration. The purpose of the present chapter is to devise the practical method, apply the developed codes on simple materials, solid argon and bulk silicon, and finally check their reliability against a "true" GW calculation. The Hedin's static COHSEX approximation [25, 91] is appealing. It is cheap, as it avoids the sum on empty states. It futher yields a self-energy, which is directly hermitian. It contains most of the physical effects carried by the GW self-energy: proper description of the Coulomb-hole and screening of the exchange operator (see chapter 3). Moreover, it has been tested on real materials [70] with relative success: COHSEX gives band gaps that are slightly too large ($\sim 10\%$). This chapter will proceed essentially with these two approximations. It will occasionally consider the bare and screened exchange approximations in addition.

8.2 Representation of quasiparticle wavefunctions and Hamiltonian on a restricted LDA basis set

In the present section, the term "quasiparticle wavefunctions" will stand generically for any of the following wavefunctions: Hartree-Fock, screened exchange, COHSEX or GW ones. In order to keep the calculations tractable even for complex materials, the quasiparticle wavefunctions $\phi_{\mathbf{k}i}^{\mathrm{QP}}$ will be expanded in the basis set of LDA wavefunctions $\phi_{\mathbf{k}j}^{\mathrm{LDA}}$:

$$|\phi_{\mathbf{k}i}^{\mathrm{QP}}\rangle = \sum_j c_{\mathbf{k}ij}|\phi_{\mathbf{k}j}^{\mathrm{LDA}}\rangle, \quad (8.2)$$

where projection coefficients $c_{\mathbf{k}ij} = \langle \phi_{\mathbf{k}j}^{\mathrm{LDA}} | \phi_{\mathbf{k}i}^{\mathrm{QP}} \rangle$ were introduced. In others words, the quasiparticle wavefunctions are constrained to be linear combination of LDA wavefunctions.

This procedure requires to calculate and diagonalize the full matrix $\langle \mathbf{k}i | \Sigma^{\mathrm{QP}} | \mathbf{k}j \rangle$. Within quasiparticle approximation, the self-energy is hermitian: only one half of matrix is actually computed. Moreover, an hermitian self-energy ensures that the eigenvalues are real and the eigenvectors are orthonormalized. The matrix of $c_{\mathbf{k}ij}$ coefficients is, as a consequence, a unitary matrix:

$$^t c.c = 1 \tag{8.3}$$

By iterating the process, the Hamiltonian is represented in the basis set of the solution of previous iteration. By converging the calculation, the quasiparticle Hamiltonian matrix tends to be diagonal. Its diagonalization gives the set of coefficients $c_{\mathbf{k}ij}^{(n)}$ that connects the new quasiparticle wavefunction to the previous one:

$$|\phi_{\mathbf{k}i}^{\mathrm{QP}\,(n)}\rangle = \sum_j c_{\mathbf{k}ij}^{(n)} |\phi_{\mathbf{k}j}^{\mathrm{QP}\,(n-1)}\rangle. \tag{8.4}$$

The final $c_{\mathbf{k}ij}$ coefficients are hence given by the matrix product $c = c^{(n)}.c^{(n-1)}\ldots c^{(1)}$. As all the $c^{(i)}$ are unitary, so is c.

This scheme requires to evaluate $\langle \phi_{\mathbf{k}i}^{\mathrm{QP}\,(n)} | V_H[\rho^{\mathrm{QP}\,(n)}] + \Sigma^{\mathrm{QP}\,(n)} | \phi_{\mathbf{k}j}^{\mathrm{QP}\,(n)} \rangle$, which is performed via a direct calculation, and $\langle \phi_{\mathbf{k}i}^{\mathrm{QP}\,(n)} | h_0 | \phi_{\mathbf{k}j}^{\mathrm{QP}\,(n)} \rangle$, which is calculated thanks to a change of basis set:

$$\langle \phi_{\mathbf{k}i}^{\mathrm{QP}\,(n)} | h_0 | \phi_{\mathbf{k}j}^{\mathrm{QP}\,(n)} \rangle = \sum_{mn} c_{\mathbf{k}im}^* c_{\mathbf{k}jn} \langle \phi_{\mathbf{k}m}^{\mathrm{LDA}} | h_0 | \phi_{\mathbf{k}n}^{\mathrm{LDA}} \rangle \tag{8.5}$$

The last matrix is then obtained, for practical reasons, by removing $\langle m | V_H[\rho^{\mathrm{LDA}}] + V_{xc} | n \rangle$ to the known LDA Hamiltonian represented on LDA wavefunctions $\epsilon_{\mathbf{k}m} \delta_{mn}$.

A natural question arises concerning this procedure: is the LDA basis set well-suited for the representation of quasiparticle wavefunctions? Of course, if one had used as many LDA states as the number of plane-waves used to represent the LDA wavefunctions, one would have a complete basis set, hence as justified as the basis of plane-waves. But for practical purposes, one would like to use only few of them to make this scheme computationally interesting. Is that truncation well-founded?

Let us address this issue by comparing the two basis sets (planes-waves and LDA wavefunctions) in the case of a simpler approximation, the Hartree-Fock approximation. Intuitively, Hartree-Fock approximation is expected to be quite different from LDA approximation. Therefore, if a limited LDA basis set is able to represent the HF wavefunctions, no problems should appear for the representation of wavefunctions closer to the LDA starting point, as the other quasiparticle wavefunctions are expected to be. The
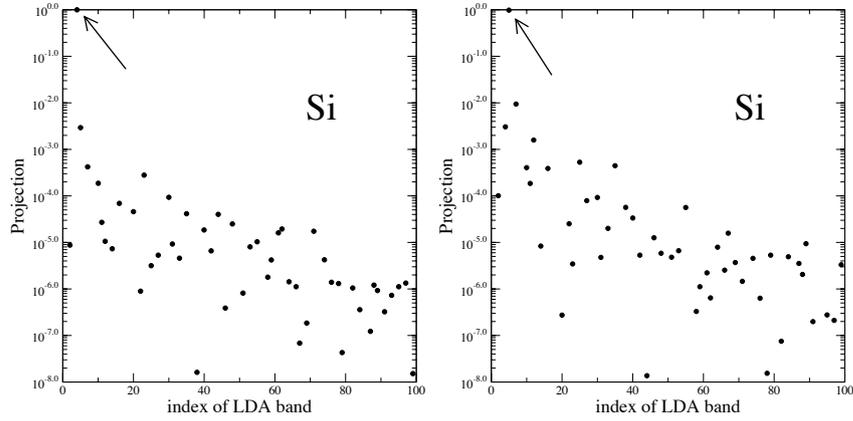
Figure 8.1: Projection of Hartree-Fock (after only one iteration) last valence band (left panel) and first conduction band at **k**-point (-1/8, -3/8, 1/4) in silicon (a logarithmic scale is used on vertical axis), in the LDA states.

practical reason for comparing HF only wavefunctions is that the calculation of nonlocal operators in reciprocal space is prohibitive on the plane-wave basis set, even for very simple materials. As exchange self-energy is a one-index operator in reciprocal space, the scaling with respect to the number of plane-waves $N_{\mathbf{G}}$ is $N_{\mathbf{G}}^3$:

$$\langle \mathbf{k} + \mathbf{G} | \Sigma_x | \mathbf{k} + \mathbf{G}' \rangle = -\frac{4\pi}{V} \sum_{\mathbf{k}_1 \mathbf{G}_1} \sum_{iocc} \frac{\phi_{\mathbf{k}_1 i}(\mathbf{G}_1 - \mathbf{G}) \phi_{\mathbf{k}_1 i}^*(\mathbf{G}_1 - \mathbf{G}')}{|\mathbf{k}_1 - \mathbf{k} + \mathbf{G}_1|^2}. \quad (8.6)$$

Calculation of the true GW or the COHSEX wavefunctions would have scaled as $N_{\mathbf{G}}^4$, as it requires to handle the nondiagonal matrix $\varepsilon_{\mathbf{GG}'}^{-1}$.

The figures 8.1 and 8.2 show the projection of the HF wavefunction j (after only one iteration) on the LDA state i at a given **k**-point:

$$|c_{ij}|^2 = |\langle \phi_{\mathbf{k}i}^{\text{LDA}} | \phi_{\mathbf{k}j}^{\text{HF}} \rangle|^2. \quad (8.7)$$

The **k**-point was chosen to be as representative as possible. I chose therefore a point with a large weight. As a consequence, the number of c_{ij} coefficient that vanishes for symmetry reasons is the lowest. The difference between the full self-consistent HF wavefunctions and the first iteration ones has been tested to be rather small. Moreover, the issue here is just to assess or not the flexibility of a restricted LDA basis set to represent other wavefunctions. A logarithmic scale had to be used, as the projection decreases very fast with the index of the LDA state. Calculations for silicon were performed with 307 plane-waves (that corresponds to a 9 Ha cut-off), and for argon, with 609 plane-waves (that corresponds to a 14 Ha cut-off).

The first statement is the large overlap between LDA wavefunction j and HF wavefunction j: from 99.5 % for the last valence band of silicon to 98.3
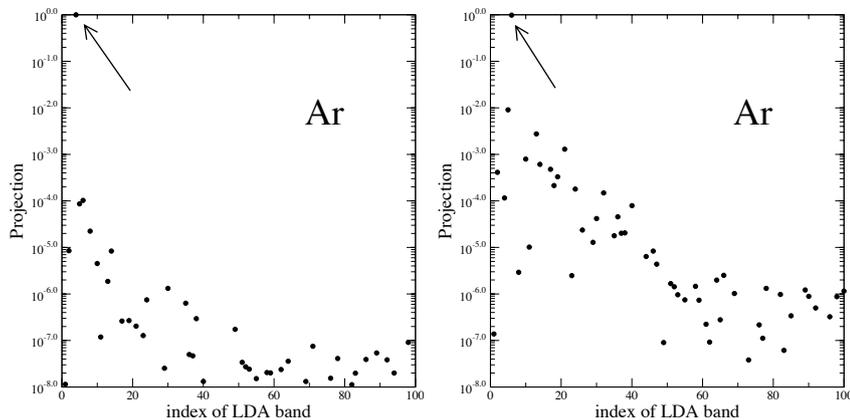
Figure 8.2: Projection of Hartree-Fock (after only one iteration) last valence band (left panel) and second conduction band at **k**-point (-1/8, -3/8, 1/4) in solid argon (a logarithmic scale is used on vertical axis), in the LDA states.

% for the second conduction band of argon (look at the point designated by an arrow, which is very close to 1 in figures 8.1 and 8.2). Second, to reach a given accuracy (let us say we project only states that have a weight larger than 5.10^{-4}), the valence bands would need less bands than conduction bands. Third, the LDA basis set seems to be a bit more adequate for argon than for silicon. But the general conclusion that can be drawn from these figures is the efficiency of a restricted LDA basis set.

To make even clearer the ability of the LDA basis set to represent other wavefunctions, let us plot the corresponding wavefunctions in real space on figure 8.3 for the worst case: the second conduction band of argon. The figure shows how fast the restricted LDA basis set converges. Only 10 LDA states for a basis set do not allow enough flexibility to represent the true HF wavefunction. But with the increase of the number of basis set functions, the representation becomes better and better. In practical applications, 30 LDA wavefunctions will be really sufficient. The number of matrix elements to be computed will be 30^2, instead of 609^2 for argon, if one would have used the plane-wave basis set. This procedure will hence allow one to evaluate self-energy operators, which are nonlocal in real and reciprocal space, as the COHSEX one, or the *GW* one.

8.3   Testing the code against published data

At this point, it has been shown that the representation via a linear combination of LDA wavefunctions makes calculation of wavefunctions using non-local self-energies feasible. The code I wrote is a modification from the *GW*
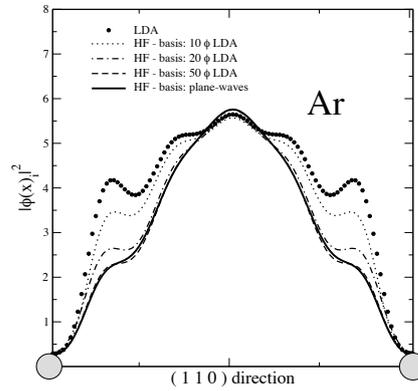
Figure 8.3: Squared modulus of different representation or approximation of the second conduction band at **k**-point (-1/8, -3/8, 1/4) in solid argon along the (1 1 0) direction in real space. The grey circles symbolize the argon atoms. LDA wavefunction is depicted with the large dots. HF wavefunction on plane-wave basis set is plotted with the full line, HF wavefunction's projection on the 10 first LDA bands with the dotted line, HF wavefunction's projection on the 20 first LDA bands with the dot-dashed line, HF wavefunction's projection on the 50 first LDA bands with the dashed line (hardly distinguishable from the solid line).

subroutines of the ABINIT package [67, 69]. It allows self-consistent calculations within the following approximations, namely Hartree-Fock, screened HF, COHSEX, and full GW. The initialization is made using LDA inputs, as in a usual GW calculation. Note that what is called "wavefunction" here, should be strictly named pseudowavefunction, as all the calculations rely on a pseudopotential scheme. Due to the pseudopotentials used, the effect of the core on the valence is always taken into account via LDA interaction. This may have some importance as pointed out by P. Rinke *et al.* [92] and as discussed in chapter 13 for the study of Cu_2O.

To assess the reliability of the code, let us provide comparison with previously published results in table 8.1. The agreement is pretty good. In particular, the values for solid argon agree very well with the present work, although a different basis set (gaussians) was used by S. Baroni *et al.* [22, 94], and although the present calculations use an LDA pseudopotential. The value concerning silicon are systematically slightly smaller than the ones from reference [70]. This could be due to different causes: different pseudopotentials, different levels of convergence. Hybertsen and Louie calculations were a pioneering work and maybe not converged within today's standards.

8.4   Silicon and argon wavefunctions within some historical approximations

It is now time to make use of the previous developments to carry out a detailled study of wavefunctions within different approximations, namely LDA, Hartree-Fock, screened Hartree-Fock and COHSEX. All these approximations have been previously defined in chapter 3.

Figure 8.4 shows the behavior of a valence wavefunction upon achievement of the self-consistency in a COHSEX calculation. The self-consistency is reached very rapidly: the main part of the difference is gained after the first step and after two steps, the wavefunction is indistinguishable with the final result. The same statement holds for conduction states and also for solid argon.

LDA and HF approximation should be considered as two extreme cases. LDA is exact in the limit of homogeneous systems. On the contrary, HF usually performs well for localized systems, like atoms. The common statement is that LDA overbinds atoms, whereas HF underbinds them; LDA gives too small band gaps, whereas HF yields band gaps much too large. One would expect the *true* wavefunction to be in between LDA and HF ones. Figure 8.5 provides self-consistent valence and conduction wavefunctions of silicon at a particular **k**-point within approximations of increasing complexity. Although the projection of both valence and conduction HF states on LDA are greater than 98.3 %, the difference is easily noticed. The

Table 8.1: Comparison of theoretical band gaps (indirect gap or direct one at Γ) in eV for silicon and argon from this work and from previously published data, within the self-consistent HF approximation (SCF HF) or within the perturbative COHSEX approximation (only one iteration starting from LDA).

	Silicon		Argon	
	this work	literature	this work	literature
Γ gap SCF HF	8.66	9.00^a, 9.27^b	17.97	17.93^c
Ind. gap SCF HF	6.21	6.87^b	—	—
Γ gap pert. COHSEX	3.52	3.85^d	14.98	14.62^e
Ind. gap pert. COHSEX	1.51	1.70^f	—	—

[a]Reference [16]
[b]Reference [93]
[c]Reference [22]
[d]Reference [81]
[e]Reference [94]
[f]Reference [70]
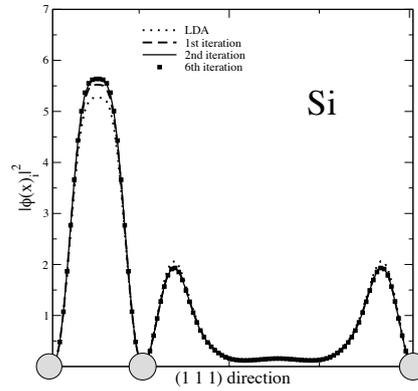
Figure 8.4: Squared modulus of the last valence band at **k**-point (-1/8, -3/8, 1/4) in silicon along the (1 1 1) direction in real space within the COHSEX approximation. The grey circles symbolize the silicon atoms. The dotted line is the LDA wavefunction, the dashed the wavefunction after the first COHSEX iteration, the full the wavefunction after the second COHSEX iteration, the square symbols represent the wavefunction after the sixth COHSEX iteration.

Figure 8.5: Squared modulus of the last valence band (left panel) and first conduction band (right panel) at **k**-point (-1/8, -3/8, 1/4) in silicon along the (1 1 1) direction within different approximations. The grey circles symbolize the silicon atoms. The wavefunctions within LDA (dotted line), HF (dot-dashed line), screened HF (dashed line), and COHSEX (full line) are shown.

value of the scalar product only may not be sufficient to decide whether wavefunctions are similar or not. Starting from HF wavefunctions, one can add the screened part of the screened exchange self-energy of equation (3.29) to get the screened Hartree-Fock wavefunction. Unexpectedly, these wavefunctions are really different from both LDA and HF ones. The quality

Figure 8.6: Squared modulus of the last valence band (left panel) and second conduction band (right panel) at **k**-point (-1/8, -3/8, 1/4) in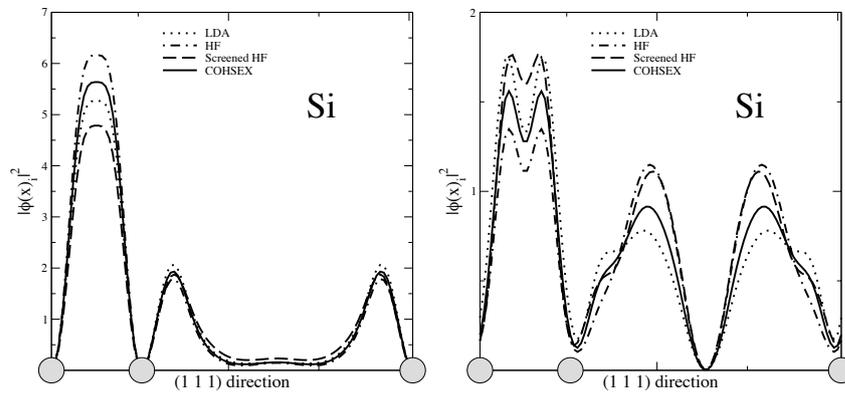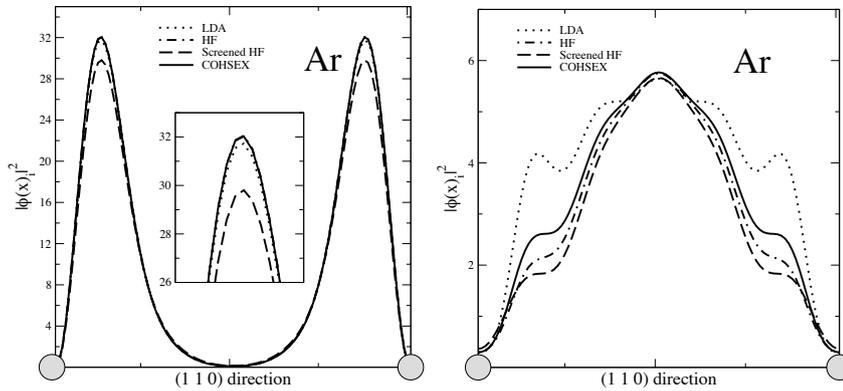 argon along the (1 1 0) direction within different approximations. The grey circles symbolize the argon atoms. The wavefunctions within LDA (dotted line), HF (dot-dashed line), screened HF (dashed line), and COHSEX (full line) are shown. The inset shows a close-up of the peak region. HF and COHSEX are here undistinguishable.

of these wavefunctions is doubtful, since screened HF yields furthermore largely too small band gaps. If one further adds the Coulomb hole contribution to the self-energy of equation (3.32), the wavefunctions that come out lay in between LDA and HF ones. The Coulomb hole term has corrected the effect of screened exchange contribution. From the presen results, the full COHSEX approximation seems to provide the best wavefunctions of all approximations tested in the present section.

Analysing the data for solid argon on figure 8.6 confirms perfectly the previous conclusions: whereas all the other approximations give very similar valence wavefunctions, the screened HF wavefunction is drastically incoherent; for the conduction band, COHSEX wavefunction is in the middle between LDA and HF.

Therefore, the following conclusions can be drawn from the presented data:

- the value of the scalar product between quasiparticle wavefunctions and LDA ones may be not sufficient to evaluate the quality and the similarity of the wavefunctions.

- one should not use a screened HF contribution to the self-energy alone.

- The use of screened exchange and Coulomb hole terms together provide very reasonable wavefunctions.

8.5   Effect of self-consistency on operators

The change of the wavefunctions and of the energies may alter the Hamiltonian operator in several different ways. It is therefore interesting to evaluate separately the effect of changing the wavefunctions and/or the energies on the different parts of the Hamiltonian. Numerical results are provided in table 8.2.

In a COHSEX calculation, the only effect due to the eigenvalues is contained in the evaluation of W. Updating the energies from one cycle to the other corrects the screening, which is usually overestimated in LDA. The difference between the first and the second rows of table 8.2 for silicon and argon is located only in $\Delta\Sigma_c$. As expected, the effect is rather small for silicon (0.27 eV), as the LDA band gap is not so wrong, and, on the contrary, rather large for argon (1.09 eV), as the LDA band gap is 60 % of the COHSEX value.

The effect of the wavefunctions may be experienced in two different manners: a change in the expression of the operators or a change of the states used for the evaluation of matrix elements. For instance, changing the wavefunctions makes the exchange operator different, but not the kinetic energy one. However, the kinetic energy matrix element is modified, since the bra and ket used are not the LDA wavefunctions any longer.

The overall effect of the wavefunctions is rather small: the difference between band gaps of the second and third rows for silicon and argon in table 8.2 is about 0.2 eV. However, one can not conclude that the effect of the wavefunction is small. Indeed, the different contributions to the band gap are modified, but compensate each other. For instance, the contribution from Hartree Hamiltonian to the band gap of argon is reduced by 0.68 eV, when using the COHSEX wavefunctions instead of the LDA ones. But

Table 8.2: Different contributions in eV to the band gap at Γ within the COHSEX approximation to the self-energy for silicon and argon using LDA or COHSEX wavefunctions and energies. ΔH_h is the contribution due to the Hartree Hamiltonian, $\Delta\Sigma_x$ the one due the exchange operator, $\Delta\Sigma_c$ the one due to the correlation part of the COHSEX self-energy.

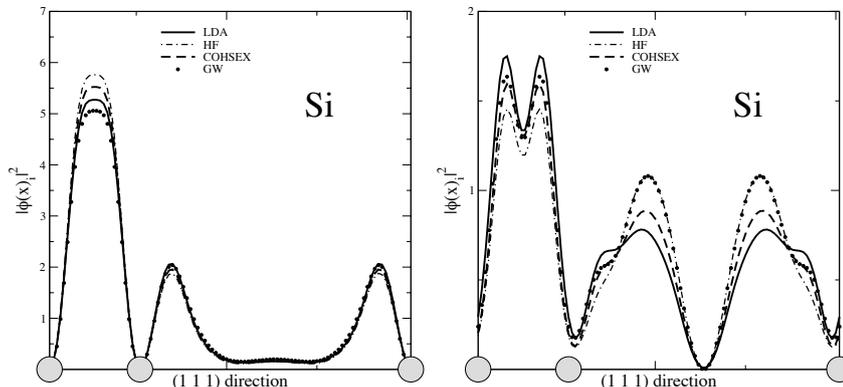|	wavefunctions	energies	ΔH_h	$\Delta\Sigma_x$	$\Delta\Sigma_c$	Band gap
	ϕ^{LDA}	ϵ^{LDA}	1.21	6.58	-4.26	3.52
Si	ϕ^{LDA}	ϵ^{CS}	1.21	6.58	-4.00	3.78
	ϕ^{CS}	ϵ^{CS}	1.09	7.08	-4.19	4.00
	ϕ^{LDA}	ϵ^{LDA}	-0.97	19.03	-2.90	14.98
Ar	ϕ^{LDA}	ϵ^{CS}	-0.97	19.03	-1.99	16.08
	ϕ^{CS}	ϵ^{CS}	-1.65	19.56	-2.03	15.88

Figure 8.7: Squared modulus of the last valence band (left panel) and second conduction band (right panel) at **k**-point (-1/8, -3/8, 1/4) in silicon along the (1 1 1) direction within different approximations. The grey circles symbolize the silicon atoms. The wavefunctions within LDA (full line), within HF (dot-dashed line), within COHSEX (full line), and within *GW* using the method of reference [90] (full circles) are shown.

the contribution due to the exchange operator is increased by $0.52\,\text{eV}$ in the meantime. Therefore the total effect remains quite small, although the details of the wavefunctions were crucial when evaluating each contribution separately. The same statements hold for silicon. In particular, the exchange operator seems to be a very sensitive quantity with respect to the wavefunctions.

8.6 Static COHSEX wavefunctions as an evaluation of *GW* wavefunctions

In this chapter, the study of COHSEX wavefunctions have not been thought a purpose on its own. The COHSEX wavefunctions have been considered as a first step *towards improved wavefunctions*. Regarding the difficulty to get the true *GW* wavefunctions for numerical and theoretical reasons, as explained in the first section of this chapter, it could be sensible to use the COHSEX wavefunctions as approximations to the *GW* ones. Is this really justified in practical applications? I have addressed this issue by comparing the COHSEX wavefunctions with the one obtained thanks to equation (8.1) [90].

Figures 8.7 and 8.8 provides the squared modulus of the pseudo-wavefunctions for the same states as previously in silicon and argon. This curves were obtained after a single iteration, due to the relative complexity of the method of reference [90]. But final conclusions can be drawn from this, as the first
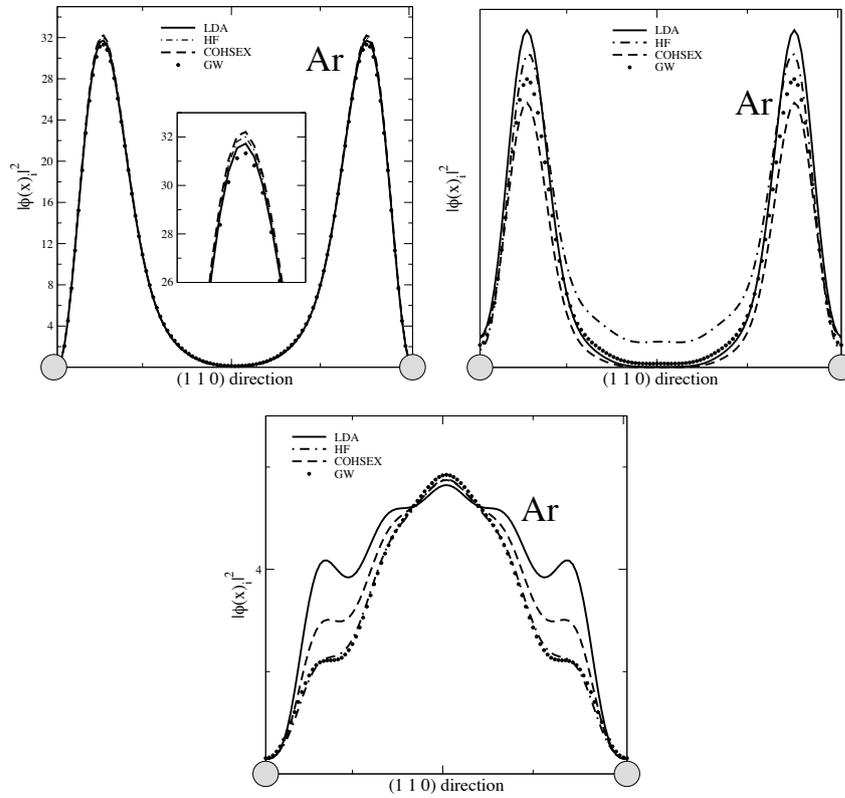
Figure 8.8: Squared modulus of the last valence band (upper left panel) and the first (upper right panel) and second conduction bands (bottom panel) at **k**-point (-1/8, -3/8, 1/4) in argon along the (1 1 0) direction within different approximations. The grey circles symbolize the argon atoms. The wavefunctions within LDA (full line), within HF (dot-dashed line), within COHSEX (full line), and within GW using the method of reference [90] (full circles) are shown. The inset shows a close-up of the peak region.

step always yields the main effect (see figure 8.4). The GW self-energy was evaluated using only 30 states for the sum over states in G, since it was explicitly checked that the wavefunctions converge much faster with respect to that parameter than the energies.

The overall conclusion is that COHSEX does not seem to be a great improvement with respect to LDA concerning the valence wavefunctions for silicon and argon. In both case, LDA, COHSEX, and GW are rather similar, but starting from LDA, COHSEX approximation goes in the wrong direction. Looking at the second conduction band of argon, one could have thought that HF wavefunctions were a very good approximation to the GW ones. But, looking at the first conduction band of argon, one can see that they largely differ. In all cases, for the conduction bands, COHSEX seems to be a good approximation to GW wavefunctions, much better than the

starting LDA wavefunctions...

The general conclusion of the present comparison is that, compared to the GW wavefunctions using equation (8.1), COHSEX approximation is not an improvement over LDA concerning valence bands (that were already quite good in LDA), but it is for conduction bands.

8.7 Self-consistent GW band structure

Concerning the performance of the self-consistent GW scheme devised in reference [90], the code written here is able to produce results using the pseudopotential plus plane-waves method. It is interesting to perform such a calculation, as it has been claimed recently [88, 89] that pseudopotentials prevent from performing good self-consistent GW calculations.

Table 8.3 displays the results for the two materials studied so far. Note that the perturbative GW results are slightly different from the usual ones, since here I have used the recipe of reference [90], where the self-energy is evaluated at the LDA energy and the Z factor of equation (5.17) is assumed to be equal to 1. One can state that the energy self-consistency yields a noticeable effect, in particular for argon. On the contrary, the change in wavefunctions accounts for slight differences for the band gaps. The final results is in pretty good agreement with respect to experiment, and furthermore in agreement with the LMTO results of Faleev and co-authors [90]. The self-consistent GW calculation using this constrained method seems to provide nice band gap values, at least for the simple materials studied here, and agrees pretty well with the all-electron results of reference [90]. In part IV, this method will be applied on the more complex case of Cu_2O.

Table 8.3: Selected features of the band structure of silicon and argon within the perturbative GW, within an energy-only self-consistent GW, or within the full self-consistent GW described by reference [90].

		pert. GW	energy scf GW	full scf GW	Expt.
Si	Direct band gap	3.37	3.42	3.48	3.40
	$\Gamma'_{25v} \rightarrow X_{1c}$	1.41	1.46	1.49	1.32
Ar	Direct band gap	13.37	14.41	14.48	14.20

Part III

Theoretical developments

Chapter 9

Derivation of TDDFT kernels from MBPT

Today's situation with absorption spectra is that, on one hand, Bethe-Salpeter equation is successful, but unfortunately cumbersome; and on the other hand, TDDFT is in principle lighter, but unfortunately, no working approximations are available.

The idea of using equality between some DFT and MBPT quantity to extract information about exchange-correlation potential or kernel has already been used a few times very recently, as shown in the introductive chapter 6. For instance, Sham-Schlüter equation starts from the equality of ground-state densities; Adragna *et al.* [64] begin with the equality of polarizabilities. In this chapter, I will benefit, in the same spirit, of the equality of time-dependent densities in order to derive an expression for the exact exchange-correlation kernel and approximations to it. This will yield a time-dependent Sham-Schlüter-like equation for the kernel. The issue of time-ordering and causality is circumvented here by using response function only for positive frequencies, where there is no difference.

9.1 Time-dependent Sham-Schlüter condition

By definition of the one particle Green's function, its diagonal yields the exact time-dependent density of the N electron system:

$$-iG(1, 1^+) = < N|\psi^\dagger(1)\psi(1)|N > = \rho(1). \qquad (9.1)$$

The time-dependent density is itself the key quantity of TDDFT and is given exactly by TDDFT.

Here a special care concerning the time-ordering in G should be taken as pointed out by R. van Leeuwen [95]. His conclusions were that if the

Keldysh contour trick is used for the time-ordering, no problem arises and all equations remain identical.

Let us differentiate the previous equation with respect to the density $\rho(2)$ to make the exchange-correlation kernel appear in the following lines:

$$\delta(1,2) = i \int d34 G(1,3)G(4,1)\frac{\delta G^{-1}(3,4)}{\delta\rho(2)}, \qquad (9.2)$$

where the derivative of the inverse has been used (equation (B.3)). Now, one uses a Dyson equation where the Kohn-Sham potential v_{KS} has been introduced (and consequently v_{xc} is subtracted) to get rid of G^{-1}:

$$G^{-1}(1,2) = G_0^{-1}(1,2) - \delta(1,2)v_{KS}(1) - \Sigma(1,2) + \delta(1,2)v_{xc}(1). \qquad (9.3)$$

G_0 corresponds to the free-electron Green's function, whose Hamiltonian only contains the kinetic energy. The variation of $v_{KS}(1)$ with respect to the density $\rho(2)$ is, by definition, the inverse of the Kohn-Sham polarizability $\chi_{KS}^{-1}(1,2)$. One obtains

$$\delta(1,2) = \int d3\chi_0(1,3)\chi_{KS}^{-1}(3,2) - i \int d34 G(1,3)G(4,1)\frac{\delta\Sigma(3,4)}{\delta\rho(2)}$$
$$- \int d3\chi_0(1,3)f_{xc}(3,2), \quad (9.4)$$

where one has used the definition of the RPA irreducible "polarizability" $\chi_0(1,2) = -iG(1,2)G(2,1)$ (defined in chapter 3) and of the TDDFT kernel f_{xc}. Then, multiplied on the left by χ_0^{-1}, this provides the central equation of this derivation:

$$f_{xc}(1,2) = \chi_{KS}^{-1}(1,2) - \chi_0^{-1}(1,2)$$
$$- i \int d345\chi_0^{-1}(1,5)G(5,3)G(4,5)\frac{\delta\Sigma(3,4)}{\delta\rho(2)}. \quad (9.5)$$

This kernel turns out to consist of two terms, namely $f_{xc}^{(1)}$ and $f_{xc}^{(2)}$. The first one

$$f_{xc}^{(1)}(1,2) = \chi_{KS}^{-1}(1,2) - \chi_0^{-1}(1,2) \qquad (9.6)$$

accounts exactly for the difference between the non-interacting response functions coming from both theories, TDDFT and many-body perturbation theory. According to the Dyson-like equation (9.6), the role of this kernel is to transform the polarizability computed with Kohn-Sham Green's functions into the one that uses the exact Green's functions. It carries all the one-quasiparticle effects.

The second part of the TDDFT kernel

$$f_{xc}^{(2)}(1,2) = -i \int d345\chi_0^{-1}(1,5)G(5,3)G(4,5)\frac{\delta\Sigma(3,4)}{\delta\rho(2)}. \qquad (9.7)$$

accounts for all the remaining interactions. In particular, the significant electron-hole interaction is present in an exact manner.

The key quantity of this approach is the derivative of Σ with respect to the density. This unknown quantity satisfies an intricate integral equation, which has to be approximated for practical applications.

9.2 Integral equation for $\delta\Sigma/\delta\rho$

In usual applications, the self-energy Σ is expressed as a function of Green's function G, for instance in the Hartree-Fock, GW approximation, etc. One can recover the expression of Σ as a function of G by using a chain rule via G. This will lead to an integral equation equivalent to the diagrammatic expansion of reference [80]. We provide here the derivation, not for solving it in practice, since this equation is as cumbersome as the Bethe-Salpeter equation, but it will be useful to design approximation to it.

First, let us forget that one only needs the variation of the self-energy with respect to the density, by introducing the Green's function thanks to the chain rule:

$$\frac{\delta\Sigma(1,2)}{\delta\rho(3)} = \int d45\, \Xi(1,5;2,4)\frac{\delta G(4,5)}{\delta\rho(3)}, \tag{9.8}$$

where $\Xi(1,5;2,4) = \delta\Sigma(1,2)/\delta G(4,5)$ is the kernel of Bethe-Salpeter equation (defined in chapter 3).

One meets the same situation as in the previous derivation, one has to evaluate variation of the Green's function with respect to the density. Therefore, one uses exactly the same tricks: replace $\delta G/\delta\rho$ by $-G(\delta G^{-1}/\delta\rho)G$ and then use Dyson equation to get rid of G^{-1}. The resulting equation

$$\frac{\delta\Sigma(1,2)}{\delta\rho(3)} = \int d4567\, \Xi(1,5;2,4)G(4,6)G(7,5)$$
$$\times \left[\delta(6,7)\chi_{KS}^{-1}(6,3) - \delta(6,7)f_{xc}(6,3) + \frac{\delta\Sigma(6,7)}{\delta\rho(3)}\right] \tag{9.9}$$

involves the exchange-correlation kernel and a new occurrence of $\delta\Sigma/\delta\rho$. According to equation (9.6), $\chi_{KS}^{-1} - f_{xc}^{(1)}$ is simply χ_0^{-1}:

$$\frac{\delta\Sigma(1,2)}{\delta\rho(3)} = \int d4567\, \Xi(1,5;2,4)G(4,6)G(7,5)$$
$$\times \left[\delta(6,7)\chi_0^{-1}(6,3) - \delta(6,7)f_{xc}^{(2)}(6,3) + \frac{\delta\Sigma(6,7)}{\delta\rho(3)}\right] \tag{9.10}$$
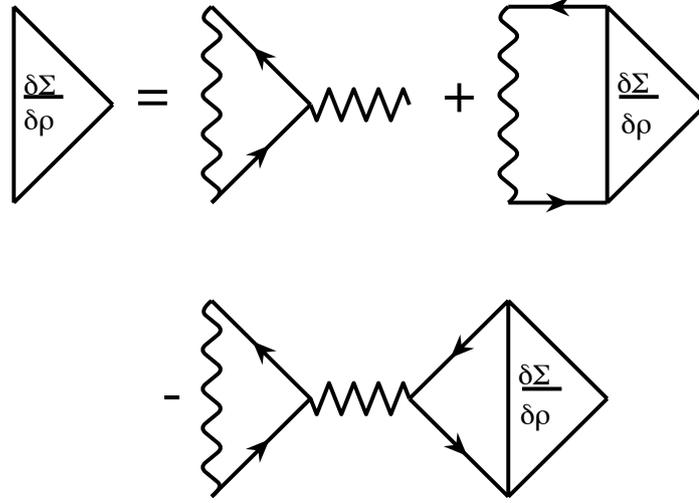
Figure 9.1: Feynman diagram representation of the integral equation (9.11) in the particular case, where $\Xi = iW$, as it is usually done when solving Bethe-Salpeter equation.

that can be recast by using the definition 9.7 for $f_{xc}^{(2)}$

$$\frac{\delta\Sigma(1,2)}{\delta\rho(3)} = \int d4567\,\Xi(1,5;2,4)G(4,6)G(7,5)\left[\delta(6,7)\chi_0^{-1}(6,3) + \frac{\delta\Sigma(6,7)}{\delta\rho(3)}\right.$$

$$\left. + i\delta(6,7)\int d8910\,\chi_0^{-1}(6,8)G(8,9)G(10,8)\frac{\delta\Sigma(8,10)}{\delta\rho(3)}\right] \quad (9.11)$$

This large integral equation has to be solved in order to get the exact value of $\delta\Sigma/\delta\rho$. This equation becomes clearer using Feynman diagrams in figure 9.1. This equation is not very useful to get an exact value as it is really intricate. But, for the practical point of view, it is very instructive for finding the right approximation among the possible ones. This functional derivation adds insight in the role of the different ingredients, with respect to the purely diagrammatic expansion of reference [80], where their unknown solution of the integral equation has no obvious interpretation.

To find a good approximation, one has to guess what is small, and what is large in the previous equation. At first sight, one could be tempted to decide that $\delta\Sigma/\delta\rho - f_{xc}$ is small and disregard its second-order. However, by investigating equation (9.10), it seems more sensible to assume that $\delta\Sigma/\delta\rho - f_{xc}^{(2)}$ is small. Indeed, expressions of $\delta\Sigma/\delta\rho$ and of $f_{xc}^{(2)}$ are very similar, whereas $f_{xc}^{(1)}$ has nothing to do with the derivative of Σ. Both $\delta\Sigma/\delta\rho$ and $f_{xc}^{(2)}$ accounts for the same physics: the electron hole-interaction, whereas $f_{xc}^{(1)}$ accounts for the quasiparticle shift. All these clues make that it is reasonable to follow a perturbative approach using the coupling parameter $\delta\Sigma/\delta\rho - f_{xc}^{(2)}$.

The zero-order kernel is obtained by neglecting all occurrences of $\delta\Sigma/\delta\rho - f_{xc}^{(2)}$. The equation (9.7) can be written as

$$-i \int d23 G(1,2)G(3,1) \left[\frac{\delta\Sigma(2,3)}{\delta\rho(4)} - \delta(2,3)f_{xc}^{(2)}(2,4) \right] = 0, \qquad (9.12)$$

which shows that the zero-order kernel is simply

$$f_{xc}^{(2)} = 0. \qquad (9.13)$$

When the previous kernel is used in the usual linear-response TDDFT equation,

$$\chi = \chi_{KS} + \chi_{KS}(v + f_{xc})\chi, \qquad (9.14)$$

it merely yields the RPA:

$$\chi = \chi_0 + \chi_0 v\chi. \qquad (9.15)$$

The following sections will give expressions for the first- and second-order results.

9.3   First-order TDDFT kernel

Let me exemplify the previous developments with the first-order kernel. According to equation (9.10), the first-order expression for $\delta\Sigma/\delta\rho - f_{xc}^{(2)}$ yields

$$\frac{\delta\Sigma(1,2)}{\delta\rho(3)} \approx \int d456 \, \Xi(1,5;2,4)G(4,6)G(6,5)\chi_0^{-1}(6,3). \qquad (9.16)$$

One has just neglected of $\delta\Sigma/\delta\rho - f_{xc}^{(2)}$ in the right-hand side of equation (9.10). Then, one can introduce this approximation in equation (9.7) to get the expression of the kernel, dropping the indexes,

$$f_{xc}^{(2)} \approx -i\chi_0^{-1}GG\Xi GG\chi_0^{-1}. \qquad (9.17)$$

This approximation needs now an approximation for Ξ.

9.3.1   Link to TD-OEP: exact-exchange

This section is dedicated to the proof that the method described here permits one to derive as a by-product the OEP kernels. In particular, the exact-exchange kernel of reference [77] is obtained when one chooses the Hartree-Fock approximation for the self-energy in equations (9.6) and (9.7) and when a further linearization approximation is applied. OEP methods refer only to Kohn-Sham quantities. The linearization step consequently removes all occurrences of the true Green's functions G.

Consider separately the equations for $f_{xc}^{(1)}$ and $f_{xc}^{(2)}$. The first one can be rewritten thanks to the multiplication on the left by χ_{KS} and on the right by χ_0 as

$$\chi_{KS} f_{xc}^{(1)} \chi_0 = -iGG + iG_{KS}G_{KS}, \qquad (9.18)$$

where the indexes are implicit throughout the derivations. Making use of the Dyson equation that links G_{KS} to G, one obtains the *exact equation*

$$\chi_{KS} f_{xc}^{(1)} \chi_0 = -i\left[G_{KS} + G_{KS}(\Sigma - v_{xc})G\right]$$
$$\times \left[G_{KS} + G_{KS}(\Sigma - v_{xc})G\right] + iG_{KS}G_{KS}. \quad (9.19)$$

In order to avoid any reference to the *true* G and χ_0, one can develop the previous equation to the first-order in $(\Sigma - v_{xc})$, following the spirit of OEP procedures. $f_{xc}^{(1)}$ is consequently a first-order quantity and $\chi_{KS} f_{xc}^{(1)} \chi_{KS} f_{xc}^{(1)} \chi_{KS} \ldots$ are higher-order quantities. Hence, the linearized equation finally reads

$$\chi_{KS} f_{xc}^{(1)} \chi_{KS} = -iG_{KS}(\Sigma - v_{xc})G_{KS}G_{KS} - iG_{KS}G_{KS}(\Sigma - v_{xc})G_{KS} \quad (9.20)$$

When the self-energy Σ is simply the bare exchange operator and the exchange-correlation v_{xc} is the corresponding OEP exact-exchange operator, this equation gives a part of the kernel derived by Kim and Görling [77]. By introducing the expression of the G_{KS} and performing the frequency integrals by means of the residue theorem, one obtains precisely the terms H_X^3 and H_X^4 of reference [77]. This relation is demonstrated in appendix C. This part approximatively accounts for the quasiparticle shift, as it implies terms like $(\Sigma - v_{xc})$. F. Sottile implemented the first-order $f_{xc}^{(1)}$ and found it rather unstable [5]. Dramatic numerical problems appear as soon as the η factor in the denominator is too small or as soon as the number of transitions is too large.

Now, let us apply the same method for the electron-hole term represented by $f_{xc}^{(2)}$. In the case of Σ equal to the exchange operator, the first-order kernel of equation (9.17) reads

$$\chi_0 f_{xc}^{(2)} \chi_0 = GGvGG. \qquad (9.21)$$

Following the linearization scheme, one can get rid of all references to G's by replacing them by G_{KS}'s. The equation for $f_{xc}^{(2)}$ finally reads

$$\chi_{KS} f_{xc}^{(2)} \chi_{KS} = G_{KS}G_{KS}vG_{KS}G_{KS}, \qquad (9.22)$$

and replacing the G_{KS} and the χ_{KS} by their expressions and performing the frequency integral with the residue theorem yield exactly the H_X^1 and H_X^2 terms of reference [77].

All this derivation proves that time-dependent exact-exchange scheme is nothing else but an approximation to the time-dependent Hartree-Fock approximation, but expressed in the TDDFT formalism. If the kernel were
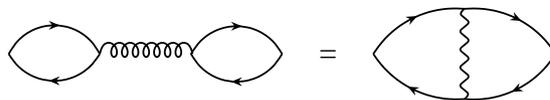
Figure 9.2: Feynman diagram representation of the first-order TDDFT kernel, using $\Xi = W$ as in Bethe-Salpeter equation.

not the first-order one, but the true one, and one had not linearized, the time-dependent densities arising from the time-dependent Hartree-Fock approximation to the self-energy and the one arising from the time-dependent exact-exchange approximation to the TDDFT would give exactly the same result. In that sense, time-dependent exact-exchange scheme is a rough approximation to time-dependent Hartree-Fock. It is well known that time-dependent Hartree-Fock yields very bad response functions, as shown in figure 3.6 for bulk silicon, with a too large band gap (the Hartree-Fock one) and too strongly bound excitons. In conclusion, time-dependent exact-exchange scheme is an approximation to a very rough approximation! Only improbable cancellations of errors from OEP linearization and from time-dependent Hartree-Fock could give realistic results for the response function. Instead Kim and Görling used an addition parameter to reduce the Coulomb interaction and produced quality spectra: it is a kind of screening!

9.3.2 Link to more realistic approximations

If one prefers to use the common approximations of the Bethe-Salpeter equation to approximate Ξ ($\Sigma = iGW$, neglect of $\delta W/\delta G$ and W static), one obtains

$$\chi_0 f_{xc}^{(2)} \chi_0 = GGWGG. \tag{9.23}$$

This equation is depicted in Feynman diagram representation in figure 9.2, where the omitted indexes in the equation can be seen. This is the very central equation of the work of Reining *et al.* [4] and Sottile *et al.* [6]. This corresponds also to the first-order kernel of the works of Adragna *et al.* [64] and of Tokatly *et al.* [65].

It has produced very good results in practical applications [5, 6, 79]. Figure 9.3 gives the example of bulk silicon calculated with the DP code [68], using the subroutines of F. Sottile [5]. Concerning the technical parameters, I used the three highest valence bands and the three lowest conduction bands, a regular grid of 512 slightly shifted k-points in the full Brillouin zone, and an imaginary part in the energy denominators $\eta = 0.1\,\mathrm{eV}$. As the figure shows, the TDLDA approach fails to reproduce the optical absorption, since both the band gap and the oscillator strengths of the main peaks are wrong. On the contrary, following our comparison between TDDFT and Green's functions, we have to evaluate the two contributions
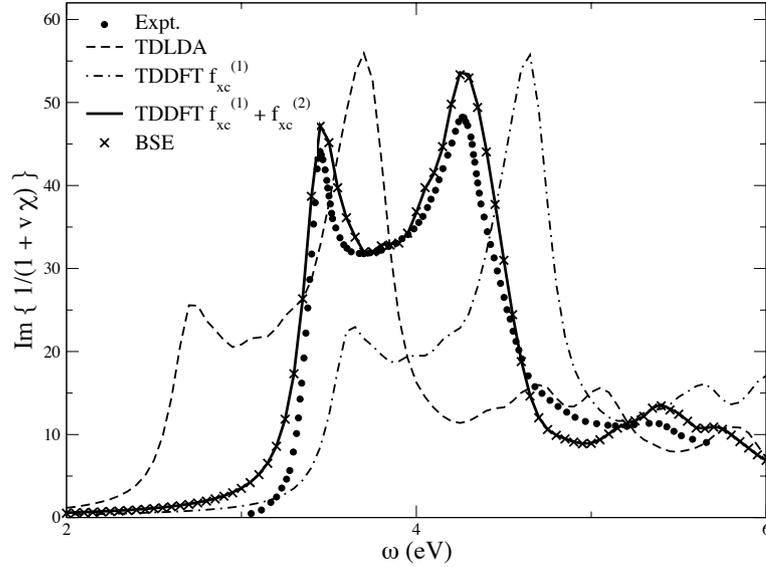
Figure 9.3: Optical absorption spectrum of bulk silicon calculated within different approximations and compared to experimental data of Ref. [30]. The dashed line represents the TDLDA curve, the dot-dashed line the TDDFT kernel using $f_{xc}^{(1)}$ of the text only, the full line the full TDDFT kernel of the text. The solution of the Bethe-Salpeter equation (crosses) and the experimental curve (full circles) are given for comparison.

to the TDDFT kernel. The first term $f_{xc}^{(1)}$ accounts for the one-quasiparticle exchange-correlation effects. It transforms the KS response function χ_{KS} into the GW independent quasiparticle χ_0. The corresponding curve in figure 9.3 gives the correct band gap. At this level, electron-hole interaction exchange-correlation effects are still absent, as it is evident in the remaining blue shift of the spectrum and the underestimation in the oscillator strength of the first excitonic peak. The second term $f_{xc}^{(2)}$ accounts for the two-particle exchange-correlation effects. If the same technical approximations as in Bethe-Salpeter equation are used (use of a static W, neglect of the derivative of W with respect to G), the corresponding curve closely reproduces the solution of Bethe-Salpeter equation.

The ability of the first-order kernel to reproduce the spectrum calculated with the Bethe-Salpeter equation is impressive, although the contributions included, or in other words the diagrams included, are not the same! This consideration will become clearer, when studying the second-order kernel.

9.4 Second-order TDDFT kernels

The Bethe-Salpeter equation provides in principle the *exact polarizability*. Provided that one uses $\Sigma = iGW$, neglects as usual $\delta W/\delta G$ and that one
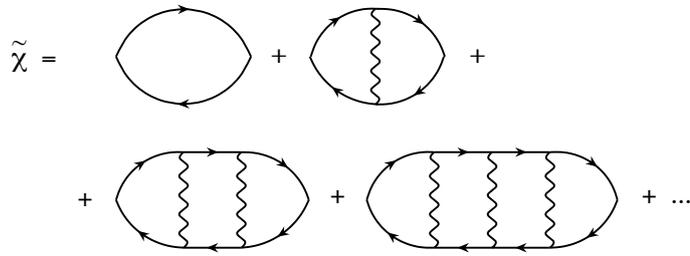
Figure 9.4: Feynman diagram representation of $\tilde{\chi}$ with the use of the Bethe-Salpeter equation, with the common assumptions (W static, neglect of $\delta W/\delta G$).
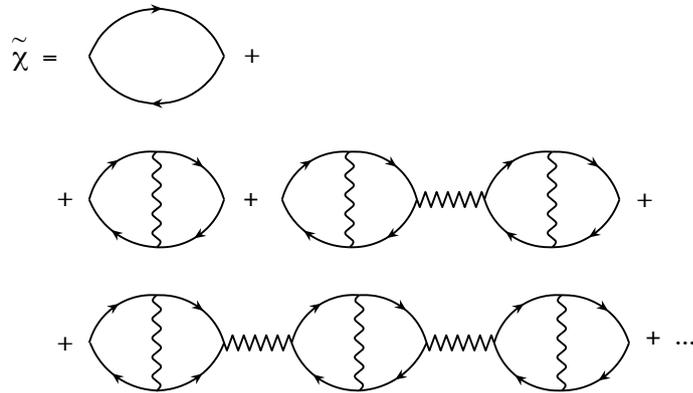
Figure 9.5: Feynman diagram representation of $\tilde{\chi}$ with the use of the first-order TDDFT kernel.

supposes W static, the reducible polarizability arising from the solution of Bethe-Salpeter looks like the diagrammatic expansion of figure 9.4. Under the same technical assumptions, our TDDFT scheme with the full kernel is also exact and should provide the *same series of diagrams*.

However, if one just uses the first order TDDFT kernel derived in the previous section, one recovers the expansion of figure 9.5. The two series corresponds only up to the second diagram. The second-order one is already different: the TDDFT-derived expansion has χ_0^{-1} terms that contracts indexes in between W interactions.

Let us show that the second order kernel does the job of replacing the wrong second order diagram in the TDDFT-derived series by the Bethe-Salpeter-derived one. This derivation is more easily seen using diagrams: figure 9.6 displays the second-order approximation to the integral equation plotted on figure 9.1.

The third term in figure 9.6 removes the "incorrect" third term in fig-
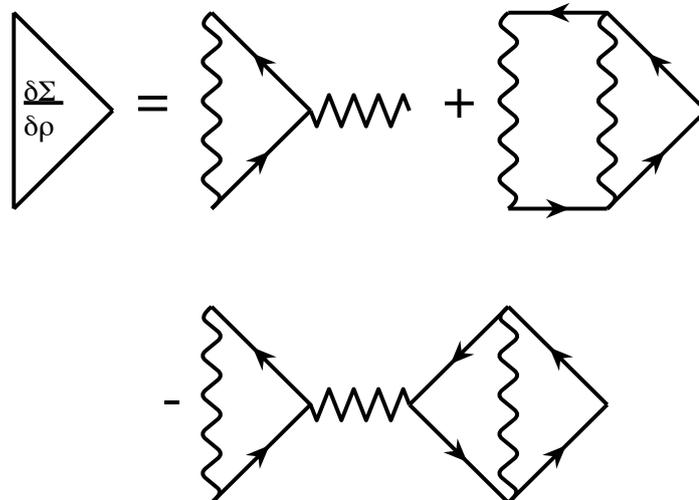
Figure 9.6: Feynman diagram representation of the derivative of Σ with respect to ρ to the second-order.
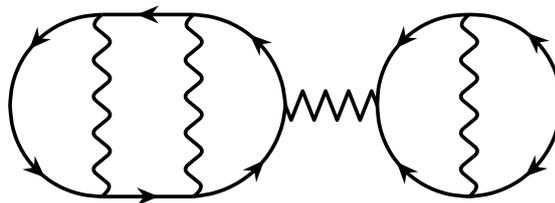
Figure 9.7: Typical spurious Feynman diagram still present in the TDDFT series, using the second-order kernel.

ure 9.5 and the second term in figure 9.6 adds the "correct" third term of figure 9.4. The TDDFT and Bethe-Salpeter series correspond now up to the fourth diagram. But, as there is still an approximation, there are still spurious diagrams in the TDDFT expansion, like the one depicted in figure 9.7.

This development up to the second-order has been explicitly shown here just to understand what is missing in a first-order kernel. It was shown in reference [80] in an analytically solvable model system, that already the first-order kernel yields very good results. This statement could have been drawn for silicon by looking at the differences between solution of the Bethe-Salpeter equation and the TDDFT result of figure 9.3: there are no differences! As a consequence, the second-order kernel should have almost no effect on an absorption spectrum. A. Marini [79] performed calculation for the first- and second-order for energy-loss spectra. His conclusion is also that the first-order is already sufficient for realistic systems for that kind of spectroscopy.

This section illustrates the need for only first-order kernels, that allows gain of computational time with respect the full solution of the Bethe-Salpeter equation. If the second-order were also needed, there would be no practical justification for using this technique instead of the diagonalization of the Bethe-Salpeter equation.

In conclusion, this section provided a simple derivation for the exact TDDFT kernel. It put into evidence the role of the quantity $\delta\Sigma/\delta\rho$. It allowed one to find approximations for the TDDFT kernel using a perturbative expansion, which are in agreement with references [64, 65], or using sensible approximations. Let us exemplify this last point. Consider the following equation that is needed for $f_{xc}^{(2)}$ (see equation (9.7)):

$$\frac{\delta\Sigma}{\delta\rho} = -WGG\frac{\delta G^{-1}}{\delta\rho}, \tag{9.24}$$

where one has to find an approximation for $\delta G^{-1}/\delta\rho$ to stop the expansion. The approximation used in our paper [96] is to argue that there may exist a local potential that gives the quasiparticle energies (supposing that all wavefunctions are equal). In this particular case, $\delta G^{-1}/\delta\rho$ can be written simply $-\chi_0^{-1}$. This is precisely equivalent to the first-order kernel derived in this chapter!

Chapter 10

How to include vertex corrections using density-functional concept

Going beyond GW has been up to now problematic. The evaluation of the vertex function $\tilde{\Gamma}(1,2;3)$ is much involved, not only because it is a 3-point function, but also it requires to solve a 4-point equation involving the Bethe-Salpeter kernel $\Xi(1,2;3,4)$ (equation (3.18)). This is clearly the bottleneck for any attempt to go farther than $\Sigma = iGW$.

Few works exist that evaluate the vertex corrections beyond GW using approximate vertex in very simple models. E. Shirley [97] applied the single-ladder diagram correction with respect to GW using RPA screening in atoms. Y. Takada used some averaging technique to transform the 4-point Bethe-Salpeter kernel into a 3-point one and evaluated it in the case of an homogeneous electron gas [98]. R. Del Sole and coworkers [99] used the LDA approximation to solve the vertex equation (3.18) for silicon. Mahan and Sernelius did the same for the homogeneous electron gas few years before [100]. F. Aryasetiawan and coauthors [101] calculated a sum on some specific class of diagrams (the cumulant expansion) in the realistic case of Na and Al. Very recently, Marini and Rubio studied the influence of vertex corrections on lifetimes of single-particle excitations [102].

It is tempting to think that it is a waste to solve an equation with 4-point quantities to get 3-point ones. The following study describes the proposition made in my work with F. Sottile, V Olevano, R. Del Sole, and L. Reining (reference [96]) to use theorems of TDDFT to simplify somehow the vertex equation, to make it conserve its 3-point nature from the beginning to the end.

10.1 Density-functional concept

Consider the following equation, which is the definition of the self-energy (equation (3.10)):

$$\Sigma(1,2) = -i \int d34 v(1^+, 3) G(1,4) \frac{\delta G^{-1}(4,2)}{\delta U(3)}. \qquad (10.1)$$

Σ is defined as a linear response to variations of a fictitious local external potential U. Remember that U was just introduced to permit the use of the Schwinger derivative trick (see chapter 3).

TDDFT is based on the fact that there exists a one-to-one mapping between time-dependent external potentials and time-dependent densities under certain assumptions. In Runge-Gross theorem [55], once the initial state Ψ_0 is fixed, the existence of a one-to-one mapping is proven, when the potential U is Taylor-expandable around the initial state. As there is a one-to-one relation between U and ρ, one can alternatively consider variations with respect to U or variations with respect to ρ:

$$\Sigma(1,2) = -i \int d345 v(1^+, 3) G(1,4) \left[\frac{\delta G^{-1}(4,2)}{\delta \rho(5)} \frac{\delta \rho(5)}{\delta U(3)} \right]. \qquad (10.2)$$

One can now use Dyson equation and differentiate with respect to ρ

$$
\begin{aligned}
\frac{\delta G^{-1}(1,2)}{\delta \rho(3)} &= -\delta(1,2) \frac{\delta U(1)}{\delta \rho(3)} - \delta(1,2) \frac{\delta v_h(1)}{\delta \rho(3)} - \frac{\delta \Sigma(1,2)}{\delta \rho(3)} \\
&= -\delta(1,2) \left[\chi^{-1}(1,3) + v(1,3) \right] - \frac{\delta \Sigma(1,2)}{\delta \rho(3)}. \qquad (10.3)
\end{aligned}
$$

This finally gives the expression of the self-energy

$$
\begin{aligned}
\Sigma(1,2) = i \int d34 v(1^+, 3) G(1,4) \Bigg[& \delta(4,2)\delta(4,3) \\
& + \int d5 \left(\delta(4,2) v(4,5) \chi(5,3) + \frac{\delta \Sigma(4,2)}{\delta \rho(5)} \chi(5,3) \right) \Bigg], \quad (10.4a)
\end{aligned}
$$

where the polarizability $\chi(1,2) = \delta G(1,1^+)/\delta U(2)$ can be worked out in the same manner

$$
\begin{aligned}
\chi(1,2) = -i G(1,2) G(2,1) - i \int d345 G(1,3) G(4,1) \\
\times \left[\delta(3,4) v(3,5) + \frac{\delta \Sigma(3,4)}{\delta \rho(5)} \right] \chi(5,2). \quad (10.4b)
\end{aligned}
$$

One can identify in the polarizability equation the kernel $f_{xc}^{(2)}$ defined in the previous chapter in equation (9.7) and rewrite this equation as

$$\chi(1,2) = \chi_0(1,2) + \int d34 \chi_0(1,3) \left[v(3,4) + f_{xc}^{(2)}(3,4) \right] \chi(4,2), \qquad (10.5)$$

or, introducing also $f_{xc}^{(1)}$,

$$\chi(1,2) = \chi_{\text{KS}}(1,2) + \int d34 \chi_{\text{KS}}(1,3) \left[v(3,4) + f_{xc}^{(1)}(3,4) + f_{xc}^{(2)}(3,4) \right] \chi(4,2),$$
(10.6)

which is just the TDDFT equation within linear-response.

Concerning the other occurrence of $\delta\Sigma/\delta\rho$ in the self-energy equation, one can not consider $\delta\Sigma/\delta\rho$ as negligible, as stated in the previous chapter: it is more convenient to consider the difference $\delta\Sigma/\delta\rho - f_{xc}^{(2)}$ as small. The definition of $f_{xc}^{(2)}$ has been given in equation (9.7). To account for this statement, one can add and substract the quantity $f_{xc}^{(2)}\chi$ in equation (10.4a) and obtain

$$\Sigma(1,2) = i\tilde{W}(1^+,2)G(1,2) + i \int d34 v(1^+,3)G(1,4)\Delta\Gamma(4,2;3), \quad (10.7)$$

with the following definitions:

$$\tilde{W}(1,2) = \delta(1,2) + \int d3 \left[v(1,3) + f_{xc}^{(2)}(1,3) \right] \chi(3,2)$$
(10.8)

is the testcharge-testelectron screened Coulomb interaction, and

$$\Delta\Gamma(1,2;3) = \int d4 \left[\frac{\delta\Sigma(1,2)}{\delta\rho(4)} - \delta(1,2)f_{xc}^{(2)}(1,4) \right] \chi(4,3)$$
(10.9)

is the three-point part of the vertex function.

The modified screened Coulomb interaction $\tilde{W}$ just introduced has to be considered as an improvement over the usual W. The polarizability χ, used to construct it, is still the exact one (as in W). But $\tilde{W}$ accounts also for the 2-point part of the vertex contained in the equation of Σ. In physical words, W being sensitive to $1 + v\chi$, feels *classically* the charge variations of the quantum system ($\chi = \delta\rho/\delta U$). Exactly as a point charge (positive or negative) added to the system of N electrons does. On the contrary, $\tilde{W}$ is sensitive to $1 + [v + f_{xc}^{(2)}]\chi$. This means that a charge, on which $\tilde{W}$ acts, is sensitive to charge variations also via exchange-correlation processes (contained in $f_{xc}^{(2)}$). The added charge does not experience anymore just the classical electric field but also an exchange-correlation field with the fermions of the quantum system. This is due to the quantum nature of the extra-particle.

The introduced 3-point quantity $\Delta\Gamma$ can also be considered as an "improvement" over the bare vertex $\tilde{\Gamma}$. I mean that $\Delta\Gamma$ is a difference of two quantities accounting for the same category of effect: the electron-hole interaction. Therefore, $\Delta\Gamma$ is expected to be smaller than $\tilde{\Gamma}$. The complete neglect or approximations made on $\Delta\Gamma$ should be less dramatic than made on $\tilde{\Gamma}$. It is always sensible to make rough approximations on something small, than doing the same on something large.

In conclusion, it is helpful for practical applications to reformulate the equation (10.4a) in order to emphasize $\tilde{W}$ and $\Delta\Gamma$. Moreover, the link with the usual GW approximation of Hedin's equations is thus made obvious.

10.2 Practical applications: initiating with $\Sigma = v_{xc}^{\mathbf{LDA}}$

For practical purposes, one has to choose a starting approximation for the Σ operator of the right-hand sides of equations (10.4). A simple choice is to approximate Σ by the LDA potential and consistently the Green's functions by the LDA ones. This is straightforward.

Concerning the derivative of Σ with respect to the density, a further assumption has to be made to consider the dependence of v_{xc}^{LDA} with respect to the density. One will use the usual *adiabatic assumption* presented in the introductive chapter on TDDFT (chapter 4). One considers that the exchange-correlation kernel is "local in time" or in other words, exchange-correlation has no memory. This gives an additional $\delta(t_1 - t_2)$ in the derivative of $v_{xc}^{\mathrm{LDA}}(1)$ with respect to $\rho(2)$.

Consequently, the equation (10.4b) is nothing else but the usual equation for the adiabatic LDA polarizability. As the self-energy is equal to a Kohn-Sham potential v_{xc}^{LDA}, there is no $f_{xc}^{(1)}$ part in the kernel (to be used in equation (10.6)), that would have mapped the Kohn-Sham polarizability χ_{KS} onto the independent quasiparticle polarizability χ_0.

The other equation of the scheme (equation (10.7)) gives the self-energy. As the self-energy in $\Delta\Gamma$ is is equal to the Kohn-Sham potential $= v_{xc}^{\mathrm{LDA}}$, $\Delta\Gamma$ vanishes. In $\tilde{W}$ (see equation (10.8)), a second occurrence of the adiabatic LDA kernel accounts for the so-called vertex corrections. And finally, $\tilde{W}$ involves the testcharge-testelectron screening within adiabatic LDA. This derivation of the adiabatic LDA vertex correction is compliant with Del Sole *et al.* [99].

Table 10.1 presents the values of the direct band gap at Γ within different approximations for two very different materials: bulk silicon shows a strong screening and continuum excitons, and solid argon shows almost no screening and strongly bound electron-hole pairs. The calculation param-

Table 10.1: Direct gap (in eV) at Γ in bulk silicon and solid argon, calculated using a local approximation (LDA) for the starting self-energy.

	LDA	GW^{RPA}	$GW^{\mathrm{TC\text{-}TC}}$	$G\tilde{W}$	Expt.
Si	2.53	3.17	3.08	3.18	3.40
Ar	8.18	12.95	12.64	12.75	14.2

eters are set to the minimum meaningful value, to remain consistent with the more cumbersome calculations of the next section. In particular, the number of bands used to evaluate the screening has been 17 for silicon and 16 for argon. This is sufficient to converge the energy difference (the band gap), but not the absolute value. That is why this piece of information is not displayed in the table. The screening matrix has been represented on the basis set of 169 plane-waves for both material. This value is converged with no doubt. A plasmon-pole model (described in chapter 5) has been used to evaluate the dynamical behavior of the screening matrix. Therefore, one had to calculate the screening matrix only at two frequencies along the imaginary axis.

The table first shows the value of the band gap within the starting approximation, LDA. It underestimates largely the experimental values from references [21, 23]. Therefore, the screening W will be overestimated. As a reference, the table then provides the usual GW result, labeled GW^{RPA}, that neglects the two occurrences of f_{xc}. It gives the usual results: the silicon band gap is in agreement with the experimental value, whereas in argon, it is 1.25 eV too small. If one further adds the contribution of the adiabatic LDA to the polarizability χ, one obtains the $GW^{\mathrm{TC\text{-}TC}}$ column of the table. This contribution slightly closes the band gap in both cases. When the second occurrence of f_{xc} is included to get the testcharge-testelectron screening $\tilde{W}$, it acts in the opposite direction. One finally obtains a band gap value almost similar to the original GW^{RPA} one. Generally, the effect of the adiabatic LDA kernel is small. This may be due to the lack of the proper long-range component of the true TDDFT kernel [4, 63]. Note that the effect of this kernel was already small on absorption spectra of solids (see figure 4.1). These findings are consistent with earlier work [99].

10.3 Practical applications: initiating with $\Sigma = \Sigma_{\mathrm{COHSEX}}$

Let us now turn to a more realistic approximation of the Σ and G of right-hand side of equations (10.4). One will use the static COHSEX approximation of L. Hedin [25], for different reasons.

The first justification to use COHSEX inputs is that the derivative of Σ^{CS} with respect to G gives precisely the approximate kernel used in practical solutions of the Bethe-Salpeter equation: the static screened Coulomb interaction iW_0. Furthermore, Reining *et al.* have shown that, when inserted in equation (9.17), this approximation yields a TDDFT kernel that presents the correct long-range behavior proportional to $1/q^2$ [4]. This long-range contribution has been shown to be crucial to describe properly the excitonic effect in optical absorption spectra, either for continuum excitons,

as in silicon, or for bound excitons, as in argon. One has to check whether this feature is also significant for vertex corrections on the band gap.

A second reason to use COHSEX inputs is that, according to the first column of table 10.2, the band gap within COHSEX, though slightly overestimated, is pretty close to the true quasiparticle band gap, and in any case, closer than the corresponding LDA value. As a consequence, the evaluation of the G's in right-hand side of equations (10.4), can be thought as more realistic.

One will then proceed in the table with the same method as previously with the LDA inputs, adding one-by-one corrections to standard GW. But, difficulties arise due to the non local nature of COHSEX self-energy. First, the COHSEX wavefunctions are assumed to be equal to the LDA ones throughout the results and the COHSEX quasiparticle energies are the perturbative ones (not self-consistent), because the fully self-consistent code I developped (see chapter 8) did not exist yet when I performed these vertex calculations. Fortunately, the self-consistency does not change so much eigenvectors and eigenfunctions with respect to the first perturbative step for these materials. As COHSEX approximation is not a Kohn-Sham potential, the $f_{xc}^{(1)}$ of equation (10.6) is not zero now. In practice, since $f_{xc}^{(1)}$ exactly accounts for the quasiparticle shift, I directly used equation (10.5), where the effect of $f_{xc}^{(1)}$ is already taken into account via the χ_0's. Final difficulty: as COHSEX approximation to the self-energy is non local, there is a non vanishing $\Delta\Gamma$, that accounts for the three-point nature of the vertex function. I have to immediately warn that no calculations of the $\Delta\Gamma$ contribution to the band gap have been done by us so far. Just Marini and Rubio have included an analogous correction in the calculation of quasiparticle lifetimes and found it rather significant for a large gap insulator [102]. The convergence parameters are all exactly equal to the ones used starting from LDA inputs.

Under the previous assumptions, table 10.2 shows the effect of the two occurrences of $f_{xc}^{(2)}$ in equations (10.4) on the direct band gap of silicon and argon, compared to the reference GW^{RPA} calculation. As noticed with the LDA inputs, the effect of using an improved polarizability χ, which includes exchange-correlation via $f_{xc}^{(2)}$, is slight on the band gap ($< 0.2\,\mathrm{eV}$ if one

Table 10.2: Direct gap (in eV) at Γ in bulk silicon and solid argon, calculated using a non-local approximation (COHSEX) for the starting self-energy.

	COHSEX	GW^{RPA}	$GW^{\mathrm{TC\text{-}TC}}$	$G\tilde{W}$	Expt.
Si	3.64	3.30	3.18	3.32	3.40
Ar	14.85	14.00	14.16	14.76	14.2

compares column $GW^{\text{TC-TC}}$ to the GW^{RPA}). The account for the correct long-range tail of the exchange-correlation kernel does not yield noticeable improvement over the adiabatic LDA χ. In addition, the second kernel $f_{xc}^{(2)}$ in $\tilde{W}$ gives rise to the two-point part of the vertex function. Its effect is to open the gap, slightly for silicon, where one recovers more or less the initial GW^{RPA} result, and noticeably for argon, where the final gap is $0.5\,\text{eV}$ larger than experiment. The subsequent contribution $\Delta\Gamma$ still needs to be evaluated, but it can be considered as a higher-order contribution, since the meaningful perturbation parameter has been shown to be $\delta\Sigma/\delta\rho - f_{xc}^{(2)}$ in the previous chapter.

The band gap of simple materials results of the sum of different vertex contributions that generally cancel out. The main effect for these simple materials does not come from the vertex corrections, which are indeed relatively small corrections, but from the different starting Green's functions. Starting from LDA Green's function or from COHSEX Green's function can change the band gap up to $1\,\text{eV}$ for argon. Finally, the self-consistency is expected to have a greater impact on the band gap than vertex corrections. This is indeed the case according to chapter 8. Because of the cancellation of the vertex contributions, it is reasonable to hope that, in the case of not highly correlated materials, the main corrections beyond the standard perturbative GW approach will be due to the self-consistency. This is computationally simpler than to evaluate the vertex corrections and will be carried out for Cu_2O in chapter 14.

In conclusion, the present chapter provides a theoretical and practical scheme to produce vertex corrections, beyond Hedin's GW approximation. The link with theorems of TDDFT has been proven useful to simplify the expression of the vertex functions. Three contributions beyond GW have been identified. First, there is the electron-hole interaction in the polarizability. Second, there are two components (a local and a non-local one), which express the property that the added particle (electron or hole) in a photoemission experiment is not only a point charge, but also a quantum object, subjected to exchange and correlation with the other electrons of the system. In particular, GW expression includes a spurious self-screening contribution, that has to be removed by the vertex corrections.

Part IV

Electronic excitations of Cu$_2$O

Chapter 11

Presentation of Cu$_2$O

The study of Cu–O bonding is nowadays an important issue for the understanding of cuprate high-T$_c$ superconductors. These materials have planes of CuO$_2$, inside which the superconductivity occurs. Cu$_2$O is a good candidate to start such a study, as its geometry is very simple. It has no magnetic properties, except a rather small spin-orbit splitting of the band structure (~ 0.13 eV). And, in contrast with some other transition metal oxides, the electronic correlation is expected to be relatively small, thanks to the closed shell (d^{10} configuration, in a pure ionic model Cu$^+$, O^{2-}).

However, Cu$_2$O is an original material to many respects: unusual linear coordination of copper atoms, possible direct Cu-Cu bondings [103, 104], and, historically important, several famous exciton series [1, 2, 9, 105]. These uncommon features have made the theoretical study tougher than expected, but also more interesting.

11.1   Structure

Cuprous oxide, Cu$_2$O, crystallizes in a simple cubic Bravais lattice, with space group O_h^4 (or $Pn\bar{3}m$, space group number 223) [17]. Inside the unit cell, oxygen atoms are located on a body-centered-cubic sublattice, whereas copper atoms form a face-centered-cubic lattice. If one chooses the origin on an oxygen atom, copper atoms are at positions $(\frac{1}{4}, \frac{1}{4}, \frac{1}{4})$, $(\frac{1}{4}, \frac{3}{4}, \frac{3}{4})$, $(\frac{3}{4}, \frac{1}{4}, \frac{3}{4})$, and $(\frac{3}{4}, \frac{3}{4}, \frac{1}{4})$. This gives two Cu$_2$O formulas per unit cell. This structure called cuprite is depicted on figure 11.1. X-ray diffraction gives a lattice parameter $a = 8.068$ a.u. or 4.2696 Å [17].

Each oxygen atom is surrounded by a tetrahedron of copper atoms and each copper atom is twofold coordinated with oxygen atoms. This material is a unique occurrence of O–Cu–O linear geometry. This configuration is not explained by simple ionic forces, which state that the O^{2-}–O^{2-} and Cu$^+$–Cu$^+$ sublattices repel each other. The attractive interaction that stabilizes the material suggests some direct Cu–Cu covalent-like bondings.
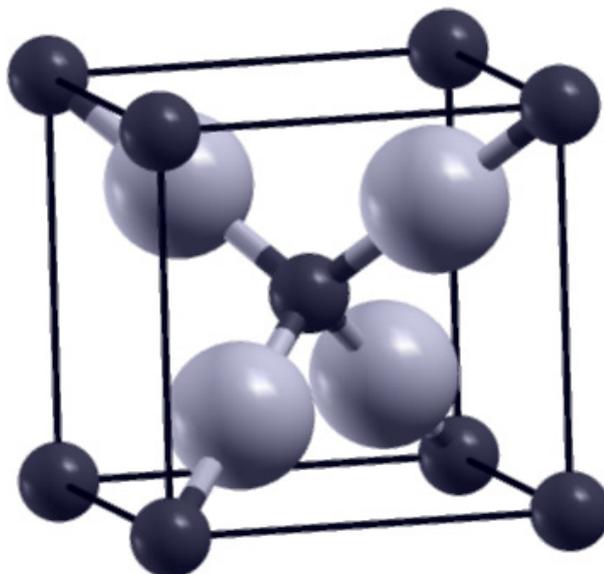
Figure 11.1: Atomic structure of Cu$_2$O. Large grey spheres represent copper atoms, small dark spheres represent oxygen atoms.

11.2   Cu-Cu bonding

Direct Cu–Cu bonds would explain the unexpected stability of Cu$_2$O within the cuprite structure. Direct evidence of such an interaction is very difficult to measure. Zuo *et al.* [103, 104] have first claimed to have measured it experimentally. Using combined electron diffraction and X-ray diffraction experiments, they deduced a maximum in the electron density difference (density of the solid minus density of superimposed Cu$^+$, O^{2-} ions) right in the unoccupied center of four neighboring copper atoms, corresponding in figure 11.1 to the center of the faces of the cubic cell. They evaluated the maximum of electron density difference to be $\sim 0.2\,e\,\text{Å}^{-3}$ (that is comparable to the maximum density difference between two silicon atoms in bulk silicon). This maximum was interpreted by the authors as a direct proof of Cu–Cu covalent bondings.

These conclusions were much debated in the electronic structure community. Other measurements were performed [106] that showed on the contrary a minimum of electron density in that empty tetrahedral site. Some recent calculations within a "modified LDA" scheme [107], which artificially lower the hybridization of LDA, tend to show that there might be a maximum of density here, but four times smaller that the one measured by Zuo *et al.*.

This issue is still much questionned. However, some conclusions can be drawn from these studies. The total charge transfer from the copper

atoms to the oxygen atoms is evaluated to be 1.01 by Zuo *et al.* (this means a Cu$^+$, O^{2-} configuration). But, a simple ionic model of Cu$^+$ would deplete the charge from $4s^1$ and keep the $3d^{10}$ unchanged. Cu$^+$ cathion would have then a perfectly isotropic electron density. According to the previous studies, some anisotropy can in fact be measured, which is the proof for hybridization between $3d$ and $4s$ shells, especially between $3d_{z^2}$ and $4s$ (due to symmetries). Zuo *et al.* measured a d hole on copper of about 0.22 electron per atom. This would mean that conduction bands have also some non-negligible d character.

In this context, state-of-the-art *ab initio* calculations of the electronic structure are really necessary to judge the contradicting experimental data.

11.3   Exciton series

Cu$_2$O is moreover famous and often cited in textbooks for two exciton series arising from a dipole forbidden transition [9]. The early work of Baumeister in the 60's [1] already provided very accurate data concerning the whole series: the green and the yellow series. The two series are just separated by the spin-orbit splitting. The binding energy, the band gap and the spin-orbit splitting have been evaluated and even refined later by measurements at lower temperature (4.5 K) [105]: $E_b = 0.139\,$eV, $E_g = 2.1720\,$eV, and $\Delta_{SO} = 0.1338\,$eV. A schematic picture of the band structure of Cu$_2$O around the band gap is provided in figure 11.2 [9].

As the transition from the last valence state to the first conduction state at Γ is forbidden ($\Gamma_7^+ \rightarrow \Gamma_6^+$ transition), the first peak of the corresponding excitonic series can not be observed by single photon absorption. The selection rule can be overcome in a two photon absorption experiment, as in the work of Uihlein *et al.* [105]. All theses measurements confirms the theoretical analysis of Elliott [108].

But, the story of the excitons of cuprous oxide does not stop here. Optical reflectivity and absorption measurements performed at higher energy [2, 3] proved the existence of at least two other excitonic series: the blue and the blue-violet series, which comes from transitions respectively $\Gamma_7^+ \rightarrow \Gamma_8^-$ and $\Gamma_8^+ \rightarrow \Gamma_8^-$. The figure 11.3 displays the measurement of Balkanski *et al.* [2] and uses the peaks' names introduced by Brahms [3]. The blue and blue-violet excitons are respectively labelled E_B and E_{BV}. They are separated by the spin-orbit splitting of the last valence band and occur just at the absorption threshold 2.59 and 2.72 eV. The binding energy of these series seemed very low to experimentalists ($E_o \approx E_B$), therefore one can assess the position of the second conduction band (Γ_8^-): 2.59 eV above the top valence band. Peaks E_1, E_2, and E_3 are also suspected to be excitonic, since their sharpness depends strongly on temperature.

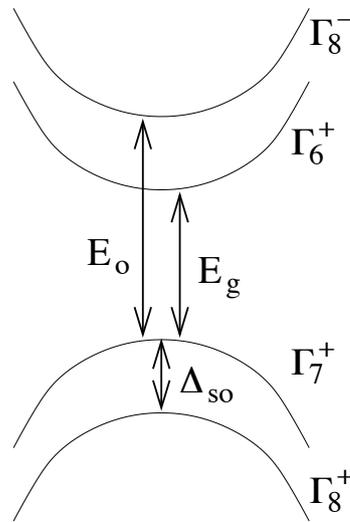The study of the optical spectra gave us very accurate experimental data

Figure 11.2: Schematic representation of the band structure around the band gap E_g. The top valence band at Γ is splitted into Γ_7^+ and Γ_8^+ due to the spin-orbit splitting Δ_{SO}. The transition from Γ_7^+ to the bottom conduction band Γ_6^+ is dipole forbidden. On the contrary, the transition from Γ_7^+ to Γ_8^- is authorized and gives rise to the optical threshold E_o.
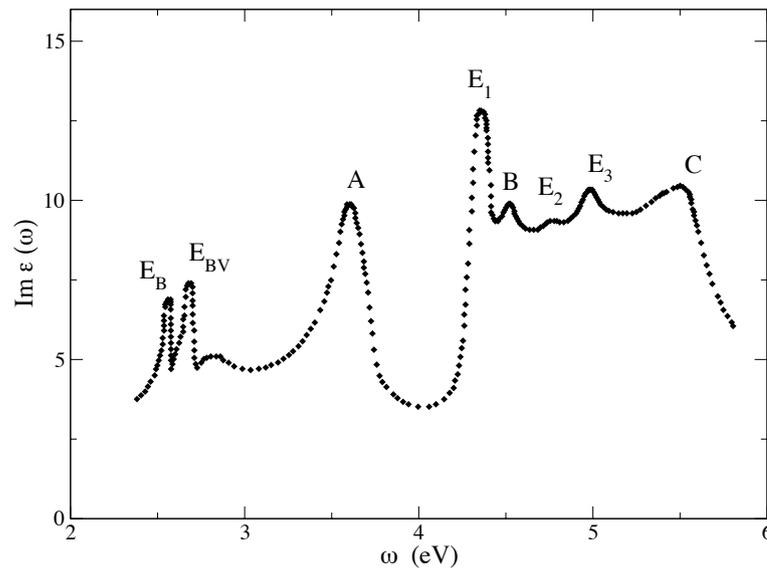

Figure 11.3: Imaginary part of the dielectric function of Cu_2O, obtained by reflectivity experiment [2] and further Kramers-Kronig transforms.

concerning the conduction band structure. Indeed, one precisely knows the location of the two first conduction bands Γ_6^+ and Γ_8^- with respect to the

top valence band Γ_7^+. However, the interpretation of the spectra is not yet known for sure. Experiments give hints on the nature of transitions giving rise the additional peaks labelled A, B, C, and E_i, but no proof, no certitude. These issues are typically the questions that can be answered by *ab initio* calculations of the band structure and of the optical absorption spectrum.

Chapter 12

DFT study of Cu_2O

This chapter proposes to calculate the ground-state properties of Cu_2O in the DFT framework. The structural properties, like the equilibrium lattice parameter a_0 and the bulk modulus B_0 can be reached this way. Following the common practice, the Kohn-Sham band structure is also studied and compared to photoemission spectroscopy experiment, although it has been stressed in the introductive chapters, that Kohn-Sham eigenvalues and eigenvectors have, strictly speaking, no physical meaning. Indeed, except the usual band gap underestimation, Kohn-Sham band structure agrees generally well with experimental data for simple materials.

The whole study is based on the plane-wave basis set using ABINIT package [67, 69]. Therefore, the first task is to choose a core-valence partition, and to generate suitable pseudopotentials. Some of the following results are presented in reference [109].

12.1   Issue of semicore states of copper

The generation of pseudopotentials is not an harmless operation. First, one has to define which states will be considered as frozen in the atomic configuration, and consequently, will not participate to chemical bondings. The second step is to choose a cut-off radius for each angular channel, beyond which the pseudo wavefunction is strictly equal to the all-electron wavefunction. This supposes that the core region of the valence wavefunctions (below the cut-off radius) is not important in order to describe the properties under study. All the atomic calculations and pseudopotential generations are made using the fhiPP code [110, 111].

The choice of the core-valence partition in oxygen offers no problem: the core is obviously $1s^2$, and the valence $2s^2 2p^4$. This has already been used successfully at "Laboratoire des Solides Irradiés" in many previous studies of oxides [62, 112].

On the contrary, the choice is not so straightforward concerning the copper atoms. One can distinguish three groups of electrons in copper:

the core electrons $1s^2 2s^2 2p^6$, the semicore electrons $3s^2 3p^6$, and the valence electrons $3d^{10} 4s^1$. This splitting into three groups is based on energetic arguments. Table 12.1 provides the calculated energies of the different levels of the atom of copper within LDA. There are more than 800 eV between the chosen core and the semicore states and there is an energetic separation of about 65 eV between the semicore and the valence states. Table 12.1 also compares the measured binding energies in Cu_2O and the calculated atomic level of Cu. This is, of course, not directly comparable even for deep states, as the crystal field is missing, and as LDA is known to be a crude approximation for localized states. But, it can give an idea on how accurate are the energy differences between electronic levels. The agreement is rather clear.

Considering energetic arguments, it seems sensible to consider the semi-core as frozen in the core, since they are more than 65 eV below the $3d$ states. But, if one draws the all-electron atomic wavefunctions corresponding to the $3s$, $3p$, and $3d$ levels as in figure 12.1, one finds that the maximum of the three wavefunctions is located approximatively at the same radius $r \sim 0.6$ a.u.. The overlap between the different orbitals is therefore very large and one can doubt that a separation in between $3s$ and $3p$ on one side and $3d$ on the other side would be justified.

Since they are contradicting clues concerning the core-valence partition, the study will be resumed with two different pseudopotentials: one considering the semicore as frozen in the core, the other one treating explicitly the semicore as valence states. The second approach is expensive, because one has to deal with 8 electrons more per copper atom, and one has to describe the very localized states $3s$ and $3p$ using plane-waves! However, the semicore has been shown to be necessary for further GW calculations [114, 115].

The pseudopotentials of copper are generated on the configuration Cu^+ $3d^{10} 4s^0$. Starting from the neutral configuration does not change much.

Table 12.1: Energy levels (eV) of Cu^+ ion within LDA compared to the XPS binding energy of Cu_2O. The experimental data for $2p$ and $3p$ are splitted due to the spin-orbit coupling.

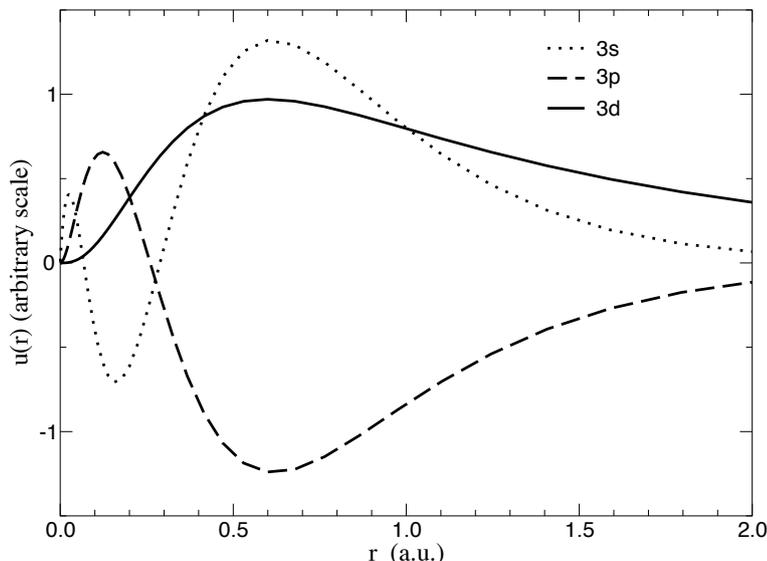| Cu^+ state	$\epsilon_i^{\mathrm{LDA}}$	XPS binding energy[a]
$1s$	8842.1	—
$2s$	1068.8	1071.5
$2p$	924.9	931.7 - 951.6
$3s$	122.8	119.5
$3p$	80.75	75.3 - 75.3
$3d$	14.01	—

[a]Reference [113]

Figure 12.1: All-electron radial wavefunctions corresponding to levels $3s$ (dotted line), $3p$ (dashed line), and $3d$ (full line) of the copper atom.

The pseudopotential scheme is Troullier and Martins [116] (unless otherwise specified), and Kleinman-Bylander separable form is used [117]. For oxygen, the cut-off radii are $r_{c_s} = 1.6$ a.u., $r_{c_p} = 1.5$ a.u. and the local component is p. For copper without semicore, the cut-off radii are $r_{c_s} = 1.19$ a.u., $r_{c_p} = 1.19$ a.u. using Hamann type [118] and $r_{c_s} = 2.08$ a.u. (these values come from Marini's work [119]). The local component is s. For copper with semicore, the cut-off radii are $r_{c_s} = 0.80$ a.u., $r_{c_p} = 1.17$ a.u. using Hamann type [118] and $r_{c_s} = 1.19$ a.u.. The local component is p.

Figure 12.2 exemplifies how the pseudo wavefunctions account for the all-electron wavefunctions. Above the cut-off radius, both coincide perfectly. Below, the all-electron wavefunction representing e.g. the $3s$ state has two zeros, whereas the pseudo wavefunction does not have any. It is therefore a $1s$ type wavefunction. In the same way, the $3p$ wavefunction is represented by a $2p$ pseudo wavefunction, and the $3d$ by a $3d$ one.

12.2   DFT theoretical structure

A first test concerning the quality of the generated pseudopotential is to address the issue of the geometrical structure. As mentionned earlier, the inclusion of semicore states in valence is costly. The corresponding cut-off energy is 80 Ha, whereas 40 Ha are sufficient to converge the calculations that do not treat the semicore states. The **k**-point sampling is a Monkhorst-Pack grid [120] $4 \times 4 \times 4$. The LDA exchange-correlation potential used is
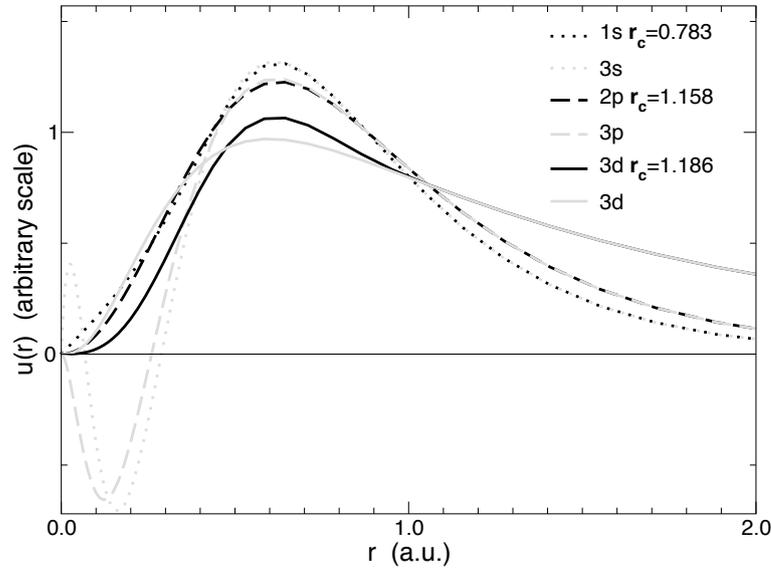
Figure 12.2: All-electron (grey curves) and pseudo (black curves) radial wavefunctions corresponding to levels $3s$ (dotted lines), $3p$ (dashed lines), and $3d$ (full lines) of the copper atom. The radius where the all-electron and pseudo wavefunctions actually match is also displayed.

Perdew-Wang [49], and the GGA one is PBE [51].

Figure 12.3 shows the total energy curves as a function of the volume for the two pseudopotentials described in the previous section. The structural parameters can be extracted by fitting a Murnaghan equation of state (see equation (1.7)). The results are summarized in table 12.2. The difference between the calculations with or without semicore states is huge. They respectively underestimate the equilibrium lattice parameter by 2.4 % and 0.3 % with respect to the experimental value. The two bulk moduli are overestimated with respect to neutron scattering experimental values [19]. Note that the calculation *a priori* dirtier with no explicit treatment of the semicore states in the solid yields results in good agreement with experiment. And that the better calculation with semicore states correctly treated in the solid goes away from experiment. Such a discrepancy is more or less the upper limit of the usual deviation of LDA with respect to experiment.

The difference between the LDA and GGA (GGA is defined in chapter 4) total energy curves is displayed in figure 12.4. The corresponding Murnaghan fit parameters are presented in table 12.2. Whereas LDA underestimates the lattice parameter and overestimates the bulk modulus, GGA yields opposite trends. This statement is usual.

The only modern DFT structural calculation found in the literature is the work of Martínez-Ruiz *et al.* [121], who carried out a study of Cu_2O using the FPLAPW method using GGA of reference [51]. This is an all-
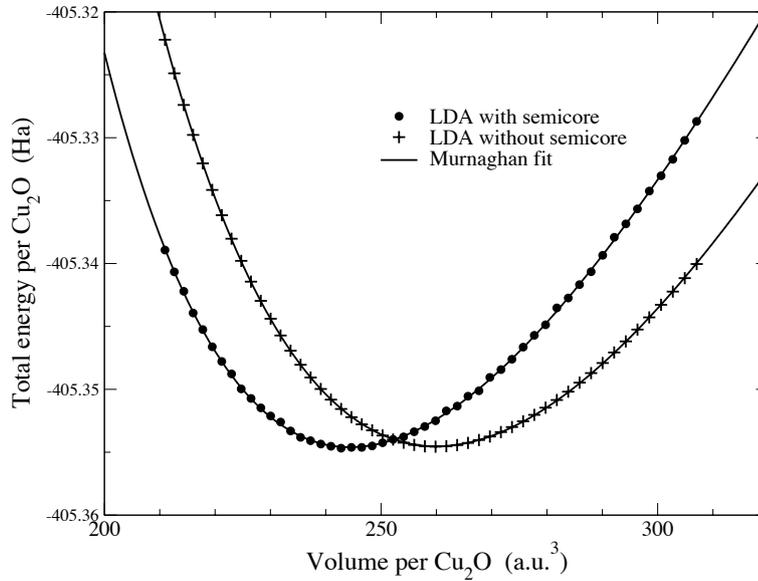
Figure 12.3: E(V) curve for Cu$_2$O within LDA for calculations with semi-core states fully taken into account (full circles) or semicore frozen in the pseudopotential (crosses). A Murnaghan fit on the two curves (full lines) has been applied to extract equilibrium lattice parameter and bulk modulus. The energy reference has been changed in order to plot the two curves on the same graph.

electron method. Therefore, one can think naively that it should be closer to the calculation with semicore states than to the one without. Indeed, their results are in very good agreement with my result with semicore: they find a lattice parameter of 8.126 a.u. and a bulk modulus of 108 GPa, which should be compared to the fourth column of table 12.2. This agreement is really convincing: the use of a pseudopotential with semicore is able to reproduce all-electron calculations, although the potential is modeled in

Table 12.2: Cuprous oxide structure parameters according to different approximations and to experiment.

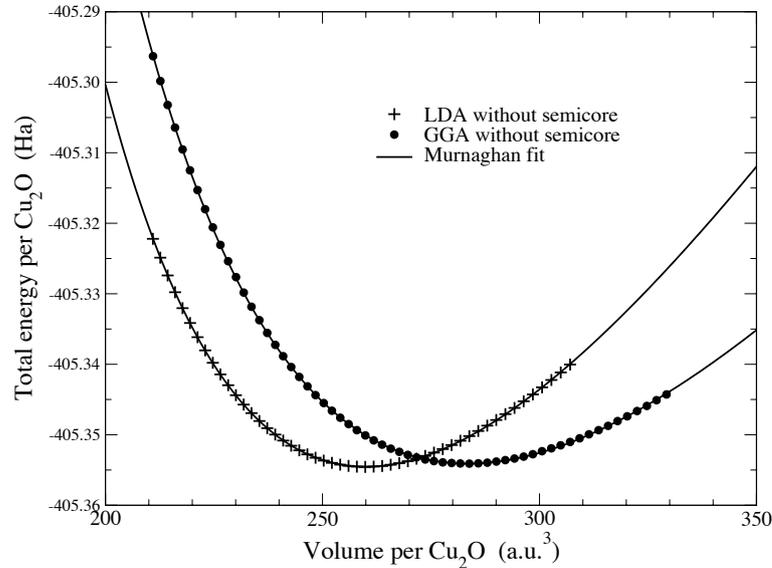| semicore	LDA		GGA		Expt.
	without	with	without	with	
a_0 (a.u.)	8.041	7.877	8.276	8.122	8.068[a]
B_0 (GPa)	136.1	147.7	103.3	110.7	112 ± 8[b]
B_0'	4.672	5.220	4.488	4.616	–

[a]Reference [17]
[b]Reference [19]

Figure 12.4: E(V) curve for Cu_2O within LDA (crosses) or GGA (circles) for calculations with semicore states frozen in the pseudopotential. A Murnaghan fit on the two curves (full lines) has been applied to extract equilibrium lattice parameter and bulk modulus. The energy reference has been changed in order to plot the two curves on the same graph.

the core region and the wavefunctions of the pseudopotential scheme show no nodes. On the contrary, the pseudopotential that freezes the semicore is clearly insufficient to reproduce the *true LDA or GGA results*, concerning the structural properties.

12.3 Kohn-Sham band structure

12.3.1 Technical checks

Let us turn now to the analysis of the Kohn-Sham band structure. I insisted in the introductive chapters on the fact that Kohn-Sham eigenvalues and eigenvectors have no physical meaning. This section voluntary forgets this warning, and tries to interpret Kohn-Sham eigenvalues and wavefunctions as observable expectation values. This procedure is usually rather successful in practical calculations.

First, consider the effect of the pseudopotential on the band structure in figure 12.5 calculated at the experimental lattice parameter $a_0 = 8.068$ a.u.. The maximum of the valence bands is set to the zero energy in all plots. In contrast with what is observed concerning structural properties, calculations with or without the semicore states treated at the solid level agree
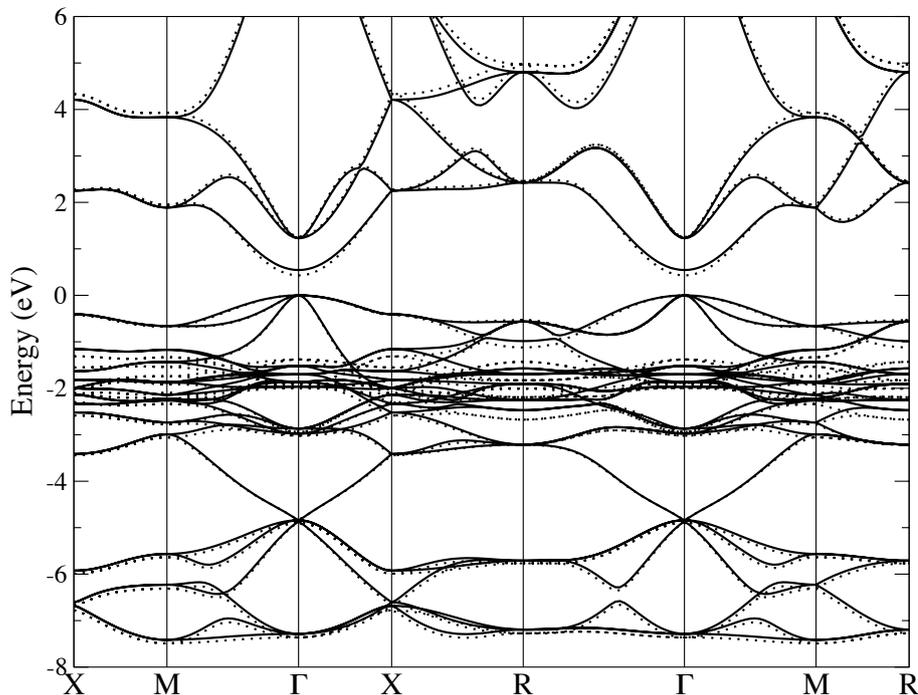
Figure 12.5: Cu$_2$O bandstructure within LDA with Cu3s, Cu3p semicore states fully taken into account (solid line) and with semicore states frozen in the pseudopotential (dotted line) at experimental lattice parameter.

pretty well. The band structure of valence states closely corresponds with both pseudopotentials. For conduction states, the agreement is less strict, but still remains reasonable. For instance, the band gap at Γ points opens from 0.42 eV without semicore to 0.54 eV with semicore.

Second, consider the effect of the DFT exchange-correlation potential on the band structure. Figure 12.6 provides the band structure at the experimental lattice parameter using either LDA [49] or GGA [51]. The agreement is once more convincing. Although GGA seemed better concerning the structural parameters, LDA and GGA perform approximatively the same for the band structure. GGA opens up the band gap at Γ of about 0.1 eV with respect to LDA. The main differences are located in the bottom of the valence bands at about -6 eV, corresponding to bands made essentially of Op states (as one will see in the next paragraph). But the maximum difference remains less than 0.2 eV. Conclusions are that the exchange-correlation potential has a small impact on the band structure, provided the same lattice parameter is used.

Let us turn now to the effect of the lattice parameter on the band structure. The dependence of the LDA band structure with respect to the lattice parameter can be noticed in figure 12.7, where the LDA band
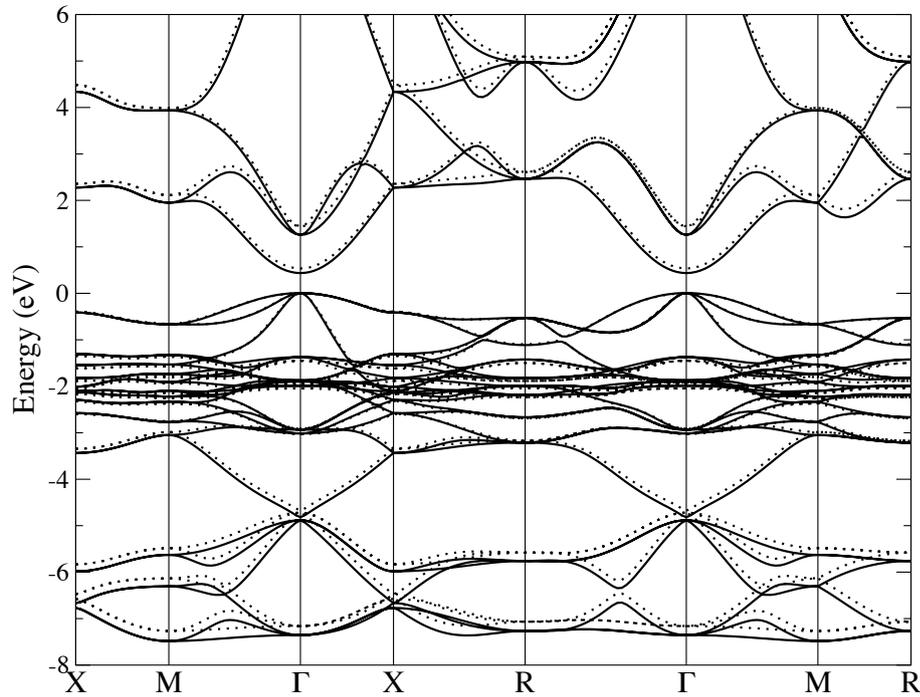
Figure 12.6: Cu$_2$O bandstructure within LDA (full line) or GGA (dotted line) using the valence Cu $3d4s$ at experimental lattice parameter.

structure has been calculated at experimental lattice parameter or at LDA equilibrium lattice parameter. The effect of using the LDA equilibrium lattice parameter instead of the experimental one is slight on the band gap (+0.2 eV) and on the second conduction band (-0.2 eV). However, the Cud band width is noticeably increased (+0.4 eV). The largest effect is undergone by the Op states, which are lowered by 0.6 eV. A smaller lattice parameter increases the coupling between Op and Cud states: this explains why the Op states are lowered and the Cud band width is enlarged. In conclusion, the dependence of the band structure on the lattice parameter is not harmless. This suggests a significant electron-lattice coupling.

12.3.2   Symmetry analysis

After the previous technical assessements, one can analyse the wavefunctions thanks to the symmetry point of view [122]. The symmetries at Γ permit to determine the compatible origins of the states in the solid. In pratice, I used subroutines written by N. Vast in the pwscf package [123]. Table 12.3 gives the possible characters of each group of states. For instance, the bottom of the O $2p$ bands have a certain Cus and Cud character, whereas the upper O $2p$ bands have some Cup component. The last valence comes from hybridization between Cud, Cus and Op atomic states. There
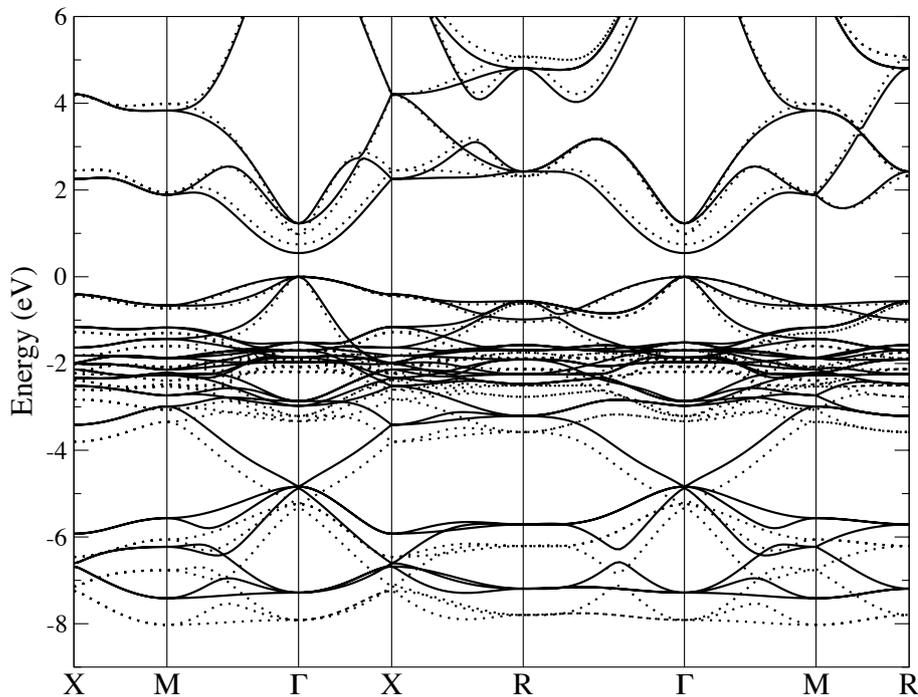
Figure 12.7: Cu$_2$O bandstructure within LDA using the pseudopotential with semicore states considered as valence ones at experimental lattice parameter $a = 8.068$ a.u. (solid line) and at LDA equilibrium lattice parameter $a = 7.877$ a.u. (dotted line).

is some Cud character in the Γ'_{25} conduction bands, therefore the Cud shell is not closed, as it would be predicted by a simple ionic model (Cu$^+$ and O^{2-}). This analysis permits to point out the particular behavior of the Γ_1 band that is located in between the two groups of Op bands. This single state does not seem to be present in photoemission experiments, where a clear gap between O $2p$ and Cu $3d$ groups can be seen. These feature of the band structure will be studied in details in the following. The symmetry analysis confirms that the transition from the last valence band to the first conduction band is forbidden, as atomic selection rules impose that $\Delta l = \pm 1$. On the contrary, the transition from the top valence band to the second conduction band is allowed for the same reason.

12.3.3 Projected and total densities-of-states

Now that the possible origins of the states is known thanks to the symmetry analysis, one can determine the actual characters of the states via a fine analysis of the wavefunctions by means of atomic projections. The projected density-of-states depends on the type of atom, labeled "atom", and on the

angular momentum, labeled l. Their expression reads

$$\text{PDOS}_{\text{atom}\,l}(\omega) = \sum_{\mathbf{k}_i i} \sum_m \sum_{\alpha \in \text{atom}} |\langle \theta(r_c - |\mathbf{r} - \mathbf{R}_\alpha|) Y_{lm}(\mathbf{r} - \mathbf{R}_\alpha)|\phi_{\mathbf{k}_i i}\rangle|^2$$

$$\times \delta(\omega - \epsilon_{\mathbf{k}_i i}), \quad (12.1)$$

where α is an index on the sites occupied by atoms of type "atom", and Y_{lm} are the usual spherical harmonics. The information provided by this quantity is averaged over the whole Brillouin zone and summed over the bands, due to the sum over $\mathbf{k}$-points and states. Figure 12.8 displays the projections on Os, Op, Cus, Cup, and Cud, with a broadening of 0.25 eV for the δ functions. One can now distinguish the nature of each region. The states at -19.45 eV arise from the atomic O $2s$ states. The two peaks at -7.30 eV and 5.75 eV are mainly O $2p$ states, with a non-negligible Cu $3d$ component. The lower peak has also some Cus character. The numerous states between -4.60 eV are essentially the Cu $3d$ states, with a certain quantity of O $2p$ character close to the top valence states. They give rise to two main peaks at -2.05 eV and -0.58eV, and two distinguishable shoulders at -2.9 eV and -1.8 eV.

Concerning the bottom of the conduction bands, the character is quite intricate. Whereas the first conduction band at Γ is clearly an hybridization of Cu $3d$ and Cu $4s$, and the other conduction bands are either Cu $4s$, or Cu $4p$, or O $2p$.

Let us quantify this information for a single $\mathbf{k}$-point. Consider table 12.4 that contains the atomic projections of the wavefunctions at Γ. These re-

Table 12.3:   Analysis of the symmetry of the bands at Γ and compatible atomic orbitals. The energies come from an LDA with semicore calculation.

Energy (eV)	Degeneracy	Symmetry	Compatible orbitals
-7.29	3	Γ'_{25}	Op, Cus, Cud
-4.87	1	Γ_1	Cus, Cud
-4.84	3	Γ_{15}	Op, Cup
-2.98	2	Γ_{12}	Cud
-2.87	3	Γ'_{25}	Op, Cus, Cud
-1.97	2	Γ_{12}	Cud
-1.86	3	Γ'_{25}	Op, Cus, Cud
-1.70	3	Γ'_{15}	Cud
-1.52	3	Γ'_{15}	Cud
0.00	3	Γ'_{25}	Op, Cus, Cud
0.54	1	Γ_1	Cus, Cud
1.23	2	Γ'_{12}	Cup
7.76	3	Γ'_{25}	Op, Cus, Cud

Figure 12.8: Projected density of states of Cu$_2$O. The projections on atomic orbitals O2s, O2p, Cu3d, Cu4s, Cu4p, and the sum of them are displayed.

sults were obtained by N. Vast using pwscf code [123]. This table gives data in agreement with the results of the symmetry analysis of table 12.3. In particular, the bottom threefold degenerate Op state has a large Cud component (30 %), whereas the top threefold degenerate Op state has no Cud component. The Γ_1 state in between the Op states is indeed a hybridization of Cud, Cus components. The same statement is valid for the first conduction band (also with symmetry Γ_1). The top valence band is clearly a hybridization between Cud and Op states.

To complete the analysis in terms of atomic orbitals, the Löwdin atomic orbital technique (see e.g. reference [124]) permits one to get useful information about the occupancy of the atomic orbitals. The knowledge of the

occupancy of the d states is physically important, since it can be considered as a measure of the on-site correlation. This type of correlation is maximum when the d shell is half occupied. For Cu_2O, the Löwdin scheme gives an occupancy of about $9.6\,e$ for the $Cu\,3d$ states (from pwscf package). This large value of the occupancy (close to the full shell) is a strong clue that the on-site correlation due to the localized $Cu\,3d$ electrons is not too high. This is confirmed by LDA+U calculations [125] performed by N. Vast, which show that varying largely the U parameter does not affect much the band structure ($Cu\,d$ width and band gap).

The total density-of-states can be compared with existing experiments. The four main peaks correspond in a straightforward manner to the four peaks A, B, C, D noticed by Ghijsen and co-workers [126], using photoemission spectroscopy. Their experiment was performed on a polycrystalline sample, therefore the **k**-point dependence is averaged out. For the HeII ray of the helium lamp they used, the cross section of copper and oxygen have more or less the same magnitude. Further, disregarding the transition matrix elements appearing in equation (2.30), their measurements are directly comparable to the calculated total density-of-states. The comparison is made in figure 12.9. There is a qualitative agreement between theory and experiment. Of course, one can play on the broadening parameter to improve the agreement on the shape, but the position of the peaks will not get improved. The maximum error in the peak position is for A and B: the difference is about $0.70\,\text{eV}$.

Table 12.4: Analysis of the atomic character at Γ. The energies come from an LDA with semicore calculation.

Energy (eV)	Degeneracy	Symmetry	O $2p$ %	Cu $3d$ %	Cu $4s$ %
-7.29	3	Γ'_{25}	61	30	8
-4.87	1	Γ_1	0	36	60
-4.84	3	Γ_{15}	98	0	0
-2.98	2	Γ_{12}	0	100	0
-2.87	3	Γ'_{25}	0	98	2
-1.97	2	Γ_{12}	0	99	0
-1.86	3	Γ'_{25}	0	99	0
-1.70	3	Γ'_{15}	0	100	0
-1.52	3	Γ'_{15}	0	99	0
0.00	3	Γ'_{25}	20	68	12
0.54	1	Γ_1	0	58	21
1.23	2	Γ'_{12}	0	0	0^a
7.76	3	Γ'_{25}	16	4	70

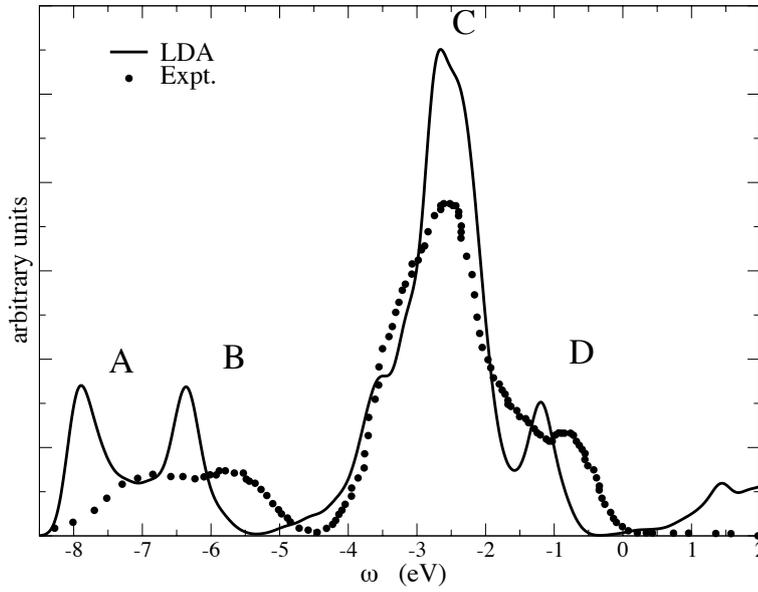^{a}This state is essentially $Cu\,4p$

Figure 12.9: LDA density of states of Cu$_2$O convoluted with a 0.20 eV broadening compared to the photoemission spectrum of reference [126].

12.3.4 Band structure features and overview of other works

There are several published band structures of Cu$_2$O in literature. And their predictions concerning the important features of the band structure largely differ. The so far identified important features are the valence O 2p band width, the valence Cu 3d band width, the band gap between O 2p and

Table 12.5: Review of published theoretical Cu$_2$O band structures.

Source	Approx.	Basis Set	Frozen Core up to level	Op band width	Cud band width	Cud–Op gap	Direct gap	Optical threshold
Kleinman [127]	Slater X	gaussians	no	2.6	2.9	0.01	1.07	3.80
Robertson [128]	empirical	LCAO	Cu 3p	2.5	3.2	1.4	2.22	2.72
Ching [129]	LDA	gaussians	Cu 3p	2.9	3.1	0.8	0.78	3.2
Ruiz [18]	HF	gaussians	no	5.2	9.1	0.	9.7	20.7
G-M [24]	HF	gaussians	no	3.1	5.5	0.	9.84	11.04
Arnaud [130]	LDA	PAW	Cu 3p	2.42	3.39	0.04	0.49	1.16
M-R,[121]	GGA	FLAPW	no	3.0	3.3	0.	0.4	1.3
this work	**LDA**	**PW**	**Cu 2p**	**2.44**	**3.44**	**-0.03**	**0.54**	**1.23**
this work	**LDA**	**PW**	**Cu 3p**	**2.47**	**3.44**	**0.07**	**0.43**	**1.25**
this work	**GGA**	**PW**	**Cu 2p**	**2.40**	**3.39**	**0.01**	**0.62**	**1.28**
this work	**GGA**	**PW**	**Cu 3p**	**2.44**	**3.34**	**0.04**	**0.54**	**1.44**
Expt.	–	–	–	$\sim 2.4^a$	$\sim 3.8^a$	$\sim 0.5^a$	2.17^b	2.55^c

[a]Reference [126]

[b]Reference [1]

[c]Reference [2]

Cu 3d, the band gap at Γ, and the optical threshold (i.e. the position of the second conduction band at Γ). Table 12.5 provides a detailed comparison of all the theoretical band structures I could find in literature. The O 2p band width is evaluated at Γ and the Cu 3d band width between the last valence band at Γ and the last Cu 3d at X point. I preferred to avoid to refer to the dispersive Γ_1 for the Cu 3d band with, as it is not sure that experimental data could notice it.

Concerning the conduction bands, all DFT-based methods are in pretty good agreement, with too small band gap and optical threshold. The Hartree-Fock calculations yield, as usual, an unrealistically large band gap. And the empirical method of Robertson [128] gives by construction almost the experimental values.

For the Cud band width, all methods except HF give a slightly too small value with respect to the experimental measurement. The Op band width is also in quite good agreement with the experimental values. The point where the methods differ largely is the presence or not of the Op–Cud gap. All DFT calculations make it vanishing except the calculation of Ching *et al.* [129] on a gaussian basis set. Also HF calculations are in deep troubles, since the Op states are intricate with Cud states, instead of having a clear separation. Finally, the empirical LCAO calculation of Robertson shows a clear gap, as it is fit on non-angular resolved photoemission spectroscopy, which shows a large gap [126]. But, a dispersive state like the Γ_1 has few chances to be detected by a measurement that integrates over the whole Brillouin zone. Indeed, even my calculations that always have this dispersive state, show a clear gap in the density-of-states provided in figure 12.9. The conclusion is at this point that one can not state whether there is a dispersive state Γ_1 in reality. The way to discover it is to perform a modern angle-resolved photoemission spectroscopy experiment, which conserves the **k**-point information. This has been done during this thesis work and will be the subject of chapter 15.

Let us analyse the surprising result of Ching *et al.* which shows a clear gap between Op and Cud, though the calculation should be analogous to the other LDA calculations. The only difference is the basis set used: they used a localized one, made of gaussians. In order to try to reproduce their calculation, I perfomed with the kind help of S. Botti a calculation using a localized basis set too. The SIESTA code [131, 132] is an *ab initio* LCAO code, which should have the same advantages and drawbacks as the code used by Ching and co-workers. In figure 12.10, the difference between the usual plane-wave result from ABINIT is compared to the SIESTA result using an accurate "double-zeta-polarized" basis set. The comparison is very convincing: just the O 2p states have moved of few tenth of eV. In particular, the Γ_1 remains as dispersive within both calculations. This does not allow one to understand the unusual result of Ching and co-workers. Also their optical threshold is quite weird. Therefore, the result of Ching
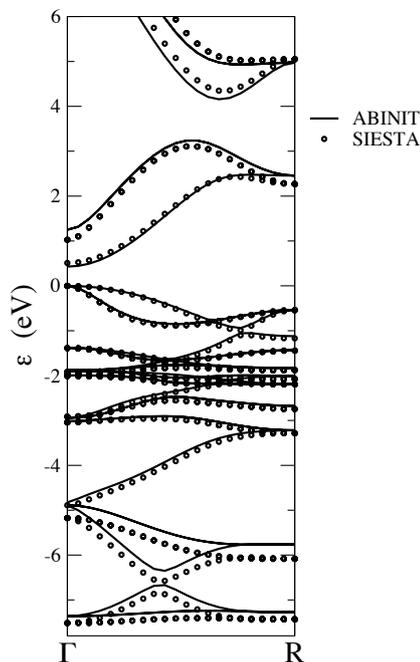
Figure 12.10: Comparison of band structure along Γ - R direction calculated with two different basis sets. ABINIT is a plane-wave code (full curve), SIESTA is a LCAO code (open circles).

is problematic from different points of view. Maybe their basis set or their convergence parameters were not sufficient (their calculation was made before 1988).

The band structure issue will be resumed in the next chapter concerning *GW* calculations, as they will provide quasiparticle band structure, that one is allowed to compare directly with experiment.

12.4 DFT charge density

DFT in principle yields the exact charge density. Of course, one used an approximation either LDA or GGA for the exchange-correlation potential, but it is still interesting to analyse the fondamental observable of DFT!

Figure 12.11 provides the plot of an isodensity surface. The shape of the surface is almost spherical around each atom, which seems to show that the Cu–O bonding is very ionic. An ionic bonding makes shells completely full, and therefore yields spherical charge density. Here, one can remark that the shape is not fully spherical, but a bit elongated along the Cu–O bonds.

In fact, to measure more precisely the ionicity of oxygen and copper, one can turn to the Bader analysis technique [133], implemented in ABINIT package. Within LDA, the charge affected at copper is 0.521 *e* and the
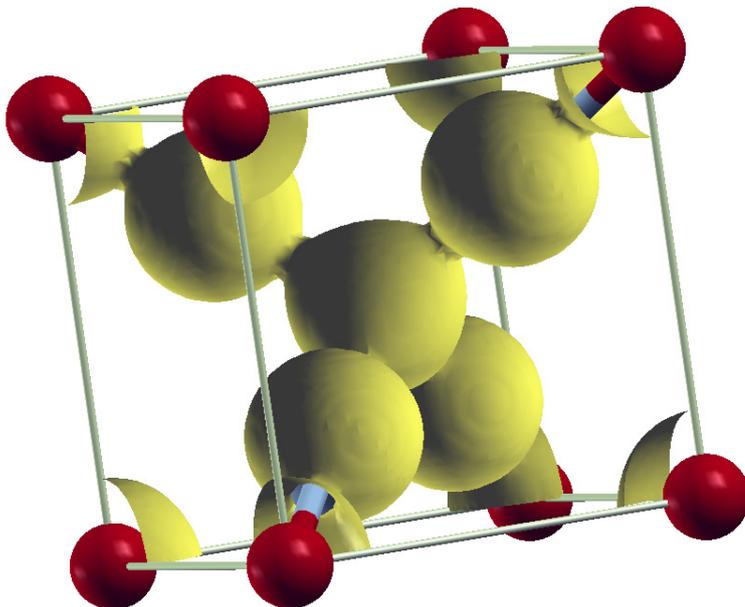
Figure 12.11: Isodensity surface $\rho = 0.1\,e\,\mathrm{a.u.}^{-3}$. The oxygen atoms form the body centered sublattice. The other atoms are the copper ones.

charge on oxygen is -1.042 e. These values are very close to the ones (+0.51 e for Cu, -1.03 e for O) of reference [107]. This proves that the simple ionic model Cu$^+$ and O^{2-} is rather far from the LDA values. Instead, Zuo *et al.* [103] measured a charge +1.01 e on copper and -2.02 e on oxygen. The LDA values are in clear contradiction with the measurements of Zuo. The statement is not modified by the use of GGA instead of LDA [107].

Let us now turn to the analysis of $\rho(\mathbf{r})$. Figure 12.12 depicts the charge density along two lines: the diagonal of a face of the cubic cell and the large diagonal of the cubic cell. The middle of direction (1 1 0) is precisely the center of a tetrahedron of four copper atoms, the point where Zuo *et al.* measured the debated local maximum of the charge density [103, 104], which was a piece of evidence of direct Cu–Cu bondings, according to those authors. On the contrary, at that point I find, within LDA, a minimum of the charge density with a value of $0.011\,e\,\mathrm{a.u.}^{-3}$, i.e. $0.077\,e\,\mathring{\mathrm{A}}^{-3}$. This should be compared to the measurement of Zuo *et al.*: they found a $0.2\,e\,\mathring{\mathrm{A}}^{-3}$ difference between the solid on the superposition ions Cu$^+$, O^{2-}. The direction (1 1 1) shows the density along the Cu–O bondings. There is almost no density in the empty site between the two oxygen atoms on the right
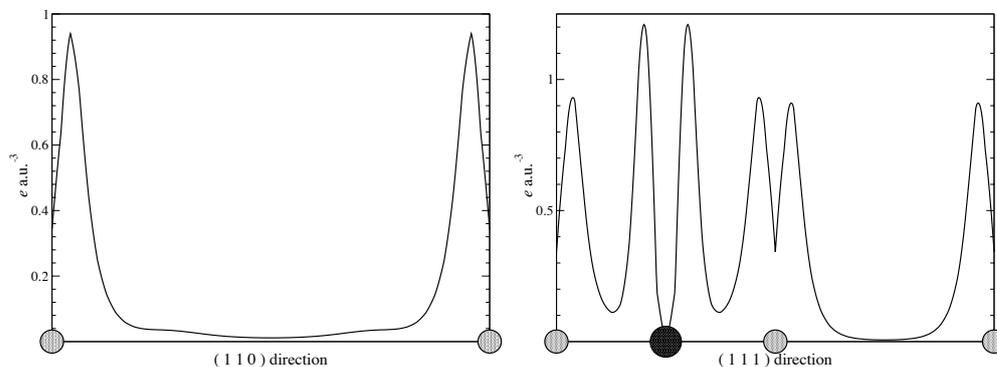
Figure 12.12: LDA density cuts in ea.u.$^{-3}$ along (1 1 0) and (1 1 1) directions. The small light grey circles represent oxygen atoms, the large dark circle represents a copper atom.
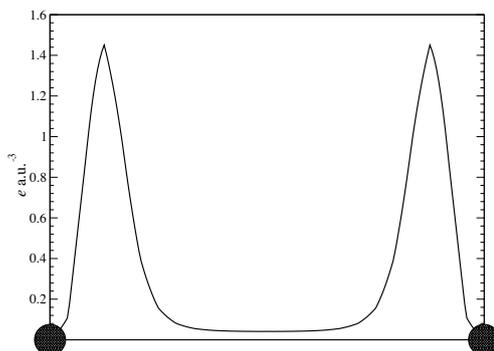

Figure 12.13: LDA density cuts in ea.u.$^{-3}$ along a line between two neighboring copper atoms. The large dark circles represent copper atoms.

hand side. (Note that the very small density present on the atoms is due to the removal of core electrons in the pseudopotential scheme.)

Going on with the analysis of the charge density, one finds, according to figure 12.13, that the density in the interstitial region is rather high in between copper atoms. It is equal to $0.28\,e\,\text{Å}^{-3}$ in the middle of the Cu–Cu line. A value of $0.2\,e\,\text{Å}^{-3}$ was already considered as a high one by experimentalists. Therefore, the LDA charge density shows clearly the presence of delocalized density around Cu atoms, not in the middle of Cu$_4$ tetrahedron as measured by Zuo and co-workers, but rather along the edges of the tetrahedron. Density along that Cu–Cu line can be understood by the presence of a neighboring oxygen atom. Instead of direct Cu–Cu bonding, the LDA result suggests reasonably bondings via the triangle Cu–O–Cu. For copper atoms, with no neighboring oxygen, there is no delocalized density.

The conclusions of Zuo and co-authors are based on indirect statements.

They have fit several parameters as the charge, and the following terms in a multipolar expansion in order to recover the measurements of their combined electron and X-ray diffraction experiment. Maybe there is no unicity of the set of fitted parameters. and allowing noticeable charge density in the earlier mentioned triangle could also explain the experimental data. From these debated measurements, one can not draw a safe conclusion concerning the reliability of the LDA predictions.

Chapter 13

Standard GW study of Cu_2O

As usual, the interpretation of Kohn-Sham eigenvalues as physical band structure yielded, in the previous chapter, valence bands that are rather correct, and band gaps that are largely underestimated. To properly describe the band gaps in theory and in practice, one has to turn to the Green's function approach, in particular, to the successful GW approximation.

But immediately, a problematic issue appears: the semicore states, whose effect on the band gap have been evaluated to be $0.1\,\mathrm{eV}$ in LDA, have a drastic effect on the Cud energies within GW approximation.

13.1 Importance of semi-core states for the GW Self-energy

Following the approach of the previous chapter, I performed both calculations with and without the semicore states considered as valence. The approximation of considering the semicore states inside the pseudopotential is even cruder than for an LDA calculation: the action of the semicore on the valence is evaluated implicitly (via the pseudopotential) as an LDA interaction. In an LDA calculation, this remains compliant, but in a GW one, the valence-valence interaction is treated with GW interaction and the core-valence is treated with LDA. This is known to give some problems in cadmium [114] and also in copper [115].

Table 13.1 shows an analysis of the difference between GW calculations with and without the semicore states in valence. It shows that the last valence and the first conduction bands, which have a large Cud character, experience a strong shift upward of about $3\,\mathrm{eV}$, when the semicore states are treated in the core. The shift is so large that the top valence bands end up above the second conduction band. Fortunately, this spurious shift is not present anylonger in the calculation with explicit semicore states in valence. A conclusion can be immediately drawn: the pseudopotential accounts very poorly for the action of the semicore states on the localized valence states.

Let us further analyse what prevents v_{xc} from giving a correct evaluation of the semicore-valence interaction. In order to have a reliable pseudopotential for a GW calculation, two conditions have to be fulfilled:

- the GW corrections (i.e. $\Sigma - v_{xc}$) arising from the valence states has to be equivalent with and without the semicore.

- the GW corrections arising from the semicore and acting on the valence states have to be zero or at least constant for all states.

The case of Cu_2O satisfies none of the previous conditions.

The third column of table 13.1 gives the difference between Σ and v_{xc} for the calculation without the semicore. This has to be compared with the GW corrections arising from the valence states in the calculation with the explicit semicore displayed in the sixth column ($\Sigma^{\mathrm{val}} - v_{xc}^{\mathrm{val}}$). One can see that GW corrections are of the same order of magnitude in both calculations, but there is a noticeable discrepancy. This discrepancy is further not constant among states. This finally yields an error of maximum $0.8\,\mathrm{eV}$, for the energy differences in the calculation without semicore states with respect to the more complete calculation.

Now, consider how bad or how good is v_{xc} to represent the effect of the semicore on the valence states. First note the correlation between semicore states and valence states Σ^{sc} vanishes, as shown by the seventh column of the table. This is expected, since the correlation part of the self-energy is a decreasing function of energy differences. The energetic separation between the semicore states and the valence is rather large ($\sim 70\,\mathrm{eV}$). As a consequence, one can consider for Σ just the exchange operator. The difference between the effect of the semicore on the valence states within Fock approximation and LDA is provided by the last column. If the LDA exchange were good, this difference would be vanishing or maybe constant. On the contrary, one can note that this value is really state dependent: the localized states as the last valence band and the first conduction band show

Table 13.1: Band structure in eV at Γ at the LDA equilibrium lattice parameter within LDA and GW, with and without semicore. The origin of the energies has been set to the LDA top valence band. Selected components of the Hamiltonian are also provided.

	ϵ^{LDA}	ϵ^{GW}	$\Sigma - v_{xc}$	ϵ^{LDA}	ϵ^{GW}	$\Sigma^{\mathrm{val}} - v_{xc}^{\mathrm{val}}$	Σ_c^{sc}	$\Sigma_x^{\mathrm{sc}} - v_{xc}^{\mathrm{sc}}$
		without semicore				with semicore		
Γ'_{25}: last VB	0.00	3.08	4.09	0.00	0.06	5.56	0.01	5.48
Γ_1: 1$^{\mathrm{st}}$ CB	0.46	4.32	5.07	0.57	1.46	6.31	0.01	5.11
Γ'_{12}: 2$^{\mathrm{nd}}$ CB	1.22	1.45	0.29	1.20	1.61	0.96	0.00	0.47

a large value (more than $5\,\mathrm{eV}$), and quite delocalized states as the second conduction band (that is mainly of Cu $4p$ nature) does not experience a large error.

The conclusion drawn for Cu$_2$O is totally compliant with earlier works of Rohlfing [114] and Marini [115] for other materials: the effect of the semicore states has to be taken into account fully at a *GW* level. To be precise, only the bare exchange part of the self-energy is in fact necessary. The Fock operator is sensitive to the density-matrix, not to the energies. Therefore the *spatial overlap between the semicore states and the valence states* (as displayed in figure 12.1) is *the* relevant criterium here to assess or not the core-valence partition. All further *GW* calculations will treat the semicore states as valence ones.

13.2   *GW* quasiparticle band structure

Once the semicore issue is fixed, one can provide *GW* band structure of Cu$_2$O according to the standard method explained in chapter 5. Remember that the *GW* method is expected to give band gaps in very good agreement with experiment, except in highly correlated materials, where other methods, in particular the Dynamical Mean-Field Theory [134], are more appropriate. Selected elements of the band structure of Cu$_2$O are provided in table 13.2. All calculations are made with a $4 \times 4 \times 4$ regular grid to represent the **k**-point integrations. The grid is either shifted or not in order to include high-symmetry points or not. The parameters used to achieve convergence of the screening calculation are 150 bands for the transition in χ_0, 5887 plane-waves to represent the wavefunctions ϕ_i and 485 plane-waves to represent the $\varepsilon^{-1}_{\mathbf{GG'}}$ matrix. The parameters used to achieve convergence of the self-energy calculation are 200 bands for the band sum in the Green's

Table 13.2: *GW* band structure features of Cu$_2$O, starting either from an LDA or GGA calculation, and compared to the experimental values. The band width of Cud, Op, the location of the dispersive Γ_{1v} band, the quasiparticle band gap ($\Gamma'_{25v} \rightarrow \Gamma_{1c}$), and the optical threshold ($\Gamma'_{25v} \rightarrow \Gamma'_{12c}$) are given.

Starting point	LDA	LDA	GGA	GGA	Expt.
Correction	–	*GW*	–	*GW*	
O $2p$ band width	2.44	2.35	2.37	2.37	2.4
$\Gamma'_{25v} \rightarrow \Gamma_{1v}$	-4.87	-5.07	-4.80	-5.52	–
Cud band width	3.44	3.57	3.39	3.79	3.8
$\Gamma'_{25v} \rightarrow \Gamma_{1c}$	0.55	1.34	0.61	1.30	2.17
$\Gamma'_{25v} \rightarrow \Gamma'_{12c}$	1.23	1.51	1.28	1.00	2.55

function, 12797 plane-waves for the wavefunctions, 12797 plane-waves for the bare exchange operator, and 485 plane-waves for the correlation part.

Concerning the band gaps, GW corrections are for sure an improvement over the LDA result. But, with $1.34\,\mathrm{eV}$, it remains far from the experimental value of $2.17\,\mathrm{eV}$. A similar statement holds for the optical threshold ($\Gamma'_{25v} \to \Gamma'_{12c}$). Such a discrepancy between experiment and GW band structure is not common. Concerning the band width, the GW corrections do not change them much. They were in pretty good agreement with experiment at the LDA level, and the GW calculation confirms this matter of facts. Concerning the dispersive Γ_{1v} band that closes the separation between O $2p$ and Cu $3d$, its position (line $\Gamma'_{25v} \to \Gamma_{1v}$ of the table) moved of only $0.2\,\mathrm{eV}$ from LDA to LDA+GW. GW calculations do assess the LDA calculations: there is a state Γ_{1v} according to state-of-the-art theoretical calculations.

A simple attempt to improve the accuracy of the calculation could be to initiate the GW step with a GGA calculation. Although the LDA and GGA band structures agree pretty well, it has been noticed in some selected case that the exchange-correlation potential can have a large effect on the wavefunctions [135]. Table 13.2 also gives GW band structure elements starting from GGA. One can notice the very good agreement for the $\Gamma'_{25v} \to \Gamma_{1c}$ between the LDA+GW and the GGA+GW calculations. Unfortunately, the GGA+GW approach gives a negative correction for the optical threshold. The "corrected" result is even farther from the experimental value than the simple Kohn-Sham value. The band gap is wrongly predicted to be the $\Gamma'_{25v} \to \Gamma'_{12c}$ transition by GGA+GW, whereas they are experimental evidence that the band gap is a dipole forbidden transition (in contrary with $\Gamma'_{25v} \to \Gamma'_{12c}$). In conclusion, the GW calculation starting from GGA is even worse than starting from LDA.

13.3   Failure of GW approximation or failure of additional assumptions?

The drastic failure of GW approximation with Cu_2O is not something one is used to. Cu_2O is not a highly correlated material, where the photoemission finds many satellite structures, like nickel. Here, the GW approximation was thought to work it out. That is why a natural question arises: what fails with the calculation? Is it a failure of the GW approximation itself or is it one of the many approximations or assumptions used in a "standard" GW calculation, as described in chapter 5.

This section intends to check carefully one by one all the approximations used in the GW recipe: use of pseudowavefunctions for ϕ_i, use of a plasmon-pole model for ε^{-1}, $\Sigma(\omega)$ considered as a first-order perturbation over h^{LDA} and use of LDA inputs...
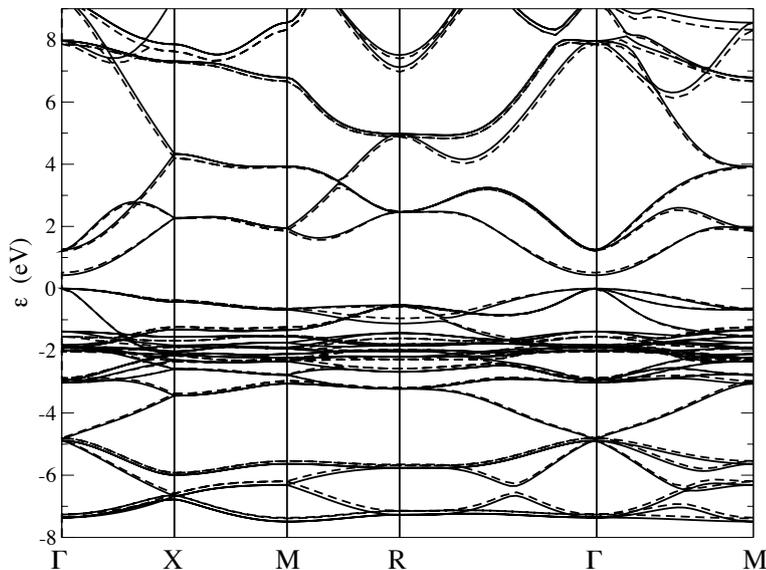
Figure 13.1: Comparison of LDA band structures using either a plane-wave plus pseudopotential scheme (solid line, this work) or the PAW method (dashed line, B. Arnaud [130].

13.3.1   Reliability of pseudo eigenvalues and eigenvectors

The pseudopotential method has been devised for being used in a DFT scheme, where the same approximation is used for the core and for the valence, and where the core region is not important for the properties under study. *GW* calculations obviously contradict the first requirement. But for Cu$_2$O, the second requirement might be not fulfilled neither. It is right that *GW* calculations based on the LDA pseudopotential have been very successful for semiconductors, where the electrons are largely delocalized. However in Cu$_2$O, the band gap consists of localized states (mainly of Cu*d* nature), therefore, next to the core region.

The reliability of the band structure in the pseudopotential plus plane-waves method at the LDA level has already been checked against the localized orbital method of the SIESTA package (see figure 12.10 in the previous chapter). B. Arnaud [130] has collaborated with me and provided an LDA band structure of Cu$_2$O using the projector augmented wave method (PAW) [136]. PAW is an all-electron method, where the true wavefunctions are constructed as plane-waves, plus projectors in the core region. The comparison with the plane-wave band structure is displayed in figure 13.1. The agreement is once more convincing. Regarding the two comparisons with localized orbitals and PAW, one can be really confident on the LDA band structure.
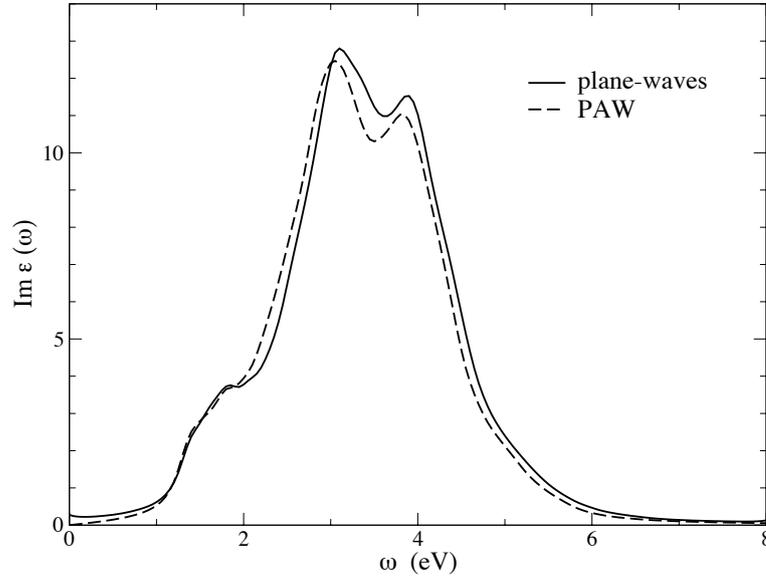
Figure 13.2: Imaginary part of the dielectric function within RPA, from
two independent calculations: solid line, this work using a plane-wave basis
set and pseudopotentials and dashed line, from B. Arnaud [130] using the
PAW method. Both calculations have used the same parameters: a $8 \times 8 \times 8$
slightly shifted **k**-point grid, 33 plane-waves for the $\epsilon_{\mathbf{GG'}}$ matrix, and 1935
plane-waves for the wavefunctions. 17 valence bands and 3 conduction
bands have been used. The imaginary $i\eta$ parameter has been set to $0.14\,\mathrm{eV}$.

But, what about the confidence on the wavefunctions? Are the pseu-
dowavefunctions well-suited to be used in a GW calculation? Unfortunately,
to my knowledge, there does not exist any all-electron GW calculation on
Cu_2O. To try answer this, B. Arnaud performed to my request an RPA
calculation of the dielectric function, shown in figure 13.2. As explained in
chapter 5, the same kind of matrix elements $\tilde{\rho}_{\mathbf{k}_i ij}(\mathbf{q} + \mathbf{G})$ are needed in a
χ_0 calculation and in a GW calculation. The solid curve used $\tilde{\rho}_{\mathbf{k}_i ij}(\mathbf{q} + \mathbf{G})$
constructed from pseudowavefunctions, instead the dashed curve (PAW)
used the *true all-electron wavefunctions* to build the $\tilde{\rho}_{\mathbf{k}_i ij}(\mathbf{q} + \mathbf{G})$. As one
can note in the figure, the two curves agree very well, better than the error
typically induced by the pseudopotential.

Finally, both wavefunctions and energies of the pseudopotential are
seemingly reliable. Of course, it would have been better to compare GW
calculations with an all-electron method, but the agreement of the response
function in figure 13.2 is already a convincing clue, that the use of pseudo
wavefunctions is justified to calculate the $\tilde{\rho}_{\mathbf{k}_i ij}(\mathbf{q} + \mathbf{G})$, and therefore, the
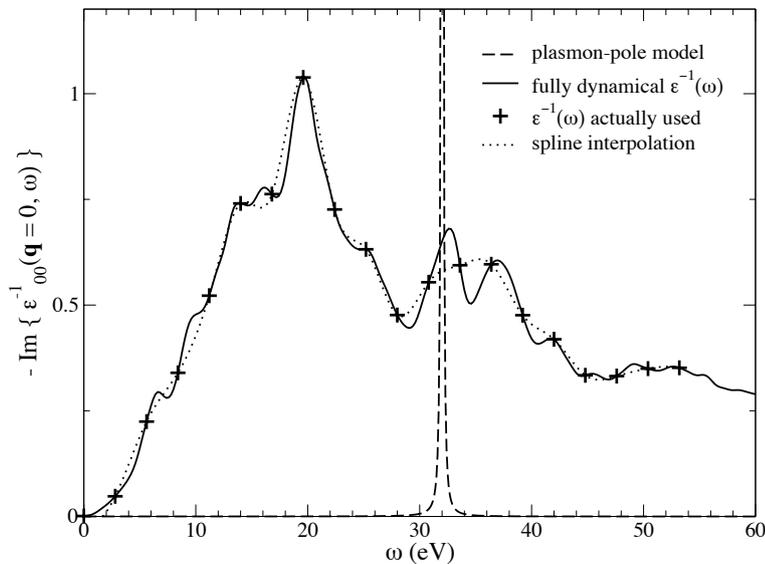self-energy.

Figure 13.3: Different assumptions concerning the loss function $-\mathrm{Im}\,\varepsilon^{-1}(\omega)$ of Cu$_2$O for vanishing **q**. The dashed line is the plasmon-pole model. The solid line that shows the fully dynamical loss function is given as a reference but never used in a *GW* calculation. The frequencies where ε^{-1} is actually computed in a *GW* calculation without plasmon-pole model are given by the plus signs. The dotted line shows the performance of the spline interpolation scheme used in the code to evaluate ε^{-1} in between the calculated frequencies.

13.3.2   Reliability of the plasmon-pole model

Looking at the loss function of Cu$_2$O in figure 13.3, that I have calculated, one can doubt that the plasmon-pole model gives an accurate description of the dynamical behavior of $-\mathrm{Im}\,\varepsilon^{-1}$. The full RPA loss function is very badly represented by the single δ peak of the plasmon-pole model. To check the reliability of the model, I ran several calculations using the algorithms implemented in chapter 7.

In the left panel of figure 13.4, the spectral function of the last valence band and of the first conduction band at Γ are displayed. The spectral function method of chapter 7 was applied with two different values for η parameter in the denominator of χ_0: a large value $\eta = 2.3\,\mathrm{eV}$ and a small value $\eta = 0.25\,\mathrm{eV}$. As already stated for silicon, the spectral function is largely dependent to this parameter. First the position of the peak of the first conduction band changes by $1.3\,\mathrm{eV}$ with the two η. Second the width of the quasiparticle peak (i.e. the inverse of the lifetime) increases much with large η. But, the overall shape of the spectral function seems rather constant, in particular the feet of the spectral function are present below
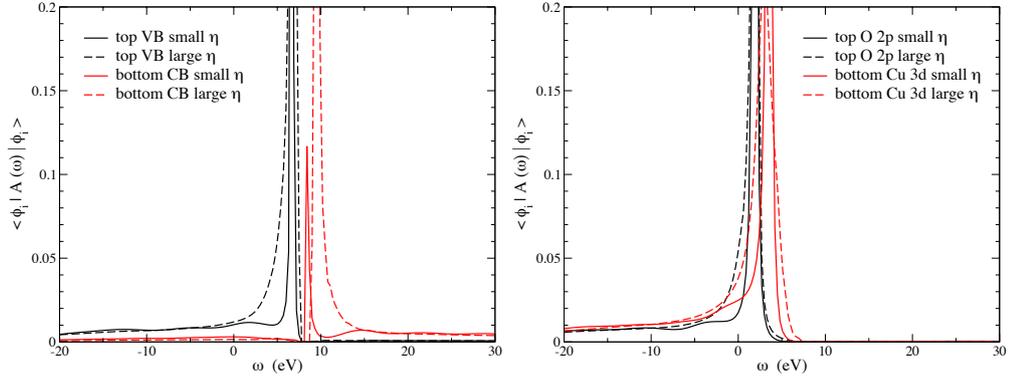
Figure 13.4: Spectral functions for different states of Cu$_2$O using the spectral function method of chapter 7 with different values of parameter η. The left panel shows states in the vicinity of the band gap and the right panel in the vicinity of the Op Cud gap.

the quasiparticle peak for valence states, and above the quasiparticle peak for conduction states. It is also interesting to turn to deeper valence state. In the right panel of figure 13.4, the spectral functions of the upper Op state and the bottom Cud at R point are displayed. They were calculated under the same conditions as the previous spectral functions. Same conclusions concerning the position and the width of the quasiparticle peaks can be drawn. Even for small η, the peaks are wider here, due to a smaller lifetime. The overall shape, in particular the feet, is not affected by the instability with respect to η.

In order to get precise quasiparticle energies, I use the contour integral method of chapter 7. The corresponding results are provided in table 13.3. The frequencies used to sample the dynamical behavior of ε^{-1} are the 20 regularly spaced frequencies displayed with crosses in figure 13.3 for the real axis plus 10 exponentially spaced frequencies ranging from 0 eV to 125 eV

Table 13.3: LDA and GW band structure features of Cu$_2$O using or not a plasmon-pole model. The zero of energies is taken at the LDA top valence band.

Band	LDA	plasmon-pole model	contour integration
Γ_{1v}	-4.871	-5.073	-4.634
top O $2p$	-4.839	-4.924	-4.803
bottom Cu $3d$	-3.442	-3.335	-3.161
Γ'_{25}	0.000	0.059	0.051
Γ_{1c}	0.545	1.438	1.400
Γ'_{12}	1.228	1.637	1.791

for the imaginary axis. Here the agreement between calculations with and without plasmon-pole model is impressive in the band gap region. They coincide better than 0.05 eV in absolute energies. The differences increase as one goes farther from the Fermi level, but remains less than 0.40 eV for all bands. For instance, the order of the Γ_{1v} and of the top O $2p$ are exchanged in the calculation with no plasmon-pole model, but it is still very far from explaining the discrepancy between calculated band structures and observed photoemission spectra.

One can conclude that the plasmon-pole model is accurate in the Fermi level region, and reasonable farther. The change induced by the use of the full ε^{-1} is orders of magnitude smaller than the change needed to explain the failure of the standard *GW* approach.

13.3.3   Reliability of first-order perturbation technique

As explained in chapter 5, a first-order perturbation technique via equation 5.15 is usually used with success in order to only get the *GW* band structure, and not the wavefunctions. This approximation is very convenient as it allows one to calculate one single expectation value of the self-energy $\langle\phi_{\mathbf{k}i}|\Sigma|\phi_{\mathbf{k}i}\rangle$, instead of a full matrix $\langle\phi_{\mathbf{k}i}|\Sigma|\phi_{\mathbf{k}j}\rangle$ and then a diagonalization.

One can of course get rid of the first-order perturbation theory, and fully calculate the Σ matrix, to check the accuracy of the assumption. This will be computationally more demanding, but conceptually not a problem. I modified the existing *GW* implementation in the ABINIT package in order to calculate not only the diagonal term, but also the full Σ matrix.

The reliability of the first-order perturbation will be demonstrated for the band gap at Γ in table 13.4. The Σ matrix of the full *GW* calculation has been represented on the LDA states from the O $2s$ to the 36$^{\text{th}}$ conduction band (i.e. 64 states). The calculation of Σ at the most highly symmetric point Γ was simplified by the numerous vanishing terms $\langle\phi_{\Gamma i}|\Sigma|\phi_{\Gamma j}\rangle$ due to symmetry selection rules. The Σ matrix has been evaluated at the frequency given by a first perturbative *GW*:

$$\Sigma_{\Gamma ij} = \langle\phi_{\Gamma i}|\Sigma(\epsilon_{\Gamma l}^{\text{pert}\,GW})|\phi_{\Gamma j}\rangle. \tag{13.1}$$

and then diagonalize to obtain the $\epsilon_{\Gamma l}^{\text{full}\,GW}$. The first column displays the *GW* energy using just the diagonal element $h_{0\,\Gamma ii}+\Sigma_{\Gamma ii}$, whereas the second column is the result of the full diagonalization of $h_0 + \Sigma$ (h_0 is the Hartree Hamiltonian). The results of the table confirm with no doubt, that the first-order perturbation correctly evaluates the *GW* band structure. The position of the bands around the band gap has moved by less than 0.01 eV when changing the method.

13.3.4   Reliability of LDA starting point

The only remaining possibility for the failure of the technical approximations used in the GW scheme is a failure of the LDA wavefunctions. As introduced in chapter 5, the LDA and GW wavefunctions are assumed to be the same from the beginning to the end of the calculation. This has been assessed by Hybertsen and Louie [70], who claimed an overlap of 99.9 % between LDA and GW wavefunctions for silicon. But for Cu_2O, for d electrons, there is no piece of evidence that this statement remains valid. Maybe the LDA wavefunctions do not have the correct character... Maybe the LDA wavefunctions are too delocalized... Maybe the LDA density does not give the correct charge on the ions...

The previous section showed nevertheless that the diagonalization and the perturbative GW yield identical results. This is a clue in the direction to the justification of the use of $\phi^{\mathrm{LDA}} \approx \phi^{GW}$. But, a change in the wavefunctions at a **k**-point where the selection rules are not so important than in Γ, can induce a change at Γ point via the density (therefore in the Hartree potential), via the density matrix (therefore in the Fock operator), and also via the screening (therefore in the correlation part).

To get rid of the uncertainty concerning the LDA starting point, one has to use an other self-consistent scheme to initiate the GW calculation. For instance, one can try to apply the approximations for the self-energy described in chapter 8. This is the topic of the next chapter.

Table 13.4: GW band structure using or not the first-order perturbation approach. (calculations done at the LDA equilibrium lattice parameter).

Band	perturbative GW	full GW
Γ'_{25}	8.898	8.894
Γ_{1c}	10.455	10.463
Γ'_{12}	10.213	10.212

Chapter 14

Quasiparticle wavefunctions of Cu₂O

As stated in the previous chapter, the only ingredients one can doubt about in a GW calculation on Cu_2O are the starting LDA wavefunctions, hence the starting LDA density also. The idea of the present chapter is to get rid of the possibly unreliable LDA inputs by performing a self-consistent calculation that would erase the influence of the starting point. The logical way to go beyond LDA eigenvalues and eigenvectors is to implement the MBPT approximations described in chapter 8.

14.1 Hartree-Fock wavefunctions

Self-consistent Hartree-Fock calculations on Cu_2O are presented here just as a test case. According to existing Hartree-Fock results [18, 24], the band structure of Cu_2O is badly predicted, with a huge band gap, and no true separation between Cu $3d$ and O $2p$ states.

The present calculation is able to reproduce this matter of fact, even using a restricted LDA wavefunction basis set. If the HF Hamiltonian were considered to differ only to first-order perturbation with the LDA Hamiltonian, the evaluated band gap value would have been 8.84 eV. This should be compared with the fully self-consistent HF calculation performed using 66 LDA bands to span the wavefunction space, which gives after convergence (5 iterations) a band gap of 9.96 eV. This last result is in pretty good agreement with the calculations presented in reference [24], that found a 9.84 eV band gap, and that were using a different basis set (gaussians). This shows that the wavefunction space spanned by only 66 LDA states is already flexible enough to allow the wavefunctions to relax from LDA to HF ones.

Moreover, when comparing figure 14.1 and references [18, 24], the agreement of the band structures is striking. The bottom of the Op states is located at about -9 eV, the top valence bands are dispersive, and the other
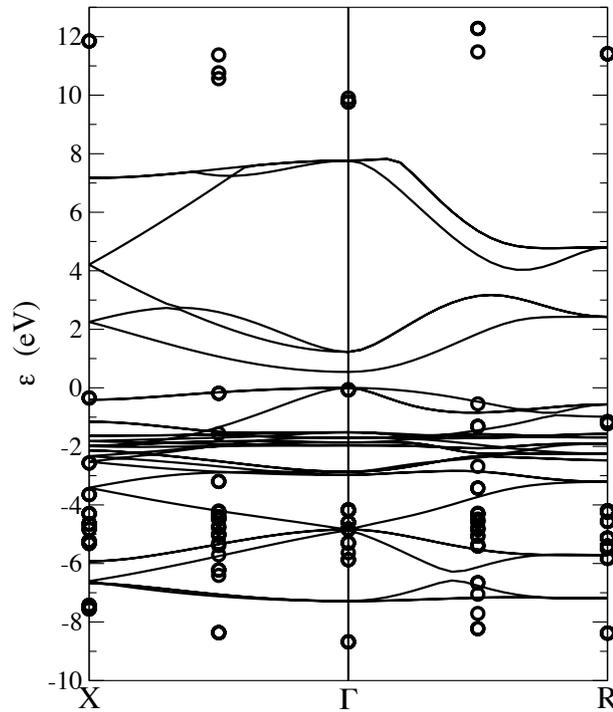
Figure 14.1: Band structure of Cu$_2$O within LDA (solid line) given as a reference and within HF (open circles) along X–Γ-R direction.

Cu $3d$ bands are not dispersive at all and mixed with the top of the Op states in the region 4-6 eV below the top valence. All these features are consistent with the two cited references. The only less clear point is the order of the three first conduction bands at Γ, which are found here very close and in the wrong order, in contrast with absorption experiments (one is dipole forbidden, the other not) and in contrast with the other HF calculations. Note that the two other HF references strongly disagree among them: the separation between these states is in one calculation about 1.5 eV and in the other one about 7 eV. The convergence of the conduction bands with a gaussian basis set may be problematic.

The conclusion of these calculation is clearly that the HF approximation is not reliable in Cu$_2$O for the band gaps (as usual) and also for the valence states. The calculated band structure has no hope to account for the integrated density of states measured by the photoemission experiments of Ghijsen *et al.* [126] (shown in figure 14.2). Besides this negative statement, this proves that even for complicated material like Cu$_2$O a restricted LDA wavefunction basis set is versatile enough to represent the HF wavefunctions, which strongly differ from the LDA wavefunctions. As COHSEX or *GW* wavefunctions are expected to be even closer to LDA ones, the restricted LDA basis set is hence fully justified.
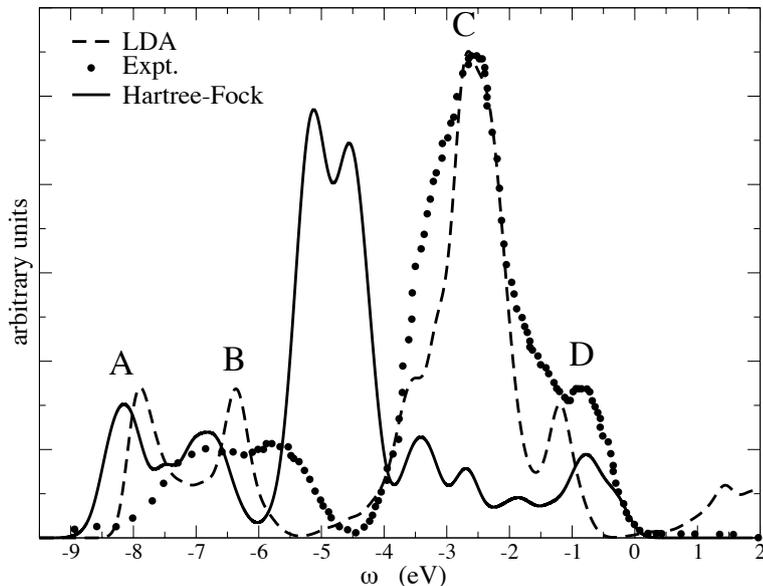
Figure 14.2: Density of states of Cu$_2$O within LDA (dashed line) given as a reference and within HF (solid line), compared to experimental photoemission data of reference [126] (large dots).

To achieve the described HF calculation, a technical point had to be addressed. In addition to the scheme described in chapter 8, I had to damp the oscillation of the electronic density in order to make the self-consistent calculation converge. In fact, the HF density is really different from the LDA density. The self-consistent procedure creates undamped oscillations in the density, which prevents the calculation from converging. As a consequence, an artificial damping has been added, by mixing the densities

$$\rho_{\text{in}}^{(n)} = \alpha \rho_{\text{out}}^{(n-1)} + (1 - \alpha)\rho_{\text{in}}^{(n-1)}, \tag{14.1}$$

where $\rho_{\text{in}}^{(n)}$ designates the density used as an input for the n-th step and $\rho_{\text{out}}^{(n-1)}$ stands for the output density of the $n - 1$-th step. A value of α lower than 0.6 has been found necessary to stabilize the calculation. It has also been checked that another value of α reaches the same self-consistent point. To show the large change of the electronic density, one considers the Hartree energy, whose value is 329.743 Ha in HF and 317.769 Ha within LDA.

14.2   Self-consistent GW

The present section is devoted to the evaluation of the self-consistent GW "wavefunctions" and energies using the model self-energy proposed by Faleev,

Kotani and van Schilfgaarde [90], using equation (8.1). This will be considered as the reference calculation to evaluate the quality of the further approximation, static COHSEX, in the last section of the chapter.

In order to make the scheme tractable for the complex material Cu_2O, the number of bands used in G has been dramatically reduced with respect to the standard GW number. Only 66 of them have been used instead of the 200 usually used. Here, GW corrections are not converged in absolute value: an almost rigid shift of 0.6-0.7 eV is experienced by the whole band structure. Fortunately, the energy differences are much better converged. Let us exemplify this with a standard GW calculation using either the reduced number of bands or the converged one. With only 66 bands, the band gap value is 1.31 eV, and the optical threshold is 1.54 eV; with 200 bands, the converged band gap is 1.34 eV, and the converged optical threshold is 1.51 eV. The eigenvalue differences are reliable up to about 0.05 eV, which is clearly sufficient with respect to the size of the effects one will be looking at.

In the method described in reference [90], the self-energy is at each step evaluated at the energy of the previous step and the Z factor of the quasiparticle equation

$$\epsilon_{\mathbf{k}_jj}^{(n)} = \epsilon_{\mathbf{k}_jj}^{(n-1)} + Z\langle\phi_{\mathbf{k}_jj}|\Sigma(\epsilon_{\mathbf{k}_jj}^{(n-1)}) - v_{xc}^{KS}|\phi_{\mathbf{k}_jj}\rangle \qquad (14.2)$$

is systematically set to 1. There is no quasiparticle renormalization in this model. This procedure gives after the first step larger GW corrections, since they are not reduced by the Z factor. For instance, the band gap is 1.51 eV, when the scheme is applied to the diagonal elements only, instead of 1.31 eV in a usual GW calculation that does include the Z factor. Consequently, as the band gap is noticeably larger, the effect of self-consistency is also slightly larger. All this makes that the scheme applied only on the diagonal (just the energies are updated, and not the wavefunctions) ends with a larger band gap than an energy self-consistent GW procedure that would include the Z factor. I have performed both calculations. The scheme of reference [90] gives a final band gap of 1.80 eV as shown in table 14.1, when applied using the energy update only. The energy only self-consistent GW scheme would give a band gap of 1.61 eV. One finally recovers more or less the 0.2 eV difference between a calculation with and without account for Z.

The procedure used seems to be rather stable. In fact, self-consistency for the diagonal scheme (update of the energies only) has been achieved starting from two very different starting points: either from the LDA energies (with a 0.54 eV band gap), or from the perturbative static COHSEX energies (with a 1.88 eV band gap). After 5 self-consistent iterations, the two calculations have ended to the *same eigenvalues* within 0.01 eV in absolute position. This clue of stability is important, as the unicity of the attractor in a self-consistent GW scheme is questioned and debated nowadays [137].
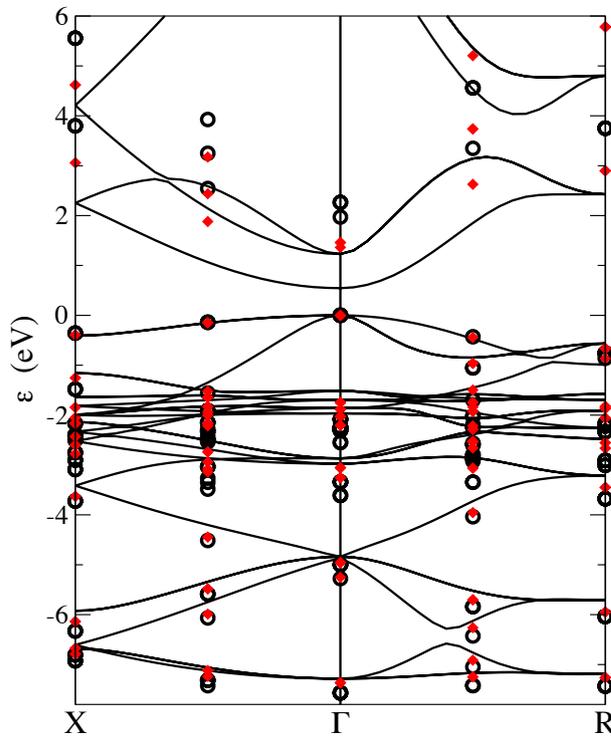
Figure 14.3: Band structure of Cu$_2$O within LDA (solid line) and one shoot *GW* (closed diamonds) given as a reference and within self-consistent *GW* (open circles) along X–Γ-R direction.

Concerning the band structure, the overall shape within self-consistent *GW* is given in figure 14.3. Self-consistency does not affect the shape of the band structure, just the band gap seems to have changed. Note in particular that the dispersive Γ_{1v} remains unchanged in between O $2p$ and Cu $3d$

Table 14.1: Band structure features within different approximations: standard *GW* using LDA inputs, model *GW* using self-consistent energies, model *GW* using self-consistent energies and wavefunctions, and experiment.

	$G_{\mathrm{LDA}}W_{\mathrm{LDA}}$	$GW[\epsilon_{GW}]$	$GW[\phi_{GW}\epsilon_{GW}]$	Expt.[a]
$\Gamma'_{25v} \rightarrow \Gamma_{1v}$	-5.07	-5.27	-5.28	–
top O $2p$	-4.86	-4.84	-5.00	$\sim$ -5.5
bottom Cu $3d$	-3.28	-3.07	-3.72	$\sim$ -3.8
$\Gamma'_{25v} \rightarrow \Gamma_{1c}$	1.34	1.80	1.97	2.17
$\Gamma'_{25v} \rightarrow \Gamma'_{12c}$	1.51	2.21	2.27	2.55

[a]References [1, 3, 126]

states. Some selected features are furthermore displayed in table 14.1. It shows the effect of respectively the update of the energies and of the update of the wavefunctions on the band structure. Some features like the dispersive band Γ_{1v} or the position of O $2p$ states are not sensitive to the self-consistency. On the contrary, the band gap and the Cud band width are noticeably affected by the change of the energies *and* of the wavefunctions. The largest improvement on the band gap is due to the energy self-consistency (0.5 eV opening), whereas the effect of the wavefunctions is smaller (0.2 eV opening), but still in the right direction. *The final band gap is in reasonable agreement with respect to experiment.* This correction was not obvious as the LDA starting point and the standard *GW* were so far away from the reality. The largest improvement on the Cu d band width is clearly due to the self-consistent wavefunctions. The use of the self-consistent *GW* energies reduced the band width, and at the opposite, the wavefunctions enlarged it by 0.7 eV in the right direction. The agreement for the Cud band width is finally rather good.

Table 14.2 allows one to elucidate the origin of the influence of the wavefunctions on the band structure. For the last valence bands Γ'_{25v} and the second conduction band Γ'_{12c}, the effect of the change of wavefunctions is rather small on the band structure (< 0.1 eV). Further, analysing the different contributions to ϵ_i shows that these states seem rather unsensitive to the change in the wavefunctions. On the contrary, the behavior of Γ_{1v} and Γ_{1c} states has to be pointed out. The overall effect of the modification of the wavefunctions is moderate (maximum 0.2 eV), but each single contribution experiences drastic changes. In particular, the change in the Hartree Hamiltonian (up to 0.7 eV!) is compensated by a change in the exchange operator expectation value (up to 1. eV!) in the opposite direction. The total effect remains bounded. It is further interesting to note

Table 14.2: Contribution to selected energies within model GW using self-consistent energies or using self-consistent energies and wavefunctions. The exhibited contributions to ϵ_i are the Hartree Hamiltonian $H_h = -\nabla^2/2 + v_{e-i} + v_h$, the exchange operator Σ_x, and the correlation part Σ_c

Approx.	band	H_h	Σ_x	Σ_c	ϵ_i
	Γ_{1v}	19.86	-22.00	5.14	3.00
	Γ'_{25v}	39.52	-38.03	6.77	8.27
$GW[\epsilon_{GW}]$	Γ_{1c}	38.76	-28.43	-0.26	10.07
	Γ'_{12c}	19.45	-6.59	-2.39	10.47
	Γ_{1v}	20.44	-22.69	5.26	3.00
	Γ'_{25v}	39.48	-37.81	6.62	8.28
$GW[\phi_{GW}\epsilon_{GW}]$	Γ_{1c}	38.22	-27.41	-0.56	10.25
	Γ'_{12c}	19.45	-6.47	-2.44	10.55

that these two wavefunctions do not change much (overlap $\sim 99.9\,\%$ with LDA wavefunctions), whereas the other wavefunctions change a bit more ($\sim 99.5\,\%$ overlap). The drastic change of the expectation values can only be explained by indirect causes. The two Γ_1 states seem more sensitive to the change of the other wavefunctions via the density for the Hartree potential, or via the density matrix for the exchange operator. It is therefore extremely important to update the Hartree potential in the self-consistent scheme, else the drastic changes in Σ_x would not have any counterpart...

Now, turning to the analysis of the wavefunctions themselves will show in particular that the GW self-energy reduces the hybridization between Op and Cud with respect to LDA. Changing the potential from LDA to self-consistent GW yields state-dependent effects. For instance, the wavefunctions of the two Γ_1 states (the dispersive band in between O $2p$ and Cu $3d$ states and the first conduction band) do not change within GW. Their overlap with the corresponding LDA states is respectively $99.91\,\%$ and $99.88\,\%$. The contrary is true for the Γ_{25}' states from the bottom of the O $2p$ and the top of the valence Cu $3d$, that are hybridization of atomic Op and Cud components. The hybridization level changes noticeably within GW. Looking at figure 14.4, one can note that the top valence bands gain much weight in the copper atoms' region, and that, on the contrary, the mainly Op bands lose some weight in these regions. The hybridization between O $2p$ and Cu $3d$ within GW is smaller than within LDA. On the contrary, the threefold degenerate top state within O $2p$ region (symmetry Γ_{15}) that was almost purely Op in LDA do remain identical within GW: the overlap is larger than $99.99\,\%$!

In the Cu $3d$ region, the number of states is huge and the energetic separation is very small. As a consequence, the mixing of states is large. For instance, at **k**-point (1/4, 1/4, 0), where the symmetry forbidden coupling elements are few, the overlap between the LDA and the GW wavefunctions is generally of the order of $95\,\%$ for the Cu $3d$ states. This is very low, as illustrated for a not degenerate state on the left panel of figure 14.5. The difference between LDA and GW approximation for one single wavefunctions is large. But, as the difference arises from mixing with the neighboring states, the sum over all Cu $3d$ wavefunctions remains almost unchanged (shown in the right panel of figure 14.5).

Finally, the electronic density is not changed much by replacing LDA by self-consistent GW. This can be measured by the change in the Hartree energy. Within LDA, it is equal to $317.769\,$Ha, whereas within GW, its value is $318.088\,$Ha. A change of $0.1\,\%$ is very small compared to the change within HF approximation ($3.8\,\%$). This shows in particular that there is no hope to recover, thanks to the self-consistent GW, the debated experimental result of Zuo *et al.* [103] concerning the charge density in the center of the Cu$_4$ tetrahedra mentioned in chapter 11.

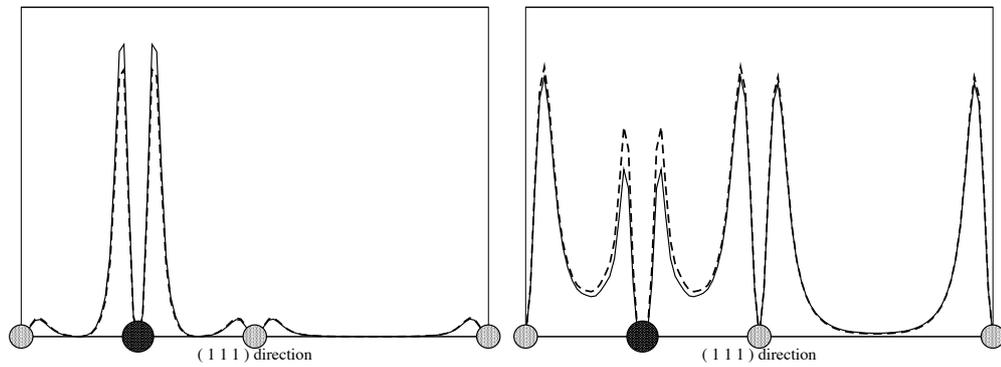To sum up these results, besides the particular issue of Cu$_2$O, where the

Figure 14.4: Sum of the squared modulus of the top three valence band wavefunctions (left panel) and bottom three valence bands wavefunctions in the Op region (right panel) at Γ point in Cu$_2$O along (1 1 1) direction. The small light grey circles symbolize the oxygen atoms. The large dark grey circle symbolizes the copper atom. The wavefunctions within LDA are displayed with the dashed line, the wavefunctions within GW with the solid line.
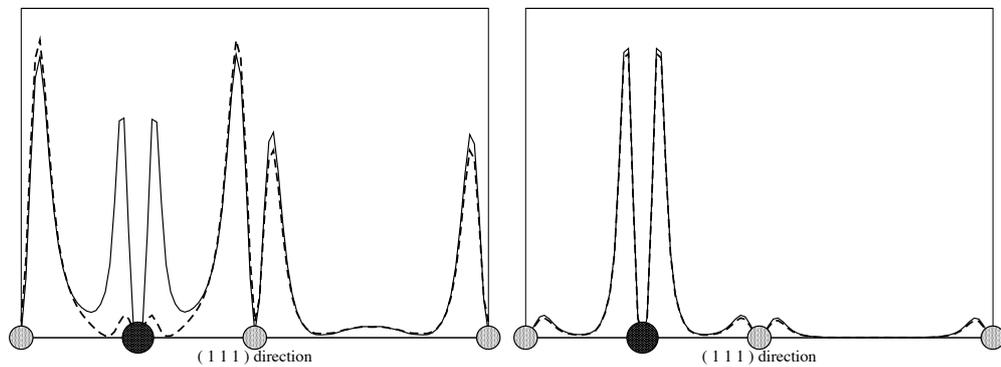

Figure 14.5: Squared modulus of the valence band number 30 wavefunction (Cu $3d$ region) (left panel) and sum of all squared moduli of Cu $3d$ valence wavefunctions (right panel) at **k**-point (1/4, 1/4, 0) in Cu$_2$O along (1 1 1) direction. The small light grey circles symbolize the oxygen atoms. The large dark grey circle symbolizes the copper atom. The wavefunctions within LDA are displayed with the dashed line, the wavefunctions within GW with the solid line.

self-consistent GW improved the agreement with experimental data (this topic will be continued in the next chapter, where the theoretical data will be compared to new angle-resolved photoemission experiments), I would like to stress on conclusions of general interest, which can be drawn from the previous calculations on Cu$_2$O:

- the *GW* self-energy reduces the hybridization between O*p* and Cu*d*,

- the model self-consistent *GW* has a unique attractor (at least when energies only are updated),

- the effect of the wavefunctions on the band structure is the sum of large compensating contributions (from Hartree and exchange parts),

- some states can remain unchanged, but yet be sensitive to the changes in the other wavefunctions at other **k**-point (via the nonlocal operators).

14.3   Self-consistent COHSEX

Following the spirit of chapter 8, it is worthwhile to evaluate the COHSEX wavefunctions and consider whether they are good approximation to the true *GW* wavefunctions.

Figure 14.6 compares the quality of the wavefunctions within different approximations, LDA, static COHSEX, and model *GW* for the critical states. As usual, the wavefunctions are evaluated at a non-symmetric **k**-point in order to allow more mixing. Looking at the O*p* states and the three top valence states, the COHSEX and the *GW* wavefunctions seem to agree rather well. The COHSEX approximation accounts pretty well for the change in O 2*p*-Cu 3*d* hybridization with respect to the LDA starting point. However, when looking at the first conduction band, COHSEX overestimates the change of the wavefunctions with respect to LDA. The general conclusion concerning the wavefunctions is that COHSEX "corrects" the LDA wavefunctions always in the good direction (thinking as *GW* as the reference), generally agrees well with *GW*, but shows sometimes some overestimation of the effects.

Concerning the band structure, table 14.3 shows that self-consistent COHSEX gives too large band gaps, as one was expecting following the examples of silicon and argon of chapter 8. When a further *GW* step is applied on top of the self-consistent COHSEX, the obtained band structure is really reasonable. The valence states agree pretty well with the model *GW* ones, and the band gaps are slightly overestimated ($\sim +10\,\%$), whereas self-consistent *GW* ones were slightly underestimated ($\sim -10\,\%$).

As a conclusion, self-consistent COHSEX is a rather accurate approximation to self-consistent *GW*. When one considers that the COHSEX calculations are much faster than the *GW* ones (due to the absence of the empty states in the COHSEX formula), the use of the simple COHSEX approximation as an evaluation of the *GW* wavefunctions seems justified. Alternatively, COHSEX approximation can be thought as a first cheaper test to the reliability of the LDA eigenfunctions and it can answer the question whether a further cumbersome self-consistent *GW* should be performed.
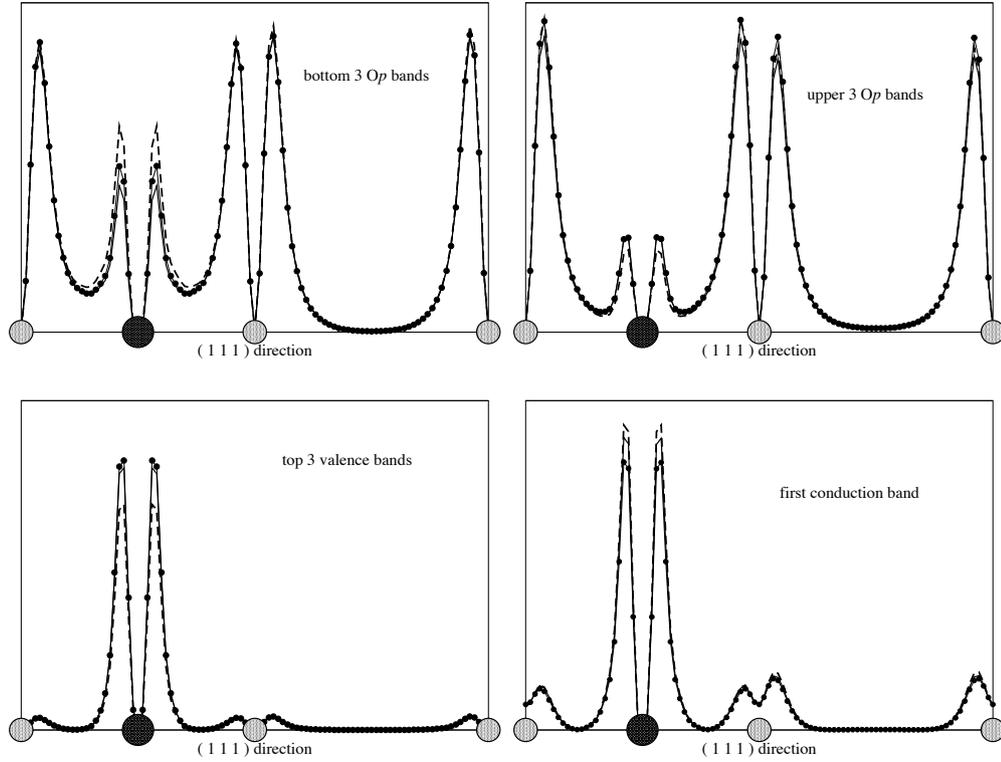
Figure 14.6: Sum of squared modulus of group of states at **k**-point $(1/4, 1/4, 0)$ in Cu$_2$O along $(1\,1\,1)$ direction. The small light grey circles symbolize the oxygen atoms. The large dark grey circle symbolizes the copper atom. The wavefunctions within LDA are displayed with the dashed line, the wavefunctions within GW with the solid line, the wavefunctions within static COHSEX with the closed circles and the thin line. The upper left panel shows the bottom three valence O $2p$ states, the upper right panel shows the upper three valence O $2p$ states, the bottom left panel shows the three last valence states, and the bottom right panel shows the first conduction state.

Table 14.3: Band structure features within different approximations: standard GW using LDA inputs, self-consistent COHSEX, GW using COHSEX inputs, model self-consistent GW, and experiment.

	$G_{\mathrm{LDA}}W_{\mathrm{LDA}}$	COHSEX	COHSEX + GW	scf GW	Expt.
$\Gamma'_{25v} \rightarrow \Gamma_{1v}$	-5.07	-5.39	-5.17	-5.28	–
top O $2p$	-4.86	-5.39	-4.73	-5.00	$\sim$ -5.5
bottom Cu $3d$	-3.28	-3.92	-3.79	-3.72	$\sim$ -3.8
$\Gamma'_{25v} \rightarrow \Gamma_{1c}$	1.34	2.87	2.58	1.97	2.17
$\Gamma'_{25v} \rightarrow \Gamma'_{12c}$	1.51	3.00	2.71	2.27	2.55

Chapter 15

Angle-resolved photoemission spectroscopy of Cu$_2$O

At this point, the valence band structure of Cu$_2$O is still not completely established. All theoretical calculations (LDA, GGA, *GW*, self-consistent *GW*) found a largely dispersive state Γ_{1v} in between the O$\,2p$ and the Cu$\,3d$ states. This state seems to be absent in the photoemission data of Ghijsen and co-workers [126]. Unfortunately, their experimental setup was not angle-resolved. It is possible that this single state has been averaged out by the Brillouin zone integration of the measurement on a polycrystalline sample.

This is one of the motivations for the measurement performed on a single crystal first at LURE with an helium lamp (fixed photon energy, 21.2 eV or 40.8 eV), second at Elettra's synchrotron, Trieste (tunable photon energy). The experiment at LURE have been performed by M. Izquierdo and F. Sirotti. The beam time at Elettra has been granted on APE beam line of G.-C. Panaccione, and has been used by M. Izquierdo, N. Barrett, and myself.

The angle resolution of the experiments gives access not only to the density of states, but also to **k**-point resolved information, from which the band structure can be inferred. Besides the energy conservation of equation (1.8), an angle-resolved photoemission on a monocrystal allows one to keep track of the momentum of the photoelectron in the crystal [138]. The momentum conservation

$$\mathbf{k}_i = \mathbf{k}_f, \qquad (15.1)$$

where $\mathbf{k}_i$ means the momentum of the electron before and $\mathbf{k}_f$ after extraction, is however not enough to evaluate $\mathbf{k}_i$. Note that the momentum of the photon has not been taken into account, as it is vanishing in the ultraviolet energy range one is interested in. In fact, an assumption on the behavior of the photoelectron is needed to link $\mathbf{k}_f$ to the measured kinetic energy. The extracted electron of energy E_f is generally *supposed to be a free electron,*

whose energy parabola starts at the bottom of the valence bands:

$$E_f = E_{kin} + \phi = \frac{\mathbf{k}_f^2}{2} + E_0, \tag{15.2}$$

where E_0 denotes the binding energy of the valence states and ϕ is the work function, which is a measure of the barrier potential upon the extraction of an electron through the surface of the sample. This permits an estimation of k_i,

$$k_i = \sqrt{2(E_{kin} + \phi - E_0)}. \tag{15.3}$$

Using this assumption, one will be able to measure the band structure of Cu_2O.

15.1   Experimental setup

Due to the very short mean free path of the photoelectrons in the solid in the ultraviolet range (few Å), the photoemission spectroscopy is indeed a surface technique. As one wants to get insight into the bulk material, the sample under study should have a very clean surface, in order to reproduce as much as possible the electronic structure of the bulk.

Our Cu_2O sample has been cut along a (111) surface. The surface preparation has been performed with great care: annealing at 450°C and sputtering by 800 eV argon ions in ultra-high vacuum (pressure $< 10^{-10}$ torr). The stability of the surface as a function of time has been very good.

Low energy electron diffraction (LEED) allowed one to evaluate the quality of the surface using electrons of the same energy as the photoelectrons in the photoemission experiments. This permits one to probe the same depth as the relevant one for photoemission. Figure 15.1 shows one of the LEED images taken by M. Izquierdo at LURE at low electron energy (E=15.9 eV). As the surface is perpendicular to (111), the LEED experiment is looking at the cubic cell of Cu_2O along the large diagonal of the cube. That is why the image shows an order 3 symmetry: 3 small spots, 3 large spots. The LEED image is clear. The surface is believed to be qualitatively good. But, LEED is a diffraction method, and is therefore sensitive to the average position of the atoms in the illuminated region. Disorder around the mean position can not be excluded.

The oxidation of the surface is also a crucial parameter. To be sure we were indeed measuring a Cu_2O surface, some care had to be taken. As shown in reference [139], a satellite at -15 eV appears in the photoemission spectrum of Cu_2O when the photon energy is at the resonance of the Cu $3p$ states (around 76 eV). This feature is characteristic for Cu_2O, as it is absent for the other copper compounds, as Cu or CuO. A critical characterization test was to check whether the sample shows this satellite. We therefore compared in figure 15.2 the measured spectrum at 76 eV to the spectrum
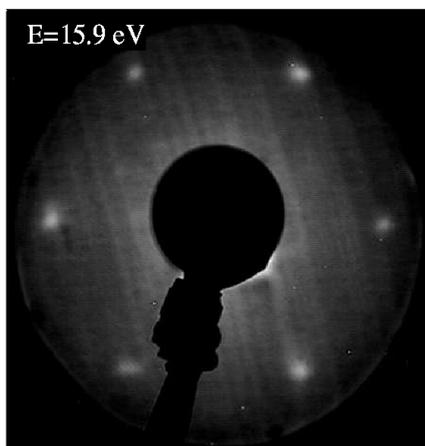
Figure 15.1: Low energy electron diffraction image of the Cu$_2$O (111) surface.
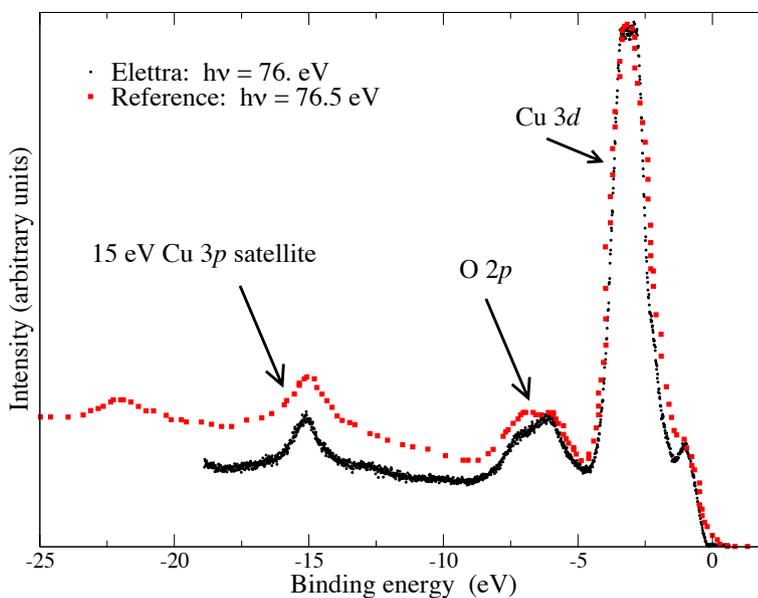

Figure 15.2: Photoemission spectrum measured at Elettra with 76 eV photons (small dots), compared to the reference spectrum of Thuler *et al.* [139] (large squares).

of Thuler and co-workers. The agreement is pretty good. Our sample does not show any of the characteristic satellites of Cu nor CuO at 10.5, 11.9, 12.9, and 14.6 eV, according to reference [139]. The oxidation of the surface

is believed close to the nominal Cu_2O formula.

Experimental uncertainties arise from different factors. First, the temperature causes a broadening of the measured spectra. All measurements have been performed at room temperature $kT \approx 25\,meV$. At Elettra, low temperature measurements have been tried. Unfortunately, the sample experienced drastic changes during cooling down and finally, only room temperature measurements have been retained as reliable.

According to the empirical curve of reference [140], the mean free path of photoelectrons in the perpendicular direction is about $5\,\text{Å}$ in the 20-80 eV energy range. The Heisenberg relation

$$\Delta k_z \Delta z \sim 1 \tag{15.4}$$

permits one to evaluate the uncertainty in momentum along the z direction. Its value is evaluated to $\Delta k_z \sim 0.2\,\text{Å}^{-1}$. This should be compared to the Γ-R length $1.27\,\text{Å}^{-1}$ in Cu_2O. This means that the uncertainty is slightly larger than 15 % of the full Γ-R length. This big value should be kept in mind. It could play a role when comparing experimental data to theoretical ones: dispersive bands will be noticeably broadened by the experimental uncertainty Δk_z.

There is also an uncertainty in directions x and y due to the finite angle resolution $\sim 0.5°$. This accounts for an integration on a finite solid angle around the measured direction. In the worst case at high photon energy ($80\,eV$), an integration angle of $0.5°$ yields an uncertainty of 3 % of the Γ-R length. This cause of broadening is very small compared to the one due to the finite mean free path of photoelectrons.

Preliminary measurements with helium lamp made at LURE by M. Izquierdo showed that there is almost no dispersion of the bands of Cu_2O when the angle of the detector (i.e. when the **k**-point) is changed. This statement has been quickly confirmed at Elettra. That is why we concentrated on changing the photon energy, keeping the detector in normal incidence. As the surface of the sample is (111), the measurement direction has been Γ-R. The available photon energies allowed one to measure a line Γ-R-Γ, changing the energy from $20\,eV$ to $85\,eV$.

Modifying the photon energy not only changes the **k**-point measures according to equation (15.3). It also changes the intensities of the lineshapes. The cross sections of the different atomic orbitals depend strongly on the energy of the incident photons. They have been calculated for the atoms within the Hartree-Fock approximation, tabulated in reference [141], and are provided here in table 15.1. Therefore, when one measures the Γ point with $20\,eV$ photons, the measured spectrum differs from the Γ point reached with $85\,eV$ photons. Moreover, according to the polarization of the incident photons, the selection rules are not identical. Using vertical or horizontal polarized photons will produce different spectra accounting for the same **k**-point. Energy and polarization are parameters one can play with, in a

synchrotron beam line. One can hope that changing the cross sections will make different states appear, which can be particularly helpful when they are so intricate, as in Cu$_2$O.

Finally, it is also needed to explain the background present in the measured spectra, as in figure 15.2. In fact, extracted electrons may experience energy losses after the interaction with the impinging photon. For instance, an electron with a binding energy of 2 eV and hence initially high kinetic energy can lose energy via some uncontrolled scattering process and finally be measured by detector. As the electron has lost some energy before measurement, it will be counted (wrongly) as an electron with a higher binding energy. That is why even in a region where there is no state, as at -20 eV in figure 15.2, the spectrum is not vanishing. Phenomenologically, the probability to measure secondary electrons is proportional to the number of states of lower binding energy.

A. D. Shirley proposed an empirical scheme to remove the background [142], in order to only retain primary electrons that have not experienced any subsequent energy-loss. Let $I(\omega)$ be the spectrum as a function of ω, the kinetic energy of the photoelectron. Let frequency ω_0 stand for the lowest measured energy, where there is no corresponding state in the solid. Therefore, the corrected spectrum $I'(\omega)$ should be equal to zero at frequency ω_0. According to Shirley's formula, the spectrum with background removed $I'(\omega)$ reads

$$I'(\omega) = I(\omega) - I(\omega_0) \left(\int_{\omega}^{+\infty} d\omega' I(\omega') / \int_{\omega_0}^{+\infty} d\omega' I(\omega') \right). \qquad (15.5)$$

The corrected spectrum is indeed zero at ω_0 and the removed background is proportional to the integral of the spectrum above the current frequency. All electrons with higher kinetic contributes to the background at ω. This procedure should be applied with care, as it might displace the position of the peaks. But it is necessary if one wants to compare the shape or the intensities of the experimental and theoretical spectra.

Table 15.1: Calculated cross section of atomic orbitals O $2p$, Cu $4s$, Cu $3d$ as a function of the impinging photon from reference [141].

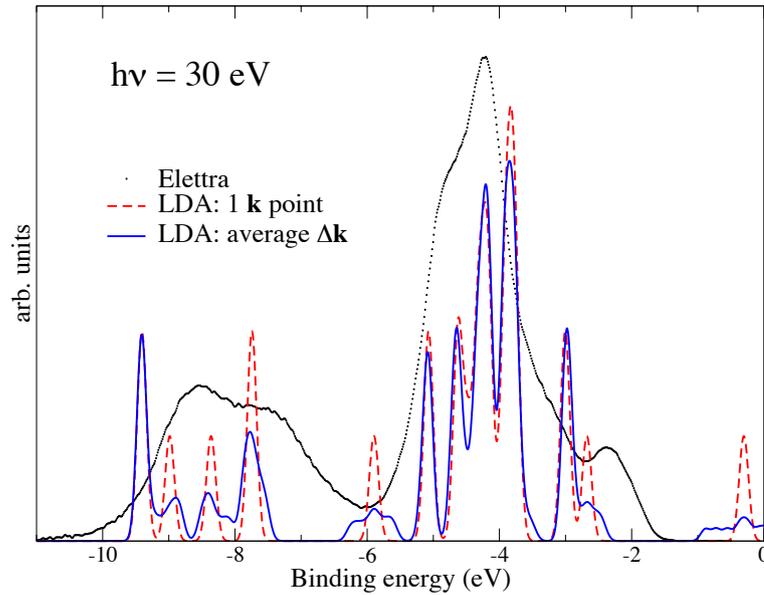| $h\nu$ (eV)	O $2p$	Cu $4s$	Cu $3d$
16.7	10.43	0.016	6.45
21.2	10.67	0.036	7.55
26.8	9.77	0.044	8.19
40.8	6.82	0.041	9.93
80	2.06	0.025	8.71
132	0.58	0.014	5.14

Figure 15.3: Photoemission spectrum measured at Elettra with 30 eV photons (small dots), compared to calculated spectra within LDA using either only one **k**-point (dashed line) or several **k**-points in the uncertainty range Δk_z (solid line).

15.2   Analysis of experimental results against theoretical predictions

In order to compare theoretical results to experimental data, one has to keep in mind the limitations exposed in the previous section. At present we cannot predict theoretically the energy dependent experimental spectra, since for this we would have to evaluate formula (2.30), including the transition matrix elements. If one uses a simple density-of-states to represent the result of the photoemission process, the theoretical predictions are not dependent on the photon energy, just on the scanned **k**-point via the band structure. In fact, the only feature which can be compared directly is the position of the states.

Let us exemplify the comparison between experiment and theory with one particular spectrum at 30 eV. This spectra is particularly interesting because it corresponds to **k**-point (1/4, 1/4, 1/4) using equation (15.3), where one has maximum chances to notice the dispersive state Γ_{1v} in between Op and Cud regions. Figure 15.3 shows the experimental curve measured at Elettra and the LDA density-of-states corresponding to the single **k**-point (1/4, 1/4, 1/4). The LDA density-of-states was constructed using gaussians of 0.1 eV half width at half maximum. This is a rough estimate of the energy resolution of the experiment, which is believed to give results with
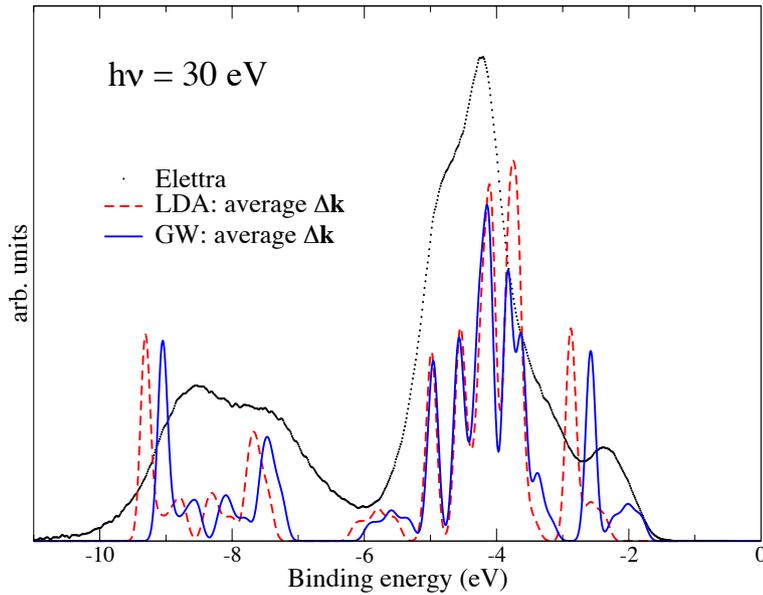
Figure 15.4: Photoemission spectrum measured at Elettra with 30 eV photons (small dots), compared to calculated spectra within LDA (dashed line) or within self-consistent GW (solid line).

a 0.05 eV accuracy. But the comparison shows here that the experimental spectrum has structures much more broadened than the theory. Even worse, theory shows that one should distinguish 4 groups of states in the Op region (-9,-7 eV). Experiments only show two very large and smooth structures. An important cause for broadening is the uncertainty in **k**-point due to the finite mean free path of the photoelectrons. In order to account for that issue, figure 15.3 shows also a spectrum, which is the sum of 7 different spectra around (1/4, 1/4, 1/4): from (0.2, 0.2, 0.2) to (0.3, 0.3, 0.3). This integration has a slight effect on the localized states (consider e.g. the lower Op band), but a significant one on the dispersive states. In particular, the top valence states and the Γ_{1v} band are somehow averaged out by this procedure. That could explain why the dispersion of the upper valence band is hardly seen in experiments. It could be also a cause why one can not see the dispersive Γ_{1v} band. That could explain why the two states in the middle of the Op region can not be distinguished, and why the spectrum in this region has simply two smooth structures.

Now studying the location of the calculated density-of-states, LDA is clearly insufficient to give a reliable account of the Cud region. The difference between the main Cud peak and the top valence is underestimated by 1 eV within LDA, and finally the whole Cud band width is largely underestimated. This is a call for improved theoretical calculations.

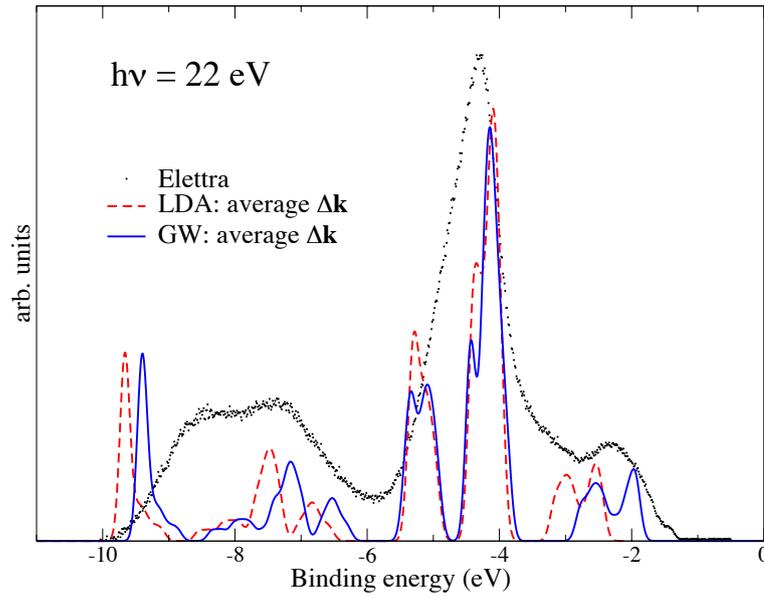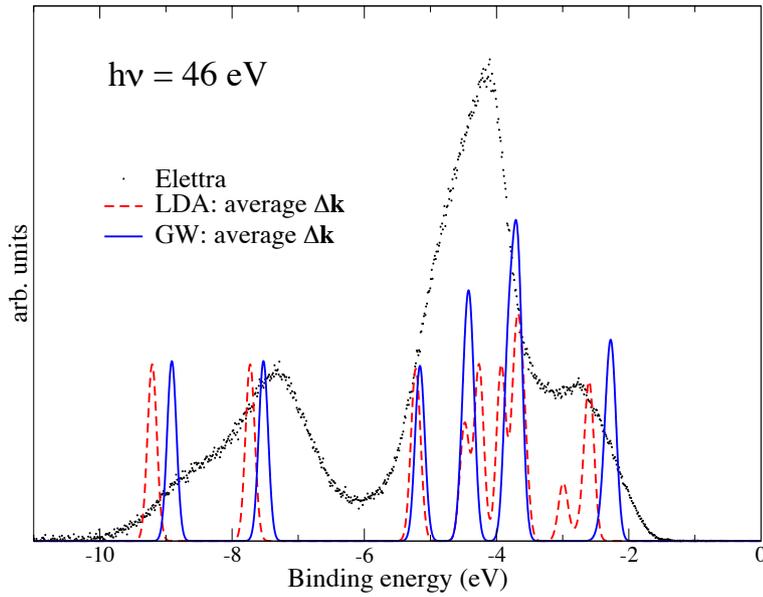Figure 15.4 shows the comparison between LDA, self-consistent GW

Figure 15.5: Photoemission spectrum measured at Elettra with 22 eV photons (small dots), compared to calculated spectra within LDA (dashed line) or within self-consistent *GW* (solid line).

density-of-states averaged over the $\Delta\mathbf{k}$ uncertainty, and the corresponding experimental measurement. Self-consistent *GW* yields great improvements over the LDA result. The location and the width of the Cu 3*d* states is now in good agreement with respect to the experimental data. The O*p* states are still slightly too low, but significantly improved. These calculations confirm the conclusion that the dispersive state Γ_{1v} is still located in between the O*p*–Cu*d* gap, but the corresponding peak will be a large smooth peak, difficult to find in the experimental curve.

Figures 15.5, 15.6 and 15.7 give the same information as the previous figure, but for different photon energies, respectively, 22 eV, 46 eV, and 76 eV. These spectra correspond to **k**-points: (0.11, 0.11, 0.11), (0.50, 0.50, 0.50) and (0.16, 0.16, 0.16) in reciprocal lattice vector units. In all spectra, self-consistent *GW* yields improvements over the LDA band structure. Note that the figures for energies 22 eV and 76 eV account for very close **k**-points (smaller than the $\Delta\mathbf{k}$), and the corresponding experimental spectra differ noticeably. This confirms that there is no hope to account for the height of the peaks with the simple theoretical density-of-states.

An other issue can be raised looking at the spectrum for 46 eV photons, in figure 15.6. This spectrum corresponds to the high symmetry point R. There, the dispersion of the bands is almost zero within $\Delta\mathbf{k}$. That is why theory predicts thin peaks. However, experimental data are as broadened as for the other **k**-point. It means that *there is an additional cause for broad-*

Figure 15.6: Photoemission spectrum measured at Elettra with $46 \, \text{eV}$ photons (small dots), compared to calculated spectra within LDA (dashed line) or within self-consistent GW (solid line).

ening. One can immediately remove the hypothesis of very short lifetimes of the excited states due to electron-electron coupling, since also the top of the valence band experiences a large broadening. Temperature accounts for only $0.05 \, \text{eV}$ via the statistical standard deviation kT. An other cause for the broadening of the structure may be the finite lifetime of excitations due to a strong electron-phonon coupling. This possibility can be considered as serious, as one has noted earlier in chapter 12 that the band structure depends drastically on the lattice parameter. A last cause for broadening could be the disorder of the surface. Even the pretty LEED pictures we got can not exclude this case. There is still some physical effect to be understood, why the experimental data are not as accurate as expected.

Concerning the problem that the dispersive Γ_{1v} state in between O $2p$ and Cu $3d$ is not distinguished in the experimental data, theory gives an additional explanation to that. Within LDA (and this statement is not changed much within self-consistent GW), this dispersive state has a strong Cu $4s$ character: the maximum is at the Γ point, where the Cu $4s$ character has a weight of 60%, the minimum is at the R point, where the state is degenerated with other Cu $3d$ states and it has hence no Cu $4s$ character anymore. This Cu $4s$ character is important to interpret the experiments, since as displayed in table 15.1, the Cu $4s$ can not be seen in photoemission in the 20-80 eV energy range. This shows that the Γ_{1v} state, being one half Cu $4s$, one half Cu $3d$, has a cross section that is half of the purely Cu $3d$
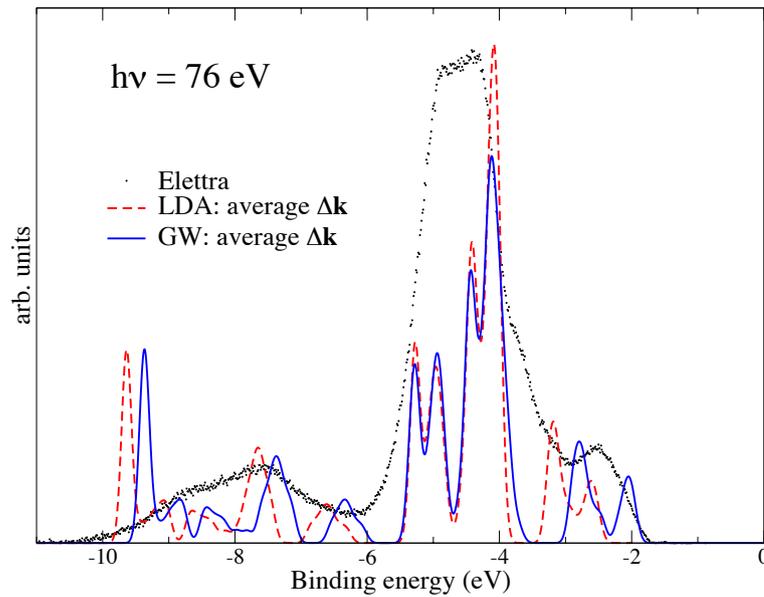
Figure 15.7: Photoemission spectrum measured at Elettra with 76 eV photons (small dots), compared to calculated spectra within LDA (dashed line) or within self-consistent *GW* (solid line).

states. This fact in addition to the dispersiveness of the state can explain the fact that it is not present in any experimental measurement. Experiments do not give the proof that this state does not exist, in contrast with our first suspicion. The presence of this state in theory should not be held anymore as a failure of the theoretical approach. This state can indeed be located here.

Chapter 16

Calculation of neutral excitations in Cu_2O

The comparison of the calculated band structure with the valence state photoemission data has been done in the previous chapter. However, one has just few insights into the conduction band structure. The only available information are results from optical absorption [1, 3], which stated that transition from the top valence band to the first conduction band is dipole forbidden and the next one (from top valence band to second conduction band) is allowed. Optical absorption, reflectivity and also energy-loss spectroscopy give thus important insights on the electronic structure of solids. Unfortunately, these measurements yield data that are not interpretable in a straightforward way.

In a photoemission spectrum, the position of a peak is as a first step simply interpreted as the energy of a state. In optical measurements instead, the peaks are linked not directly to the states, but to transitions between pairs of states. Moreover, the "straightforward" interpretation as transitions can be prevented by the excitonic effects that may change drastically the energies and lineshape of the spectra. Therefore *ab initio* calculations of the optical or energy-loss spectra are a useful tool for interpretation, that one also use in order to detect whether the underlying band structure corresponds to reality or not. In our case, the comparison with experimental data may confirm whether the calculated band structure within the cumbersome self-consistent *GW* approach is indeed an improvement over LDA or standard *GW*.

In this chapter, I will show the *ab initio* prediction of the energy-loss and optical absorption spectra.

16.1 Energy-loss spectra

The present study of energy-loss spectroscopy in Cu_2O is to be rather succinct, since there is no experimental data to compare with. I would just
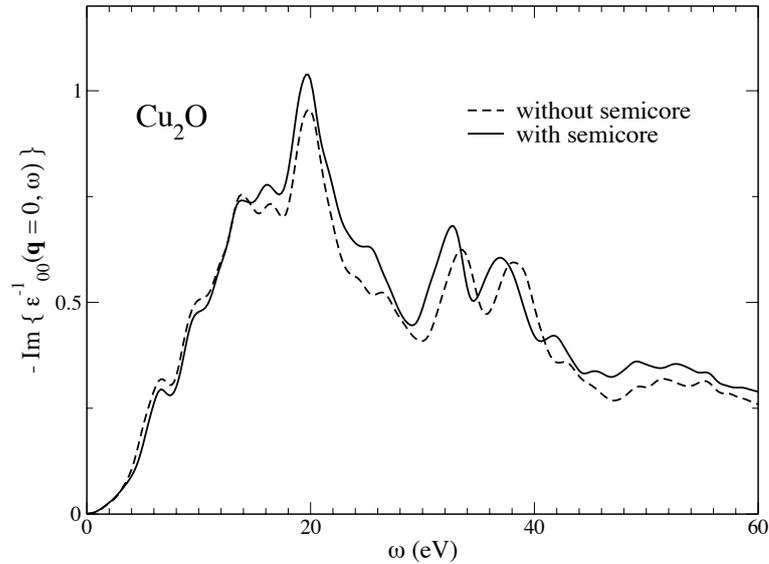
Figure 16.1: Energy-loss spectrum of Cu_2O for vanishing momentum transfer using energies and wavefunctions coming from the pseudopotential with semicore or without semicore states, respectively.

like to address the issue of the effect of the semicore states on energy-loss spectra, which is a debated topic [62, 109].

Figure 16.1 shows the energy-loss spectra of Cu_2O using the two pseudopotential schemes described earlier in chapter 12: including or not the semicore $3s$, $3p$ states of copper in the valence. The spectra are computed at vanishing momentum transfer $\mathbf{q} \to 0$ using 216 slightly shifted $\mathbf{k}$-points, up to 166 bands, within RPA. The small shift used follows the recipe of reference [143]: one eighth of the spacing between $\mathbf{k}$-points in some direction. RPA is known to give in general a rather good evaluation of the energy-loss spectra (see e.g. reference [62]. The figure shows that there is no important effect of the semicore on the spectra in the 0-60 eV energy range. The position of the peaks does not change at least up to 30 eV.

Two important conclusions can be drawn so far. First the eigenvalues and eigenvectors arising from the two pseudopotentials give very similar transition energies and matrix elements $\tilde{\rho}_{ij}$ (remember that $\tilde{\rho}_{ij}$ is the Fourier transform of $\phi_i(\mathbf{r})\phi_j^*(\mathbf{r})$). Therefore, the presence of more nodes in the core region of the wavefunctions corresponding to the pseudopotential with semicore in valence does not affect the matrix elements. This point has already been discussed in section 13.3.1 with the comparison with PAW results. Second, the addition of the semicore states might have contributed to the screening, hence changed the real part of the dielectric function, and consequently, the loss function even at energies lower than the semicore threshold. This is indeed not the case: the real part of ε remains
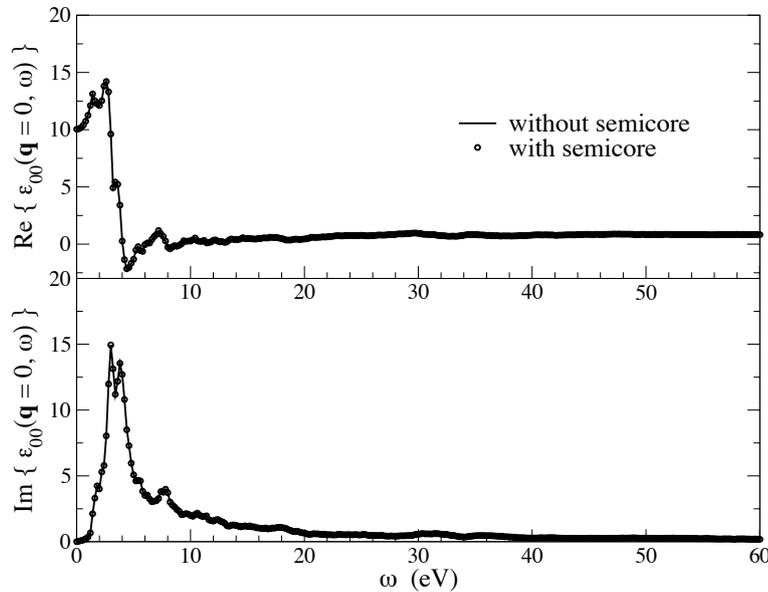
Figure 16.2: Real (upper panel) and imaginary (lower panel) part of the dielectric function of Cu$_2$O using the pseudopotential with semicore. The solid curve shows the results when the contribution of the semicore to the dielectric function is removed by eliminating transitions from these states and the open circles, when the contribution of the semicore is fully included.

unchanged when the $3s$ and $3p$ states of copper are added. This is assessed by figure 16.2. This means that the slight difference between the two curves in figure 16.1 is only due to the different pseudowavefunctions.

Of course, the inclusion of the semicore will have effects for sure in the region where they give contribution to the imaginary part of the dielectric function, i.e. in the 70 eV region.

16.2   Optical absorption spectra

Optical spectra have been studied in detail during the sixties and the seventies, because of the famous dipole forbidden excitonic series, that arises from transitions from Γ'_{25} to Γ'_1 [1, 105]. This series is still out of reach of *ab initio* calculation, because the corresponding spectra has low intensity and shows very thin structures: one would need an energetic resolution of 0.01 eV (compatible with the binding energy of the excitonic series). On the contrary, it reasonable to address the issue of calculating the rest of the optical spectrum between 2 and 8 eV, where experimental data are also numerous [2, 3]. This part of the optical spectrum shows also several excitonic series.
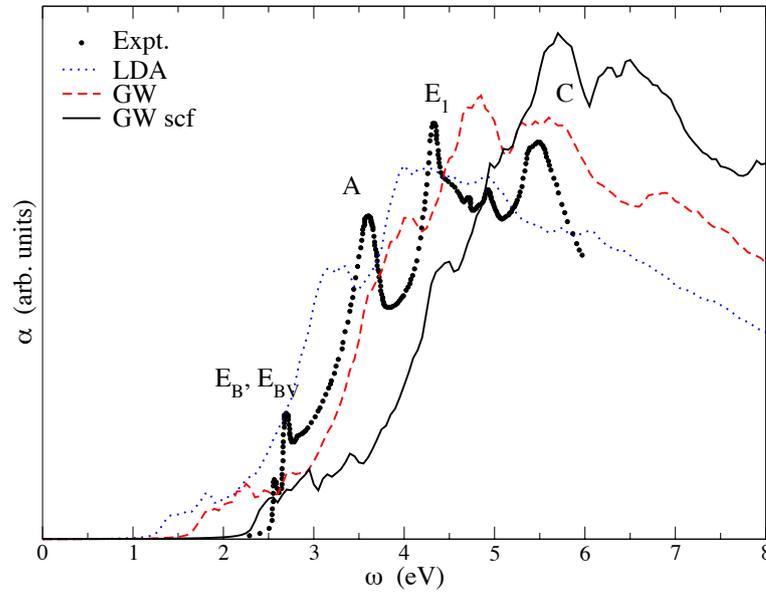
Figure 16.3: Optical absorption spectra within RPA using different eigen-values: LDA (dotted line), standard GW (dashed line) and self-consistent GW of the previous chapter (solid line), compared to the experimental data of reference [3] (filled circles).

One will concentrate in this section on the calculation of the absorption coefficient $\alpha(\omega)$ (defined in chapter 1), since this is the raw experimental data. α does therefore not require any additional Kramers-Kronig transform or assumption on the high frequency region. From the point of view of calculations, α is easily obtained from the obtained values of $\mathrm{Re}\,\varepsilon$ and $\mathrm{Im}\,\varepsilon$.

Let us first show that the inclusion of excitonic effects in mandatory to calculate realistic absorption coefficient $\alpha(\omega)$. Figure 16.3 shows the RPA spectra using different approximations of the quasiparticle energies. In all calculations of the present section, a regular $8 \times 8 \times 8$ set of slightly shifted **k**-points, the 7 upper valence bands and the 4 first conduction bands have been included in the calculation. The η parameter in the energy denominator has been set to $0.05\,\mathrm{eV}$. As concluded earlier, all depicted schemes predict correctly that the first transition is dipole forbidden, and therefore it is not seen in the linear-response calculation displayed here. But, the LDA or the standard perturbative GW energies give a largely underestimated optical threshold compared to experiment. On the contrary, self-consistent GW evaluates it to $2.2\,\mathrm{eV}$: it is now only slightly underestimated. Within all these approximations, it is impossible to recognize the experimental peaks (A, E_1, C following the notation of Brahms *et al.* [3]). This means that either the quasiparticle energies are wrong, and/or the excitonic effects are significant and can drastically change the lineshape.
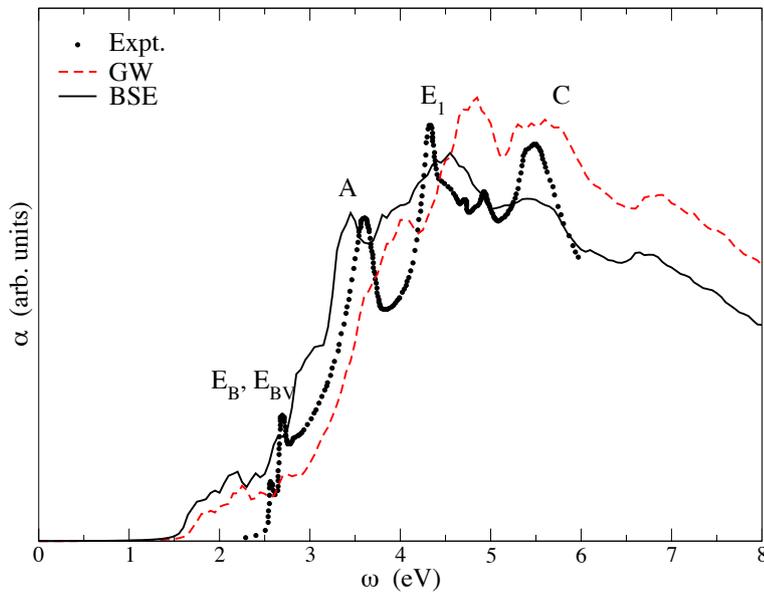
Figure 16.4: Optical absorption spectra within the usual practical scheme for the solution of Bethe-Salpeter equation: first consider the RPA approximation using standard *GW* energies (dashed line), then add the excitonic effect by means of the static RPA *W* (calculated with LDA energies) in the Bethe-Salpeter equation (solid line) and compare to experiment (filled circles) [3].

As a reference, figure 16.4 shows what would be a solution of the Bethe-Salpeter equation using the usual ingredients: use of perturbative *GW* energies and LDA wavefunctions, use of the LDA static RPA screening W_{LDA}. One can remark that the lineshape is changed with respect to the RPA curve using standard *GW* energies (proof for important excitonic effects), but the agreement with experiment is still poor.

Finally, figure 16.5 shows the most complete calculations I could perform using the improved self-consistent *GW* energies, that gave a realistic optical threshold. As noted earlier, the corresponding RPA curve (denoted GWscf) is far from being comparable to experimental data. However, when the excitonic effects are switched on, via the solution of the Bethe-Salpeter equation, the correspondance between theoretical and experimental spectra becomes obvious. If one uses, as it is most often done, the LDA screening, excitonic peaks are damped: consider, in particular, peaks labeled A and E_1. This is understood by the overestimation of the screening within LDA, due to the four times too small band gap.

If the screening is reduced by using the self-consistent W_{GW}, that corresponds to a 2 eV band gap, the excitonic peaks have a noticeable sharpness in A and E_1. The agreement with respect to experiment is now striking.
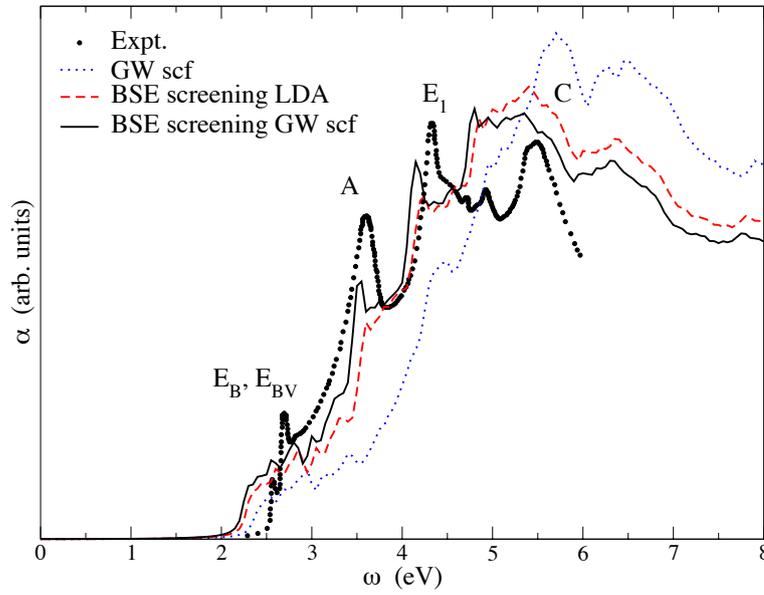
Figure 16.5: Optical absorption spectra within an "improved" practical scheme for the solution of Bethe-Salpeter equation: first start from the RPA approximation using self-consistent GW energies (dotted line), then add the excitonic effect by means of the W in the Bethe-Salpeter equation. W is either calculated using LDA energies (dashed line) or using self-consistent GW energies (solid line). Experiment [3] is displayed with filled circles.

Of course, there are some remaining discrepancies. The E_B (and E_{BV}, its spin-orbit twin) cannot be identified: probably due to the too small number of **k**-points in the Γ region. The shape of peak C is not perfect: maybe the quasiparticle energies is that energy region are not so realiable.

In conclusion, nevertheless, the agreement between the self-consistent GW plus Bethe-Salpeter equation and experimental data is a strong clue that the underlying quasiparticle band structure is realistic. Moreover, the subsequent static screening calculated with self-consistent GW energies provides the correct shape of the excitonic peaks. Therefore, the corresponding index of Cu_2O should be close to the experimental value. Note that all these calculations have been performed with the use of LDA wavefunctions. The self-consistent GW scheme also provides new wavefunctions. Though close to the LDA wavefunctions, it would have been interesting to evaluate the impact of the GW wavefunctions on the optical spectra. Unfortunately, this would have been possible only for the small **k**-point set $4 \times 4 \times 4$, which yields not converged spectra.
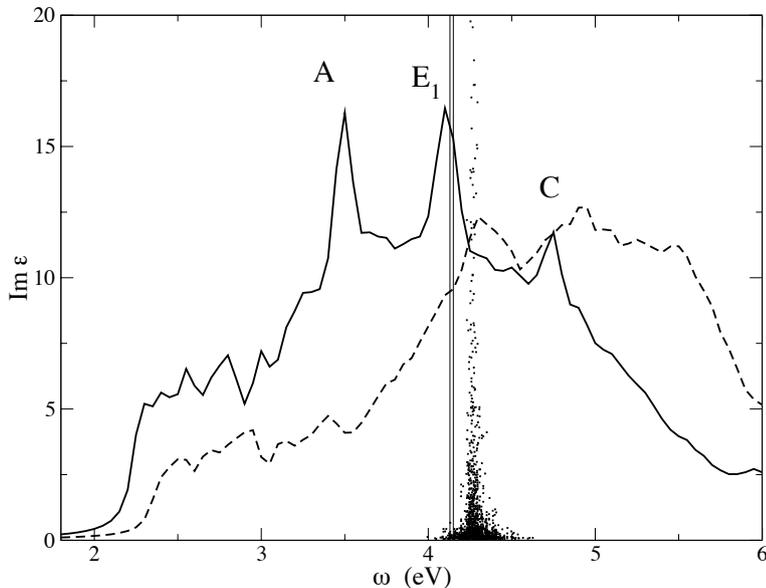
Figure 16.6: Imaginary part of the dielectric function of Cu$_2$O within RPA (dashed line) or within Bethe-Salpeter equation (solid line) using self-consistent GW inputs. The transitions contributing to the excitonic spectrum between the two vertical lines are displayed at their independent quasiparticle transition energy (black dots).

16.3 Analysis of the excitonic spectrum

The solution of a Bethe-Salpeter equation using self-consistent GW inputs has been shown to give a reliable representation of the absorption spectrum of Cu$_2$O. We can further make use of this to analyse this complex absorption spectrum. It will be more straightforward to concentrate on the imaginary part of the dielectric function Im ε, instead of α, in order to carry on the analysis.

The analysis is dedicated to identify, which independent quasiparticle transitions contribute to a given excitonic peak. In other words, it allows one to know which peak from the RPA curve becomes the excitonic peak under consideration. This representation is convenient, because the code that solves the Bethe-Salpeter equation [144] is written in the transition space [35, 38]. All quantities are expanded in the basis of the $\phi_v(\mathbf{r})\phi_c^*(\mathbf{r})$ matrix elements (as e.g. in equation (6.11)). Therefore, the obtained solution of the Bethe-Salpeter equation is automatically decomposed in terms of these transitions. The excitonic effects come from the mixing of the transitions. Instead, if the mixing is not allowed, one obtains the usual RPA spectrum.

In figure 16.6, we consider the transitions that give rise to peak E$_1$ using
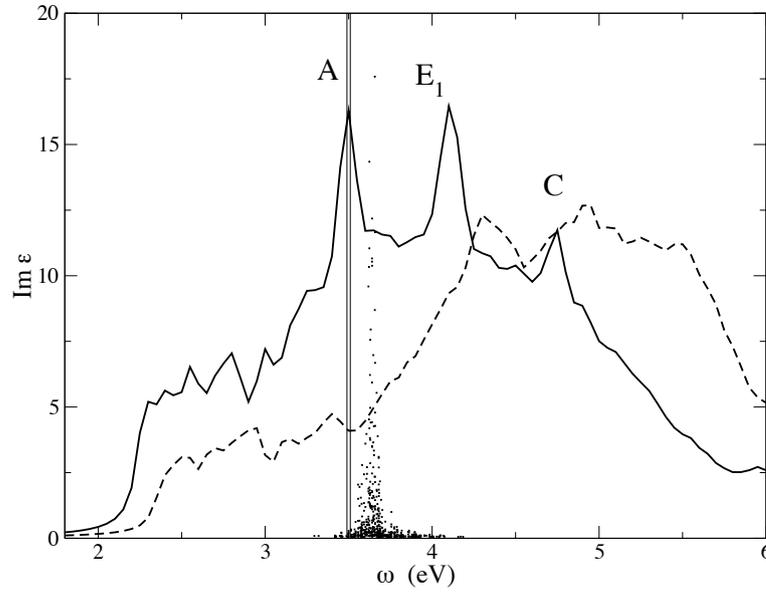
Figure 16.7: Imaginary part of the dielectric function of Cu_2O within RPA (dashed line) or within Bethe-Salpeter equation (solid line) using self-consistent GW inputs. The transitions contributing to the excitonic spectrum between the two vertical lines are displayed at their independent quasiparticle transition energy (black dots).

the notations of Brahms et $al.$ [3]. The independent transitions (black dots) that are mixed to create the peak are located at about $0.12\,eV$ above the peak, in a region of width $0.10\,eV$. The nature of the exciton is similar to the continuum exciton in silicon, with a low binding energy, and transitions coming from a restricted energy area. The figure shows that the peak in the RPA curve in the vicinity of the black dots is the one that gives rise to the E_1 excitonic peak. This peak can be qualified as "excitonic", since its shape and intensity changed drastically thanks to the excitonic term of the Bethe-Salpeter equation. Nevertheless, this peak was already present in the RPA curve.

On the contrary, if one now looks at peak labeled A in figure 16.7, one states that the transitions giving rise to peak A do not create any peak in the independent quasiparticle picture. The excitonic effect is drastic here. It is similar to the case of bound excitons of rare gaz solids, for which a continuum of independent transitions of low intensity can generate a sharp peak within the band gap. The binding energy for the excitonic peak is once more about $0.14\,eV$ and the width of the contributing region is about $0.12\,eV$. According to calculations, it is not possible indeed to state that the contributing transitions come from a given region of the Brillouin zone: many $\mathbf{k}$-points do contribute, and moreover, different bands contribute.
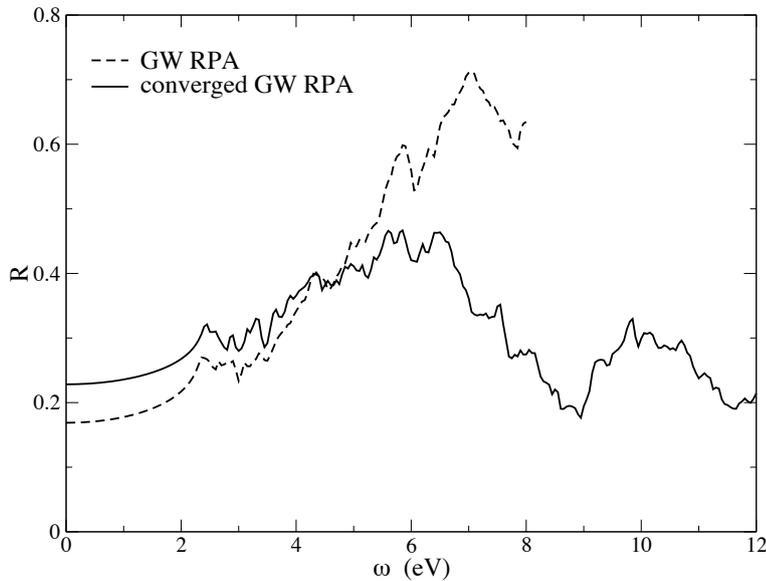
Figure 16.8: Reflectivity spectrum of Cu_2O within RPA using self-consistent *GW* inputs. The dashed line uses only 7 valence bands and 4 conduction bands, whereas the solid line uses 26 valence bands and 22 conduction bands.

This conclusion contradicts the usual statement of experimentalists [3], who claims that A peak arises from transition in the vicinity of the M high symmetry point. Interestingly, the calculation shows that only the two top valence bands contribute to that peak.

The previous analysis allowed one to established that some peaks in the imaginary part are due to peaks in the RPA spectrum and that the excitonic effect sharpened these features (peak E_1). Some other peaks are completely absent in the independent quasiparticle picture and are entirely created by the excitonic effect (peak A).

Finally, the calculated spectra can be used to predict the outcome of reflectivity experiments published in literature [2, 3]. Reflectivity spectra are rather difficult to calculate, since they depend strongly on the real part of ε and therefore, require much more bands for adequate convergence. Figure 16.8 illustrates this property: the converged reflectivity curve required much more bands than the usual number of bands for absorption (7 valence and 3 conduction bands). The intensity changed drastically, however the location of the peaks, at least up to $6\,\mathrm{eV}$, is rather meaningful even for the low-convergence curve. This allows one to compare the results of the Bethe-Salpeter equation obtained with few bands (for numerical reasons) with experiment in figure 16.9. If one forgets about overall intensity due to the small number of bands, the agreement in peak locations is once more striking. Peaks A, E_1, and C are present in the calculated curve and their

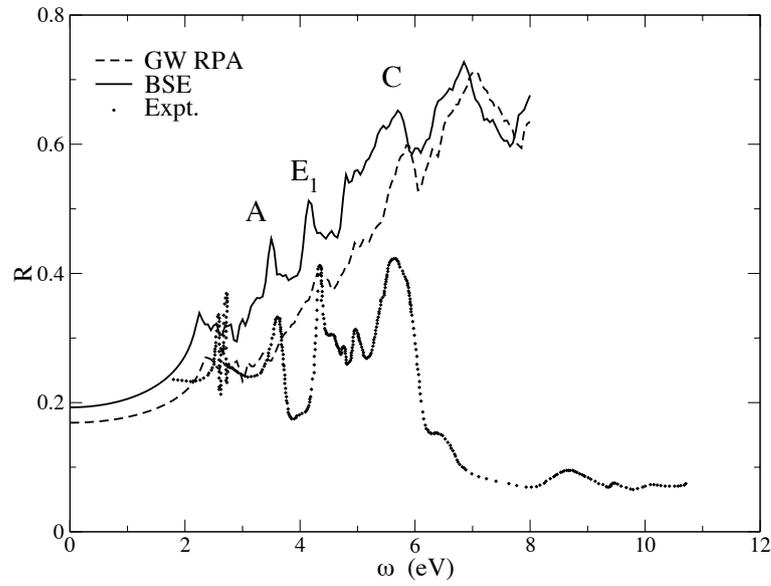Figure 16.9: Reflectivity spectrum of Cu$_2$O within RPA (dashed line), within Bethe-Salpeter (solid line) using self-consistent *GW* inputs. A few bands have been used 7 valence bands and 4 conduction bands. Experiment from reference [3] is given with filled dots.

position is accurate by $0.3\,$eV. This agreement assesses the underlying band structure obtained from the model self-consistent *GW* method.

Conclusion

This work has led to various conclusions. Having originally the purpose to correctly describe the electronic structure of Cu_2O, it finally brought progresses concerning different aspects of underlying theory, of technical points, and, in general, of the physics of this material. Moreover, in order to test the developments, I carried out a study of well known textbook examples: bulk silicon and solid argon.

Technical developments

From the technical point of view, in order to assess and to improve the existing results, I had to write parts of code, to go beyond the usually applied approximations. As an outcome, a GW code without plasmon-pole model for W, a self-consistent Hartree-Fock, COHSEX and GW code are now available. I also implemented for test purposes a Hartree-Fock code based on the plane-wave basis set (compared to the self-consistent Hartree-Fock in a LDA basis, this is of course not efficient!). This part of my work did not yield immediate breakthroughs in physics, since the algorithms were inspired from existing works from other groups [82, 83, 90]. But, the resulting codes were necessary for the study of Cu_2O. Moreover, they made available to our group and to colleagues within the NANOQUANTA European network pieces of code that, I hope, will be useful in the future for other applications. Indeed, some of the developments are already in use by my collaborators. Furthermore, the pieces of code are based on the GPL package ABINIT [67, 69]. I am thinking about delivering the new subroutines to the whole community through this medium.

Theoretical developments

From the theoretical point of view, the original, ambitious purpose of this thesis was to devise a elegant way to include vertex correction beyond the GW approximation of the self-energy, in order to possibly apply them to Cu_2O. The idea was to link DFT (or TDDFT) to the Green's function formulation of the many-body problem, starting from the experience of the group in Palaiseau [4–6]. This study yielded a new way to approach

the problem of vertex corrections to the self-energy. Moreover, it led to unexpected results concerning TDDFT exchange-correlation kernels.

In particular, I derived a Sham-Schlüter inspired equation for the time-dependent kernel of TDDFT. The derivation allowed me to write a systematic expression for the kernel, and to shed light on the link between the approaches currently used for the derivation of TDDFT kernels: the mapping technique of Palaiseau's group [4, 6], the perturbative approach of Rome's group [64, 79], the time-dependent OEP framework by Kim and Görling [77, 78], and the diagrammatic derivation of references [65, 80]. I discussed in particular the striking example that, if time-dependent exact-exchange were not linearized in the TD-OEP procedure, it would give exactly the time-dependent Hartree-Fock result, which is a rough approximation for optical spectra of solids.

The recipe elaborated in this thesis to include vertex corrections into the self-energy starts from an opposite point of view. In fact, it uses the insights given by the theorems of TDDFT in order to make the Hedin's equations more tractable in practice. These developments were first thought as an approximation to the exact scheme: just *considering the variations of the self-energy with respect to the density, instead of the variations with respect to the full Green's function*. But, it finally ended up with the conclusion that, provided that the TDDFT theorems are fulfilled, the previous statement is exact. The scheme has been applied to simple materials, but still neglecting the small (to my opinion) but very cumbersome three-point part of the vertex corrections. Cancellations of the vertex contributions were pointed out.

Advances in the comprehension of physics

By means of the self-consistent quasiparticle scheme implemented in this work, I showed that the GW or COHSEX wavefunctions can differ from LDA ones more than what had been stated in previous works [70, 145]. Moreover, a small change in the wavefunctions can induce large changes in the Hartree potential or in the exchange operator acting on a particular state. However these variations mainly compensate, leading to an overall small effect for silicon and argon. Nevertheless, they induce a significant opening of the band gap for cuprous oxide.

This self-consistent GW scheme allowed us to predict theoretically the electronic structure of Cu_2O in reasonable agreement with respect to experimental data. The major improvements are the correction of the band gap, which was found to be unexpectedly 60 % of the experimental value within the standard GW approximation, the correction of the first dipole allowed transition, and an optical absorption spectrum in nice agreement with experiments. Considering the complexity of the Cu_2O optical spectrum due to several excitonic series, the calculated spectrum is strikingly good. This

last fact proves that the underlying band structure is rather reliable and that the self-consistently evaluated screened Coulomb interaction W (that screens the excitons) is also good.

The self-consistent GW approach also allowed to improve the comparison with the newly performed angle-resolved photoemission experiments, made by myself and my collaborators. The experiments confirmed that the LDA describes the valence bands relatively well, except for a few features. In particular, the LDA underestimates the band width of the Cud states. This property is properly corrected within the self-consistent GW calculation. Concerning the Γ_{1v} valence state, that is theoretically predicted to be in between the Op and Cud states, it can not be revealed both in the existing [126, 146] and in the new experiments, although all LDA, COHSEX, GW and self-consistent GW calculations found its presence. Actually my calculations allowed me to show that this state, that is about half Cu$4s$ and half Cu$3d$, has a low photoemission cross section. For this reason, this state is expected to be difficult or even impossible to distinguish in the experimental spectra.

Open issues

Of course, there are open issues raised by the present work, which have no clear answers yet.

The vertex correction scheme devised here avoids to address the problem of causality: TDDFT is a causal theory, whereas Green's function framework uses time-ordered quantities. Linking both theories may cause some problems. The problem of causality was already given an answer by R. van Leeuwen [57, 95], using the Keldysh contour technique. It should be verified in the scheme presented here, whether the Keldysh contour is indeed needed and if yes, how? Nevertheless, the procedure derived in this thesis is mainly intended for practical use. We do not have so far found any case, where the causality/time-ordered difference creates problems in practice, provided that the formulas are evaluated in a consistent way.

One may further wonder how important is the disregarded three-point part of the vertex function $\Delta\Gamma$. The evaluation of this function would need much coding, and will lead for sure to very cumbersome calculations, even for simple materials. This is out of reach at present. It would have been also interesting to evaluate the impact of the vertex on the "less studied features" of the Green's functions: the satellites, the lifetimes, etc. Work along these lines is planned.

Concerning the future of the written codes, as I now have a self-consistent GW code in my toolbox, it is perfectly feasible to calculate the GW total energy of a bulk material. This will lead to cumbersome calculations even for simple materials, but within reach of the available computers. The GW approximation is believed to yield very good total energies [87, 147] in ho-

mogenous system. Moreover, it is tightly linked to the RPA total energy [148], that is known to give account for the physically important van der Waals interactions [149]. The self-consistent GW code uses the model of reference [90], whose accuracy is not fully assessed yet. This calculation could be a critical test for the model. It could be an important application of the code developments I did.

For the electronic structure of Cu_2O, one should still try to understand the details of the experimental photoemission spectra. A way towards that goal could be to calculate within simple approximations the theoretical spectra which take into account the final states, instead of assuming a free electron final state. This will produce spectra that depend on the photon energy and will give cross sections more accurate than the ones calculated with the atomic orbitals [141] within Hartree-Fock. This will allow one to evaluate the momentum of the extracted electron before the interaction with the photon more precisely than with the assumed free electron final state. Besides this, a point of the experimental spectra that is not yet fully understood is their surprisingly broadened peaks. This thesis proposes an interpretation for that, either disorder at the surface of the sample or strong electron-lattice coupling. Further calculations or measurements to assess these possible hypothesis would be welcome.

As one could see, there are still a lot of additional calculations and developments that could be made starting from the present manuscript. I would have desired to do them all on my own, before the end of my thesis. Of course, one should stop somewhere, but it is difficult to write down the final point of this three year long study. I hope this work will be used as a basis for future developments, for me or for my collaborators.

Palaiseau, 18th October 2005

Appendices

Appendix A

Fourier transforms

This chapter is not intended to be a extended review on Fourier transforms. It will just provide useful relations for understanding the manuscripts, and give as by-product, general solid-state results, as the Bloch theorem.

A.1   General definitions

The definition of the Fourier transform of a general function f is

$$\tilde{f}(\omega) = \int dt\, f(t) e^{-i\omega t} \tag{A.1a}$$

and the reverse Fourier transform is

$$f(t) = \frac{1}{2\pi} \int d\omega\, \tilde{f}(\omega) e^{i\omega t}. \tag{A.1b}$$

Let us apply this general definition to the peculiar case of periodic functions. Consider a function f of period T. From equation (A.1a),

$$
\begin{aligned}
\tilde{f}(\omega) &= \int dt\, f(t) e^{-i\omega t} \\
&= \sum_{n\in\mathbb{Z}} \int_{-\frac{T}{2}+nT}^{\frac{T}{2}+nT} dt\, f(t) e^{-i\omega t} \\
&= \int_{-\frac{T}{2}}^{\frac{T}{2}} dt\, f(t) e^{-i\omega t} \sum_{n\in\mathbb{Z}} e^{-in\omega T} \tag{A.2}
\end{aligned}
$$

The last line arises from the variable change $t' = t - nT$ and from the periodicity of $f(t)$. The last sum is non zero, if and only if ωT is a multiple of 2π. This defines discrete values

$$\omega_n = \frac{2\pi}{T} n, \tag{A.3}$$

the so-called reciprocal lattice, were Fourier coefficient are non-vanishing. The Fourier transform of a periodic function is nothing but a Fourier series:

$$\tilde{f}(\omega_n) = \int_{-\frac{T}{2}}^{\frac{T}{2}} dt f(t) e^{-i\omega_n t} \tag{A.4a}$$

and

$$f(t) = \frac{1}{T} \sum_{n\in\mathbb{Z}} \tilde{f}(\omega_n) e^{i\omega_n t}. \tag{A.4b}$$

Let us take the limit $T \to \infty$, and recover the standard Fourier transform. First, it is obvious that expression (A.4a) tends to equation (A.1a). Second, when T increases, the distance between ω_n vanishes and the sum in equation (A.4b) tends to the integral (as it is a Riemann sum):

$$f(t) = \frac{1}{T} \int_{-\infty}^{+\infty} \frac{d\omega}{d\omega/dn} \tilde{f}(\omega) e^{i\omega t}. \tag{A.5}$$

As $d\omega/dn = 2\pi/T$, this derivation yields exactly the original expression for the reverse Fourier transform in equation (A.1b).

It is straightforwardly extended to three-dimensional periodic functions with periods $\mathbf{a}_1$, $\mathbf{a}_2$, $\mathbf{a}_3$:

$$f(\mathbf{r}) = \frac{1}{\Omega} \sum_{\mathbf{G}} \tilde{f}(\mathbf{G}) e^{i\mathbf{G}.\mathbf{r}} \tag{A.6a}$$

and, reversely,

$$\tilde{f}(\mathbf{G}) = \int_{\Omega} d\mathbf{r} f(\mathbf{r}) e^{-i\mathbf{G}.\mathbf{r}}, \tag{A.6b}$$

where Ω designates the unit cell (or its volume), and where $\mathbf{G}$ are vectors of the so-called reciprocal lattice, spanned by $\mathbf{b}_1$, $\mathbf{b}_2$, $\mathbf{b}_3$:

$$\mathbf{G} = n_1\mathbf{b}_1 + n_2\mathbf{b}_2 + n_3\mathbf{b}_3, \quad \text{with } \{n_1, n_2, n_3\} \in \mathbb{Z}^3. \tag{A.7}$$

A.2 One-index functions of a crystal, Born-von Karman conditions, and Bloch theorem

A crystal has periodic structure, with a unit cell Ω repeated along 3 directions. Therefore, all observables of a crystal are invariant by application of the same translations. Nevertheless, wavefunctions are not observable, and, by consequence, are not periodic functions of $\mathbf{a}_1$, $\mathbf{a}_2$, $\mathbf{a}_3$.

Born-von Karman condition is an assumption on the boundary condition experienced by functions in a crystal: all functions $f(\mathbf{r})$ are considered as

periodic in a large volume $V = N_1 N_2 N_3 \Omega$. N_i designates the number of unit cells contained in the large volume in the i direction. Therefore, the Fourier transform $\tilde{f}(\mathbf{K})$ of any of these functions is a Fourier series, where $\mathbf{K}$ vector are restricted to

$$\mathbf{K} = \frac{n_1}{N_1}\mathbf{b_1} + \frac{n_2}{N_2}\mathbf{b_2} + \frac{n_3}{N_3}\mathbf{b_3}, \quad \text{with } \{n_1, n_2, n_3\} \in \mathbb{Z}^3. \qquad (A.8)$$

It is furthermore useful to decompose the vector $\mathbf{K}$ as a crystal reciprocal lattice vector $\mathbf{G}$ plus a vector $\mathbf{k}$ that belongs to the first Brillouin zone. Then,

$$f(\mathbf{r}) = \frac{1}{V} \sum_{\mathbf{k},\mathbf{G}} \tilde{f}(\mathbf{k} + \mathbf{G}) e^{i(\mathbf{k}+\mathbf{G}).\mathbf{r}} \qquad (A.9)$$

and reversely,

$$\tilde{f}(\mathbf{k} + \mathbf{G}) = \int_V d\mathbf{r} f(\mathbf{r}) e^{-i(\mathbf{k}+\mathbf{G}).\mathbf{r}}. \qquad (A.10)$$

In particular, a wavefunction $\phi(\mathbf{r})$ that satisfies Born-Von Karman conditions can be written as a sum of wavefunctions $\phi_\mathbf{k}(\mathbf{r})$ with a definite $\mathbf{k}$ momentum:

$$\phi(\mathbf{r}) = \sum_{\mathbf{k}} \phi_\mathbf{k}(\mathbf{r}), \qquad (A.11)$$

where $\phi_\mathbf{k}(\mathbf{r})$ simply reads

$$\phi_\mathbf{k}(\mathbf{r}) = \sum_{\mathbf{G}} \tilde{\phi}_\mathbf{k}(\mathbf{G}) e^{i\mathbf{G}.\mathbf{r}} e^{i\mathbf{k}.\mathbf{r}}. \qquad (A.12)$$

Since $\mathbf{G}$ vectors are reciprocal lattice vectors, the function $u_\mathbf{k}$,

$$u_\mathbf{k}(\mathbf{r}) = \sum_{\mathbf{G}} c_\mathbf{k}(\mathbf{G}) e^{i\mathbf{G}.\mathbf{r}}, \qquad (A.13)$$

has the periodicity of the unit cell. The coefficient $c_\mathbf{k}$ are consistently defined by

$$\begin{aligned} c_\mathbf{k}(\mathbf{G}) &= \frac{1}{V} \int_V d\mathbf{r}\, u_\mathbf{k}(\mathbf{r}) e^{-i\mathbf{G}.\mathbf{r}} \\ &= \frac{1}{\Omega} \int_\Omega d\mathbf{r}\, u_\mathbf{k}(\mathbf{r}) e^{-i\mathbf{G}.\mathbf{r}}, \end{aligned} \qquad (A.14)$$

where the periodicity of function $u_\mathbf{k}$ has been used to reduce the volume of the integral to a single unit cell.

As a consequence, the wavefunctions $\phi_\mathbf{k}(\mathbf{r})$ are simply the product of a phase factor $e^{i\mathbf{k}.\mathbf{r}}$ and of a periodic function of the unit cell $u_\mathbf{k}(\mathbf{r})$. This is nothing else but the Bloch theorem.

As a by-product, one can notice that the number of $\mathbf{k}$-points $N_\mathbf{k}$ allowed in the first Brillouin zone is given by $-N_i/2 < n_i \leq N_i/2$ in equation (A.8). The number of $\mathbf{k}$-points is therefore equal to $N_1 N_2 N_3$.

A.3   Two-index periodic functions of a crystal

The Fourier transform of a periodic two-index quantity should be expressed as

$$f(\mathbf{r}_1, \mathbf{r}_2) = \frac{1}{V} \sum_{\mathbf{q}_1 \mathbf{q}_2} \sum_{\mathbf{G}_1, \mathbf{G}_2} e^{i(\mathbf{q}_1 + \mathbf{G}_1).\mathbf{r}_1} \tilde{f}(\mathbf{q}_1 + \mathbf{G}_1, \mathbf{q}_2 + \mathbf{G}_2) e^{-i(\mathbf{q}_2 + \mathbf{G}_2).\mathbf{r}_2}, \quad \text{(A.15)}$$

where $\mathbf{q}_1$ and $\mathbf{q}_2$ are restricted to the first Brillouin zone. But, thanks to the translationaly invariance of the crystal, this can be simplified: let us show that, indeed, only one $\mathbf{q}$ vector is needed. For any vector $\mathbf{R}$ of the direct lattice, the equality

$$f(\mathbf{r}_1 + \mathbf{R}, \mathbf{r}_2 + \mathbf{R}) = f(\mathbf{r}_1, \mathbf{r}_2) \quad \text{(A.16)}$$

holds and its Fourier transform reads

$$\sum_{\mathbf{q}_1 \mathbf{q}_2} \sum_{\mathbf{G}_1, \mathbf{G}_2} e^{i(\mathbf{q}_1 + \mathbf{G}_1).(\mathbf{r}_1 + \mathbf{R})} \tilde{f}(\mathbf{q}_1 + \mathbf{G}_1, \mathbf{q}_2 + \mathbf{G}_2) e^{-i(\mathbf{q}_2 + \mathbf{G}_2).(\mathbf{r}_2 + \mathbf{R})}$$

$$= \sum_{\mathbf{q}_1 \mathbf{q}_2} \sum_{\mathbf{G}_1, \mathbf{G}_2} e^{i(\mathbf{q}_1 + \mathbf{G}_1).\mathbf{r}_1} \tilde{f}(\mathbf{q}_1 + \mathbf{G}_1, \mathbf{q}_2 + \mathbf{G}_2) e^{-i(\mathbf{q}_2 + \mathbf{G}_2).\mathbf{r}_2}. \quad \text{(A.17)}$$

By definition of a reciprocal lattice vector, $e^{i\mathbf{G}.\mathbf{R}}$ is equal to 1. Hence, equation (A.17) becomes:

$$\sum_{\mathbf{q}_1 \mathbf{q}_2} \left(e^{i(\mathbf{q}_1 - \mathbf{q}_2).\mathbf{R}} - 1 \right)$$

$$\times \sum_{\mathbf{G}_1, \mathbf{G}_2} e^{i(\mathbf{q}_1 + \mathbf{G}_1).\mathbf{r}_1} \tilde{f}(\mathbf{q}_1 + \mathbf{G}_1, \mathbf{q}_2 + \mathbf{G}_2) e^{-i(\mathbf{q}_2 + \mathbf{G}_2).\mathbf{r}_2} = 0. \quad \text{(A.18)}$$

Then, for any direct lattice vector $\mathbf{R}$,

$$e^{i(\mathbf{q}_1 - \mathbf{q}_2).\mathbf{R}} = 1 \quad \text{(A.19)}$$

means that $\mathbf{q}_1 - \mathbf{q}_2$ is a reciprocal lattice vector. As $\mathbf{q}_1$ and $\mathbf{q}_2$ are restricted to the first Brillouin zone, $\mathbf{q}_1 - \mathbf{q}_2 = 0$.

Finally, the expression of any two-index function of a crystal can be cast as

$$f(\mathbf{r}_1, \mathbf{r}_2) = \frac{1}{V} \sum_{\mathbf{q}} \sum_{\mathbf{G}_1, \mathbf{G}_2} e^{i(\mathbf{q} + \mathbf{G}_1).\mathbf{r}_1} \tilde{f}_{\mathbf{G}_1, \mathbf{G}_2}(\mathbf{q}) e^{-i(\mathbf{q} + \mathbf{G}_2).\mathbf{r}_2} \quad \text{(A.20a)}$$

with

$$\tilde{f}_{\mathbf{G}_1, \mathbf{G}_2}(\mathbf{q}) = \frac{1}{V} \int_V d\mathbf{r}_1 d\mathbf{r}_2 \; e^{-i(\mathbf{q} + \mathbf{G}_1).\mathbf{r}_1} f(\mathbf{r}_1, \mathbf{r}_2) e^{i(\mathbf{q} + \mathbf{G}_2).\mathbf{r}_2}. \quad \text{(A.20b)}$$

This section provides all the tools needed to express the Fourier transform of one-index periodic functions, as the electron density, the Fourier transform of one-index non-periodic functions, as the mono-electronic wavefunctions, and the Fourier transform of two-index periodic functions, as the response functions.

A.4   Fourier transform convention

Throughout the text, we use the following convention for Fourier transform with respect to time and space:

$$\tilde{f}(\mathbf{k}, \omega) = \int d\mathbf{r} dt \ f(\mathbf{r}, t) e^{-i(\mathbf{k}.\mathbf{r} - \omega t)} \tag{A.21a}$$

and the reverse Fourier transform is

$$f(\mathbf{r}, t) = \frac{1}{(2\pi)^4} \int d\mathbf{k} d\omega \ \tilde{f}(\mathbf{k}, \omega) e^{i(\mathbf{k}.\mathbf{r} - \omega t)}. \tag{A.21b}$$

Appendix B

Functional analysis

Here are some useful definitions of functional analysis (from reference [15]).
Definition of the inverse:

$$\int d3 F(1,3) F^{-1}(3,2) = \int d3 F^{-1}(1,3) F(3,2) = \delta(1,2). \qquad (B.1)$$

Derivative of the product:

$$\frac{\delta(F(1)G(2))}{\delta H(3)} = \frac{\delta F(1)}{\delta H(3)} G(2) + F(1) \frac{\delta G(2)}{\delta H(3)} \qquad (B.2)$$

Derivative of the inverse:

$$\frac{\delta F(1,2)}{\delta G(3)} = -\int d45 F(1,4) \frac{\delta F^{-1}(4,5)}{\delta G(3)} F(5,2). \qquad (B.3)$$

Chain rule:

$$\frac{\delta F[G[H]](1)}{\delta H(2)} = \int d3 \frac{\delta F[G](1)}{\delta G(3)} \frac{\delta G[H](3)}{\delta H(2)}. \qquad (B.4)$$

Appendix C

Link to time-dependent exact-exchange

This appendix provides the detail of the calculation mentioned in chapter 9, where the derived equations are claimed to yield precisely the same expression as the exact-exchange kernel of Kim and Görling [77].

Introducing all indexes in equation (9.20) gives

$$
\int d24\chi_{\text{KS}}(1,2)f_{xc}^{(1)}(2,4)\chi_{\text{KS}}(4,6) =
$$

$$
= -iG_{\text{KS}}(1,6)\int d35G_{\text{KS}}(6,5)(\Sigma_x(5,3) - v_{xc}(5)\delta(5,3))G_{\text{KS}}(5,1)
$$

$$
- iG_{\text{KS}}(6,1)\int d24G_{\text{KS}}(1,2)(\Sigma_x(2,4) - v_{xc}(4)\delta(2,4))G_{\text{KS}}(4,6) \quad \text{(C.1)}
$$

and in equation (9.22)

$$
\int d24\chi_{\text{KS}}(1,2)f_{xc}^{(2)}(2,4)\chi_{\text{KS}}(4,6) =
$$

$$
= \int d23G_{\text{KS}}(1,2)G_{\text{KS}}(3,1)v(2,3)G_{\text{KS}}(2,6)G_{\text{KS}}(6,3). \quad \text{(C.2)}
$$

For simplification, let us name T_1^a the first term of $\chi_{\text{KS}}f_{xc}^{(1)}\chi_{\text{KS}}$, T_1^b the second one, and $T_2 = \chi_{\text{KS}}f_{xc}^{(2)}\chi_{\text{KS}}$.

By introducing the expression of G_{KS}

$$
G_{\text{KS}}(\mathbf{r}_1,\mathbf{r}_2,\omega) = \sum_i \frac{\phi_i(\mathbf{r}_1)\phi_i^*(\mathbf{r}_2)}{\omega - \epsilon_i - i\operatorname{sign}(\mu - \epsilon_i)\eta}, \quad \text{(C.3)}
$$

where ϕ_i and ϵ_i are the Kohn-Sham wavefunctions and energies for index i (that contains also the $\mathbf{k}$-point information), into the definition T_1^a, T_1^b and T_2 will finally give the different parts of the TDEXX.

C.1   Calculation of T_2

Let us first deal with T_2 that reads after Fourier transform into frequency domain

$$T_2(\mathbf{r}_1, \mathbf{r}_6, \omega) = \frac{1}{(2\pi)^2} \sum_{ijkl} \phi_i(\mathbf{r}_1)\phi_j^*(\mathbf{r}_1) \int d\omega_1 \frac{1}{(\omega + \omega_1 - \epsilon_i)(\omega_1 - \epsilon_j)}$$

$$\times \langle ik|v|jl \rangle \phi_k^*(\mathbf{r}_6)\phi_l(\mathbf{r}_6) \int d\omega_2 \frac{1}{(\omega + \omega_2 - \epsilon_k)(\omega_2 - \epsilon_l)}, \quad \text{(C.4)}$$

as the products in time space have become convolutions of frequencies. The Coulomb integral

$$\langle ik|v|jl \rangle = \int d\mathbf{r}_2 d\mathbf{r}_3 \phi_i^*(\mathbf{r}_2)\phi_k(\mathbf{r}_2) \frac{1}{|\mathbf{r}_1 - \mathbf{r}_2|} \phi_j(\mathbf{r}_3)\phi_l^*(\mathbf{r}_3) \quad \text{(C.5)}$$

has been introduced. The $\pm\eta$ factors in the denominators are still here, but not written, since they are unchanged with respect to the definition of G_{KS}.

Now the frequency integrals are performed thanks to the residue theorem on a path, either closed in the upper plane, or closed in the lower plane. Contributions with all poles in the same half-plane are null, as used in the derivation of χ_0 in chapter 5. Finally,

$$\int d\omega_1 \frac{1}{(\omega + \omega_1 - \epsilon_i)(\omega_1 - \epsilon_j)} = 2\pi i \frac{f_j - f_i}{\omega - (\epsilon_i - \epsilon_j) + i\eta \operatorname{sign}(f_j - f_i)} \quad \text{(C.6)}$$

and hence

$$T_2(\mathbf{r}_1, \mathbf{r}_6, \omega) = -\sum_{ijkl} (f_j - f_i) \frac{\phi_i(\mathbf{r}_1)\phi_j^*(\mathbf{r}_1)}{\omega - (\epsilon_i - \epsilon_j) + i\eta \operatorname{sign}(f_j - f_i)}$$

$$\times \langle ik|v|jl \rangle (f_l - f_k) \frac{\phi_k^*(\mathbf{r}_6)\phi_l(\mathbf{r}_6)}{\omega - (\epsilon_k - \epsilon_l) + i\eta \operatorname{sign}(f_l - f_k)}. \quad \text{(C.7)}$$

This expression for T_2 is similar to the H_X^1 and H_X^2 terms of reference [77], except that the small $i\eta$ factors for antiresonant terms are opposite. In fact, the present derivation gives time-ordered quantities, and the Kim and Görling one ends with causal quantities. This difference is not felt the imaginary part at positive frequencies.

C.2   Calculation of T_1^a and T_1^b

Let us now turn to T_1^a contribution to the TDDFT kernel. Σ_x is a static approximation for the self-energy, hence in the frequency space, T_1^a reads

$$T_1^a(\mathbf{r}_1, \mathbf{r}_6, \omega) = -\frac{i}{2\pi} \sum_{ijk} \int d\omega_1 \frac{\phi_i(\mathbf{r}_1)\phi_i^*(\mathbf{r}_6)}{\omega + \omega_1 - \epsilon_i}$$

$$\times \frac{\phi_j(\mathbf{r}_6)}{\omega_1 - \epsilon_j} \langle j|\Sigma_x - v_{xc}|k \rangle \frac{\phi_k^*(\mathbf{r}_1)}{\omega_1 - \epsilon_k}, \quad \text{(C.8)}$$

where the $\pm i\eta$ factors in the denominators were omitted for conciseness.

Performing the integration on ω_1 thanks to residue theorem gives a vanishing contribution if the i, j, k states are all occupied or all empty. If i and j are occupied and k is empty, let us close the path of integration in the lower half plane. The obtained poles are the $\epsilon_k - i\eta$ and yield the residues:

$$-2\pi i \frac{\theta(\mu - \epsilon_i)\theta(\mu - \epsilon_j)\theta(\epsilon_k - \mu)}{(\omega - (\epsilon_i - \epsilon_k) - 2i\eta)(\epsilon_k - \epsilon_j)}. \tag{C.9}$$

If i and k are occupied and j is empty, closing the path analogously in the lower half plane retains the poles $\epsilon_j - i\eta$ and gives the residues:

$$-2\pi i \frac{\theta(\mu - \epsilon_i)\theta(\epsilon_j - \mu)\theta(\mu - \epsilon_k)}{(\omega - (\epsilon_i - \epsilon_j) - 2i\eta)(\epsilon_j - \epsilon_k)}. \tag{C.10}$$

If j et k are occupied and i is empty, this gives poles on $\epsilon_i - \omega - i\eta$ and residues:

$$2\pi i \frac{\theta(\mu - \epsilon_i)\theta(\epsilon_j - \mu)\theta(\epsilon_k - \mu)}{(\omega - (\epsilon_i - \epsilon_j) - 2i\eta)(\omega - (\epsilon_i - \epsilon_k) - 2i\eta)}. \tag{C.11}$$

Now, there is 3 other terms for 2 empty states and 1 occupied. The path of integration will be closed in the upper half plane, in order to retain only the poles from occupied states. T_1^a finally gives rise to 6 terms. T_1^b will account for 6 analogous terms. The sum of T_1^a and T_1^b if written extensively is exactly the terms $H_X^3 + H_X^4$ of Kim and Görling, except once more that the small $i\eta$ factors are changed for antiresonant transitions.

This appendix showed that the first-order kernel, plus linearization of the Green's function G into G_{KS} applied on the Fock self-energy gives precisely the time-dependent exact-exchange kernel of reference [77].

List of Publications

- *TDDFT from molecules to solids: the role of long-range interactions*,
  F. Sottile, F. Bruneval, A. G. Marinopoulos, L. K. Dash, S. Botti,
  V. Olevano, N. Vast, A. Rubio, and L. Reining,
  Int. J. Quant. Chem. **102**, 684 (2005).

- *Many-body perturbation theory using the density-functional concept:
  beyond the GW approximation*,
  F. Bruneval, F. Sottile, V. Olevano, R. Del Sole, and L. Reining,
  Phys. Rev. Lett. **94**, 186402 (2005).

- *A brief introduction to the ABINIT software package*,
  X. Gonze, G.-M. Rignanese, M. Verstraete, J.-M. Beuken, Y. Pouillon,
  R. Caracas, F. Jollet, M. Torrent, G. Zerah, M. Mikami, Ph. Ghosez,
  M. Veithen, J.-Y. Raty, V. Olevano, F. Bruneval, L. Reining, R. W. Godby,
  G. Onida, D. R. Hamann, and D. C. Allan,
  Z. Kristallogr. **220**, 558 (2005).

- *Many-Body Perturbation Theory Using the Density-Functional Concept*,
  F. Bruneval, F. Sottile, V. Olevano, R. Del Sole, and L. Reining,
  Psi-k Newsletter No. **69** (June 2005).

- *Comment on "Quantum Confinement and Electronic Properties
  of Silicon Nanowires"*,
  F. Bruneval, S. Botti, and L. Reining,
  Phys. Rev. Lett. **94** 219701 (2005).

- *Electronic excitations: ab initio calculations of electronic spectra and
  application to zirconia ZrO_2, titania TiO_2 and cuprous oxide Cu_2O*
  L. K. Dash, F. Bruneval, V. Quequet, N. Vast, and L. Reining,
  Comp. Mat. Sci. (2005) *submitted*.

- *Effect of self-consistency on quasiparticles in solids*
  F. Bruneval, N. Vast, and L. Reining, *in preparation*.

- *Electronic excitations of Cu_2O: theory and experiment*
  F. Bruneval, N. Vast, L. Reining, M. Izquierdo, F. Sirotti, and N. Barrett,
  in preparation.

- *Ab initio simulation of IXSS*
  H.-C. Weissker, J. Serrano, F. Bruneval, F. Sottile, V. Olevano, L. Reining, S. Huotari, G. Monaco, and M. Krich, *in preparation.*

- *Creation, annihilation of poles within TDDFT*
  F. Bruneval, F. Sottile, V. Olevano, and L. Reining, *in preparation.*

- *Beyond time-dependent exact-exchange: the need for correlation*
  F. Bruneval, F. Sottile, V. Olevano, and L. Reining, *in preparation.*

- *Using the density functional concept in many-body perturbation theory: obstacles and progress*
  F. Bruneval, F. Sottile, V. Olevano, R. van Leeuwen, R. Del Sole, and L. Reining, *in preparation.*

Bibliography

[1] P. W. Baumeister, Phys. Rev. **121**, 359 (1961).

[2] M. Balkanski, Y. Petroff, and D. Trivich, Sol. State Com. **5**, 85 (1967).

[3] S. Brahms, S. Nikitine, and J. P. Dahl, Phys. Lett. **22**, 31 (1966).

[4] L. Reining, V. Olevano, A. Rubio, and G. Onida, Phys. Rev. Lett. **88**, 066404 (2002).

[5] F. Sottile, Ph.D. thesis, Ecole Polytechnique, Palaiseau, France (2003).

[6] F. Sottile, V. Olevano, and L. Reining, Phys. Rev. Lett. **91**, 056402 (2004).

[7] E. K. U. Gross, E. Runge, and O. Heinonen, *Many-Particule Theory* (Adam Hilger, Bristol, Philadelphia and New-York, 1986).

[8] W. M. C. Foulkes, L. Mitas, R. J. Needs, and G. Rajagopal, Rev. Mod. Phys. **73**, 33 (2001).

[9] G. Grosso and G. P. Parravicini, *Solid State Physics* (Academic Press, San Diego, London, 2000).

[10] F. Murnaghan, Proc. Nat. Acad. Sci. USA **30**, 244 (1944).

[11] A. L. Fetter and J. D. Walecka, *Quantum Theory of Many-Particule Systems* (Dover, Mineola, New York, 1971, 2003).

[12] V. M. Galitskii and A. B. Migdal, Sov. Phys.-JETP **7**, 96 (1958).

[13] L. J. Sham and M. Schlüter, Phys. Rev. Lett. **51**, 1888 (1983).

[14] L. Hedin, J. Phys.: Condens. Matter **11**, R489 (1999).

[15] G. Strinati, Rivista del Nuovo Cimento **11**, 1 (1988).

[16] M. Causà, R. Dovesi, and C. Roetti, Phys. Rev. B **43**, 11937 (1991).

[17] R. W. G. Wyckoff, *Crystal Structures*, vol. 1 (Wiley, New York, 1965).

[18] E. Ruiz, S. Alvarez, P. Alemany, and R. Evarestov, Phys. Rev. B **56**, 7189 (1997).

[19] M. M. Beg and S. M. Shapiro, Phys. Rev. B **13**, 1728 (1976).

[20] S. Massida, M. Posternak, and A. Baldereschi, Phys. Rev. B **48**, 5058 (1993).

[21] Landolt and Börnstein, *Numerical Data and Functional Relationships in Science and Technology* (Springer, Berlin, 1982).

[22] S. Baroni, G. Grosso, and G. P. Parravicini, Phys. Rev. B **23**, 6441 (1981).

[23] Phys. Rev. Lett. **23**, 1160 (1969).

[24] S. Galamić-Mulaomerović, Ph.D. thesis, Department of Physics, Trinity College, University of Dublin, Dublin, Ireland (2004).

[25] L. Hedin, Phys. Rev. **139**, A796 (1965).

[26] J. Hubbard, Proc. Roy. Soc. **A240**, 539 (1957).

[27] V. Olevano, oral tradition (2000).

[28] F. Aryasetiawan and O. Gunnarsson, Rep. Prog. Phys. **61**, 237 (1998).

[29] W. G. Aulbur, L. Jönsson, and J. W. Wilkins, Solid State Phys. **54**, 1 (1999).

[30] P. Lautenschlager, M. Garriga, L. Vina, and M. Cardona, Phys. Rev. B **36**, 4821 (1987).

[31] S. L. Adler, Phys. Rev. **126**, 413 (1962).

[32] N. Wiser, Phys. Rev. **129**, 62 (1963).

[33] W. Hanke and L. J. Sham, Phys. Rev. Lett. **43**, 387 (1979).

[34] W. Hanke and L. J. Sham, Phys. Rev. B **21**, 4656 (1980).

[35] G. Onida, L. Reining, and A. Rubio, Rev. Mod. Phys. **74**, 601 (2002).

[36] G. Onida, L. Reining, R. W. Godby, R. Del Sole, and W. Andreoni, Phys. Rev. Lett. **75**, 818 (1995).

[37] M. Rohlfing and S. G. Louie, Phys. Rev. Lett. **83**, 856 (1999).

[38] S. Albrecht, L. Reining, R. Del Sole, and G. Onida, Phys. Rev. Lett. **80**, 4510 (1998).

[39] L. X. Benedict, E. L. Shirley, and R. B. Bohn, Phys. Rev. Lett. **80**, 4514 (1998).

[40] F. Bechstedt, K. Tenelsen, B. Adolph, and R. Del Sole, Phys. Rev. Lett. **78**, 1528 (1997).

[41] A. Marini and R. Del Sole, Phys. Rev. Lett. **91**, 176402 (2003).

[42] L. H. Thomas, Proc. Cambridge Phil. Soc. **23**, 542 (1927).

[43] E. Fermi, Rend. Accad. Naz. Linzei **6**, 602 (1927).

[44] P. Hohenberg and W. Kohn, Phys. Rev. **136**, B864 (1964).

[45] R. M. Dreizler and E. K. U. Gross, *Density Functional Theory* (Springer-Verlag, Berlin, 1990).

[46] W. Kohn and L. J. Sham, Phys. Rev. **140**, A1133 (1965).

[47] D. M. Ceperley and B. J. Alder, Phys. Rev. Lett. **45**, 566 (1980).

[48] J. P. Perdew and A. Zunger, Phys. Rev. B **23**, 5048 (1981).

[49] J. P. Perdew and Y. Wang, Phys. Rev. B **33**, 8800 (1986).

[50] R. O. Jones and O. Gunnarsson, Rev. Mod. Phys. **61**, 689 (1989).

[51] J. P. Perdew, K. Burke, and M. Ernzerhof, Phys. Rev. Lett. **77**, 3865 (1996).

[52] J. P. Perdew, S. Kurth, A. Zupan, and P. Blaha, Phys. Rev. Lett. **82**, 2544 (1999).

[53] M. Fuchs and X. Gonze, Phys. Rev. B **65**, 235109 (2002).

[54] A. Zangwill and P. Soven, Phys. Rev. A **21**, 1561 (1980).

[55] E. Runge and E. K. U. Gross, Phys. Rev. Lett. **52**, 997 (1984).

[56] M. A. L. Marques and E. K. U. Gross, Annu. Rev. Phys. Chem. **55**, 427 (2004).

[57] R. van Leeuwen, Phys. Rev. Lett. **80**, 1280 (1998).

[58] R. van Leeuwen, Int. J. Mod. Phys. B **15**, 1969 (2001).

[59] E. K. U. Gross and W. Kohn, Phys. Rev. Lett. **55**, 2850 (1985).

[60] F. Sottile, F. Bruneval, A. G. Marinopoulos, L. K. Dash, S. Botti, V. Olevano, N. Vast, A. Rubio, and L. Reining, Int. J. Quant. Chem. **102**, 684 (2005).

[61] F. Bruneval, S. Botti, and L. Reining, Phys. Rev. Lett. **94**, 219701 (2005).

[62] N. Vast, L. Reining, V. Olevano, P. Schattschneider, and B. Jouffrey, Phys. Rev. Lett. **88**, 037601 (2002).

[63] P. Ghosez, X. Gonze, and R. W. Godby, Phys. Rev. B **56**, 12811 (1997).

[64] G. Adragna, R. Del Sole, and A. Marini, Phys. Rev. B **68**, 165108 (2003).

[65] I. V. Tokatly, R. Stubner, and O. Pankratov, Phys. Rev. B **65**, 113107 (2002).

[66] S. Botti, F. Sottile, N. Vast, V. Olevano, H.-C. Weissker, L. Reining, G. Onida, A. Rubio, R. W. Godby, and R. D. Sole, Phys. Rev. B **69**, 155112 (2004).

[67] URL `http://www.abinit.org/`.

[68] URL `http://theory.polytechnique.fr/codes/dp/`.

[69] X. Gonze, G.-M. Rignanese, M. Verstraete, J.-M. Beuken, Y. Pouillon, R. Caracas, F. Jollet, M. Torrent, G. Zerah, M. Mikami, P. Ghosez, M. Veithen, J.-Y. Raty, V. Olevano, F. Bruneval, L. Reining, R. W. Godby, G. Onida, D. R. Hamann, and D. C. Allan, Z. Kristallogr. **220**, 558 (2005).

[70] M. S. Hybertsen and S. G. Louie, Phys. Rev. B **34**, 5390 (1986).

[71] L. J. Sham and W. Kohn, Phys. Rev. **145**, 561 (1966).

[72] L. J. Sham and M. Schlüter, Phys. Rev. B **32**, 3883 (1985).

[73] R. W. Godby, M. Schlüter, and L. J. Sjam, Phys. Rev. Lett. **56**, 2415 (1986).

[74] Y. M. Niquet, M. Fuchs, and X. Gonze, J. Chem. Phys. **118**, 9504 (2003).

[75] A. Görling, Phys. Rev. B **53**, 7024 (1996).

[76] W. G. Aulbur, M. Städele, and A. Görling, Phys. Rev. B **62**, 7121 (2000).

[77] Y.-H. Kim and A. Görling, Phys. Rev. B **66**, 035114 (2002).

[78] Y.-H. Kim and A. Görling, Phys. Rev. Lett. **89**, 096402 (2002).

[79] A. Marini, R. Del Sole, and A. Rubio, Phys. Rev. Lett. **91**, 256402 (2003).

[80] R. Stubner, I. V. Tokatly, and O. Pankratov, Phys. Rev. B **70**, 245119 (2004).

[81] M. S. Hybertsen and S. G. Louie, Phys. Rev. Lett. **55**, 1418 (1985).

[82] S. Lebègue, B. Arnaud, M. Alouani, and P. E. Bloechl, Phys. Rev. B **67**, 155208 (2003).

[83] F. Aryasetiawan, Phys. Rev. B **46**, 13051 (1992).

[84] M. M. Rieger, L. Steinbeck, I. D. White, H. N. Rojas, and R. W. Godby, Comp. Phys. Com. **117**, 211 (1999).

[85] A. Fleszar and W. Hanke, Phys. Rev. B **56**, 10228 (1997).

[86] J. E. Ortega and F. J. Himpsel, Phys. Rev. B **47**, 2130 (1993).

[87] B. Holm and U. von Barth, Phys. Rev. B **57**, 2108 (1998).

[88] W. Ku and A. G. Eguiluz, Phys. Rev. Lett. **89**, 126401 (2002).

[89] W. Ku, Ph.D. thesis, University of Tennessee, Knoxville, Tennessee, USA (2000).

[90] S. V. Faleev, M. van Schilfgaarde, and T. Kotani, Phys. Rev. Lett. **93**, 126406 (2004).

[91] L. Hedin and S. Lundqvist, Solid State Phys. **23**, 1 (1969).

[92] P. Rinke, A. Qteish, J. Neugebauer, C. Freysoldt, and M. Scheffler, New J. of Phys. (2005), to be published.

[93] F. Gygi and A. Baldereschi, Phys. Rev. B **34**, 4405 (1986).

[94] S. Baroni, G. Grosso, and G. P. Parravicini, Phys. Rev. B **29**, 2891 (1983).

[95] R. van Leeuwen, Phys. Rev. Lett. **76**, 3610 (1996).

[96] F. Bruneval, F. Sottile, V. Olevano, R. Del Sole, and L. Reining, Phys. Rev. Lett. **94**, 186402 (2005).

[97] E. L. Shirley and R. M. Martin, Phys. Rev. B **47**, 15404 (1993).

[98] Y. Takada, Phys. Rev. Lett. **87**, 226402 (2001).

[99] R. Del Sole, L. Reining, and R. W. Godby, Phys. Rev. B **49**, 8024 (1994).

[100] G. D. Mahan and B. E. Sernelius, Phys. Rev. Lett. **62**, 2718 (1989).

[101] F. Aryasetiawan, L. Hedin, and K. Karlsson, Phys. Rev. Lett. **77**, 2268 (1996).

[102] A. Marini and A. Rubio, Phys. Rev. B **70**, 081103 (2004).

[103] J. M. Zuo, M. Kim, M. O'Keeffe, and J. C. H. Spence, Nature **401**, 49 (1999).

[104] J. M. Zuo, Rep. Prog. Phys. **67**, 2053 (2004).

[105] C. Uihlein, D. Fröhlich, and R. Kenklies, Phys. Rev. B **23**, 2731 (1981).

[106] T. Lippmann and J. R. Schneider, Acta Crystallogr. A **56**, 575 (2000).

[107] R. Laskowski, P. Blaha, and K. Schwarz, Phys. Rev. B **67**, 075102 (2003).

[108] R. J. Elliott, Phys. Rev. **124**, 340 (1961).

[109] L. K. Dash, F. Bruneval, V. Quequet, N. Vast, and L. Reining, Comp. Mat. Sci. (2005), submitted.

[110] URL `http://www.fhi-berlin.mpg.de/th/fhi98md/fhi98PP/`.

[111] M. Fuchs and M. Scheffler, Comput. Phys. Commun. **119**, 67 (1999).

[112] L. K. Dash, N. Vast, P. Baranek, M.-C. Cheynet, and L. Reining, Phys. Rev. B **70**, 245116 (2004).

[113] S. L. Hulbert, B. A. Bunker, F. C. Brown, and P. Pianetta, Phys. Rev. B **30**, 2120 (1984).

[114] M. Rohlfing, P. Krüger, and J. Pollmann, Phys. Rev. Lett. **75**, 3489 (1995).

[115] A. Marini, G. Onida, and R. Del Sole, Phys. Rev. Lett. **88**, 016403 (2002).

[116] N. Troullier and J. L. Martins, Phys. Rev. B **43**, 1993 (1991).

[117] L. Kleinman and D. M. Bylander, Phys. Rev. Lett. **48**, 1425 (1982).

[118] G. B. Bachelet, D. R. Hamann, and M. Schlüter, Phys. Rev. B **26**, 4199 (1982).

[119] A. Marini, G. Onida, and R. Del Sole, Phys. Rev. B **64**, 195125 (2001).

[120] H. J. Monkhorst and J. D. Pack, Phys. Rev. B **13**, 5188 (1976).

[121] A. Martínez-Ruiz, M. G. Moreno, and N. Takeuchi, Solid State Sci. **5**, 291 (2003).

[122] F. Bassani and G. P. Parravicini, *Electronic States and Optical Transitions in Solids* (Pergamon Press, Oxford, 1975).

[123] URL `http://www.pwscf.org/`.

[124] M. Springborg, *Methods of Electronic-Structure Calculations, From Molecules to Solids* (John Wiley & Sons, Chichester, 2000).

[125] V. I. Anisimov, F. Aryasetiawan, and A. I. Lichtenstein, J. Phys.: Condens. Matter **9**, 767 (1997).

[126] J. Ghijsen, L. H. Tjeng, J. van Elp, H. Eskes, J. Westerink, G. A. Sawatzky, and M. T. Czyzyk, Phys. Rev. B **38**, 11322 (1988).

[127] L. Kleinman and K. Mednick, Phys. Rev. B **21**, 1549 (1980).

[128] J. Robertson, Phys. Rev. B **28**, 3378 (1983).

[129] W. Y. Ching, Y.-N. Xu, and K. W. Wong, Phys. Rev. B **40**, 7684 (1989).

[130] B. Arnaud, private communication (2003).

[131] URL `http://www.uam.es/departamentos/ciencias/fismateriac/siesta/`.

[132] J. M. Soler, E. Artacho, J. Gale, A. García, J. Junquera, P. Ordejón, and D. Sánchez-Portal, J. Phys.: Condens. Matter **14**, 2745 (2002).

[133] R. F. W. Bader, *Atoms in Molecules - A Quantum Theory* (Oxford University Press, London, 1990).

[134] A. Georges, G. Kotliar, W. Krauth, and M. J. Rozenberg, Rev. Mod. Phys. **68**, 13 (1996).

[135] J.-L. Li, G.-M. Rignanese, E. K. Chang, X. Blase, and S. G. Louie, Phys. Rev. B **66**, 035102 (2002).

[136] P. E. Blöchl, Phys. Rev. B **50**, 17953 (1994).

[137] K. Delaney, private communication (2004).

[138] A. Damascelli, Phys. Scripta **T109**, 61 (2004).

[139] M. R. Thuler, R. L. Benbow, and Z. Hurych, Phys. Rev. B **26**, 669 (1982).

[140] M. P. Seah and W. A. Dench, Surf. Interface Anal. **1**, 2 (1979).

[141] J. J. Yeh and I. Lindau, Atomic data and nuclear data tables **32**, 1 (1958).

[142] D. A. Shirley, Phys. Rev. B **5**, 4709 (1971).

[143] L. X. Benedict, E. L. Shirley, and R. B. Bohn, Phys. Rev. B **57**, R9385 (1998).

[144] URL http://theory.polytechnique.fr/codes/exc/.

[145] R. W. Godby, M. Schlüter, and L. J. Sjam, Phys. Rev. B **37**, 10159 (1988).

[146] Z.-X. Shen, R. S. List, D. S. Dessau, F. Parmigiani, A. J. Arko, R. Bartlett, B. O. Wells, I. Lindau, and W. E. Spicer, Phys. Rev. B **42**, 8081 (1990).

[147] P. García-González and R. W. Godby, Phys. Rev. B **63**, 075112 (2001).

[148] Y. M. Niquet, M. Fuchs, and X. Gonze, Phys. Rev. A **68**, 032507 (2003).

[149] J. Jung, P. García-González, J. F. Dobson, and R. W. Godby, Phys. Rev. B **70**, 205107 (2004).